ATOMIC ADSORPTIONS ON ACTINIDE SURFACES: PATHWAYS TO NUCLEAR ENERGY

by

DAYLA RENEE MORRISON

Presented to the Faculty of the Graduate School of

The University of Texas at Arlington in Partial Fulfillment

of the Requirements

for the Degree of

MASTER OF SCIENCE IN PHYSICS

THE UNIVERSITY OF TEXAS AT ARLINGTON

August 2012

ACKNOWLEDGEMENTS

I would like to thank everyone that helped me get through the work involved with completing this thesis. Dr. Ray was always available to give advice throughout the entire process. I really appreciate Dr. Ma and Dr. Wang for teaching me how to use the programs necessary for the work. I would also like to thank everyone from the Theoretical Condensed Matter Group that gave advice and criticism to improve my project. That includes Dr. Atta-Fynn, Dr. Dholabhai, Dr. Huda, Mr. Adhikari, Mr. Chen, Ms. Duesman, Ms. Hernandez, Ms. Lee, Ms. Pathak, and Mr. Wanaguru. In addition, I would like to show my appreciation to Dr. Fazleev, Dr. Mohanty, Dr. Ray, Dr. Rubins, and Dr. Zhang for their support and generous words of encouragement. Also, my fiancé was always there supporting me along the way.

August 18, 2012

ABSTRACT

ATOMIC ADSORPTIONS ON ACTINIDE SURFACES:

PATHWAYS TO NUCLEAR

ENERGY

Dayla Renee Morrison, M. S.

The University of Texas at Arlington, 2012

Supervising Professor: Asok Ray

The generalized gradient approximation (GGA) to density functional theory (DFT) and hybrid density functional theory have been used to compute the layer-by-layer properties of γ-uranium (γ-U) in the (100) symmetry. Guided by bulk results which have been analyzed at six different levels of theory, the surface calculations have been performed at the non-magnetic level including spin-orbit coupling. The ground state bulk lattice constant and bulk modulus are found to be 3.46 A and 113.75 GPa, respectively at the non-magnetic with spin-orbit coupling level (NM+SOC) of theory. The monolayer displays a significant shrinking of the "effective" lattice constant of about 23.55% from bulk theoretical values. Further analysis of the change in energy per added "bulk" indicates that after 5 layers the energy stabilizes and does not change by more than 10 mRy. The surface energy and the work function of the γ-U (100) surface are predicted to be 1.56 J/m^2 and 3.24 eV respectively. Electronic density of states plots of atoms located at the surface, subsurface and center of a hexa-layer slab indicate *some* localization of the *5f* electrons

at or near the Fermi level with a gradual trend toward delocalization with increased depth within the slab.

Analysis of the adsorption of a H atom on the (100) surface of a 5 layer slab of bcc γ-U indicates an exothermic reaction with the bridge site as the preferred site with a chemisorption energy of 3.80 ev at the fully relativistic level of theory. H bound to the lattice in interstitial regions was also found to be exothermic in nature, also, with the interstitial bridge site being the most stable at 2.13 ev at the nonmagnetic state with spin-orbit coupling included in the calculation. Two potential wells were found under the surface. Other properties of the H-γ-U system were calculated including the ground state magnetic configuration, change in work function, change in magnetic moment on the surface and change in charge.

Similarly, the adsorption of the O atom on the (100) surface of γ-U was also analyzed. It is found to be an exothermic reaction with chemisorption energy at the most stable bridge site of 8.43 eV including SOC. The preferred magnetic ordering of the atomic spins is nonmagnetic, which does not agree with experimental findings of O adsorption on α-U, indicating the need for further study on the O-γ-u system. The O atom is not likely to diffuse into the solid due to a potential barrier very near the surface of approximately 3 eV. Interstitial binding of the O atom to the lattice is an endothermic reaction indicated by the negative chemisorption energies in those sites. Chemisorption energies at interstitial bridge site came to -0.53 eV with SOC at the nonmagnetic level of theory.

TABLE OF CONTENTS

ACKNOWLEDGEMENTS iii

ABSTRACT iv

LIST OF ILLUSTRATIONS viii

LIST OF TABLES xiv

Chapter Page

1. INTRODUCTION 1

2. THEORY AND COMPUTATIONAL FORMALISM 11

2.1 Density Functional Theory 11

2.1.1 Hohenberg-Kohn Theorem 12

2.1.2 The Method of Constrained Search 15

2.1.3 The Kohn-Sham Method 16

2.1.4 Generalized Gradient Approximation: GGA 21

2.1.5 Hybrid Density Functional Theory 23

2.1.6 Scalar Relativistic Approximations 24

2.2 Computational Formalism 26

2.2.1 Linear Augmented Plane Wave Method: LAPW 27

2.2.2 Augmented Plane Wave Plus lo Method: APW+lo 28

2.2.3 Full Potential and Spin-Orbit Interaction 30

3. QUANTUM SIZE EFFECTS IN THE ELECTRONIC STRUCTURE PROPERTIES OF γ–URANIUM (100) NANOLAYERS……..……31

3.1 Computational Method 31

3.2 Bulk Results and Discussions 33

3.3 Results and Discussion for (100) Nanolayers 43

4. ATOMIC H AND O ADSORPTIONS AND DIFFUSION ON THE γ-U (100) NANOLAYER 56

4.1 Computational Method 56

4.2 Results and Discussions 62

4.2.1 Surface adsorption of H on the (100) γ-U surface 62

4.2.2 Interstitial lattice sites for H inside (100) oriented γ-U slab..... 102

4.2.3 Surface adsorption of O on the (100) γ-U surface..... 124

4.2.4 Interstitial lattice sites for O inside (100) oriented γ-U slab 161

5. CONCLUSIONS 200

APPENDIX

A. OPTIMIZED ATOMIC POSITIONS FOR THE (100) γ-U SLAB AND ITS ADSORBATES……..……..……200

B. FORTRAN CODE FOR CHANGE IN CHARGE DENSITY PLOTS……207

REFERENCES……..209

BIOGRAPHICAL INFORMATION…….……218

LIST OF ILLUSTRATIONS

Figure Page

2.1 Flow-chart for DFT self-consistency loop....21

3.1 Optimization of the lattice constant at the NM DFT level of theory with (b) and without SOC (a)....35

3.2 Optimization of the lattice constant at the NM HYB-DFT level of theory with (b) and without SOC (a)....36

3.3 Optimization of the lattice constant at the FM DFT level of theory with (b) and without SOC (a)....37

3.4 Optimization of the lattice constant at the FM HYB-DFT level of theory with (b) and without SOC (a)....38

3.5 Optimization of the lattice constant at the AFM DFT level of theory with (b) and without SOC (a)....39

3.6 Optimization of the lattice constant at the AFM HYB-DFT level of theory with (b) and without SOC (a)....40

3.7 Density of states for the ground state with experimental ultraviolet photoelectron spectroscopy (UPS-HeII spectrum) data for U bulk metal is plotted in black for comparison [47]....42

3.8 Optimization of the “effective” lattice constant for the monolayer....43

3.9 Optimization of the “effective” lattice constant for the di-layer....44

3.10 Optimization of the “effective” lattice constant for the tri-layer....44

3.11 Optimization of the “effective” lattice constant for the tetra-layer....45

3.12 Optimization of the “effective” lattice constant for the penta-layer....45

3.13 Optimization of the “effective” lattice constant for the hexa-layer....46

3.14 Surface energy per unit area, γ (J/m2) versus the number of layers with and without SOC 51

3.15 Work function (eV) versus the number of layers at the NSOC and SOC levels of theory 53

3.16 Gaussian broadened total density of states plot for the 6-layer slab 54

3.17 Density of states for the surface (a), subsurface (b) and center (c) regions of the 6 layer slab 55

4.1 Top view (left) and side view (right) of the top (a) and (b) center (c) bridge adsorption site on the (100) surface of γ-U 60

4.2 (a) Inner top; (b) inner center; and (c) inner bridge sites under the (100) surface of γ-U 61

4.3 Optimized E_c of H atom at the top site at the NM (a), FM (b) and AFM (c) level 63

4.4 Optimized E_c of H atom at the center site at the NM (a), FM (b) and AFM (c) level 64

4.5 Optimized E_c of H atom at the bridge site at the NM (a), FM (b) and AFM (c) level 65

4.6 Atomic positions for the 1st and 2nd layers 70

4.7 Change in partial charge for the H atom at the NM top site 79

4.8 Change in partial charge for the H atom at the NM center site 80

4.9 Change in partial charge for the H atom at the NM bridge site 81

4.10 Change in partial charge for the H atom at the FM top site 83

4.11 Change in partial charge for the H atom at the FM center site 84

4.12 Change in partial charge for the H atom at the FM bridge site 85

4.13 Change in partial charge for the H atom at the AFM top site 86

4.14 Change in partial charge for the H atom at the AFM center site 87

4.15 Change in partial charge for the H atom at the AFM bridge site 88

4.16 LDOS for the 6*d* and 5*f* electrons of the surface (U1) and subsurface (U2) atoms of the bare γ-U (100) slab at the NM level of theory 90

4.17 LDOS for H adsorption at the top site with the NM level of theory 91

4.18 LDOS for H adsorption at the center site with the NM level of theory 92

4.19 LDOS for H adsorption at the bridge site with the NM level of theory 93

4.20 LDOS for the 6d and 5f electrons of the surface (U1) and subsurface (U2) atoms of the bare γ-U (100) slab at the FM level of theory 94

4.21 LDOS for H adsorption at the top site with the FM level of theory 95

4.22 LDOS for H adsorption at the center site with the FM level of theory 96

4.23 LDOS for H adsorption at the bridge site with the FM level of theory 97

4.24 LDOS for the 6d and 5f electrons of the surface (U1) and subsurface (U2) atoms of the bare γ-U (100) slab at the FM level of theory..... 98

4.25 LDOS for H adsorption at the top site with the AFM level of theory..... 99

4.26 LDOS for H adsorption at the center site with the AFM level of theory..... 100

4.27 LDOS for H adsorption at the bridge site with the AFM level of theory..... 101

4.28 Optimized Ec of H atom at the interstitial bridge site for the NM (a), FM (b) and AFM (c) cases 103

4.29 Change in charge density for the H atom at the interstitial NM top site 115

4.30 Change in charge density for the H atom at the interstitial NM center site 116

4.31 Change in charge density of the H atom at the interstitial NM bridge site..... 117

4.32 change in charge density of the H atom at the interstitial FM top site..... 118

4.33 Change in charge density for the H atom at the interstitial FM center site..... 119

4.34 Change in charge density for the H atom at the FM interstitial bridge site..... 120

4.35 change in charge density of the H atom at the interstitial AFM top site 121

4.36 Change in charge density for the H atom at the interstitial AFM center site 122

4.37 Change in charge density for the H atom at the AFM interstitial bridge site 123

4.38 LDOS for the surface (U1), subsurface (U2), and center (U3) atoms of the 5 layer slab at the NM level of theory 125

4.39 LDOS for H at the top interstitial site at the NM level of theory. U1 is the surface atom and U3 is the center atom..... 126

4.40 LDOS for H at the center interstitial site at the NM level of theory. U2 is the subsurface and U4 is the subcenter atom. 127

4.41 LDOS for H at the bridge interstitial site at the NM level of theory. U1 is the surface atom and U2 is the subsurface atom 128

4.42 LDOS for the 6d and 5f electrons of the surface (U1) subsurface (U2) and center (U3) atoms of the bare γ-U (100) slab at the FM level of theory..... 129

4.43 LDOS for H adsorption at the top interstitial site with the FM level of theory. U1 is the surface U atom and U3 is the center U atom of the slab. 130

4.44 LDOS for H adsorption at the center interstitial site with the FM level of theory. U2 is the subsurface U of the slab. 131

4.45 LDOS for H adsorption at the bridge interstitial site with the FM level of theory. U1 is the surface U atom and U2 is the subsurface U atom of the slab. 132

4.46 LDOS for the 6d and 5f electrons of the, surface (U1), subsurface (U2) and center (U3) atom of the bare γ-U (100) slab at the AFM level of theory 133

4.47 LDOS for H adsorption at the top interstitial site with the AFM level of theory. U1 is the surface U atom and U3 is the center U atom of the slab. 134

4.48 LDOS for H adsorption at the center interstitial site with the AFM level of theory. U2 is the subsurface U of the slab. 135

4.49 LDOS for H adsorption at the bridge interstitial site with the AFM level of theory. U1 is the surface U atom and U2 is the subsurface U atom of the slab. 136

4.50 Optimized E_c of O atom at the top site at the NM (a), FM (b), and AFM (c) level 137

4.51 Optimized E_c of O atom at the center site at the NM (a), FM (b), and AFM (c) level 138

4.52 Optimized E_c of H atom at the bridge site at the NM (a), FM (b), and AFM (c) level 139

4.53 Change in charge density for the O atom at the NM top site 147

4.54 Change in charge density for the O atom at the NM center site 148

4.55 Change in charge density for the O atom at the NM bridge site 149

4.56 Change in charge density for th O atom at the FM top site 150

4.57 Change in charge density for the O atom at the FM center site 151

4.58 Change in charge density for the O atom at the FM bridge site 152

4.59 LDOS for the 6*d* and 5*f* electrons of the surface (U1) and subsurface (U2) atoms of the bare γ-U (100) slab at the NM level of theory 153

4.60 LDOS for O adsorption at the top site with the NM level of theory 154

4.61 LDOS for O adsorption at the center site with the NM level of theory 155

4.62 LDOS for O adsorption at the bridge site with the NM level of theory 156

4.63 LDOS for the 6d and 5f electrons of the surface (U1) and subsurface (U2) atoms of the bare γ-U (100) slab at the FM level of theory 157

4.64 LDOS for O adsorption at the top site with the FM level of theory 158

4.65 LDOS for O adsorption at the center site with the FM level of theory 159

4.66 LDOS for O adsorption at the bridge site with the FM level of theory 160

4.67 Optimized E_c of O atom at the interstitial bridge site for the NM (a), FM (b) and AFM (c) cases 162

4.68 Change in charge density for the O atom at the NM interstitial top site 173

4.69 Change in charge density for the O atom at the NM interstitial center site 174

4.70 Change in charge density for the O atom at the NM interstitial bridge site 175

4.71 Change in charge density for the O atom at the FM interstitial top site 176

4.72 Change in charge density for the O atom at the FM interstitial center site 177

4.73 Change in charge density for the O atom at the FM interstitial bridge site 178

4.74 Change in charge density for the O atom at the AFM interstitial top site 179

4.75 Change in charge density for the O atom at the AFM interstitial center site 180

4.76 Change in charge density for the O atom at the AFM interstitial bridge site 181

4.77 LDOS for the surface (U1), subsurface (U2), and center (U3) atoms of the 5 layer slab at the NM level of theory 183

4.78 LDOS for O at the top interstitial site at the NM level of theory. U1 is the surface atom and U3 is the center atom. 184

4.79 LDOS for O at the center interstitial site at the NM level of theory. U2 is the subsurface and U4 is the subcenter atom. 185

4.80 LDOS for O at the bridge interstitial site at the NM level of theory. U1 is the surface atom and U2 is the subsurface atom 186

4.81 LDOS for the 6d and 5f electrons of the surface (U1), subsurface (U2) and center (U3) atoms atom of the bare γ-U (100) slab at the FM level of theory 187

4.82 LDOS for O adsorption at the top interstitial site with the FM level of theory. U1 is the surface U atom and U3 is the center U atom of the slab. 188

4.83 LDOS for O adsorption at the center interstitial site with the FM level of theory. U2 is the subsurface U of the slab. 189

4.84 LDOS for O adsorption at the bridge interstitial site with the FM level of theory. U1 is the surface U atom and U2 is the subsurface U atom of the slab. 190

4.85 LDOS for the 6d and 5f electrons of the surface (U1), subsurface (U2) and center (U3) atom of the bare γ-U (100) slab at the AFM level of theory 192

4.86 LDOS for O adsorption at the top interstitial site with the AFM level of theory. U1 is the surface U atom and U3 is the center U atom of the slab. 193

4.87 LDOS for O adsorption at the center interstitial site with the AFM level of theory. U2 is the subsurface U of the slab. 198

4.88 LDOS for O adsorption at the bridge interstitial site with the AFM level of theory. U1 is the surface U atom and U2 is the subsurface U atom of the slab..... 199

LIST OF TABLES

Table Page

3.1 Lattice constants (Å) and bulk moduli (GPA) and their difference from experimental values (Δ) of bulk γ – U at different levels of theory 34

3.2 Total energy differences obtained at each level of theory, spin-polarization energy Esp (mRy/unit cell) and spin-orbit coupling energy Eso (mRy/unit cell). 41

3.3 Optimized lattice constants for N=1-6 layers 46

3.4 Total energy and incremental energy ΔE per atom (Ry/atom) with and without SOC..... 47

3.5 Spin-orbit coupling energy, E_{so}, for layers 1 through 6 48

3.6 The fitted and theoretical bulk energies, E_B, with and without SOC..... 49

3.7 Surface energy,γ, of the nanolayers 50

3.8 Work function for each N layer slab..... 52

4.1 Difference in energy of a 5 layer slab of γ-U at the NM, FM and AFM magnetic configuration..... 58

4.2 Distances and chemisorption energies of the H atom on γ-U(100) at the NM, FM and AFM levels of theory 68

4.3 $\Delta\Phi$ and surface dipole moment μ_{dipole} for the adsorption of the H atom at the NM, FM, and AFM level of theory..... 69

4.4 Spin and orbital magnetic moment for surface adsorption of the H atom at FM level of theory..... 71

4.5 Spin and orbital magnetic moment for surface adsorption of the H atom at AFM level of theory 72

4.6 Partial charges inside muffin-tin spheres for H at the top, center and bridge sites with SOC for the NM magnetic configuration 76

4.7 Partial charges inside muffin-tin spheres for H at the top, center and bridge sites with SOC for the FM magnetic configuration 77

4.8 Partial charges inside muffin-tin spheres for H at the top, center and bridge sites with SOC for the AFM magnetic configuration 78

4.9 Distances and chemisorption energies of the H atom in γ-U(100) lattice 105

4.10 Change in work function and surface dipole moment for the H atom inside the lattice at the NM, FM, and AFM level of theory 106

4.11 Spin and orbital magnetic moment for the H atom inside the lattice at FM level of theory 108

4.12 Spin and orbital magnetic moment for the H atom inside the lattice at AFM level of theory 109

4.13 Partial charges inside muffin-tin spheres for H at the top, center and bridge interstitial sites for the NM magnetic configuration 111

4.14 Partial charges inside muffin-tin spheres for H at the top, center and bridge interstitial sites for the FM magnetic configuration 112

4.15 Partial charges inside muffin-tin spheres for H at the top, center and bridge interstitial sites for the AFM magnetic configuration 113

4.16 Distances and chemisorption energies of the O atom on γ-U(100) at the NM, FM and AFM levels of theory 140

4.17 $\Delta\Phi$ and surface dipole moment μ_{dipole} for the adsorption of the O atom at the NM and FM level of theory 141

4.18 Spin and orbital magnetic moment for surface adsorption of the O atom at FM level of theory 143

4.19 Partial charges inside muffin-tin spheres for O at the top, center and bridge sites with SOC for the NM magnetic configuration 144

4.20 Partial charges inside muffin-tin spheres for O at the top, center and bridge sites with SOC for the FM magnetic configuration 145

4.21 Distances and chemisorption energies of the O atom in γ-U(100) lattice at the NM, FM and AFM levels of theory 164

4.22 Change in work function and surface dipole moment for the O atom inside the lattice at the NM, FM, and AFM level of theory 165

4.23 Spin and orbital magnetic moment for the O atom inside the lattice at FM level of theory 167

4.24 Spin and orbital magnetic moment for the O atom inside the lattice at AFM level of theory 168

4.25 Partial charges inside muffin-tin spheres for O at the top, center and bridge interstitial sites for the NM magnetic configuration 170

4.26 Partial charges inside muffin-tin spheres for O at the top, center and bridge interstitial sites for the FM magnetic configuration 171

4.27 Partial charges inside muffin-tin spheres for O at the top, center and bridge interstitial sites for the AFM magnetic configuration 172

CHAPTER 1

INTRODUCTION

During the past few decades, considerable theoretical efforts have been devoted to studying the electronic and geometric structures and related properties of surfaces. Such efforts are particularly important for systems like the actinides for which experimental work is relatively difficult to perform due to material problems and toxicity. The actinides are characterized by a gradual filling of the 5f-electron shell with the degree of localization increasing with the atomic number Z along the last series of the periodic table. The open shell of the *5f* electrons determines the atomic, molecular, and solid state properties of the actinide elements and their compounds and understanding the quantum mechanics of the *5f* electrons is the defining issue in the chemistry and physics of actinide elements. These elements are also characterized by the increasing prominence of relativistic effects and their studies can, in fact, help us understand the role of relativity throughout the periodic table. However, the electronic and geometric structures of the actinides, specifically the trans-uranium actinides and the roles of the 5f electrons in chemical bonding are still *not* well understood. This is crucial not only for our understanding of the actinides but also for the fact that the actinides constitute “the missing link” between the d transition elements and the lanthanides. The *5f* orbitals have properties intermediate between those of localized 4f and delocalized 3d orbitals. Thus, a proper understanding of the actinides will help us understand the behavior of the lanthanides and transition metals as well. In fact, there is an urgent need for continued e*xtensive and detailed* theoretical research in this area to provide significant and deep understandings of the electronic and geometric structures of the actinides.

Electronically speaking, the actinide series features a gradual filling of the 5*f*-electron shell and increase in localization of the valence electrons with increase in atomic number. In addition, with the increase of atomic number relativistic effects induced by spin-orbit interaction and electron-electron correlation become more pronounced through the series indicating that theoretical research of the actinides could help to understand the role of relativity throughout the periodic table. [1–3] The most noted application of the actinides, especially uranium (U), is their usefulness as a nuclear fuel and weapons resource.

The actinides have a long history of Nobel Prize winning research in the 20th century. In 1934, Enrico Fermi provided the first scientific evidence of the existence of actinide elements by reporting the results of a study in which uranium and thorium atoms were bombarded with neutrons. The elements were not specifically identified except for the possibility of elements with atomic number greater than 92. [4] Further investigations by Hahn and Strassmann [5], while following up on observations made by Joliot-Curie and Savitch [6], found that isotopes of barium were formed as a result of bombardment of uranium with neutrons. Meitner and Hahn explained the results by suggesting that the uranium nucleus splits into two near equal parts after neutron capture, coining the term nuclear fission, and suggesting the possibility of a fission chain reaction followed by particle decay and the existence of uranium isotopes based on the radioactive signatures detected. [7] Later, from 1940 to 1958, Seaborg, *et al.* at UC, Berkeley, using a cyclotron, effectively synthesized plutonium, americium, curium, berkelium, californium, einsteinium, fermium, mendelevium, nobelium and later seaborgium. They also created more than 100 actinide isotopes. Based on his work, Seaborg also proposed the “actinide concept” suggesting that these newly synthesized elements should be considered in a different period of the period table than the lanthanides. Seaborg’s work and discoveries in transuranium eventually earned him the 1951 Nobel Prize in chemistry. Now, the actinide family constitutes a highly complex group of radioactive elements starting from actinium with Z=89 and proceeding to lawrencium with Z=103 on the periodic table. Most of the actinides are created by bombardment

of uranium or its derivatives with slow neutrons, deuterons, or alpha particles. A few of these elements are byproducts of the fission of nuclear material. [8]

With the demand for electricity on the rise, dependence on fossil fuel, its impact on the environment, and whether there is enough to sustain our needs for the future are growing concerns. Nuclear energy is a low-carbon-emission alternative that currently produces 14% of the global electricity but questions lie as to whether it is sustainable. There is enough U available, to date, to support the demand of nuclear energy until the end of the 21st century at the current rate of consumption. However, if the necessity of nuclear power increases, as expected, it would provoke the requirement to either find additional sources of U or increase the efficiency of the nuclear power plants. Currently, there are two types of nuclear reactors in commercial employment. Most reactors in service have an open fuel cycle which exploits uranium based fuels and utilizes only 1% of the total energy potential of the fuel before it is considered spent and discarded. The disadvantages to this fuel cycle are that sustainability of the uranium fuel source is directly related to the amount of mined or available U and a large amount of spent nuclear fuel is left for geological disposal stirring unease over environmental contamination with dangerous radioactive material. The advantage, on the other hand, the discarded material from this fuel cycle is not a threat for weapons proliferation because the plutonium is not separated from the spent fuel. Closed fuel cycle reactors with reprocessing, used in a few reactors worldwide, decrease the demand of U about 10% by recycling of spent nuclear fuel and thus lessen the amount of spent nuclear fuel produced and eventually discarded, although this fuel cycle will result in the separation of more plutonium leading to concerns over nuclear weapons proliferation and environmental nuclear contamination. There are many ideas that are being researched for even more efficient reactors. Proposals for highly efficient reactors intended for commercial use include advanced heavy-water reactors (AHWRs), supercritical water-cooled reactors (SCWRs), high-temperature gas-cooled reactors (HTGRs) [also called very high-temperature reactors (VHTRs)], and molten salt reactors (MSRs), all of which require new fuels and equipment that needs to be investigated and tested before commercial implementation. [9] The next-generation

nuclear energy reactor is a fast *breeder* reactor which is similar to that used in the Manhattan Project to produce weapons grade plutonium in that any form of U fuel is exploited to continuously create fissile material while also producing energy, significantly reducing the dependence on newly mined U. In the breeding process, the final product has more fissile material than the fuel that began the process, leading to proliferation, storage, transport and safety worries. It has been found that it is possible to reduce the amount of plutonium in spent nuclear fuel and weapons grade plutonium by burning these products with inert-matrix fuels (IMF) [10]. Combining these two ideas the fast *breeder* reactor can produce electricity without creating highly dangerous and radioactive spent fuel and significantly reduce the amount of nuclear waste and weapons grade plutonium already in storage. In addition, recycling techniques could be employed to virtually eliminate dependence on newly mined U. Of course, these techniques will probably not be employed until the cost of newly mined U outweighs that of recycling. One such reactor, titled the Experimental Breeder Reactor II, was successfully built, employed and tested at Argonne National Laboratory in Idaho [11]. Although it is now decommissioned and disassembled, its success in both production in energy and safety has led it to be the prototype for the Integral Fast Reactor (IFR). This next-generation reactor is capable of breeding any fission fertile material into usable nuclear fuel or burning down radioactive material until it no longer contains plutonium or other actinides [9]. A commercial version of the IFR, called the PRISM, has been patented by GE-Hitachi Nuclear Energy and is approved for testing by the Department of Energy at the Savannah River site in South Carolina [12].

The IFR has a unique design utilizing a liquid-sodium coolant system allowing for better performance of metallic fuels which have the highest density of fissile material of all the fuel cycles [13]. In addition, the Nuclear Non-Proliferation Treaty (NPT), in an attempt to deter new development of weapons grade nuclear material and development of nuclear weapons and limit the amount of highly enriched U in test reactors, has mandated only 20% enriched U be used in research and test reactors [14]. These events have encouraged interest in metal alloy fuels such as molybdenum (Mo) doped γ-U which has been identified as a capable replacement to UAl_x and

U_3Si_2 fuels in current use. Studies on irradiated γ-U-Mo ranging from 2 wt% Mo to 10 wt% Mo show good irradiation performance at weights above 7% and results are promising at 10 wt% Mo with no decomposition to the α-phase. Neutron diffraction pattern measurements taken of γ-U powder samples with varying Mo content have shown identical bcc structures, but with slightly different lattice dimensions. [15–30] Despite the new-found rush of experimental research on γ-U alloys, little is known about pure γ-U due to its high temperature dependence, making experimentation on the material difficult and dangerous.

U, in general, is the heaviest naturally occurring element. Located in the middle of the early part of the actinide series, it is regarded as a light actinide. It has three temperature dependent crystallographic phases in the solid state: the orthorhombic α-phase below 970 K followed by the body-centered tetragonal β-phase between 970 K and 1050 K and then the body-centered cubic (bcc) γ-phase before melting at 1405 K. [31] Its electronic structure is characterized by a less than half filled 5*f* shell containing three delocalized electrons hybridizing with the 6*d* and 7*s* electrons and demonstrating itinerant behavior. This itinerant behavior of the 5*f* shell leads to Peierls distortion of the crystal structure at ambient temperature [32]. A study of the electronic structure of U could provide major clues regarding the transition from delocalized to localized 5*f*-electron behavior because the proportion of *s* and *d* electrons of the outer shell is larger in U compared to plutonium (Pu) [33]. Uranium has received great notoriety for its nuclear properties and the nuclear energy that it can provide. Other properties largely determined by the electronic properties in the solid of uranium metal, however, receive less attention. A few remarkable properties of uranium include low temperature charge density waves transitions [34], anisotropic thermal expansion [35], and a relatively complex ground-state crystal structure (orthorhombic) at room temperature [36]. Another interesting feature of U is its magnetic state and tendency to become superconducting and have unusual magnetic characteristics while bound to other elements. [37–40] The localization of the 5*f* electrons can cause strong paramagnetic, ferromagnetic or even antiferromagnetic properties [41] due to the characteristics of its open 5*f* shell [32]. It is well known that actinides can become magnetic spontaneously. U at

ambient temperature has been found to have spin and orbital moments that couple parallel rather than antiparallel, as inferred by Hund's Third Rule, resembling the induced magnetic field characteristics of a 3*d* ferromagnet despite it being shown experimentally to be paramagnetic from 20° to 350°C [42], [43]. This effect is thought to be due to the large spin-orbit coupling in U. A surface magnetic moment has been found through density-functional calculations for α-U in slab geometry using the generalized-gradient and local spin-density approximations, including spin-orbit coupling [44] showing that the more localized behavior of the 5*f* electrons of the surface atoms may be dominant in a slab configuration. While looking at γ – U alloys with transition metals specifically, Kurihara *et al.* calculated that the relation of the 3*d* orbital energy and the radius of the transition metal atom is an indication of γ – U forming alloys with and adsorbing certain 3*d* transition metals [45].

It is thought that aspects of the electronic bonding and structures in bulk uranium are apt to be enhanced at a surface or in a thin layer of uranium adsorbed on a substrate, due to the reduced atomic coordination of a surface atom and the narrow bandwidth of the surface states. For this reason, uranium surfaces and films and adsorptions on such may provide a valuable source of information about the bonding in uranium. A study of a five layers slab of (100) γ-uranium surface using the film-linearized-muffin-tin-orbitals (FLMTO) method suggested that surface enhancement of 5*f* localization (relative to bulk) is much stronger for uranium than for plutonium, with important consequences for surface reconstruction, chemisorption, and other surface behavior. [33] The phase diagram of uranium has been studied to 100 GPa by *in situ* diamond-anvil-cell x-ray/laser-heating experiments [46]. Based on their results and free energy calculations, the authors conjectured that the γ- phase is induced by partial localization of the 5*f* electrons at high temperatures. In contrast, using surface spectroscopic techniques such as XPS, UPS, and AES, it was concluded that the localization effects in U films are weak when compared to Pu films, although binding with the substrate did occur in both the Pu and U cases [47]. Considering the narrow bandwidth of the surface states, any transition from itinerant to localized behavior probably first takes place at the U surface with *possible* relaxations and reconstructions.

Using relativistic DFT to parameterize the U element by using the dimer interaction potential energy profile of U_2, it was found that uranium microclusters prefer to form three-dimensional compact structures. [48]

The chemical breakdown of nuclear material due to interaction with environmental gases, such as water vapor, is an innate dilemma concerning storage of spent nuclear fuel. Long term storage of radioactive materials, primarily uranium, represents very important scientific, technological, and environmental challenges. The corrosion behavior of nuclear materials is often unusual and difficult to interpret because of the complex electronic structures of these elements and their radioactivity. This requires detailed and fundamental understandings of the behavior of actinides in various allotropes, as well as the interaction of these forms with the environment. The main concern with the storage of spent fuel is the corrosion that occurs during storage and corrosion products formed in the process, like metallic dust and uranium hydride [49]. The most obvious environmental factor to be concerned with would be uranium's interaction with moist air and water. Many studies indicate that the interaction of uranium and water leads to dissociation of the water molecule and in turn atomic adsorption of the elements oxygen (O) and hydrogen (H) [50–54]. As a matter of fact, the reversible process of the dissociation of water into O_2 and H_2 gas is a well established one, especially in the presence of hot or metallic surfaces. [55]

Hydrogen interaction with U forms uranium hydride (UH_3) either by direct exposure to H_2 gas described as follows [56]:

$$2\ U + 3\ H_2 \leftrightarrow 2\ UH_3$$

Or through exposure to water as in:

$$7\ U + 6\ H_2O \rightarrow 3\ UO_2 + 4\ UH_3$$

UH_3 itself is highly pyrophoric at room temperature and is known to spontaneously combust when exposed to air. It has two cubic crystallographic forms: β which forms above 523 K and α that forms below 523 K. Above 180 K, both forms are paramagnetic, while at cooler temperatures they are ferromagnetic [57]. The volatility of UH_3 has caused several incidents during long-term storage of spent nuclear fuel cells where the problem was attributed to moisture condensed on

the uranium fuel plates or brought into the system. Exposure of U to water vapor was conducted under observed laboratory conditions at 85 K and resulted in warming of the U to 298 K, indicating the electrochemical interaction of liquid water with the uranium surface and the possible formation of uranium hydride [54]. It is possible to create U powder by diffusing H into the metal which forms fragile UH_3 along the grain boundaries of a polycrystalline material and then separate U and H by annealing at or above 773 K [58]. Metallographic and mechanical observations have shown that the formation of UH_3 precipitates is a primary source of embrittlement in uranium-hydrogen alloys and that maximum embrittlement occurs in alloys containing approximately 2.5 ppm H [59]. Further work by Condon shows that hydride formation is favored when certain metallic contaminates are present and less favored in the presence of O [60]. A density functional study substantiates this evidence reporting that the energy of H absorption in α-U bulk adjacent to chemical impurities, like C, Si and S, was lowered by an amount proportional to the size of the impurity atom [61]. They also estimate the diffusion barrier of H in α-U to be 0.49 eV and report that H diffusion into (100) surface of α-U bulk is an endothermic reaction with the lowest absorption energy of 0.39 eV. Therefore, in the case of water dissociation, H and O compete for adsorption sites. Using UH_3 as a nuclear fuel source is also being considered in a self-regulating nuclear power module [62].

Oxidation of metallic uranium surface gets its industrial importance primarily due to the atmospheric corrosion of uranium, and the formation of passivation layers protecting further corrosion attack [50], [51]. Using x-ray photoelectron spectroscopy, Auger electron spectroscopy and second ion mass spectroscopy to study O_2, CO and CO_2 on thorium and uranium surfaces, it has been shown that the adsorbed molecules dissociate, where the oxygen remains on the surfaces forming an oxide. The chemisorbed oxygen formed islands on the uranium surface, later spreading to cover the surface. In addition, the spectrum of uranium at saturation oxygen coverage closely resembles to that of UO_2 [50], [53]. Using ultraviolet photo-spectroscopy to study the reaction of O_2 on uranium surface showed that dissociative chemisorption of oxygen is followed by the formation of sub-stoichiometric UO_{2-x} and hyper-stoichiometric UO_{2+x} on the

surface at 73 K [63]. They also found that O_2 adsorption results in a decrease of Fermi level emission and the increase of the U 5*f*^{2} and O 2*p* emission, which means the withdrawal of the 5*f* electrons from the Fermi level and their transfer into O 2*p* and the localized U 5*f*^{2} level. Studies on the magnetism of UO_{2+x} suggest that stoichiometric formations up to $UO_{2.07}$ hold the antiferromagnetic properties of UO_2 [64]. For oxidation to continue beyond the surface layer the diffusion of adsorbed gas atoms through the oxide layer is required. This diffusion process is strongly influenced by the defect structure and electronic properties of the oxide layer. It was shown that no activation energy is needed for the uranium and O_2 to form metastable states, and from these metastable structures a small amount of energy is needed to form additional stable UO_2. In addition, in this study, the uranium 5*f* atomic orbital electrons dominated in the formation of the U – O bonds, noting that these experiments were done below 970 K with pure U in an orthorhombic phase. [65] This may not be the case for γ-U because the close-packed bcc structure suggests *d*-electron dominant bonding [32].

A lot of theoretical work has been conducted on the U-O system. For instance, using the linear combination of Gaussian type orbitals – fitting function (LCGTO-FF) method within the GGA approximation of DFT (GGA-DFT), Boettger and Ray have carried out detailed electronic structure studies of crystalline UO_2 and its magnetic ordering [66], [67]. Hybrid DFT with relativistic effective core potentials (RECP) has been used by Kudin *et al* [68]to study the insulating gap of UO_2. The density functional study of O_2 adsorption on the (100) surface of γ-uranium shows that dissociative adsorption of O_2 is more favorable compared to molecular adsorption [69]. Recently, the gas-phase chemi-ionization reaction between uranium and oxygen atoms has been studied theoretically and potential energy curves have been calculated [70]. A reliable set of experimental data was chosen to construct a phase diagram and determine the oxygen chemical potential in a thermodynamic review of the U-O system. It concluded that a three sub-lattice model is appropriate to describe complex oxides such as $UO_{2\pm x}$. [71] Dholabhai and Ray conducted a density functional study using DMol3 for the adsorption of atomic O on the (100) surface of γ-U but only at the nonmagnetic (NM) and ferromagnetic (FM) states. They

reported the chemisorption energy of the most preferred site to be 7.887 eV and 7.965 eV for the NM and FM states, respectively.[72], [73] This thesis is organized as follows: 1) an overview of the theory and computational formalism involved with the study; 2) results and discussion of a study on the electronic, geometric and magnetic properties of ultra-thin films of (100) γ-U; and 3) results and discussion over atomic H and O adsorptions and diffusion on the (100) surface of γ-U.

CHAPTER 2

THEORY AND COMPUTATIONAL FORMALISM

2.1 Density Functional Theory

Many electronic structure calculations for solids are based on density functional theory (DFT), which results from the work of Hohenberg, Kohn and Sham [74], [75]. DFT is currently the most popular method in condensed matter physics and quantum chemistry for solving the many body quantum mechanical problems. In this chapter we describe the density functional method for electronic structure calculations. We first present the physical interpretation of the density functional equations followed by their formal derivations. Conceptually simpler and formally rigorous DFT provides an elegant way of mapping a *N* variable system to a single variable, the system's density, and hence reducing the computational cost significantly over the traditional *ab initio* theories such as Hartree-Fock theory, while retaining much of the computational accuracy. In principal, DFT is an 'exact' theory and is applicable to any interacting system with an external potential. Approximations enter while treating the exchange-correlation effect by the functionals and the accuracy of the calculations depends on the representability of the functionals, though the conditions for the representability of the functionals are still not well defined. However, continual developments of the functionals by including the local, semi-local and, recently, the dynamic effects (in DFT nomenclature, these are called LDA, GGA and meta-GGA, respectively) increase the predictability and accuracy of computations. In the following we will present a short description of DFT following mostly the reviews of Lieb [76], Parr and Yang [77], [78], Capelle [79] and Nagy and Andrejkovics [80–82].

2.1.1 Hohenberg-Kohn Theorem

In a system of N electrons under the influence of a time-independent external potential the Hohenberg-Kohn theorem states that, the external potential $v(\vec{r})$ is determined solely by the electron density $\rho(\vec{r})$, within a trivial additive constant. The basic difference from the traditional quantum mechanics is that in DFT we solve for the density rather than the wave functions. Then it is possible to obtain the wave function from the density by:

$$\rho(\vec{r}) = N\int \Psi^*(\vec{x}_1, \vec{x}_2, \ldots, \vec{x}_N)\Psi(\vec{x}_1, \vec{x}_2, \ldots, \vec{x}_N)d\vec{x}_1 d\vec{x}_2 d\vec{x}_3 \ldots d\vec{x}_N \tag{2.1}$$

where Ψ is assumed to be normalized to unity; and $\vec{x}_i$'s include both spin and spatial variables which, in equation (2.1), are integrated out for *i* = 1 to *N*. So once the density of electrons is known all other electronic properties can also be computed. For example, we can find the total number of electrons which is given by:

$$N = \int \rho(\vec{r})d\vec{r} \tag{2.2}$$

Another example, applicable only to the Coulomb potential, is from Kato's theorem [83] which says that the electron density has a cusp at the location of the nuclei satisfying the equation:

$$Z_\beta = -\frac{1}{2\rho(\vec{r})}\frac{\partial\rho(\vec{r})}{\partial r}\bigg|_{r=R_\beta} \tag{2.3}$$

where the partial derivatives are taken at the nuclei β. From equation (2.3) we can see that once the density is found the position of the nuclei, R_β, and the atomic number Z_β can be defined. In general $v(\vec{r})$ in the Hohenberg-Kohn theorem is not restricted to the Coulomb potentials.

Let us now proceed to prove the Hohenberg-Kohn theorem following the original approach of their papers. The original proof was both simple and elegant, and was done by

reduction ad absurdum, basically for the non-degenerate systems. However the general conclusion is applicable to degenerate system as well. The proof follows like this:

Let us suppose that, in addition to $v(\vec{r})$, there exists another potential $v'(\vec{r})$ due to the same density $\rho(\vec{r})$ and that $v(\vec{r}) \neq v'(\vec{r}) + c$, where *c* is just an additive constant. Now due to these two potentials we will have two ground state wave functions Ψ and Ψ' corresponding to two Hamiltonians H and H' with the ground state energies of E and E', respectively. The Hamiltonians are defined as:

$$H = T + V_{ee} + \sum_{i}^{N} v(\vec{r}_i), \tag{2.4}$$

where T and V_{ee} are the kinetic energy and electron-electron repulsion operators defined as:

$$T = -\frac{1}{2}\sum_{i}^{N} \nabla_i^2 , \tag{2.5}$$

$$V_{ee} = \sum_{i<j}^{N} \frac{1}{r_{ij}}, \tag{2.6}$$

Here we use the atomic units where

$$e^2 = \hbar = m_e = 1.$$

where *e* is the electronic charge, $\hbar$ is the Plank's constant and m_e is the electron mass, in which unit energies are given in Hartrees, 1*H* = 27.2116 eV and distances are in Bohr, $a_o = 0.529$ Å.

From Rayleigh_Ritz variational principal it follows that

$$E = \langle \Psi | H | \Psi \rangle < \langle \Psi' | H | \Psi' \rangle = \langle \Psi' | H' | \Psi' \rangle + \langle \Psi' | V - V' | \Psi' \rangle$$

$$E < E' + \int \rho(\vec{r}) [v(\vec{r}) - v'(\vec{r})] dr \tag{2.7}$$

Similarly, using the variational principle for the Hamiltonian H' with the trial wave function Ψ, we have

$$E' = \langle \Psi' | H' | \Psi' \rangle < \langle \Psi | H' | \Psi \rangle = \langle \Psi | H | \Psi \rangle + \langle \Psi | V' - V | \Psi \rangle$$

$$E' < E + \int \rho(\vec{r})[v'(\vec{r}) - v(\vec{r})]dr \quad (2.8)$$

Addition of equation (2.7) and (2.8) leads to

$$E_0 + E_0' < E_0' + E_0 \quad (2.9)$$

which clearly is a contradiction, so we can conclude that given the electronic density, the external potential is determined, and therefore all the other electronic properties, including the total energy.

Let us write the total energy as,

$$E_v(\rho) = T(\rho) + V_{ne}(\rho) + V_{ee}(\rho) \quad (2.10)$$

where,

$$= \int \rho(\vec{r}) v(\vec{r}) d\vec{r} + F_{HK}[\rho]$$

$$F_{HK}[\rho] = T(\rho) + V_{ee}[\rho] \quad (2.11)$$

Here V_{ee} includes both the classical and non-classical (for example, Coulomb and exchange interactions) contributions and F_{HK} is the Hohenberg-Kohn functional, which does not depend on the external potential as can be seen from equation (2.11) and so is a universal functional of $\rho(\vec{r})$.

The second Hohenberg-Kohn theorem states that for a trial density $\tilde{\rho}(\vec{r})$, such that $\tilde{\rho}(\vec{r}) \geq 0$, and $\int \tilde{\rho}(\vec{r}) d\vec{r} = N$,

$$E_0 \leq E_v[\tilde{\rho}] \quad (2.12)$$

where, $E_v[\tilde{\rho}]$ is the energy functional of equation (2.10). The proof will be done by the use of variational principle. For any trial density $\tilde{\rho}(\vec{r})$, according to the Hohenberg-Kohn first theorem, it has its own potential $v(\vec{r})$, Hamiltonian *H* and wave function $\tilde{\Psi}$. So we get the following equation (2.10),

$$\left\langle \tilde{\Psi} \middle| H \middle| \tilde{\Psi} \right\rangle = \int \tilde{\rho}(\vec{r}) v(\vec{r}) d\vec{r} + F_{HK} = E_v[\tilde{\rho}] \tag{2.11}$$

Now the variation of total energy with the constraint that the total electrons are fixed, we get,

$$\delta\left\{E_v[\tilde{\rho}] - \mu\left[\int \tilde{\rho}(\vec{r}) d\vec{r} - N\right]\right\} = 0 \tag{2.12}$$

which leads to the Euler-Lagrange equation

$$\mu = \frac{\delta E_v[\tilde{\rho}]}{\delta \tilde{\rho}(\vec{r})} = v(\vec{r}) + \frac{\delta F_{HK}}{\delta \tilde{\rho}(\vec{r})} \tag{2.13}$$

where the Lagrange multiplier μ is the chemical potential. Now if the exact form of the functional F_{HK} is known, the equation (2.12) then would be an exact equation for the ground state electron density. The functional F_{HK} is defined only for those trial densities $\tilde{\rho}(\vec{r})$ which are *v*-representable, meaning that $\tilde{\rho}(\vec{r})$ corresponds to an anti-symmetric ground state wave function of some Hamiltonian with external potential $v(\vec{r})$. The conditions for the density to be *v*-representable is yet unknown. However it turned out that DFT can be formulated on a density which satisfies a weaker constraint than that of *v*-representability, namely *N*-representability. A density is *N*-representable if it can be derived from some anti-symmetric wave function. Based on the *N*-representable density, Levy's constrained search method is described below which eliminates the degeneracy limitations in the proof of the original Hohenberg-Kohn theorem.

2.1.2 The Method of Constrained Search

This method was first developed by Levy and Lieb [76], [84]. A universal function $F[\rho]$ defined as a sum of kinetic and Coulomb repulsion energies:

$$F[\rho] = \underset{\Psi \to \rho}{Min} \langle \Psi | T + V_{ee} | \Psi \rangle \tag{2.14}$$

$F[\rho]$ searches all wave functions Ψ which yield the fixed trial density ρ, and the ρ need not be *v*-representable. Now the ground state energy can be written as:

$$E_0 = \underset{\Psi\to\rho}{Min}\left\langle \Psi \left| T + V_{ee} + \sum_i^N v(r_i) \right| \Psi \right\rangle \tag{2.15}$$

$$= \underset{\rho}{Min}\left\{ \underset{\Psi\to\rho}{Min}\left\langle \Psi \left| T + V_{ee} + \sum_i^N v(r_i) \right| \Psi \right\rangle \right\}$$

$$= \underset{\rho}{Min}\left\{ \left[\underset{\Psi\to\rho}{Min}\left\langle \Psi \left| T + V_{ee} \right| \Psi \right\rangle + \int v(\vec{r})\rho(\vec{r})d\vec{r} \right] \right\} \tag{2.16}$$

Using the definition of $F[\rho]$ from equation (2.14) we can write equation (2.16) as:

$$E_0 = \underset{\rho}{Min}\left\{ F[\rho] + \int v(\vec{r})\rho(\vec{r})d\vec{r} \right\}$$

$$= \underset{\rho}{Min}\, E[\rho] \tag{2.17}$$

where

$$E[\rho] = F[\rho] + \int v(\vec{r})\rho(\vec{r})d\vec{r}. \tag{2.18}$$

In the constrained search formula for the functional $F[\rho]$ there is no reference that ρ needs to be *v*-representable ground state density, as long as it is constructed from an anti-symmetric wave function. However, when ρ is *v*-representable we get:

$$F[\rho] = F_{HK}[\rho] \tag{2.19}$$

The functional $F[\rho]$ is universal because it does not depend on the external potential $v(\vec{r})$. This constrained search method removes the degeneracy problem from the original Hohenberg-Kohn theorem because in this approach only one set of degenerate wave functions corresponding to the given ρ is selected.

2.1.3 The Kohn-Sham Method

The ground state electron density can be in principle determined by solving the Euler-Lagrange equation

$$\frac{\delta F(\rho)}{\delta \rho} + v(\vec{r}) = \mu. \tag{2.20}$$

where μ is the Lagrange multiplier associated with the constraint:

$$\int \rho(\vec{r})d\vec{r} = N$$

Here the exact form of the functional $F[\rho]$ in equation (2.20) is not known:

$$F(\rho) = T[\rho] + V_{ee}[\rho]. \tag{2.21}$$

As can be seen from the above equation the basic problem is to evaluate the kinetic energy term. Kohn-Sham proposed an indirect approach to this problem, which is described in the following section.

Let us consider a non-interacting system where electrons move independently in a common local potential v_s, where the electronic density $\rho(\vec{r})$ is the same as the interacting electronic system. This can be done as long as we ensure that the wave functions, from which $\rho(\vec{r})$ is constructed, are *N*-representable. The Hamiltonian is:

$$H_s = \sum_i^N \left(-\frac{1}{2}\nabla_i^2 \right) + \sum_i^N v_s(\vec{r}_i). \tag{2.22}$$

Notice in the above Hamiltonian there is no electron-electron repulsion term. For this system we can write the non-interacting wave-function as the Slater determinant:

$$\Psi_s = \frac{1}{\sqrt{N!}} \det[\psi_1 \psi_2 \cdots \psi_N] \tag{2.23}$$

where ψ_i are the *N* lowest eigenstates of the one-electron Hamiltonian h_s:

$$h_s \psi_i = \left[-\frac{1}{2}\nabla_i^2 + v_s(\vec{r}_i) \right] \psi_i = \varepsilon_i \psi_i \tag{2.24}$$

The kinetic energy of this non-interacting system is,

$$T_s[\rho] = \langle \Psi_s | \sum_{i=1}^N \left(-\frac{1}{2}\nabla_i^2 \right) | \Psi_s \rangle = \sum_i^N \langle \psi_i | -\frac{1}{2}\nabla_i^2 | \psi_i \rangle \tag{2.25}$$

while the density of the non-interacting system

$$\rho(\vec{r}) = \sum_{i}^{N} |\psi_i(\vec{x}_i)|^2 \tag{2.26}$$

is equal to that of an interacting one.

The kinetic energy functional $T[\rho]$ in equation (2.21), as mentioned before, is unknown, so we simply take the kinetic energy functional $T_s[\rho]$ of non-interacting system instead of $T[\rho]$. Let the difference between these two functional be $T_c = T - T_s$, and substituting this in equation (2.21) we get:

$$F[\rho] = T_s[\rho] + V_{ee}[\rho] + T_c[\rho] \tag{2.27}$$

The last two terms on the right hand side of equation (2.27) represent the electron-electron interaction and we can rewrite them as the Coulomb and exchange-correlation terms, respectively:

$$V_{ee}[\rho] + T_c[\rho] = J[\rho] + E_{xc}[\rho] \tag{2.28}$$

So, equation (2.27) can be written as:

$$F[\rho] = T_s[\rho] + J[\rho] + E_{xc}[\rho] \tag{2.29}$$

So, with the above functional the total energy of equation (2.18) can be written as:

$$E[\rho] = T_s[\rho] + J[\rho] + E_{xc}[\rho] + \int \rho(\vec{r}) v(\vec{r}) d\vec{r} \,. \tag{2.30}$$

The variation of equation (2.30) gives the Euler-Lagrange equation:

$$\mu = \frac{\delta E[\rho]}{\delta \rho} = \frac{\delta}{\delta \rho} \int \rho(\vec{r}) v(\vec{r}) d\vec{r} + \frac{\delta T_s[\rho]}{\delta \rho} + \frac{\delta J[\rho]}{\delta \rho} + \frac{\delta E_{xc}[\rho]}{\delta \rho}$$

$$= v(\vec{r}) + \frac{\delta T_s[\rho]}{\delta \rho} + \frac{\delta J[\rho]}{\delta \rho} + \frac{\delta E_{xc}[\rho]}{\delta \rho} \tag{2.31}$$

$$= v_{eff}(\vec{r}) + \frac{\delta T_s[\rho]}{\delta \rho} \tag{2.32}$$

where the Kohn-Sham effective potential is defined by:

$$v_{eff} = v(\vec{r}) + \frac{\delta J[\rho]}{\delta \rho} + \frac{\delta E_{xc}[\rho]}{\delta \rho}$$

$$= v(\vec{r}) + \int \frac{\rho(\vec{r}')}{|\vec{r} - \vec{r}'|} d\vec{r}' + v_{xc}(\vec{r}) \tag{2.33}$$

here we also defined the exchange-correlation potential as:

$$v_{xc}(\vec{r}) = \frac{\delta E_{xc}(\rho)}{\delta \rho} \tag{2.34}$$

Now let us rewrite equation (2.30) in terms of one electron orbitals:

$$E(\rho) = \sum_i^N \int \psi_i^* \left(-\frac{1}{2} \nabla^2 \right) \psi_i d\vec{r} + J(\rho) + E_{xc}[\rho] + \int v(\vec{r}) \rho(\vec{r}) d\vec{r} \tag{2.35}$$

and the electron density is, as in equation (2.26):

$$\rho(\vec{r}) = \sum_i^N |\psi_i|^2$$

So, in equation (2.35) the energy is expressed in terms of *N* orbitals.

Now, taking the variation of energy in equation (2.35) with respect to the one-electron orbital ψ_i, along with the constraint that these oribitals are orthonormal to each other:

$$\int \psi_i^* \psi_j d\vec{x} = \delta_{ij} \tag{2.36}$$

We get,

$$\delta \left[E[\rho] - \sum_i^N \sum_j^N \varepsilon_{ij} \int \psi_i^*(\vec{x}) \psi_i(\vec{x}) d\vec{x} \right] = 0 \tag{2.37}$$

In equation (2.37) ε_{ij} are the Lagrange multipliers. Let us now consider the variation in the energy $E[\rho]$ given by the equation (2.35),

$$\delta E[\rho] = \left[\frac{\delta}{\delta \psi_i^*} \sum_i^N \int \psi_i^* \left(-\frac{1}{2} \nabla^2 \right) \psi_i d\vec{r} + \frac{\delta J}{\delta \psi_i^*} + \frac{\delta E_{xc}}{\delta \psi_i^*} + \frac{\delta}{\delta \psi_i^*} \int v(\vec{r}) \left(\sum_i^N |\psi_i|^2 \right) d\vec{r} \right] \delta \psi_i^* \tag{2.38}$$

Using chain rule for functional derivative, the first term in the right hand side gives,

$$\frac{\delta}{\delta\psi_i^*}\sum_i^N\int\psi_i^*\left(-\frac{1}{2}\nabla^2\right)\psi_i d\vec{r}=\frac{\partial\psi_i^*}{\partial\psi_i^*}\left(-\frac{1}{2}\nabla^2\right)\psi_i+\psi_i^*\frac{\partial}{\partial\psi_i^*}\left\{\left(-\frac{1}{2}\nabla^2\right)\psi_i\right\}$$

$$=-\frac{1}{2}\nabla^2\psi_i \tag{2.39}$$

where derivative in the second term is zero. Similarly the last term in the variation of energy in equation (2.38) gives,

$$\frac{\delta}{\delta\psi_i^*}\int v(\vec{r})\left(\sum_i^N|\psi_i|^2\right)d\vec{r}=v(\vec{r})\psi_i \tag{2.40}$$

So, from equation (2.37), for any arbitrary variation of $\delta\psi_i^*$, we get using equations (2.39) and (2.40),

$$h_{eff}\psi_i=\left[-\frac{1}{2}\nabla^2+\frac{\delta J[\rho]}{\delta\rho}+\frac{\delta E_{xc}[\rho]}{\delta\rho}+v(\vec{r})\right]\psi_i=\sum_j^N\varepsilon_{ij}\psi_j$$

$$\Rightarrow h_{eff}\psi_i=\left[-\frac{1}{2}\nabla^2+v_{eff}(\vec{r})\right]\psi_i=\sum_j^N\varepsilon_{ij}\psi_j \tag{2.41}$$

where $v_{eff}(\vec{r})$ is defined by equation (2.33). Now in equation (2.41) the Hamiltonian h_{eff} is a Hermitian operator, hence ε_{ij} is a Hermitian matrix which can be diagonalized by unitary transformation, which leads to the Kohn-Sham equations:

$$\left[-\frac{1}{2}\nabla^2+v_{eff}(\vec{r})\right]\psi_i=\varepsilon_i\psi_i \tag{2.42}$$

Equation (2.42) (or equation (2.41)) is the central equation in the application of density function theory. These equations are usually solved by self-consistent methods which can be represented by the following flow-chart:

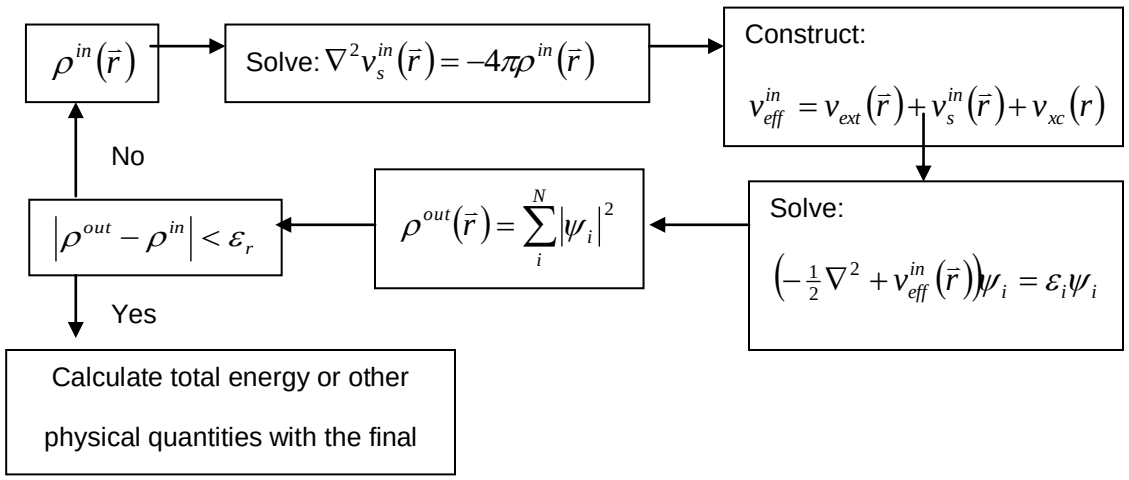

Figure 2.1 Flow-chart for DFT self-consistency loop

The solution of Kohn-sham equation is in principle exact, but as can be seen from the above discussion of the Kohn-Sham procedure that, it does not give any prescription for obtaining the exchange-correlation functionals. Depending on the system at hand, different levels of approximations were made to deal with this functional. In the following we will describe the local and generalized density approximations to these functionals.

2.1.4 Generalized Gradient Approximation: GGA

Logically the first step to improve upon the LDA is to take into account the spatial change in electronic density, i.e., the gradient of the density, $\nabla\rho(\vec{r})$, to take into account the non-homogeneity of the true electron density. This method is named as the gradient expansion approximation (GEA). This can be done by a Taylor series expansion of the exchange-correlation functional,

$$E_{xc}^{GEA}[\rho_\alpha, \rho_\beta] = \int \rho(\vec{r})\varepsilon_{xc}(\rho_\alpha, \rho_\beta)d\vec{r} + \sum_{\sigma,\sigma'}\int C_{xc}^{\sigma,\sigma'}(\rho_\alpha, \rho_\beta)\frac{\nabla\rho_\sigma}{\rho_\sigma^{2/3}}\frac{\nabla\rho_\beta}{\rho_{\sigma'}^{2/3}}d\vec{r} + \cdots \qquad (2.53)$$

The coefficient $C_{xc}^{\sigma,\sigma'}$ in equation (2.53) was found to be proportional to $1/\rho^{4/3}$. Unfortunately, GEA did not give a systematic improvement on the LDA approximation. The reason is that the exchange correlation interaction was not found physically meaningful in this definition. In addition, higher order corrections of $\nabla\rho$ are exceedingly difficult to calculate. However, a more sophisticated approach to include the gradient of densities was proposed by Perdew and others [85–87], the generalized gradient approximation (GGA), which defines the exchange-correlation functional in the following manner,

$$E_{xc}^{GGA}[\rho_\alpha,\rho_\beta]=\int f(\rho_\alpha,\rho_\beta,\nabla\rho_\alpha,\nabla\rho_\beta)d\vec{r} \tag{2.54}$$

In practice, E_{xc}^{GGA} is divided into its exchange and correlation contributions,

$$E_{xc}^{GGA}=E_x^{GGA}+E_c^{GGA}, \tag{2.55}$$

and the approximations for the functionals are usually made individually.

Several suggestions for the explicit dependence of *f* on the densities and their gradients have been proposed over the years, including the functionals which include the parameters that are calibrated against some reference system. Among the most widely used functionals are the 1986 Perdew functions, where the correlation functional contains an empirical parameter. The Perdew-Wang 1991 functional (PW91) incorporates no empirical parameters and is determined from the uniform electron gas approximations and with exact constraints. A refinement on PW91 was done by Perdew, Burke and Ernzerhof called the PBE functional [87]. Another popular functional for correlation is from Lee, Yang and Parr (LYP) [88], which is not based on uniform electron gas, and obtains the correlation energy as an explicit functional of the density's gradient. The LYP functional contains one empirical parameter. This correlation functional is often combined with Becke's exchange functional [89–91] and is known as B3LYP which combines Hartree-Fock and DFT functionals, a method termed Hybrid-DFT which will be discussed below.

It should be mentioned here that GGA does not provide a complete non-local functional. In true mathematical sense, $\rho(\vec{r})$ and its gradient $\nabla\rho(\vec{r})$ depend only on $\vec{r}$, and is independent

of any $\rho(\vec{r}')$, where $\vec{r}' \neq \vec{r}$. The only advantage GGA has is that it includes the local variation of the densities. Also GGA in its original form does not produce the simultaneous asymptotic behavior for both the energy and the potentials. In modern day functionals, a cut-off procedure on density is used to produce the satisfactory results. However, GGA functionals do show improvements over LDA functionals in many systems in condensed matter physics and quantum chemistry, with the exception of a long range weakly bound system, for instance the van der Waals interaction.

2.1.5 Hybrid Density Functional Theory

Most calculations of the electronic structure of solids are performed using DFT but it is well-known that systems with strong electron correlation can be improperly described by LDA and GGA. In DFT calculations of these strongly correlated systems an incorrect magnetic ordering for the ground state is obtained or, for partially-filled narrow band systems, bands are inappropriately amassed around the Fermi level. It is believed that the problem lies in the "local and very approximate treatment of the exchange energy" [92] in DFT and the self-interaction error, where the mean-field Coulomb interaction of an electron density with itself is not considered [93]. On the other hand, the Hartree–Fock (HF) theory provides an exact treatment of the exchange functional and produces no self-interaction error because the Hartree self-repulsion energy is exactly cancelled by the Fock exchange interaction but it is deficient in describing chemical bonding, neglects the correlation between electrons and represents solids poorly due to the nonlocal nature of the exchange potential.

By combining the two theories, the strengths of each could be exploited to obtain a proper description of highly correlated chemical systems while also being computationally inexpensive [94]. This approach led to the design of the *Hybrid* density functional theory (HYB-DFT) [94–96], in which the exchange-correlation functional is represented as a combination of the exact non-local HF exchange with the approximate local DFT exchange and retaining the DFT correlation functional. Hence, the self-interaction error in DFT functional is reduced due to the

addition of HF exchange and consequently, significant improvements compared to LDA/GGA in electronic structure properties, for example, band gaps and magnetism of localized *d* and *f* electron systems, can be expected. In certain strongly correlated systems for which DFT has failed to perform well, HYB-DFT has been proven to work reasonably well. However, the success of HYB-DFT appears to be dependent on the system. For example the PBE0 hybrid functional, a combination of 25% HF exchange with PBE exchange–correlation functional, yielded experimental anti-ferromagnetic insulating ground state of UO_2 while DFT predicted a ferromagnetic metal. Also, the experimentally measured non-zero band gap of UO_2 was correctly obtained whereas DFT yielded a zero band gap. [68] HYB-DFT with the PBE exchange–correlation functional was used by our group to study the ground state properties of δ-Pu and results, particularly the atomic volume and electronic spectra, showed significant deviations from experimental data at the expense of producing a non-magnetic ground state [97].

In its simplest form, a hybrid XC functional, E_{xc}^{HYB} containing a fraction, *λ,* of HF exchange is expressed by:

$$E_{xc}^{HYB} = \lambda E_x^{HF} + (1-\lambda)E_x^{DFT} + E_c^{DFT}$$

where the subscripts *X* and *C* denote the exchange and correlation terms, respectively. Several different types of hybrid density functional have been developed over the years. In addition to the B3LYP hybrid functional mentioned previously, other widely used hybrid functionals are the PBE0 [91] and HSE [98].

2.1.6 Scalar Relativistic Approximations

For the heavier atoms in the periodic table relativistic corrections to the electronic energy levels are important. The relativistic effects in the electronic structure of compounds containing heavy atoms has can be linked to phenomena associated with these compounds, such as phosphorescence, magnetism or the propensity for high valence numbers in chemical reactions. A frequently cited example is that without relativistic corrections to the energy level calculation of

gold atoms, its color would look like silver. Also if we consider one electron moving around a mercury nucleus, the relativistic mass corrections for the electron is almost 23% and the speed of the electron is almost 53% of the speed of light. In the following we present a short introduction of scalar relativistic approximations. [99–101]

The four-component Dirac equation can be written as,

$$i\hbar \frac{\partial \Psi(\vec{r},t)}{\partial t} = \left(c\alpha \cdot \hat{p} + \beta mc^2\right)\Psi(\vec{r},t) \tag{2.56}$$

where $\Psi(\vec{r},t)$ is a four-component wave-function:

$$\Psi(\vec{r},t) = \Psi(\vec{r})e^{-iWt} = \begin{pmatrix} \Psi_1(\vec{r}) \\ \Psi_2(\vec{r}) \\ \Psi_3(\vec{r}) \\ \Psi_4(\vec{r}) \end{pmatrix} e^{-iWt} \tag{2.57}$$

and, $W = \alpha \cdot pc + \beta mc^2$.

Here α and β are 4×4 matrices,

$$\alpha = \begin{pmatrix} 0 & \vec{\sigma} \\ \vec{\sigma} & 0 \end{pmatrix}, \ \beta = \begin{pmatrix} I & 0 \\ 0 & -I \end{pmatrix}$$

where σ_x, σ_y, σ_z are Pauli-spin matrices, and have the following properties,

$$\alpha^2 = \beta^2 = 1, \quad \{\alpha, \beta\} = 0 \text{ and } \{\alpha_i, \alpha_j\} = 0.$$

Here the $\{\ \}$ represents the anti-commutation.

It is very difficult to solve 4-component Dirac equations for a large system. One approach is to use Breit-Pauli Hamiltonian, which is a limit of the Dirac equation in Hermitian form, correct to the order of $\frac{1}{c^2}$:

$$H_{BP} = H_0 + H_{MV} + H_D + H_{SO} \tag{2.58}$$

where, H_0 is the non-relativistic Hamiltonian, H_{MV} is the mass-velocity term, $H_{MV} = -\frac{\alpha^2}{8}\sum_i p_i^4$, H_D is the Darwin term, $H_D = \frac{\alpha^2}{8}\left(\nabla^2 V\right)$, and the potential *V* is given by, $V = -Z\sum_i \frac{1}{r_i} + \sum_{i<j}\frac{1}{r_{ij}}$. This is a contribution to the energy that has no classical analogue. It comes from the fact that electrons cannot be regarded as a point particle but is spread out over a volume of the order of Compton wave-length $(\hbar^3/mc)^3$.

H_{SO} is the spin-orbit coupling term,

$$H_{SO} = \frac{\alpha^2}{2}\left(\sum_i \frac{Z}{r_i^3}\left(L_i \cdot S_i\right) - \sum_{i\neq j}\frac{1}{r_{ij}^3}\left(r_{ij}\times P_i\right)\cdot\left(S_i + 2S_j\right)\right). \quad (2.59)$$

In all of the above equations, α is the fine structure constant. In the scalar relativistic approximations this term is not included in the calculations.

2.2 Computational Formalism

All calculations for this work have been performed with the generalized gradient approximation (GGA) to DFT with the Perdew-Burke-Ernzerhof exchange-correlation functional of 96 (PBE96) where the Kohn-Sham equations were solved using the method implemented in the *WIEN2k* suite of software. *WIEN2k* is a full-potential linearized/augmented plane waves + local orbitals (L/APW + lo method). Full potential in *WIEN2k* implies no shape approximation to the potential or density and uses DFT for the treatment of electron exchange and correlation. Based on Slater's augmented plane wave (APW) method [102], the unit cell is divided into non-overlapping atom-centered muffin tin spheres S_α with radius R_{MT}^α and an interstitial region I, where α is the atomic index. The Kohn-Sham wave function is expanded in terms of atomic-like orbitals inside the muffin tin spheres and plane waves in the interstitial region. Two types of basis functions are implemented in *WIEN2k*. These are the LAPW basis functions and APW+lo basis

functions, each with local orbitals (LO) extension, which, as will be explain later, is not the same as lo. The difference between the LAPW and APW+lo methods arises from the linearization of the basis functions inside the atomic spheres. We briefly describe the underlying formalism below. [103]

2.2.1 Linear Augmented Plane Wave Method: LAPW

In the LAPW method, originally proposed by Anderson [104], the energy of the radial solution to the Schrödinger equation $u_l^\alpha(r', E)$ is expanded by performing a Taylor series expansion up to a linear term about a fixed energy E_l:

$$u_l^\alpha(r', E) = u_l^\alpha(r', E_l) + (E - E_l)\dot{u}_l^\alpha(r', E_l) + O((E - E_l)^2), \tag{2.60}$$

where $\dot{u}_l^\alpha(r', E) = \left.\frac{\partial u_l^\alpha(r', E)}{\partial E}\right|_{E=E_l}$ and $\vec{r}' = \vec{r} - \vec{r}_\alpha$, with $\vec{r}_\alpha$ being the position of the atom α in the unit cell.

The LAPW basis function is then written as

$$\phi_{\vec{k}_n}(\vec{r}) = \begin{cases} \frac{1}{\sqrt{V}} e^{i\vec{k}_n \cdot \vec{r}} & \vec{r} \in I \\ \sum_{lm} \left[A_{lm,\vec{k}_n} u_l^\alpha(r', E_l) + B_{lm,\vec{k}_n} \dot{u}_l^\alpha(r', E_l) \right] Y_{lm}(\hat{r}') & r' < R_{MT}^\alpha \end{cases} \tag{2.61}$$

where Y_{lm} are the spherical harmonics, *V* is the volume of the unit cell, and $\vec{k}_n = \vec{k} + \vec{K}_n$ with $\vec{k}$ being the wave vector in the first Brillouin zone and $\vec{K}_n$ being the reciprocal lattice vectors. The expansion coefficients $A_{lm,\vec{k}_n}$ and $B_{lm,\vec{k}_n}$, which are functions of $\vec{k}_n$, are obtained by requiring the value and slope of the basis function inside the sphere to match the plane wave at the boundary of the sphere, where a particular energy E_l is chosen for each l. In certain materials, it is difficult to find a single E_l that will provide a good description for atoms with a high-lying core state (semi-

core state) and a high-lying valence state that have different principal quantum numbers n but the same orbital quantum number l. For this, another type of basis function, known as a local orbital (LO), is added to the LAPW basis function. [105]

An LO (which is $\vec{k}_n$-independent) consists of a linear combination of two radial functions at two different energies $E_{1,l}$ and $E_{2,l}$ and one energy derivative at one of these energies and is given by

$$\phi_{LAPW}^{LO}(\vec{r}) = \begin{cases} 0 & \vec{r} \in I \\ \left[A_{lm}^{LO} u_l^{\alpha}(r', E_{1,l}) + B_{lm}^{LO} u_l^{\alpha}(r', E_{2,l}) + C_{lm}^{LO} \dot{u}_l^{\alpha}(r', E_{1,l}) \right] Y_{lm}(\hat{r}') & r' < R_{MT}^{\alpha} \end{cases} \tag{2.62}$$

The coefficients A_{lm}^{LO}, B_{lm}^{LO}, and C_{lm}^{LO} are obtained by requiring the value and derivative of the LO to vanish at the boundary of the sphere and is normalized.

2.2.2 Augmented Plane Wave Plus lo Method: APW+lo

It was shown by Sjöstedt, Nordstörm, and Singh [106] that the standard method in LAPW requiring that the plane waves of the interstitial region match in value and slope to the solution inside the muffin tin sphere is not the most resourceful way to linearize Slater's APW. Therefore, they proposed the APW+lo method, for which linearization is achieved by adding a local orbital (lo) to Slater's original APW. To clarify, the APW+lo basis function is defined in two parts. The first part of the APW+lo basis function is Slater's original APW:

$$\phi_{\vec{k}_n}(\vec{r}) = \begin{cases} \frac{1}{\sqrt{V}} e^{i\vec{k}_n \cdot \vec{r}} & \vec{r} \in I \\ \sum_{lm} a_{lm,\vec{k}_n} u_l^{\alpha}(r', E_l) Y_{lm}(\hat{r}') & r' < R_{MT}^{\alpha} \end{cases} \tag{2.63}$$

where $a_{lm,\vec{k}_n}$ are obtained by matching only the value of the inside the sphere with the plane wave outside the sphere at the surface of the sphere. The second part of the APW+lo basis function is the lo part which is defined as:

$$\phi^{lo}(\vec{r}) = \begin{cases} 0 & \vec{r} \in I \\ \left[b_{lm} u_l^{\alpha}(r', E_l) + c_{lm} \dot{u}_l^{\alpha}(r', E_l) \right] Y_{lm}(\hat{r}') & r' < R_{MT}^{\alpha} \end{cases} \quad (2.64)$$

Unlike the LAPW basis function inside the sphere given in equation (2.61), the coefficients b_{lm} and c_{lm} in the expression for φ^{lo} does not depend on the wave vector $\vec{k}_n$. In this case, b_{lm} and c_{lm} are obtained by requiring that lo vanishes at the boundary of the sphere and is normalized. Just like the LAPW basis function, it is not possible in the APW+lo method to use the same E_l to treat two states with different principal quantum numbers n but with the same orbital quantum number l inside the sphere. Again, the problem is remedied by adding local orbitals (LO), which consist of a linear combination of two radial functions at two different energies. In the APW+lo method LO is defined as follows:

$$\phi_{APW+lo}^{LO}(\vec{r}) = \begin{cases} 0 & \vec{r} \in I \\ \left[a_{lm}^{LO} u_l^{\alpha}(r', E_{1,l}) + b_{lm}^{LO} u_l^{\alpha}(r', E_{2,l}) \right] Y_{lm}(\hat{r}') & r' < R_{MT}^{\alpha} \end{cases} \quad (2.65)$$

The coefficients $\vec{k}_n$-independent coefficients a_{lm}^{LO} and b_{lm}^{LO} are obtained by requiring the value of the LO to vanish at the boundary of the sphere and is normalized. It should be noted in equation (2.65) that unlike the LO for the LAPW basis in equation (2.62), equation (2.65) contains no derivatives of the radial functions.

For a given interstitial plane wave cut-off, the dimension of the APW+lo Hamiltonian matrix is slightly larger than LAPW, but APW+lo converges faster and reaches the same accuracy compared to LAPW with a smaller plane wave cut-off, *i.e.*, the additional numerical effort is greatly compensated for by faster convergence with respect to the number of basis

functions. Madsen, Blaha, Schwarz, Sjöstedt, and Nordstörm [107] have demonstrated that using a mixed basis set of LAPW/APW+lo for different angular momentum, *l*, of radial functions centered on the same atom yields a particularly accurate and efficient description. For our group's work on Pu metal for example, we have used APW+lo basis (with the addition of LOs to appropriate semi-core and valence states) to describe all s, p, d, and f (*l*=0, 1, 2, 3) states and LAPW basis to describe all higher angular momentum states in the expansion of the wave function.

2.2.3 Full Potential and Spin-Orbit Interaction

The "muffin-tin" approximation used in early band structure calculations approximated the potential inside the muffin tin sphere to be spherically symmetric and, in many implementations, the interstitial potential was set constant. This is known as the "shape approximation" to the potential (and subsequently the charge density). *WIEN2k* relaxes the shape approximation by adding non-spherical terms to the potential inside the muffin-tin and expanding the potential in the interstitial region as a Fourier series, and therefore makes no "shape approximation" to the potential or charge density. Core states are treated at the fully relativistic level while valence states are treated at the scalar (no spin-orbit interaction) or fully relativistic level (spin-orbit interaction included). Spin-orbit effects are treated perturbatively using the scalar relativistic eigenstates as the basis within a given energy window, where all eigenstates with energies below a chosen energy cutoff were included, with the so-called $p_{1/2}$ extension, which accounts for the finite character of the wave function at the nucleus for the $p_{1/2}$ state. [108]

CHAPTER 3

QUANTUM SIZE EFFECTS IN THE ELECTRONIC STRUCTURE PROPERTIES OF γ – URANIUM (100) NANOLAYERS

In this chapter, first we give a brief outline about the computational details and the theory used for our calculations, followed by the discussion of our results on the electronic, geometric and magnetic properties of bulk and ultra-thin layers of γ-uranium (γ-U). The generalized gradient approximation (GGA) to density functional theory (DFT) and hybrid density functional theory have been used to compute the layer-by-layer properties of γ-U in the (100) symmetry. Guided by bulk results which have been analyzed at six different levels of theory, the surface calculations have been performed at the non-magnetic level including spin-orbit coupling. Normally standard DFT using the local density approximation (LDA) and the generalized gradient approximation (GGA) with spin-orbit coupling (SOC) is adequate in describing these types of system as found by our group and other groups. [93], [97] However, in previous calculations on some other actinides, such as americium (Am), *hybrid* density functional theory (HYB-DFT) was needed to correctly describe the system in agreement with experimental data [109]. Thus, we have used both DFT and HYB-DFT in first studying bulk γ – U for which experimental data is available followed by the quantum size effect studies of U (100) nano-layers. This will assist us in determining the minimum number of layers required to accurately investigate the interactions of atmospheric atomic and molecular systems with the uranium surface.

3.1 Computational Method

As in mentioned previously, all calculations have been performed within the generalized gradient approximation (GGA) to density functional theory (DFT) with the Perdew-Burke-

Ernzerhof (PBE) exchange-correlation functional. The Kohn-Sham equations were solved using the all-electron full-potential linearized augmented plane wave plus local orbitals basis (FP-L/APW+lo) method as implemented in the *WIEN2k* suite of software. [103] This method makes no shape approximation to the potential or the electron density. Within the FP-L/APW+lo method, the unit cell is divided into non-overlapping muffin tins spheres and an interstitial region. Inside the muffin tin sphere, the wave functions are expanded using radial functions (solution to the radial Schrödinger equation) times the spherical harmonics and in the interstitial region, the wave functions are expanded using plane waves. For our work, we have used APW+lo basis to describe all s, p, d, and f (*l*=0, 1, 2, 3) states and LAPW basis to describe all higher angular momentum states up to $l_{wf}^{\max}$ =10 in the expansion of the wave functions. Additional local orbitals (LO) were added to the 6*s* and *6p* semi-core states of U to improve their description. The muffin-tin radii have been chosen to be 2.5 Bohr for U and $R_{MT}K_{MAX}$ = 8.0. For the bulk calculations, a uniform mesh of 1000 k-points was chosen. Calculations were done both at the scalar relativistic (with no spin-orbit coupling (NSOC) and at the fully relativistic (with spin-orbit coupling (SOC)) levels. Spin-orbit interactions are included via a second variational step using the scalar relativistic eigenstates as basis, where all eigenstates with energies below 5.0 Ry are included. Furthermore, relativistic $p_{1/2}$ orbitals have been included to account for the finite character of the $p_{1/2}$ wave function at the nucleus. The quantization axis for the SOC calculations was (001). Self consistency is achieved when total energies are converged to within 0.0001 Ry or better. The hybrid exchange-correlation energy functional$E_{XC}^{PBE+\alpha HF}$, used in this work, has the form

$$E_{XC}^{PBE+\alpha HF} = \alpha E_X^{HF} + (1-\alpha) E_X^{PBE} + E_C^{PBE} \quad (3.1)$$

where E_X^{HF} is the HF exchange, E_X^{PBE} is the PBE exchange functional and E_C^{PBE} is the PBE correlation functional. The parameter α denotes the fraction of HF exchange replacing the PBE exchange and α=25% was used for this work.

3.2 Bulk Results and Discussions

As mentioned before, the bulk calculations were performed before the surface calculations to determine the ground state electronic structure properties. The total energy was minimized at six different levels of theory: non-magnetic (NM), ferromagnetic (FM), and anti-ferromagnetic (AFM) with and without spin-orbit coupling (SOC), all at DFT and HDFT levels. At each level of theory, total energy was computed at several data points and a polynomial fit performed to arrive at the equilibrium lattice constant. The total energy was then recomputed at the equilibrium lattice constant for each level of theory. Table 3.1 lists the derived equilibrium lattice constants, a (Å), and the bulk modulus, B (GPa), both which were calculated from the Murnaghan equation of state, and their percent differences from the experimental value, where the value of 3.47 Å [1] was used for the lattice constant. For the DFT calculations without SOC, the AFM configuration resulted in the lowest energy, but with SOC included, NM was obtained as the ground state. With HYB-DFT, the NM state was also obtained when SOC is added but, without SOC, FM was found to be the ground state. We note that while the lattice constant indicates relatively little preference to the level of theory, the bulk moduli oscillates significantly. FiguresFigure 3.1 throughFigure 3.6 show plots around the minimum value of the relative energy (in relation to the minimum total energy at that level of theory) versus the lattice constant for the DFT and HYB-DFT calculations, respectively, with and without SOC. A polynomial fit was also drawn on these graphs, where the minimum of the curve would indicate the fitted lattice constant. In instances where the fitted lattice constant does not match the lattice constant obtained by way of the Murnaghan equation of state, the bulk modulus is also not consistent with experimental results. This is due to the smoothness of the $\Delta E/\Delta V$ curve, where too many bumps in the curve would cause an inconsistent bulk modulus and lattice constant calculation.

Table 3.1 Lattice constants (Å) and bulk moduli (GPA) and their difference from experimental values (Δ) of bulk γ – U at different levels of theory

Theory		a (Å)	Δa (%)	B (GPa)	ΔB (%)
DFT	NM	3.44	-0.86	134.22	18.46
	FM	3.46	-0.29	125.45	10.72
	AFM	3.44	-0.86	134.38	18.61
	NM + SOC	3.46	-0.29	113.75	0.40
	FM + SOC	3.47	0.00	100.64	-11.17
	AFM + SOC	3.59	3.46	96.33	-14.98
H – DFT	NM	3.48	0.29	111.62	-1.48
	FM	3.51	1.15	156.27	37.93
	AFM	3.51	1.15	128.76	13.65
	NM + SOC	3.49	0.58	272.89	140.86
	FM + SOC	3.65	5.19	96.23	-15.07
	AFM + SOC	3.51	1.15	501.96	343.04
Exp.		3.47	-	113.3	-

For the ground state NM HYB-DFT with SOC calculations the bulk modulus varied greatly from experiment which leaves us to conclude that while it might be a useful tool to describe some heavily correlated systems, it appears to be unreliable in predicting reasonable values for the bulk modulus for U. An energy comparison for each level was evaluated against the ground state acquired for that level of theory. Table 3.2 contains the difference in energy related by E(X) - E(ground), where X is NM, FM, or AFM. In addition, the spin-polarization (SP) and spin-orbit coupling (SOC) energies at the equilibrium lattice constant are also listed in Table 3.2. These were calculated from:

$$E_{sp} = E_{tot}(NM) - E_{tot}(level) \tag{3.2}$$

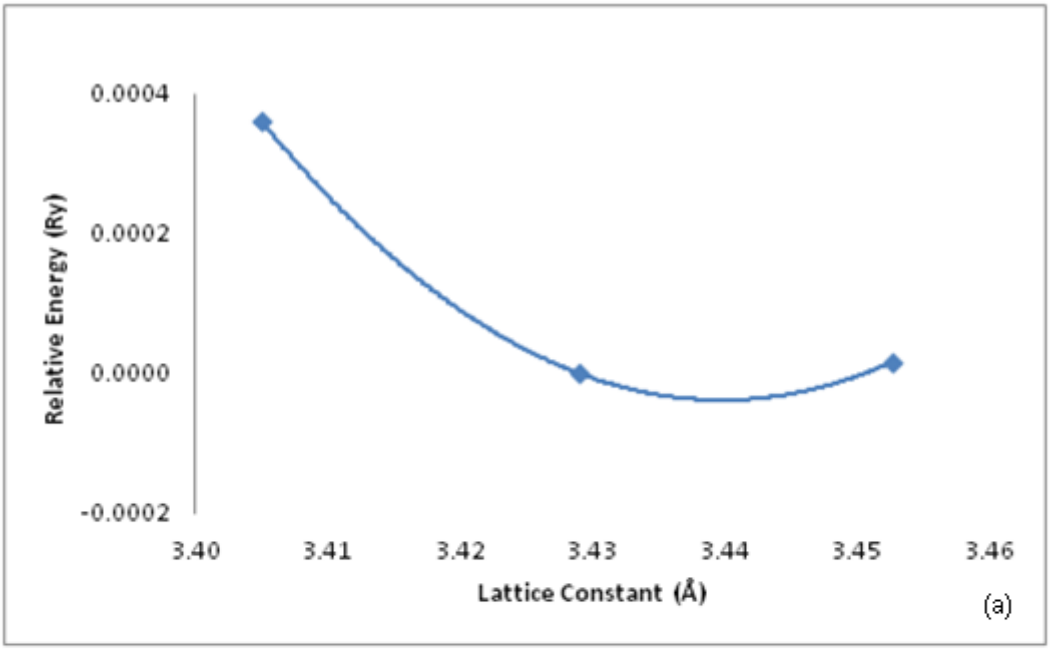

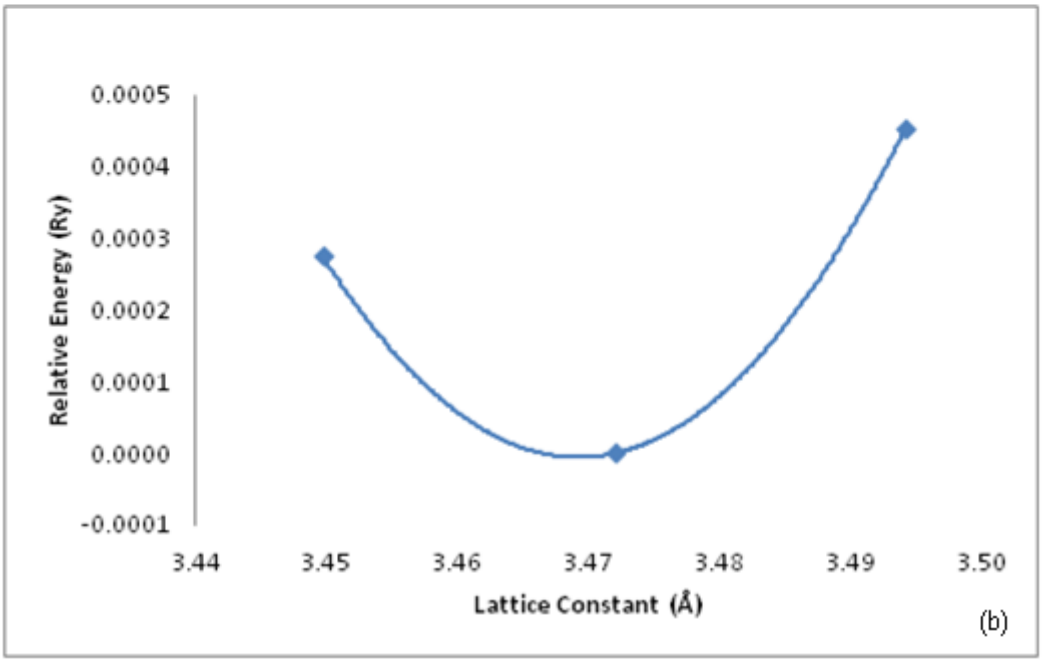

Figure 3.1 Optimization of the lattice constant at the NM DFT level of theory with (b) and without SOC (a)

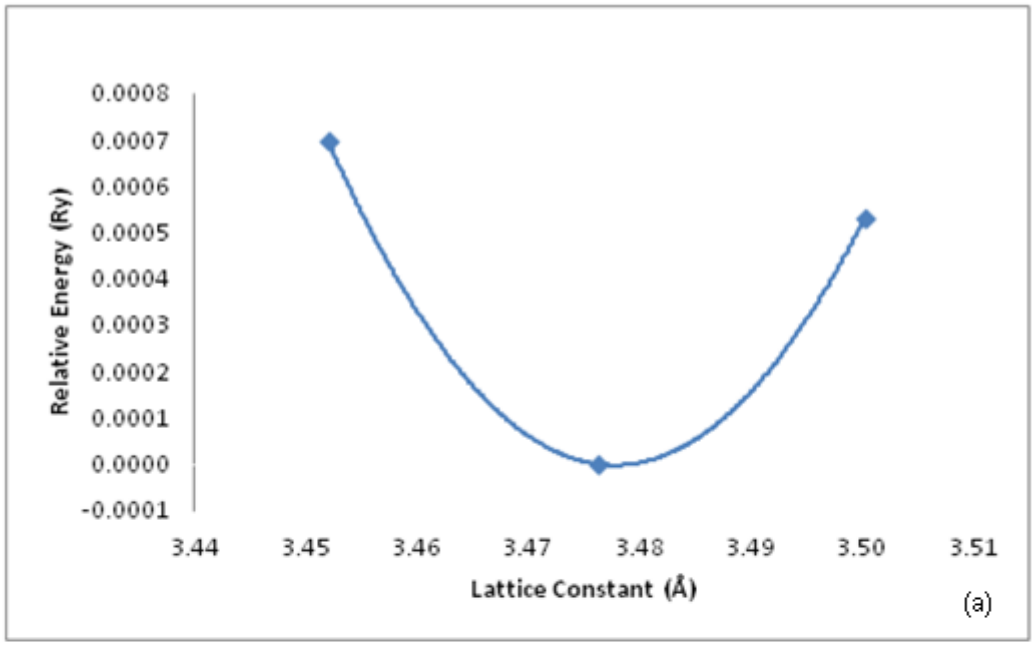

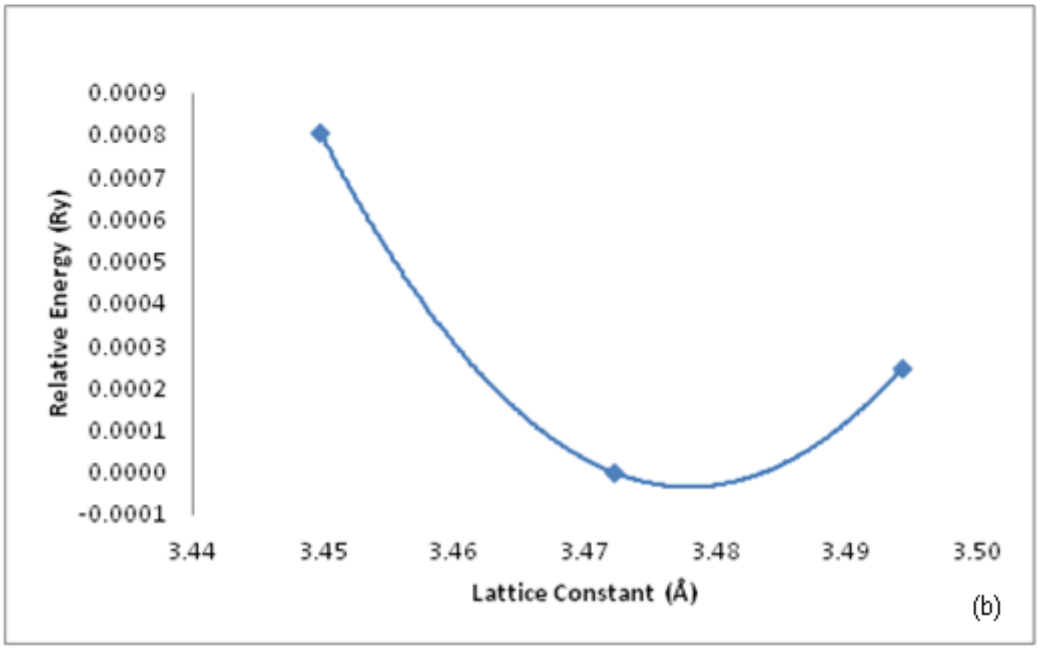

Figure 3.2 Optimization of the lattice constant at the NM HYB-DFT level of theory with (b) and without SOC (a)

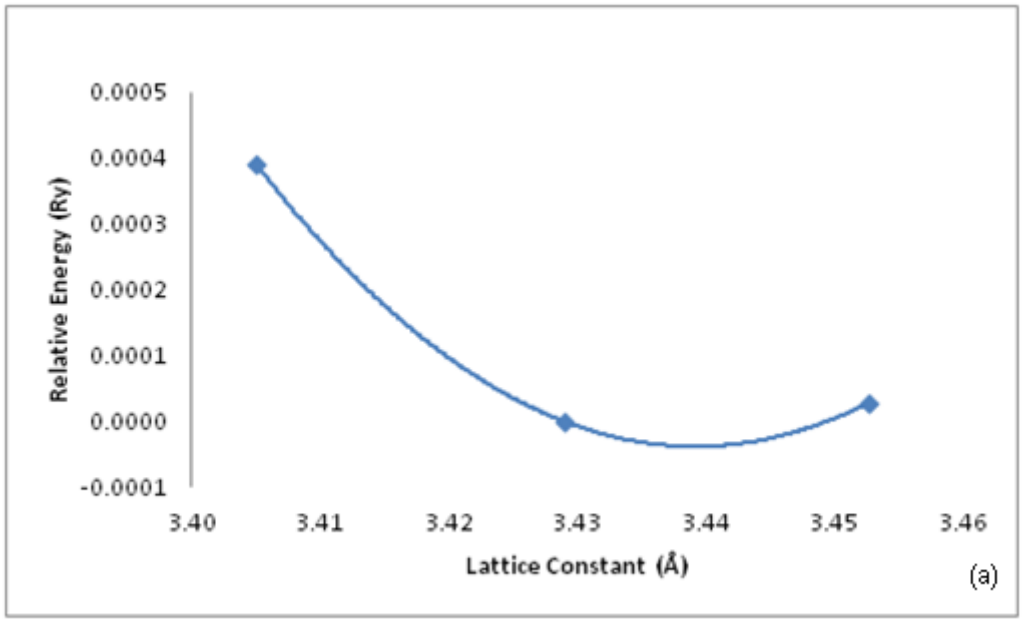

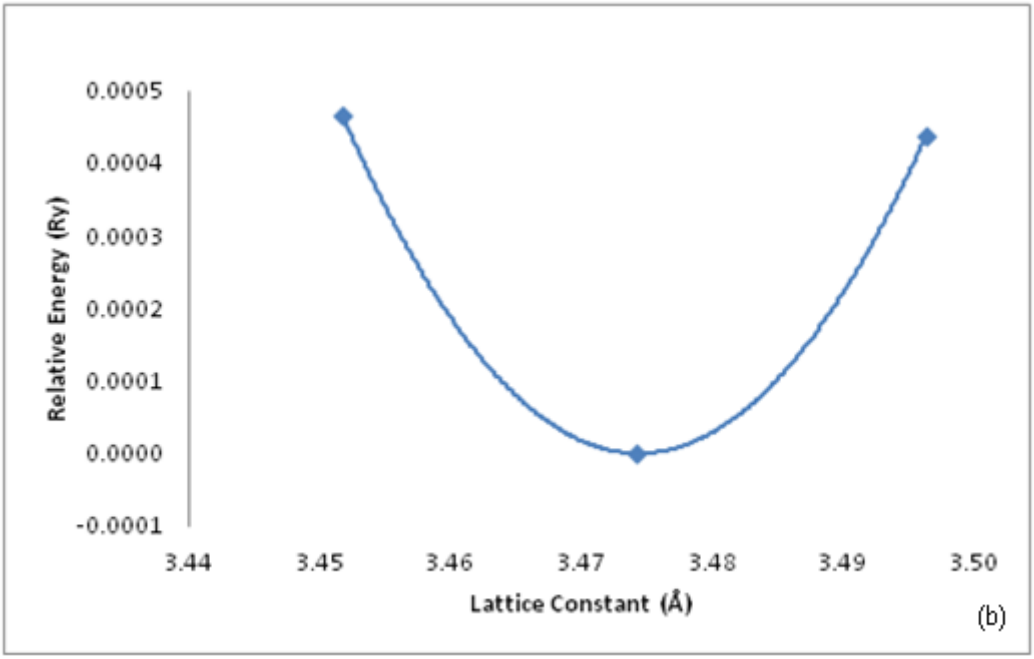

Figure 3.3 Optimization of the lattice constant at the FM DFT level of theory with (b) and without SOC (a)

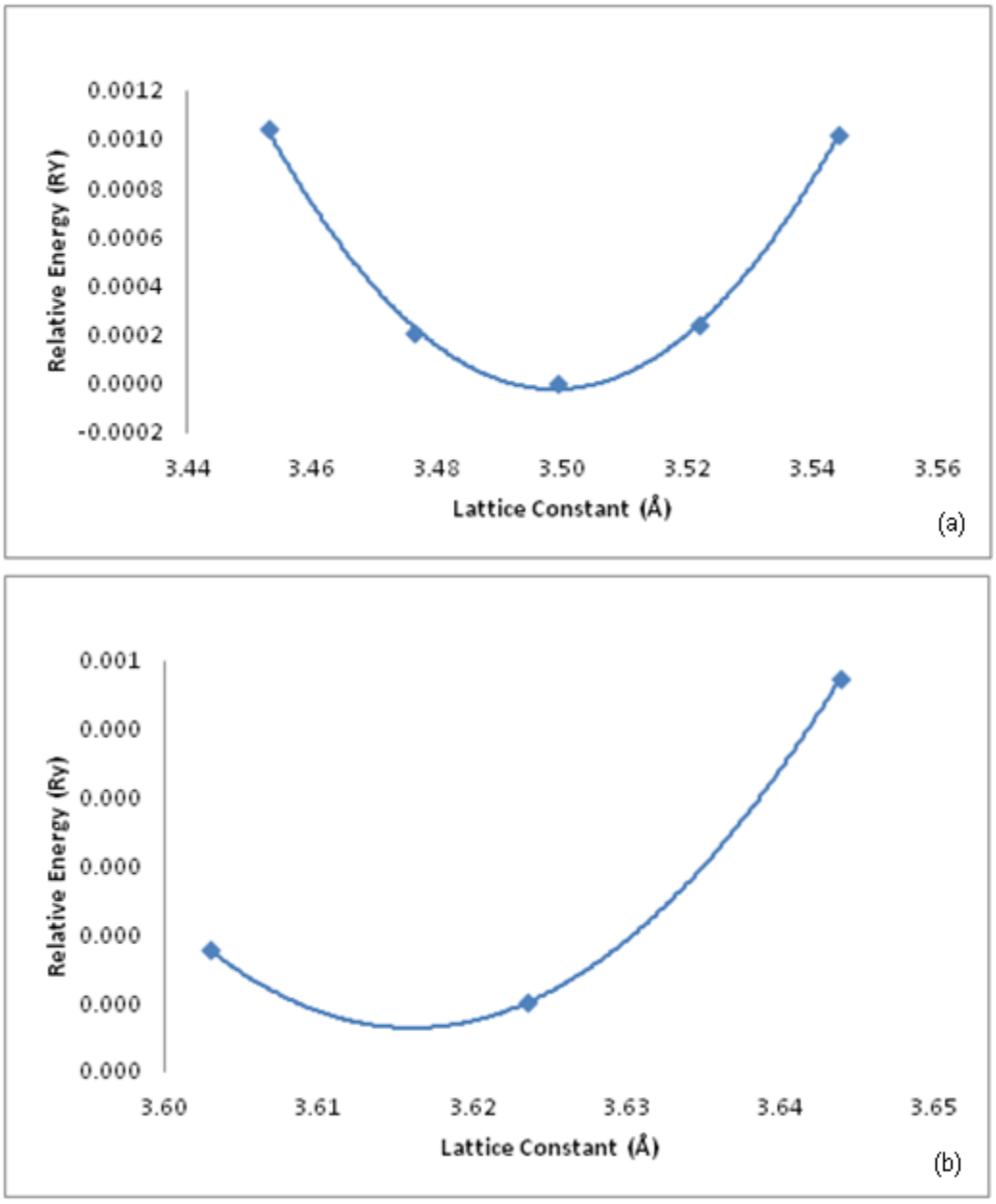

Figure 3.4 Optimization of the lattice constant at the FM HYB-DFT level of theory with (b) and without SOC (a)

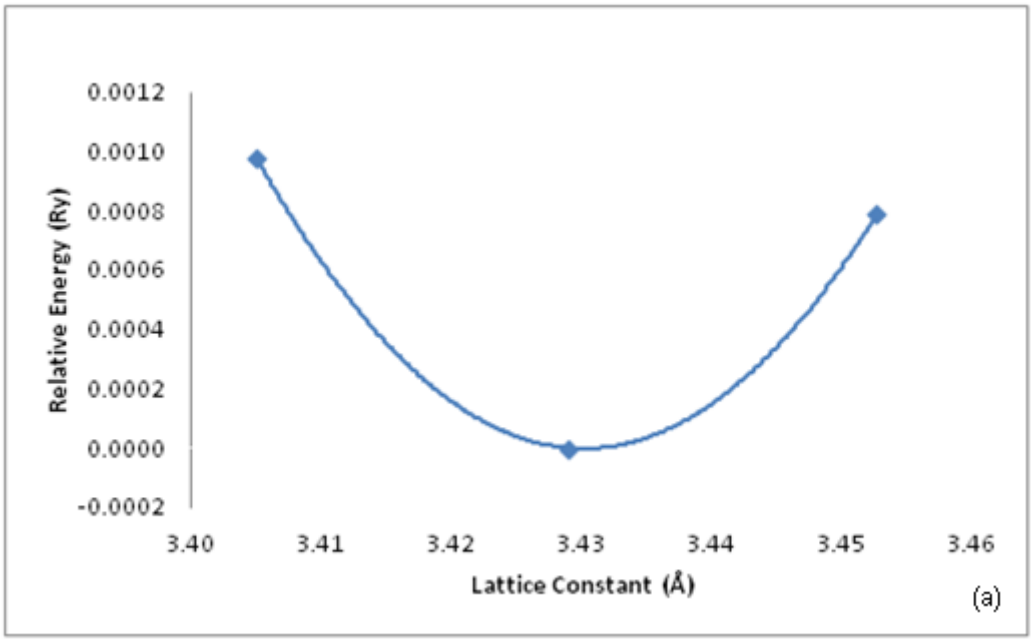

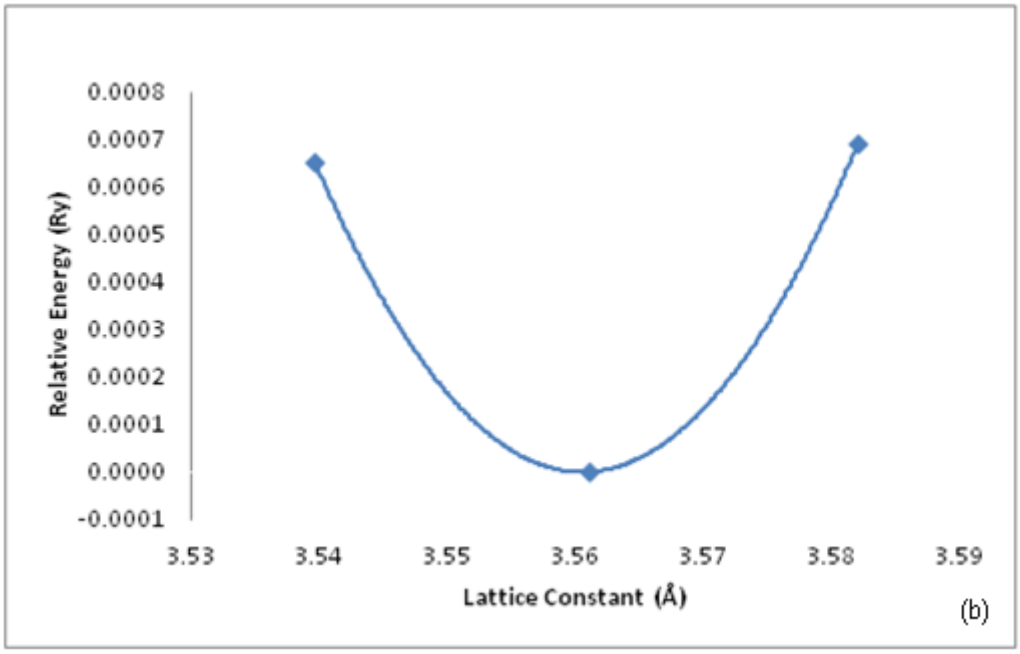

Figure 3.5 Optimization of the lattice constant at the AFM DFT level of theory with (b) and without SOC (a)

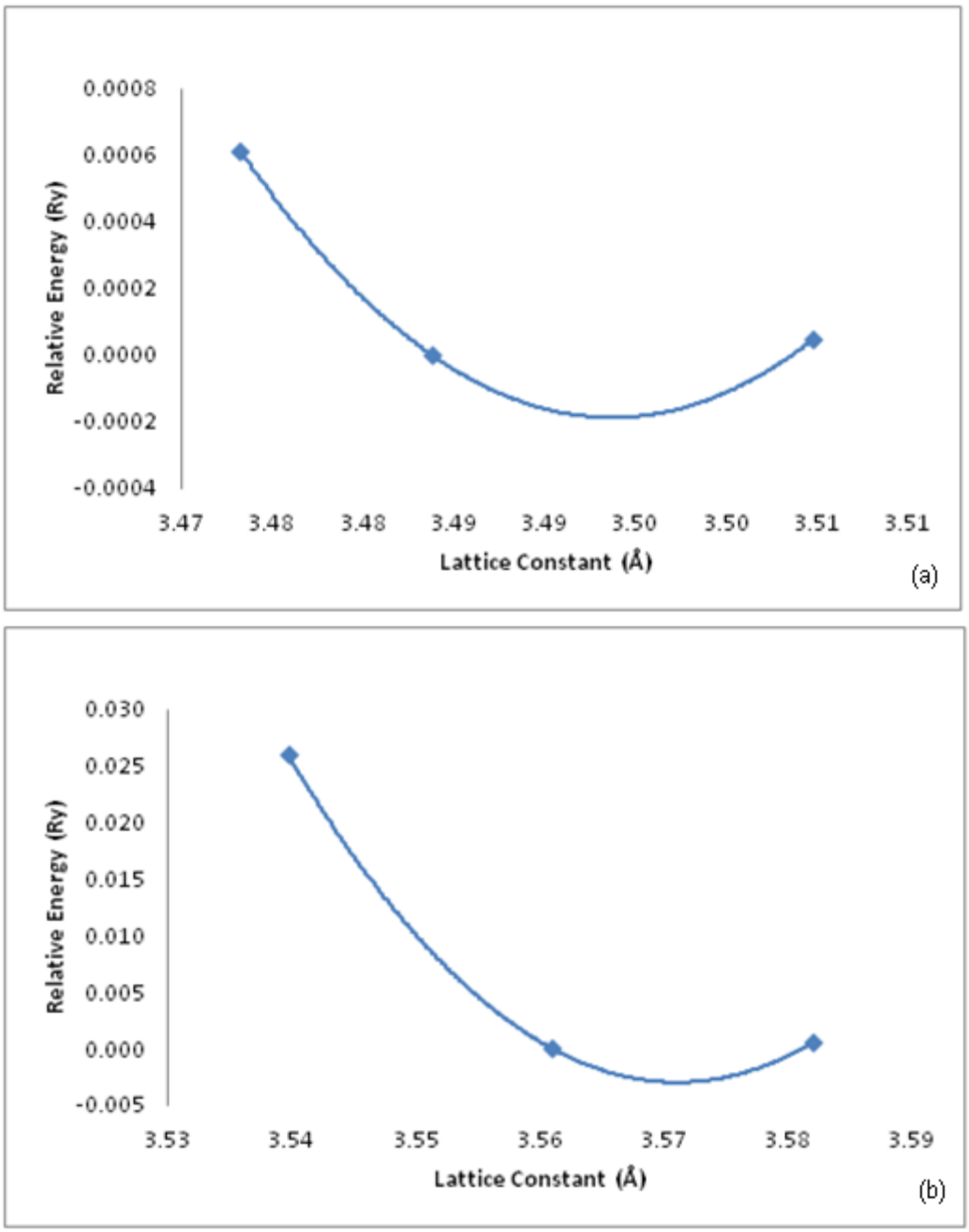

Figure 3.6 Optimization of the lattice constant at the AFM HYB-DFT level of theory with (b) and without SOC (a)

and

$$E_{so} = E_{tot}(NSO) - E_{tot}(SO) \tag{3.3}$$

For the DFT NSO FM and AFM calculations E_{sp} is negligible with near zero values. When SOC is added, the E_{sp} is near -250 mRy, showing that spin-polarization is insignificant unless SOC is considered in the calculation. NSO FM and AFM calculations for the HYB-DFT showed similar results for E_{sp}.

Table 3.2 Total energy differences obtained at each level of theory, spin-polarization energy Esp (mRy/unit cell) and spin-orbit coupling energy Eso (mRy/unit cell).

Theory		ΔE (mRy)	Esp (mRy)	Eso (mRy)
DFT				
	NM	0.12		
	FM	0.14	-0.01	
	AFM	0.00	0.12	
	NM + SOC	0.00		433.45
	FM + SOC	264.85	-264.85	168.61
	AFM + SOC	247.52	-247.52	185.81
H – DFT				
	NM	26.16		
	FM	0.00	26.16	
	AFM	0.99	25.17	
	NM + SOC	0.00		468.09
	FM + SOC	254.33	-254.33	187.59
	AFM + SOC	254.54	-254.54	188.38

A Gaussian broadened (broadening factor of σ = 0.003 Ry) density of states (DOS) plot around the Fermi energy is presented in Figure 3.7 Density of states for the ground state with experimental ultraviolet photoelectron spectroscopy (UPS-HeII spectrum) data for U bulk metal is

plotted in black for comparison [47]. for the NM case with SOC using HYB-DFT and DFT. The DFT results show no gap at the Fermi level, an indication of a metallic substance, and above the Fermi level, the results are indicative of XPS valence bands at the P_3 level found by Fuggle *et. al.* [110] in that there is a distinct peak just below 2 eV above the Fermi level. Additionally, experimental ultraviolet photoelectron spectroscopy (UPS-HeII spectrum) data by Gouder [47] is superimposed atop for the sake of comparison.The HYB-DFT DOS show similar results over the Fermi level but it does not show a distinct peak at or near the Fermi level. A comparison of the results shows no significant difference between the results of the two theories in obtaining the correct ground state, as long as SOC is added to the calculation, except that, as mentioned before, the HYB-DFT calculations do not give a good value for the bulk modulus. Also, as for the DOS plot, HYB-DFT does not give a plot resembling that of experimental findings. Thus, for this we continue analysis of the surface properties using only standard DFT.

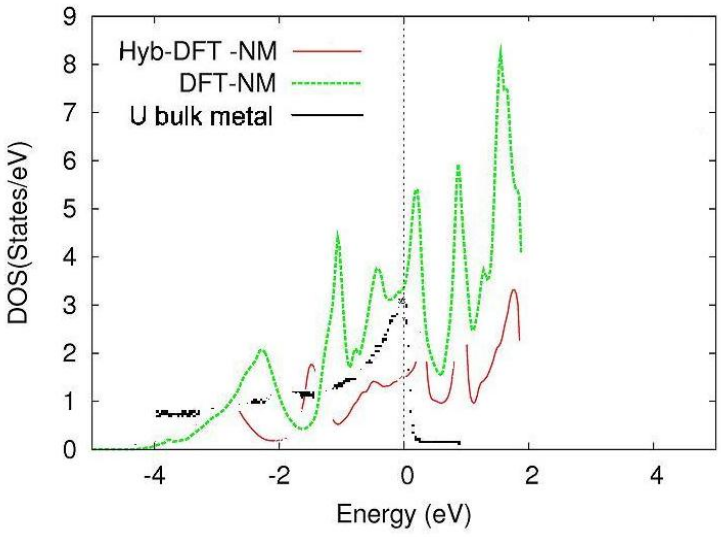

Figure 3.7 Density of states for the ground state with experimental ultraviolet photoelectron spectroscopy (UPS-HeII spectrum) data for U bulk metal is plotted in black for comparison [47].

3.3 Results and Discussion for (100) Nanolayers

For the surface calculations, the lattice constants for N = 1-6 layers were optimized with respect to volume (V) to compare the deviation of the slab lattice constants with the bulk. The vacuum layer was fixed at 30 a. u. For each slab 1-6, the energy was plotted for varying lattice constants and a polynomial harmonic fit was performed to obtain the "effective" lattice constant for each thin film as shown in Figure 3.8 through Figure 3.13. These values and the percent deviation from the theoretical bulk value are reported in Table 3.3. We note that the monolayer shows a significant contraction of 23.55%.

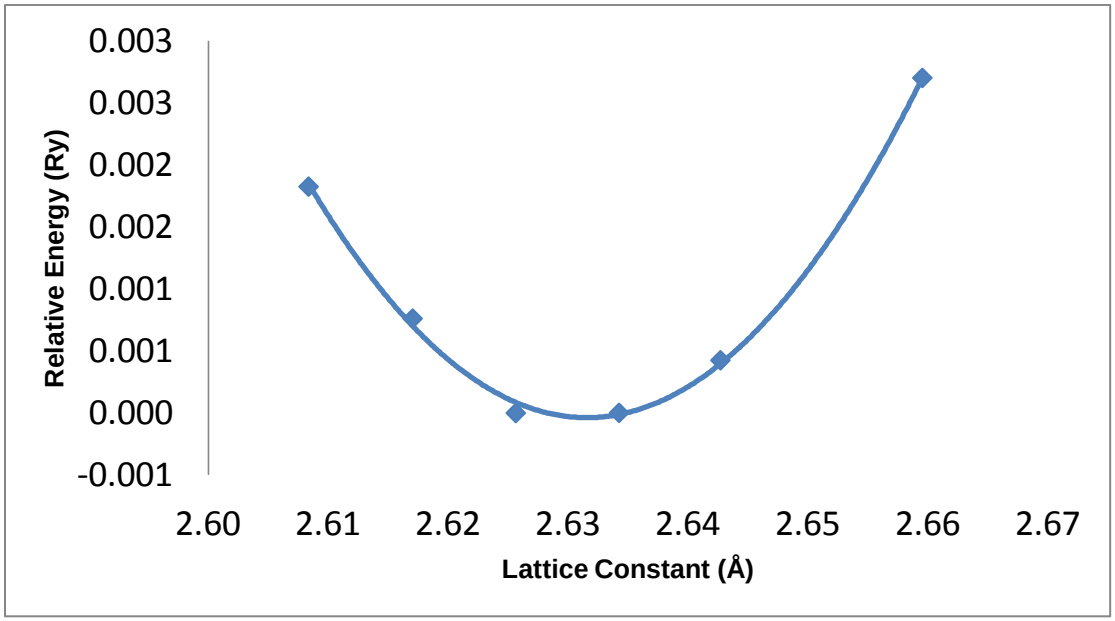

Figure 3.8 Optimization of the "effective" lattice constant for the monolayer

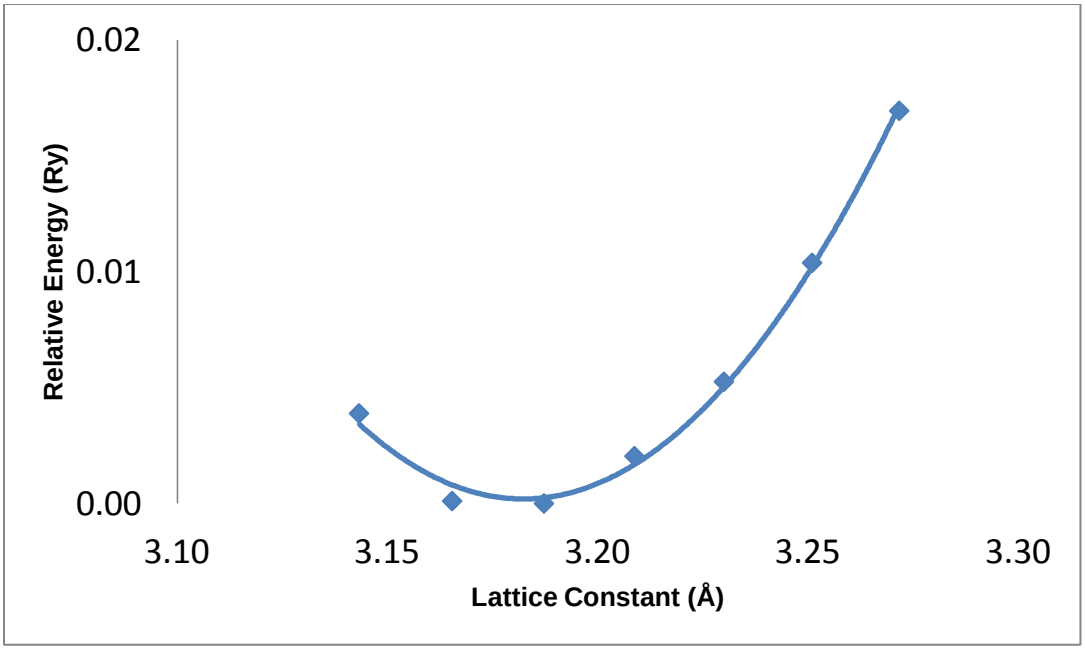

Figure 3.9 Optimization of the “effective” lattice constant for the di-layer

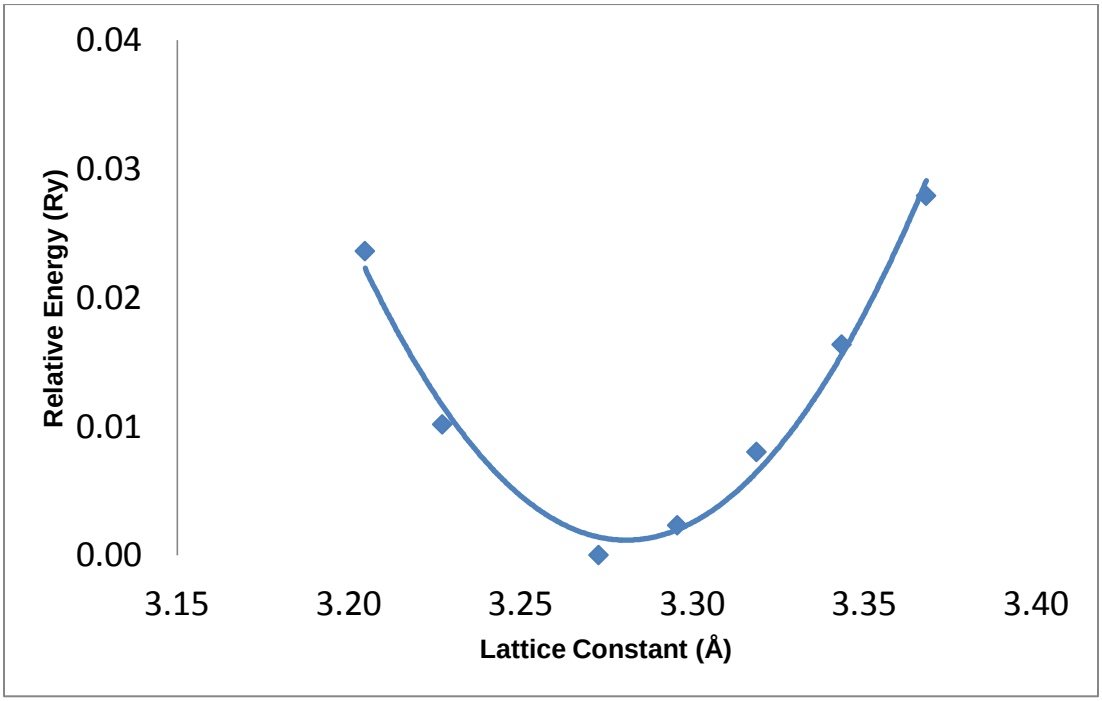

Figure 3.10 Optimization of the “effective” lattice constant for the tri-layer

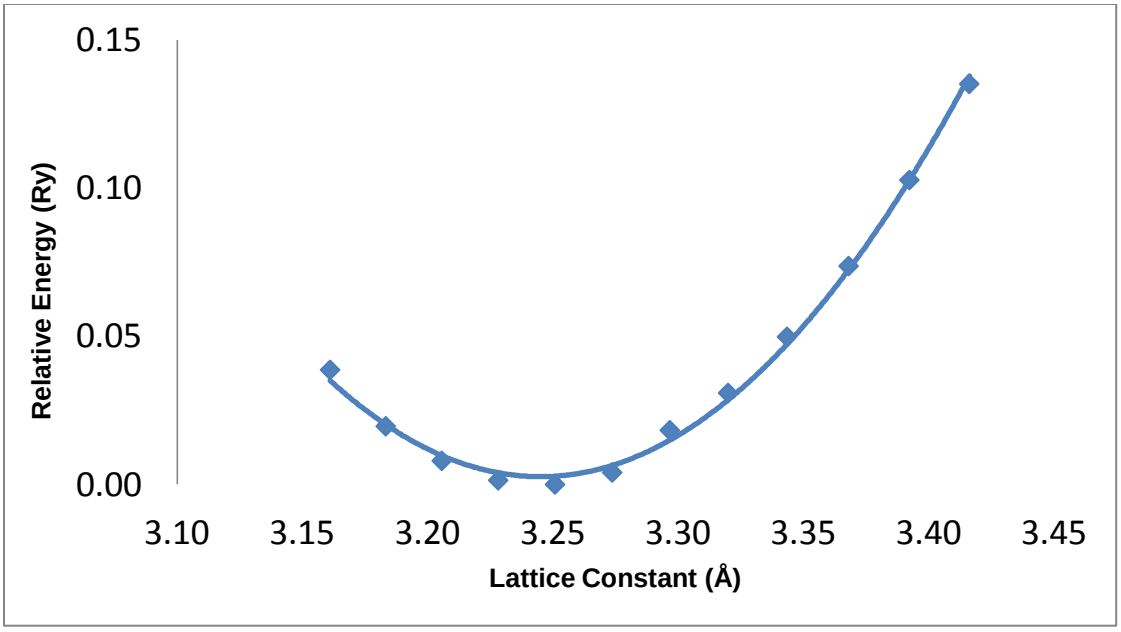

Figure 3.11 Optimization of the “effective” lattice constant for the tetra-layer

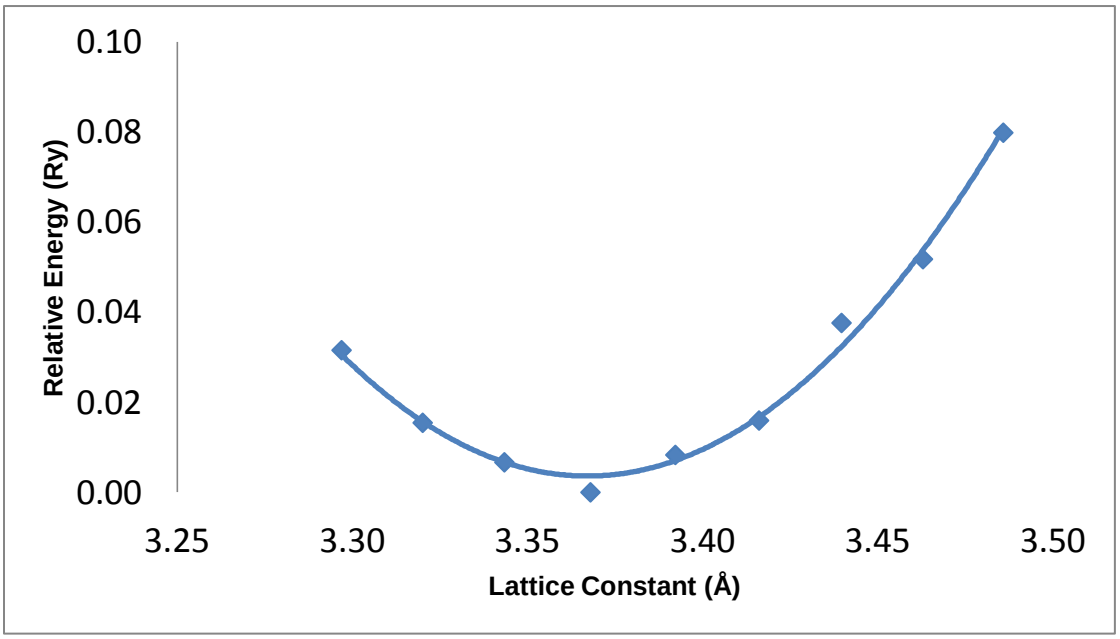

Figure 3.12 Optimization of the “effective” lattice constant for the penta-layer

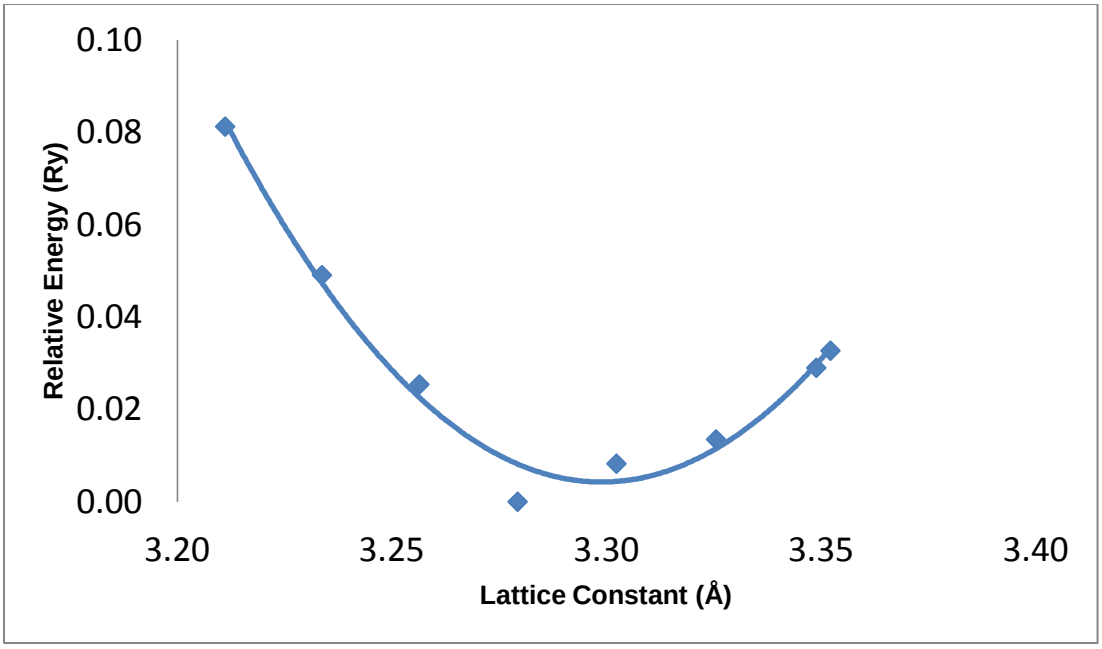

Figure 3.13 Optimization of the “effective” lattice constant for the hexa-layer

Table 3.3 Optimized lattice constants for N=1-6 layers

N	a (Å)	Δa %
1	2.63	-23.55
2	3.18	-7.56
3	3.28	-4.65
4	3.25	-5.52
5	3.37	-2.03
6	3.3	-4.07
Bulk	3.44	

These results are comparable to the results obtained in other ultra thin film (UTF) calculations performed by our group. One example is on the (0001) surface of Am-I where the maximum

contraction of its monolayer was 8.7% with respect to the theoretical bulk lattice constant and similar observations were made in DFT calculations on δ-Pu (111) and (100) monolayers. This suggests that the uranium atoms are very highly attracted to each other and have a tendency to either gather into a nanoparticle or form a crystalline structure. In fact, all the layers, up to 6 in this study, indicate varying amounts of contraction though there is a general tendency of convergence towards the "bulk" value. While oscillations of the lattice constants are seen in other actinide studies of this type, like for the (0001) surface of Am-I or the (111) and (100) surfaces of δ-Pu, the oscillations appear to be more pronounced for the (100) surface of γ – U.

Table 3.4 Total energy and incremental energy ΔE per atom (Ry/atom) with and without SOC

Theory	N	E/Atom (Ry/atom)	ΔE (mRy/atom)
NSO			
	1	-56165.8085	-
	2	-56165.8404	-31.84
	3	-56165.8865	-46.19
	4	-56165.8989	-12.35
	5	-56165.9075	-8.64
	6	-56165.9153	-7.81
Theoretical Bulk		-56165.9459	
SOC			
	1	-56166.2371	-
	2	-56166.2683	-31.21
	3	-56166.3160	-47.68
	4	-56166.3284	-12.4
	5	-56166.3384	-10.07
	6	-56166.3460	-7.59
Theoretical Bulk		-56166.3747	

We define the incremental energy, ΔE, as [111], [112]

$$\Delta E(N) = E_{tot}(N) - E_{tot}(N-1) \tag{3.4}$$

where $E_{tot}(N)$ is the total energy of an N-layer slab per atom and ΔE is the change in total energy per atom as more "bulk" is added. The values of ΔE help us to ensure increased stability with added bulk by maintaining a negative trend and to determine an adequate thickness for future surface and adsorption calculations by decreasing to a reasonably small value. Ideally, the $E_{tot}(N)$ per atom should converge to the theoretical bulk energy as $N \rightarrow \infty$.

Table 3.4 lists the total energy per atom and the incremental energy. We can see that the total energy per atom decreases with increasing bulk for calculations with and without SOC, proving that each added layer provides a more stable structure. For the first three layers a large ΔE is witnessed, indicating large quantum size effects but as more layers are added the energy per atom begins to approach that of the bulk. Once 5 layers have been added, ΔE becomes considerably small at 10.1 mRy/atom for SOC. For comparison with the bulk study, we also provided the spin-orbit coupling energy, E_{so}, as define by equation (10) for each layered structure in Table 3.5. As with the total energy per atom, the E_{so} of each layer also begins to approach that of the theoretical bulk with the addition of more layers.

Table 3.5 Spin-orbit coupling energy, E_{so}, for layers 1 through 6

Number of Layers	E_{so} (mRy/atom)
1	428.56
2	427.94
3	429.43
4	429.48
5	430.91
6	431.02
Theoretical bulk	433.39

The surface energy per unit area, γ, is defined as the energy required to cleave a surface of area A and is described by the equation [111], [112]

$$\gamma = \frac{1}{2A}[E_{tot}(N) - NE_B] \tag{3.5}$$

where $\mathrm{E_{tot}(N)}$ is the total energy of an N-layer slab, E_B is the total energy per atom of the bulk, A is the area of the surface and N is the number of layers in the slab. This can be written as

$$E_{tot}(N) = NE_B + \kappa \tag{3.6}$$

with κ = 2Aγ, giving a linear equation for a line with $\mathrm{E_{tot}(N)}$ as y, N as x, E_B the slope of that line and κ being the y-intercept. Plotting $E_{tot}(N)$ versus N we can obtain a value of E_B that is consistent with the slab calculations by taking a least squares linear fit. Table 3.6 compares the bulk energy calculated in the bulk study with the fitted bulk energy obtained from our plotted line.

Table 3.6 The fitted and theoretical bulk energies, E_B, with and without SOC

Theory		E_B (Ry/atom)	δE (mRy/atom)
NSO	Calculated	-56165.9425	
	Theoretical	-56165.9459	3.4
SOC	Calculated	-56166.3761	
	Theoretical	-56166.3747	1.4

The maximum deviation, δE, is 3.40 mRy/atom for NSO, which consistent with previous DFT calculations of this nature. Then taking our fitted value of E_B and putting it into equation (3.6) we calculated the surface energy of each N-layer slab. These values are shown in Table 3.7 and plotted in Figure 3.14. The surface energy of a slab with semi-infinite thickness is obtained by the y-intercept or γ = κ/2A and is 1.48 J/m^2 for NSO and 1.56 J/m^2 for SOC which is comparable to the experimental value of 1.45 J/m^2 obtained by Hodkin *et al*. [113] for liquid U at temperatures

between 1190 and 1600 ˚C (1463 to 1873 K). The 2-layer slab has the highest surface energy among all the layers studied at 2.16 and 2.24 J/m^2 for NSO and SOC respectively. The surface energy of the remaining slabs decreases gradually with very little fluctuation until reaching the semi-infinite value.

Table 3.7 Surface energy,γ, of the nanolayers

	N	γ (J/m^2)
NSO	1	2.08
	2	2.16
	3	1.64
	4	1.73
	5	1.59
	6	1.52
semi-infinite		1.48
SOC		
	1	2.13
	2	2.24
	3	1.71
	4	1.82
	5	1.62
	6	1.57
semi-infinite		1.56
Exp.		1.45 +/- 0.012

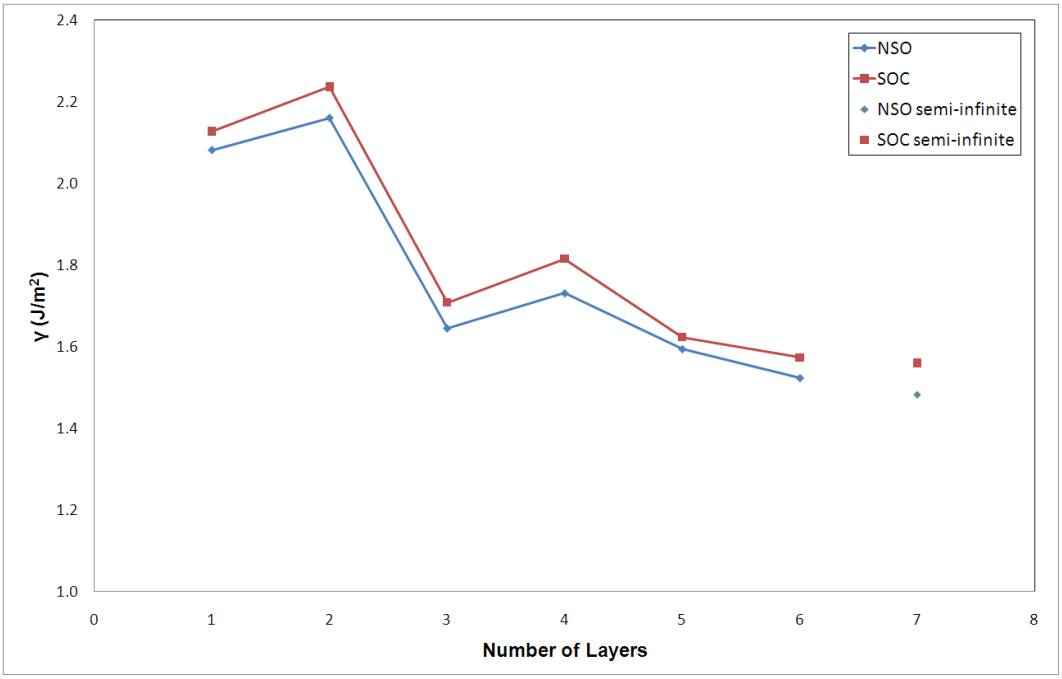

Figure 3.14 Surface energy per unit area, γ (J/m2) versus the number of layers with and without SOC

The work function, Φ, is computed as

$$\Phi = V(\infty) - E_F \tag{3.7}$$

where V(∞) is the Coulomb electrostatic potential in the vacuum region and E_F is the energy at the Fermi level. It is defined as the energy required in removing an electron from within the slab through the surface and microscopically far away from it at a temperature of 0 K. The work functions for each slab thickness at SOC and NSO levels of theory are listed in Table 3.8. For both NSO and SOC calculations, the work function for the thinnest layers starts out high but after the 5th layer is added it stabilizes to around 3.18 eV for NSO and 3.24 for SOC which agrees fairly well with the experimental value obtained by Riviere [114] of 3.2 eV for bulk α-U. Most experimental work functions for γ-U are performed on thin films on some type of substrate which cannot, as such, be compared to our results. We do note that our results are similar to experimental studies of “monolayer” thick uranium films on polycrystalline tungsten substrate

Table 3.8 Work function for each N layer slab

	N	φ (eV)
NSO	1	4.34
	2	4.25
	3	3.04
	4	3.18
	5	3.18
	6	3.11
SOC		
	1	4.38
	2	3.85
	3	3.15
	4	3.27
	5	3.24
	6	3.22
	Exp	3.20

which predicts a value of 3.53 eV using the Kelvin technique [115] and 3.45 eV using the Fowler technique [116] for the work function of high temperature γ-U.

A Gaussian broadened total DOS, with a parameter of 0.003 Ry, for a 6 layer slab is presented in Figure 3.16 Gaussian broadened total density of states plot for the 6-layer slab. From this plot we can see that the 6 layer slab total DOS is similar to that of the bulk with a distinct peak at the Fermi level (a formation customary for metallic systems) and a parallel trend with experimental findings. Figure 3.17 displays the total, in red, and the 5f electron, in green, DOS plotted for atoms located at the surface, subsurface and center of the 6 layer slab. The electrons of the atom at the surface show similar features to the total DOS of the entire slab except there is a much more distinct and sharper localized peak at/near the Fermi level. As we

look further inside the slab at the subsurface atoms we see a dramatic decrease of the peak at the Fermi level by a factor of nearly one-half and a dramatic delocalizing trend of the 5f electrons. The centrally located atom exhibits no distinct peak at Fermi level and the delocalization features are clearly evident.

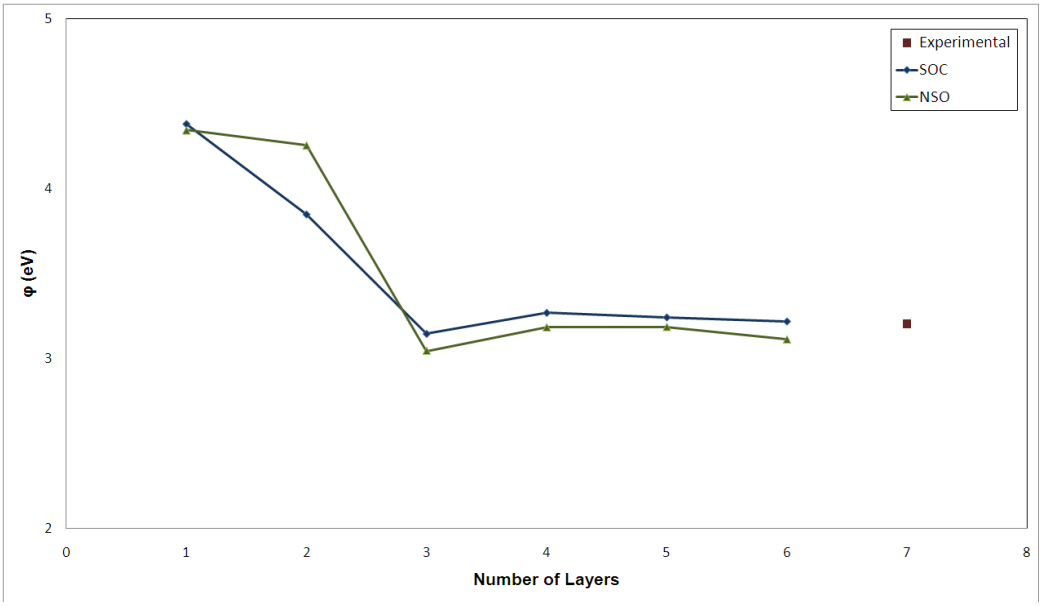

Figure 3.15 Work function (eV) versus the number of layers at the NSOC and SOC levels of theory

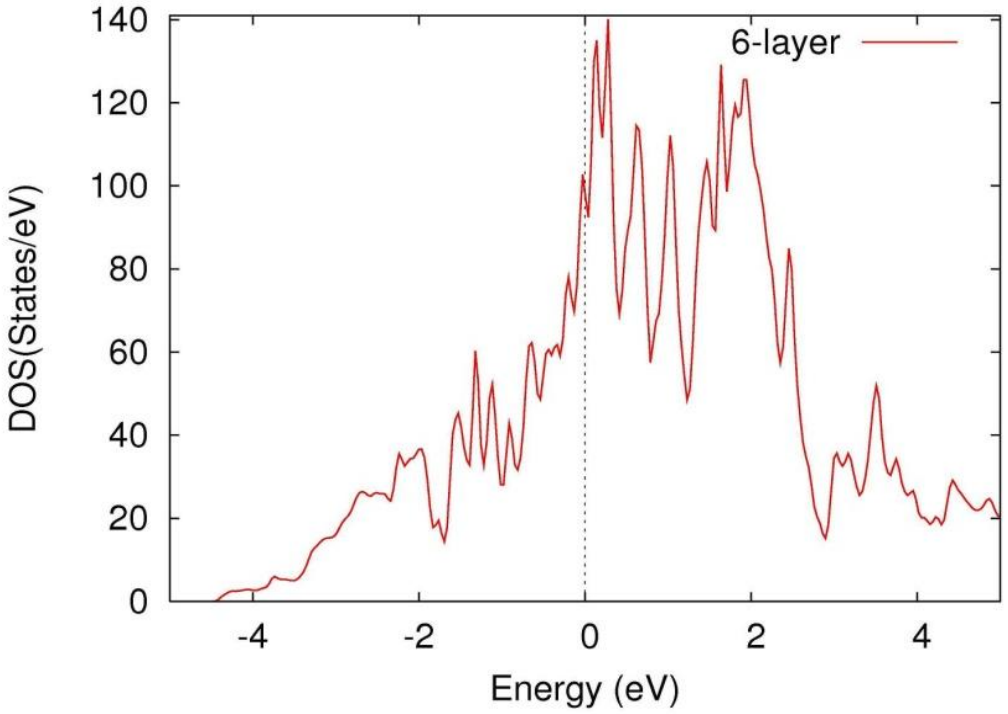

Figure 3.16 Gaussian broadened total density of states plot for the 6-layer slab

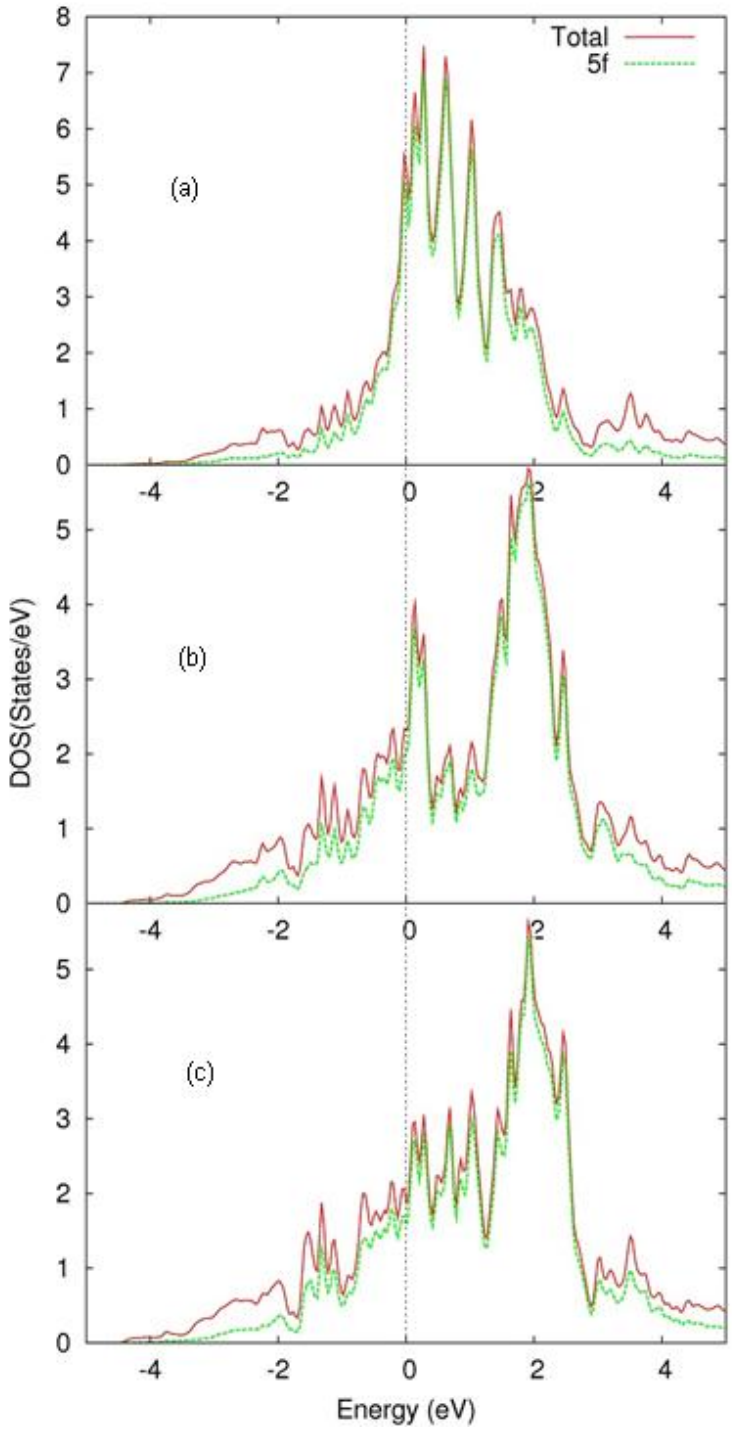

Figure 3.17 Density of states for the surface (a), subsurface (b) and center (c) regions of the 6 layer slab

CHAPTER 4

ATOMIC H AND O ADSORPTIONS AND DIFFUSION ON THE γ-U (100) NANOLAYER

Considerable theoretical efforts have been dedicated in recent years to the study of the electronic and geometric structures and related properties of surfaces to high accuracy. One of the many motivations for this burgeoning effort has been a desire to understand the detailed mechanisms that lead to surface corrosion in the presence of environmental gases; a problem that is not only scientifically and technologically challenging but also environmentally important. Such efforts are particularly important for systems such as the actinides for which experimental work is relatively difficult to perform due to material problems and toxicity. Specifically for this study we will be considering oxidation and hydride formation and embrittlement of the (100) surface of γ-U. In this chapter, we first outline the computational methods used, followed by a discussion of atomic H and O on the (100) surface of a 5 layer slab of γ-U.

4.1 Computational Method

All calculations have been performed within the GGA to DFT with the Perdew-Burke Ernzerhof exchange-correlation functional. [95] As previously mentioned, the Kohn-Sham equations were solved using the all-electron full-potential linear augmented plane wave plus local basis (FP L/APW+lo) method as implemented in the WIEN2K code. Within the FP-L/APW+lo method, the unit cell is divided into nonoverlapping muffin-tin spheres and an interstitial region. Inside the muffin-tin sphere of radius R_{MT}, the wave functions are expanded using radial functions (solution to the radial Schrödinger equation) times spherical harmonics up to $l_{wf}^{\max}$ = 10 and the expansion of the potential inside the muffin-tin spheres is carried out up to $l_{pot}^{\max}$ = 4. The

parameter $R_{MT}^{\min} K_{MAX}$, where $R_{MT}^{\min}$ is the smallest muffin-tin spherical radius present in the system and K_{MAX} is the truncation of the modulus of the reciprocal lattice vector, is used to determine the number of plane waves needed for the expansion of the wave function in the interstitial region. The parameter G_{MAX} is used to truncate the plane-wave expansion of the potential and density in the interstitial region. For this study, we have used R_{MT}(O)=1.15 a.u., R_{MT}(H)=0.60 a.u. and R_{MT}(U) =2.00 a.u., and $R_{MT}^{\min} K_{MAX}$ = 8.00 for $R_{MT}^{\min}$ =R_{MT}(U) with G_{max}= 12 a. u. $^{-1}$, $R_{MT}^{\min} K_{MAX}$ = 4.60 for $R_{MT}^{\min}$ = R_{MT}(O) with G_{MAX}=17 a. u. $^{-1}$ and $R_{MT}^{\min} K_{MAX}$ = 2.40 for $R_{MT}^{\min}$ = R_{MT}(H) with G_{MAX} = 20 a. u. $^{-1}$. These values correspond to K_{MAX} = 4 a. u. $^{-1}$ for all calculations, ensuring that all calculations have the same plane wave cut off energy. An APW+lo basis is used to describe all core states and LAPW basis for all higher angular momentum states for each atom.

As stated before, core states are treated at the fully relativistic level. Valence states are treated at either the scalar relativistic level, without spin-orbit coupling (NSOC), or at the fully relativistic level, with spin-orbit coupling (SOC) included. Spin orbit interactions for valence states are incorporated through a second variational procedure using the scalar relativistic eigenstates as basis, where all eigenstates with energies below the cutoff energy of 5.0 Ry were included. In addition, the relativistic $p_{1/2}$ orbital was included to account for the finite character of the wave function at the nucleus for the $p_{1/2}$ state. [103] We considered both the NSOC and SOC levels of theory to investigate the effects of spin-orbit coupling on chemisorption energies.

The γ-U (100) surface is modeled by a supercell consisting of a five-layer slab with four atoms per surface in the unit cell, where the periodic slabs are separated in the *z* direction by vacuum regions of 30 a.u. thick. Our use of the five-layer slab is justified by recent calculations γ-U surfaces [117] which showed that surface properties converge within the first five layers. Before the addition of the adatom, the slab was relaxed at three magnetic configurations; non-spin-polarized (NM), spin-polarized (FM), and spin-polarized with anti-ferromagnetic spin configuration (AFM). The AFM configuration consisted of alternating spin-up and spin-down ferromagnetic

sheets along the *a* axis. While this configuration is more considered *ferrimagnetic*, it allowed an AFM configuration with an equal amount of spin-up and spin-down orbitals in our five-layer slab. While performing these calculations, it became evident that, although the slab was nearly degenerate in energy for the NM, FM and AFM configurations at the NSOC level (agreeing with our previous bulk findings [117]), when SOC was added the ground state was not NM as expected but degenerate in the AFM and FM magnetic ordering. This is expected for ultra thin films because they would have a larger ratio of surface atoms, with narrower electronic bands, *versus* interior atoms, with broader bands, than bulk allowing the surface atoms to determine the magnetic ordering of the entire slab. In addition, a surface magnetic moment had been found for thin films of α-U [44] using similar theoretical techniques to our study. Table 4.1 lists the ΔE values, where

$$\Delta E = E_{tot}(X) - E_{tot}(\text{Minimum}) \tag{4.1}$$

X being NM, FM or AFM. Due to these findings all further calculations in this paper have been done at all three levels of theory in addition to NSOC and SOC treatment as stated above.

Table 4.1 Difference in energy of a 5 layer slab of γ-U at the NM, FM and AFM magnetic configuration

Theory		ΔE (eV)
NSO	AFM	0.16
	FM	0.00
	NM	0.52
SOC	AFM	0.00
	FM	1.08
	NM	14.48

After addition of the adatom, no further surface relaxations were taken into account primarily because of computational costs. We do believe, though, that the qualitative and quantitative results reported here would not change significantly upon the inclusions of

relaxations and/or reconstructions. Integrations in the Brillouin zone (BZ) were performed using the special *k* point sampling method with the temperature broadening of the Fermi surface by the Fermi distribution where a broadening parameter of 0.005 Ry has been used. This scheme avoids the instability originating from level crossings in the vicinity of the Fermi surface in metallic systems and also reduces the number of *k* points necessary to calculate the total energy of metallic systems. [118] For the present work, 25 *k* points in the irreducible part of the BZ were found to be sufficient. Self-consistency is achieved when the total-energy variation from iteration to iteration converged to a 0.1 mRy accuracy or better and the charge density variation converged to 0.001 e^-/V.

To study adsorption on the U surface, a single adatom, corresponding to a surface coverage of 0.25 ML (monolayer), was allowed to approach the surface from one side along three symmetrically different positions, as shown in Figure 4.1, (a) top site (adatom is directly on top of a U atom), (b) center site (adatom is in between four nearest neighbor U atoms), and (c) bridge site (adatom is placed in the middle of two nearest-neighbor U atoms). After absorption of the adatom into the bulk, it would then diffuse to interstitial lattice sites and saturate the metal. Therefore, we also wanted to look at electronic properties of O and H while trapped within the lattice. Specific locations are depicted in Figure 4.2 and are associated with the surface sites as a) inner top; b) inner center; and c) inner bridge.

The chemisorption energy, E_C, is optimized with respect to the height, *R,* of the adatom above the surface except for the interstitial top and center sites where this is not possible. This was done for the NM, FM and AFM cases without taking into account the spin-orbit interaction. E_C is given by

$$E_{C(}R\,) = E(M\,) + E(X\,) - E(M + X), \tag{4.2}$$

where $E(M\,)$ is the total energy of the bare metal slab, $E(X\,)$ is the total energy of the isolated adatom, and $E(M+X\,)$ is the total energy of the adatom adsorbed on the metal. To

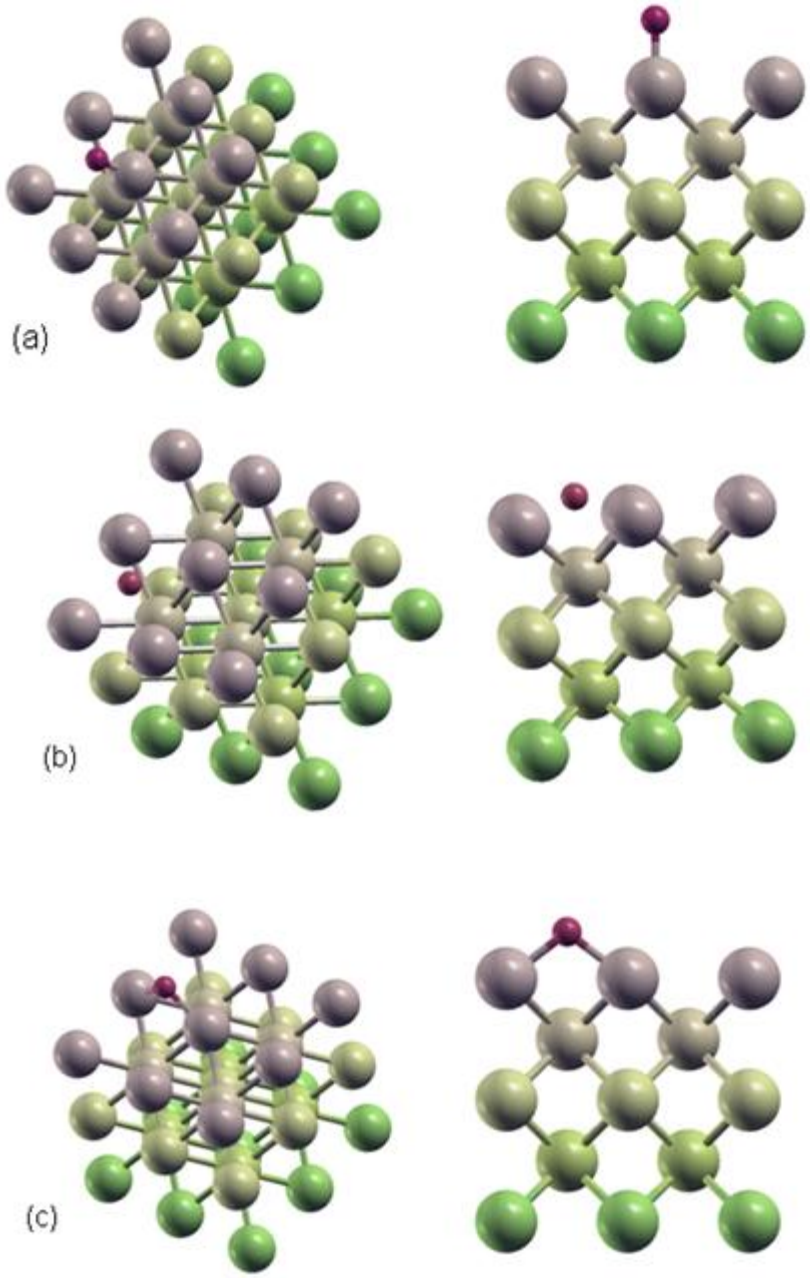

Figure 4.1 Top view (left) and side view (right) of the top (a) and (b) center (c) bridge adsorption site on the (100) surface of γ-U

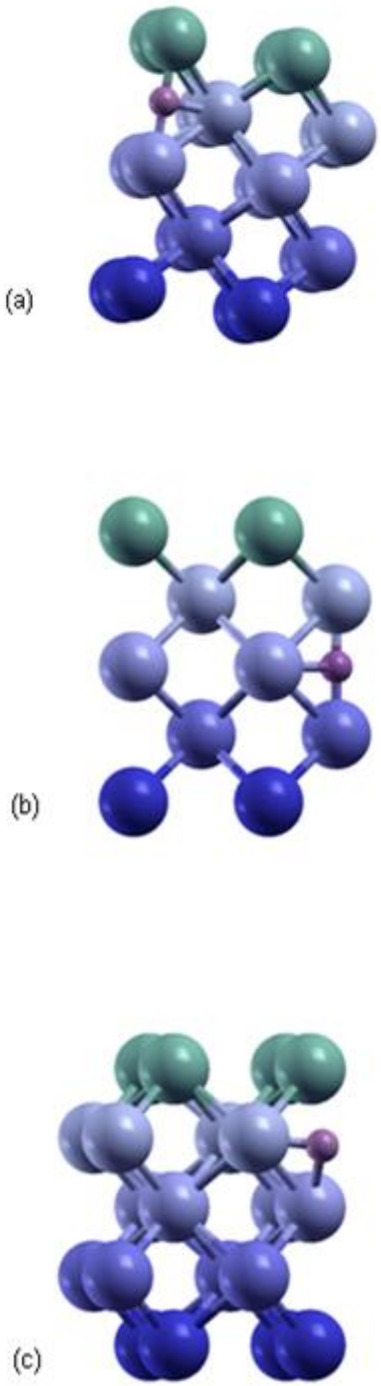

Figure 4.2 (a) Inner top; (b) inner center; and (c) inner bridge sites under the (100) surface of γ-U

calculate the total energy of the adatom, the isolated atom was simulated in a large box of side 30 a.u. and at the γ *k* point under the same set of computational conditions as stated above. For H the total energy was taken for the non-spin-polarized case and for O for the spin-polarized case because those values correspond to the ground state for those atoms. We had studied, in great detail, the effects of spin-orbit coupling on the slab-adatom geometry and the adsorption energies for C, N, and O adsorbed on the (111) surface of δ-Pu.[119–121] We noted that the inclusion of spin-orbit interaction in the scalar relativistic Hamiltonian does not alter the adsorption geometry but the binding was slightly stronger with the chemisorption energies increasing by 0.05–0.3 eV. Though we have not verified it explicitly, we expect the same result to hold for the γ-U surface. Hence in the current calculations, the geometry was optimized at the NSOC level and the final geometry was used for a single point energy calculation at the SOC level of theory so as to study spin-orbit coupling effects on the adsorption energies. [122]

4.2 Results and Discussions

4.2.1 Surface adsorption of H on the (100) γ-U surface

Taylor and Lillard [61] report in their *ab initio* study of the hydrogen-uranium system that the H_2 molecule does not dissociate as a reaction with the α-U (100) surface and is “not rate determining”. Instead, it thermally oscillates at the surface and may be pushed into a dissociated state based on the thermal energy of the molecule. Assuming the same would result for the γ-U-H_2 system, we will concentrate on the H atom adsorption of the hydride process for this section. As stated in the introduction, the adatom was allowed to approach the face of one surface and the energy was optimized with respect to distance from the surface at the NSO level of theory. A polynomial fit to the curve, which can be seen in Figure 4.3, Figure 4.4, and Figure 4.5, was used to find the minimum energy of the H-γ-U system at each site for the NM, FM, and AFM case. The optimized distance of the H atom from the surface remained roughly constant for each level of theory at about 2.07 Å for the top site, 0.57 Å for the center site, and 1.40 Å for the bridge site.

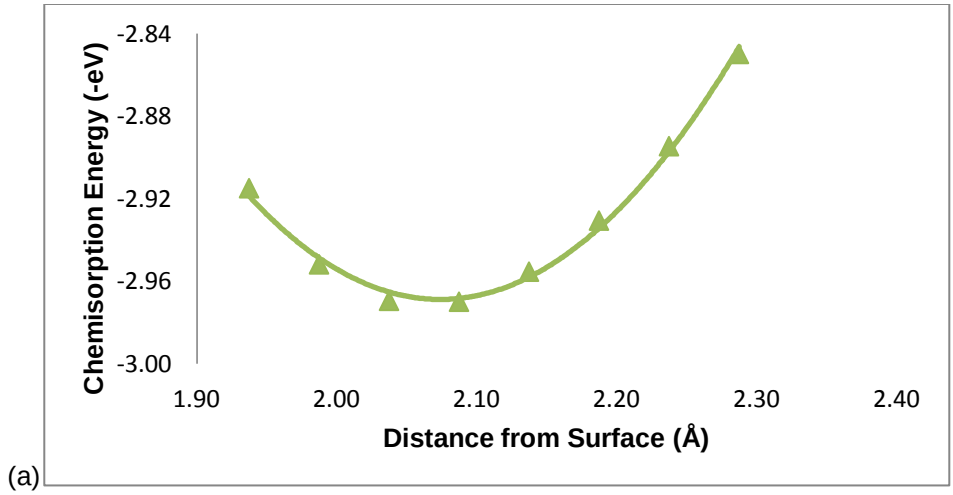

(a)

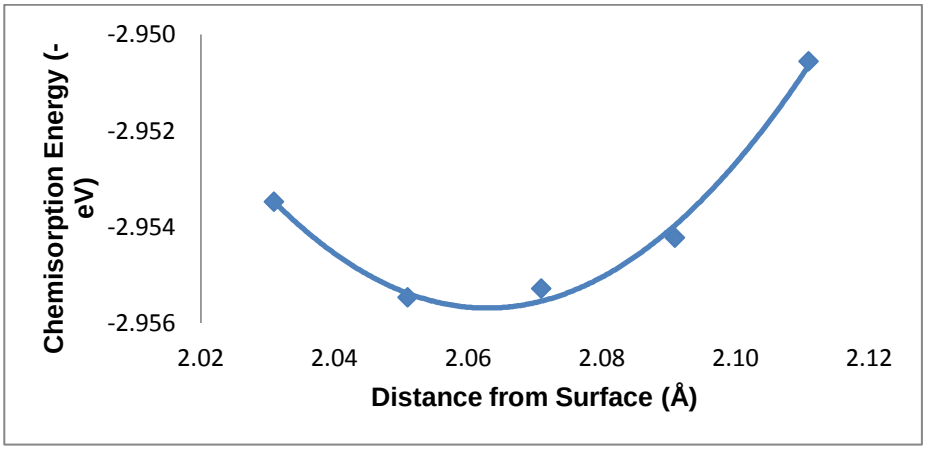

(b)

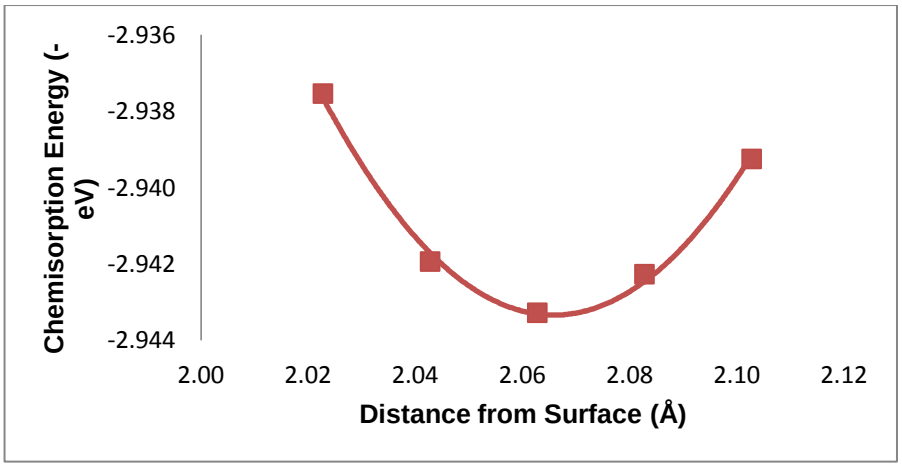

(c)

Figure 4.3 Optimized E_c of H atom at the top site at the NM (a), FM (b) and AFM (c) level

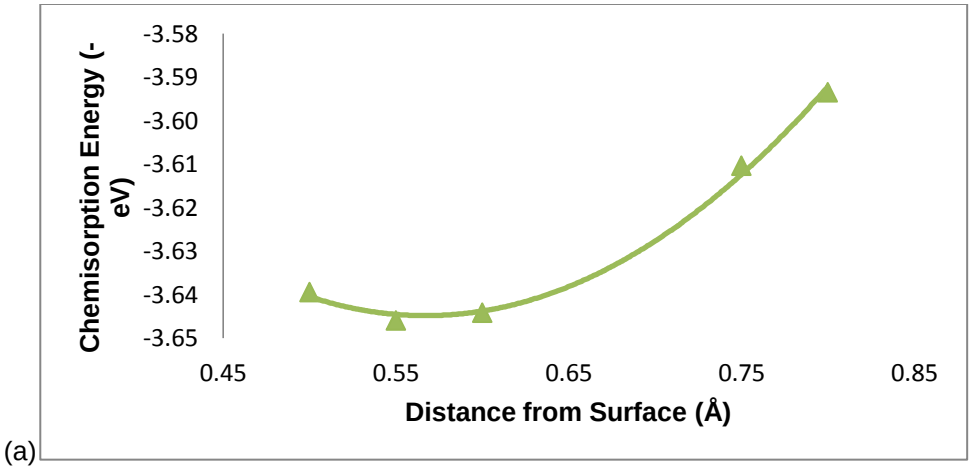

(a)

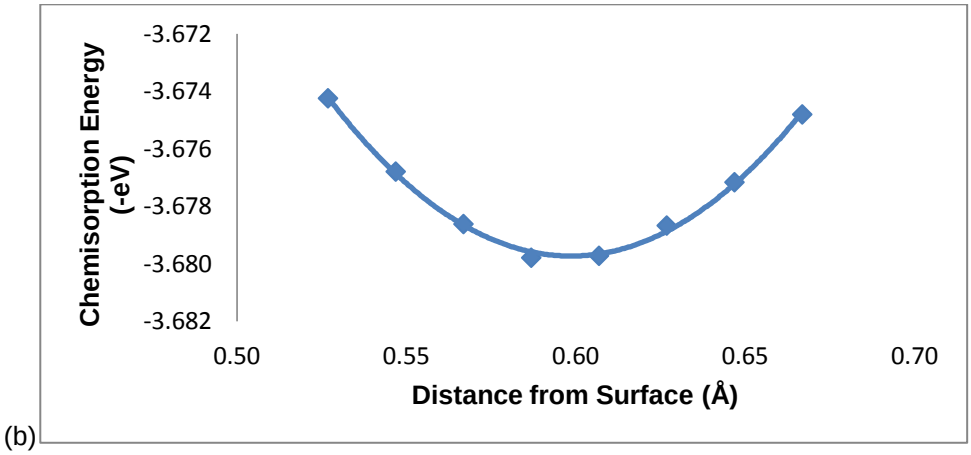

(b)

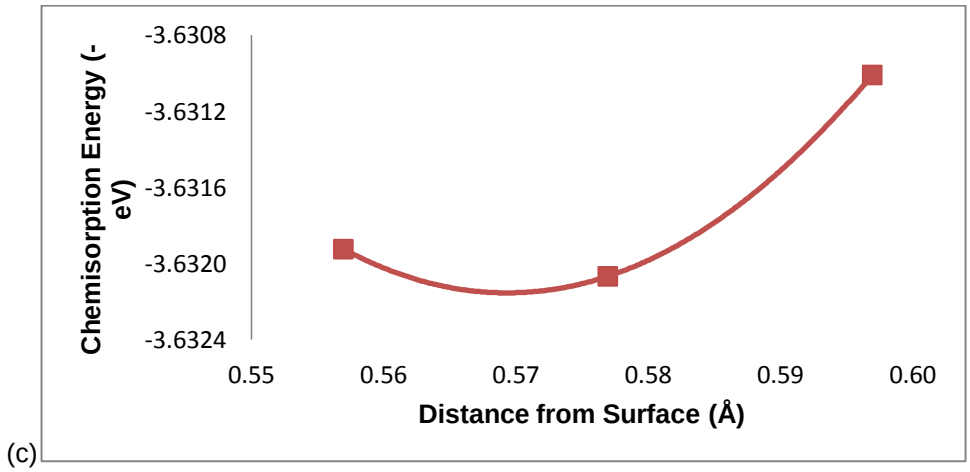

(c)

Figure 4.4 Optimized E_c of H atom at the center site at the NM (a), FM (b) and AFM (c) level

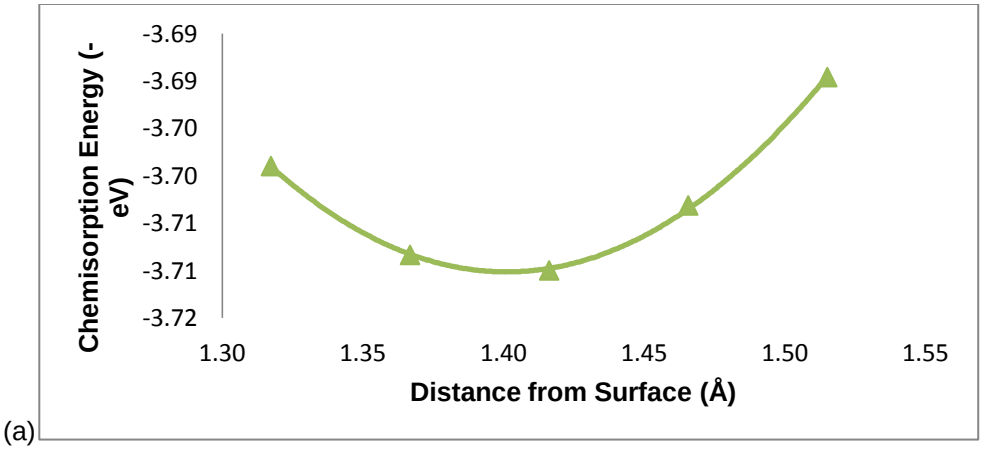

(a)

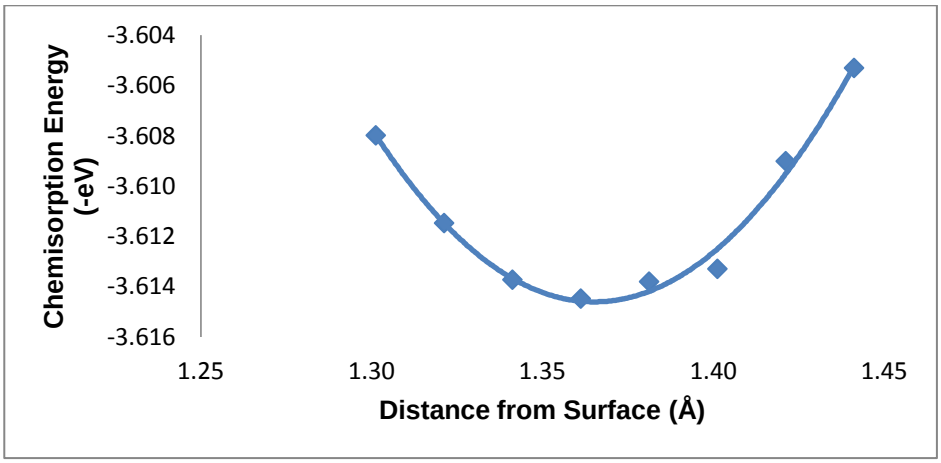

(b)

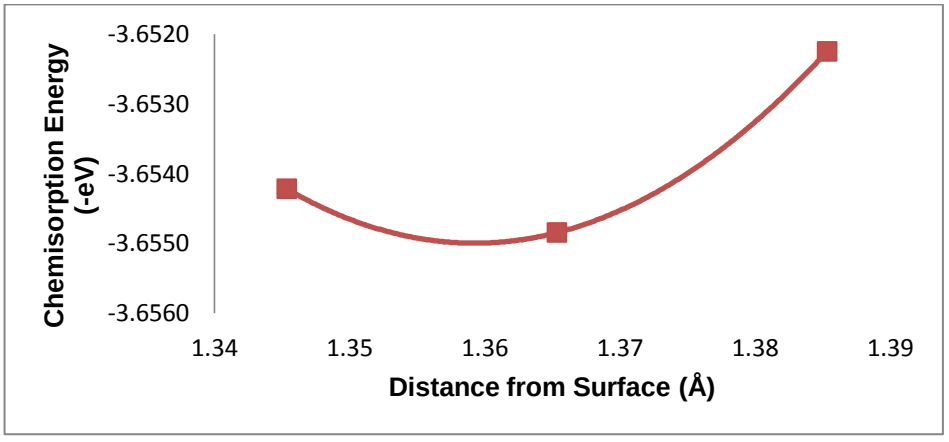

(c)

Figure 4.5 Optimized E_c of H atom at the bridge site at the NM (a), FM (b) and AFM (c) level

Table 4.2 lists the adsorption energies and associated geometrical information of the H adsorbed on the (100) surface of γ-U at the NM, FM and AFM electronic spin configurations, respectively. Also listed are the differences between the NSOC and SOC chemisorption energies at each adsorption site given by

$$\Delta E_c = E_c^{SOC} - E_c^{NSOC} \tag{4.3}$$

and the distance of the adatom to its nearest neighbor U atom, $d_{U\text{-}adatom}$. At all levels of theory, with and without SOC, an exothermic reaction between the H atom and the surface is indicated. At the NM level of theory, the NSOC and the SOC are in near agreement giving the bridge site as the most stable with chemisorption energy, E_c, of 3.80 eV and 3.71 eV, followed by the center site, at 3.62 eV and 3.65 eV, and then the top site with 3.40 eV and 2.97 eV, for SOC and NSOC respectively. The same is true for the AFM case, where the center site has the highest chemisorption energy of 3.65 eV at the NSOC level and with SOC the bridge site has the highest at 3.79 eV. For FM, the center site is found to be the most stable with 3.68 eV at the NSOC level but with the inclusion of SOC the bridge site becomes the most stable at 3.75 eV. All chemisorptions energies for H on the (100) surface of γ-U are greater than those reported in a similar adsorption study of the H atom on the (100) surface of α-U [61] by nearly 0.88 eV, when comparing the most stable sites of each study at the NM and NSOC level of theory, indicating that the γ-U-H system is more stable than the α-U-H system .

For all magnetic configurations the top site is the least stable with or without SOC and each exhibit the same trend concerning the ΔE_c, where the bridge (ΔE_c = 0.09 to 0.14 eV) and top (0.40 to 0.44 eV) sites show increased stability with the addition of SOC. In contrast, the center site showed a slight decrease in stability with a ΔE_c between -0.05 and -0.02 eV. In previous studies done by our group, a relation in the increase in distance of the adatom from the surface or from its nearest neighbor surface atom and an increased stability of the system was found [120], [121]. This is not the case for H adsorption on the (100) surface of γ-U. The distance

between the adatom and the nearest neighbor U surface atom remained fairly consistent at each level of theory, where the distance was 2.23 Å for the center site, 2.19 for the bridge site, and 2.07 for the top site. As expected the top site with the closest nearest neighbor U atom has the lowest chemisorption energy. The symmetry of the center site, being closest to the surface and yet having the furthest nearest neighbor, causes an unexpected higher chemisorption energy, although not enough to push it above the energy of the bridge site. The instability with the addition of SOC for the center site may be due to the closeness of the H atom to the surface and the exchange of electrons at that proximity. Comparing the most stable position, the bridge site, for all levels of theory, NM is clearly the most favored magnetic configuration at the NSOC level and is slightly higher in energy than AFM when SOC is added. For the center site, the second most stable site, FM has the highest chemisorption energy. These results compliment experimental findings for the ground state magnetic configuration of UH_3 which is paramagnetic above 180K and ferromagnetic at lower temperatures.

The work function is defined as the amount of energy required to move an electron from the Fermi surface into the vacuum and can be defined as follows:

$$\Phi = V(\infty) - E_{Fermi} \tag{4.4}$$

where, $V(\infty)$ is the Coulomb potential in the vacuum and E_{Fermi} is the Fermi energy of the surface. For the bare slab, Φ is 3.24 eV at the NM, FM, and AFM level of theory with the addition of SOC. It is interesting to see how the adsorption of an atom affects the work function of the slab.

The adsorbate-induced work function changes with respect to the clean metal surface is given by

$$\Delta\Phi = \Phi^{adatom/U} - \Phi^{U} \tag{4.5}$$

where Φ^{U} is the work function of the clean metal slab and $\Phi^{adatom/U}$ is for the metal surface with the adatom. Table 4.3 lists $\Delta\Phi$ for the adsorption of H atom on the surface with SOC added at

the NM, FM and AFM level of theory. These shifts can be understood in terms of the surface dipoles

Table 4.2 Distances and chemisorption energies of the H atom on γ-U(100) at the NM, FM and AFM levels of theory

NM			NSOC	SOC	
Site	R (Å)	$d_{U\text{-}adatom}$ (Å)	E_c (eV)	E_c (eV)	ΔE_c (eV)
Top	2.07	2.07	2.97	3.40	0.43
Center	0.57	2.23	3.65	3.62	-0.03
Bridge	1.40	2.19	3.71	3.80	0.09

FM			NSOC	SOC	
Site	R (Å)	$d_{U\text{-}adatom}$ (Å)	E_c (eV)	E_c (eV)	ΔE_c (eV)
Top	2.06	2.06	2.96	3.35	0.40
Center	0.60	2.26	3.68	3.63	-0.05
Bridge	1.37	2.16	3.61	3.75	0.14

AFM			NSOC	SOC	
Site	R (Å)	$d_{U\text{-}adatom}$ (Å)	E_c (eV)	E_c (eV)	ΔE_c (eV)
Top	2.07	2.07	2.94	3.38	0.44
Center	0.56	2.23	3.63	3.61	-0.02
Bridge	1.35	2.16	3.65	3.79	0.13

arising due to the partial transfer of electrons from the surface to the adsorbate. We can then evaluate the surface dipole moment caused by the addition of the adatom using the Helmholtz equation

$$12\pi\Theta\mu_{dipole} = A\Delta\Phi \tag{4.6}$$

where A is the area in $Å^2$ per (1X1) surface unit cell and Θ is the adsorbate coverage in monolayers , where μ_{dipole} is in Debye. [123] $\Delta\Phi$ for the top site, which has the closest nearest neighbor distance, is, as expected, higher than the other sites at 0.60 to 0.61 eV followed by the

Table 4.3 $\Delta\Phi$ and surface dipole moment μ_{dipole} for the adsorption of the H atom at the NM, FM, and AFM level of theory

Theory	Site	$\Delta\Phi$ (eV)	μ_{dipole} (D)
NM	Top	0.61	2.76
	Center	-0.01	-0.04
	Bridge	0.10	0.47
FM	Top	0.61	2.77
	Center	-0.01	-0.03
	Bridge	0.14	0.62
AFM	Top	0.60	2.72
	Center	-0.01	-0.06
	Bridge	0.12	0.54

bridge site, at 0.10 to 0.14 eV, and then the center site, -0.01 eV. Using the Helmholtz relation the adsorbate-induced dipole moment would be 2.76, 2.77, and 2.72 D for the top site, -0.04, -0.03, and -0.06 D for the center site and 0.47, 0.62, and 0.54 D for the bridge site at the NM, FM and AFM levels of theory, respectively. These values are also listed in Table 4.3.

The magnitude and alignment of the site projected spin magnetic moments, μ_S, and orbital magnetic moments, μ_L, inside the muffin tin sphere for each U atom on each atomic layer, as well as the net spin and orbital magnetic moment and the total magnetic moment, μ, per U

atom at the SOC theoretical level, are reported for the clean metal surface and each of the chemisorbed systems in Table 4.4 for the FM magnetic configuration and in Table 4.5 for the AFM. In these tables, layer 1 is the surface layer; layer 2 is the subsurface layer; layer 3 is the center layer; layer 4 is the subcenter layer; and layer 5 is the bottom layer. The moments of U atoms bonded to the H atoms are printed in bold. Noting that atom 1 in layer 1 is in the same position as atom 1 in layer 3 and 5 and atom 1 in layer 2 is in the same position as atom 1 in layer 4 and so on for the other atoms, it is easier to see the trend of the magnetic moment of the system. The atomic positions of layer 1 and layer 2 atoms are displayed in Figure 4.6.

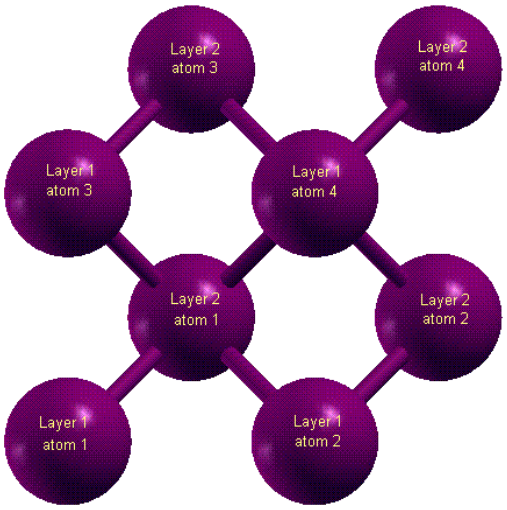

Figure 4.6 Atomic positions for the 1st and 2nd layers

Table 4.4 Spin and orbital magnetic moment for surface adsorption of the H atom at FM level of theory

FM		Layer												
H		1		2		3		4		5		net		total μ
Site	Atom	μ_S	μ_L	μ_S	μ_L	μ_S	μ_L	μ_S	μ_L	μ_S	μ_L	μ_S	μ_L	
bare	1	0.945	-0.642	0.079	-0.016	-0.075	0.013	0.080	-0.016	0.945	-0.642			
	2	0.946	-0.642	0.079	-0.016	-0.075	0.013	0.080	-0.016	0.944	-0.642			
	3	0.945	-0.641	0.079	-0.016	-0.075	0.013	0.080	-0.016	0.944	-0.642			
	4	0.946	-0.641	0.079	-0.016	-0.075	0.013	0.080	-0.016	0.944	-0.642	7.894	-5.211	2.683
Top	1	0.977	-0.653	0.072	-0.012	-0.085	0.019	0.085	-0.019	0.944	-0.638			
	2	0.926	-0.656	0.072	-0.012	-0.065	0.009	0.085	-0.019	0.944	-0.644			
	3	0.926	-0.656	0.072	-0.012	-0.065	0.009	0.085	-0.019	0.944	-0.644			
	4	**0.586**	**-0.400**	0.072	-0.012	-0.021	-0.005	0.085	-0.019	0.944	-0.645	7.580	-5.028	2.552
Center	1	0.971	-0.655	**0.050**	**-0.005**	-0.079	0.016	0.074	-0.015	0.960	-0.649			
	2	0.971	-0.655	0.095	-0.023	-0.079	0.016	0.085	-0.018	0.960	-0.649			
	3	0.971	-0.655	0.095	-0.023	-0.079	0.017	0.085	-0.018	0.960	-0.649			
	4	0.971	-0.655	0.122	-0.037	-0.079	0.017	0.081	-0.017	0.960	-0.649	8.094	-5.306	2.788
Bridge	1	0.933	-0.638	0.065	-0.010	-0.079	0.018	0.096	-0.021	0.955	-0.648			
	2	**0.682**	**-0.472**	0.065	-0.010	-0.050	0.003	0.096	-0.020	0.942	-0.640			
	3	0.933	-0.638	0.075	-0.016	-0.079	0.018	0.090	-0.020	0.955	-0.648			
	4	**0.682**	**-0.472**	0.075	-0.016	-0.050	0.003	0.090	-0.020	0.942	-0.640	7.420	-4.886	2.533

Table 4.5 Spin and orbital magnetic moment for surface adsorption of the H atom at AFM level of theory

AFM		Layer												
H		1		2		3		4		5		total		total μ
Site	Atom	μ_S	μ_L	μ_S	μ_L	μ_S	μ_L	μ_S	μ_L	μ_S	μ_L	μ_S	μ_L	
bare	1	0.876	-0.634	0.000	0.000	-0.144	0.056	0.000	0.000	0.875	-0.634			
	2	-0.871	0.631	0.000	0.000	0.143	-0.055	0.000	0.000	-0.870	0.630			
	3	0.876	-0.634	0.000	0.000	-0.144	0.056	0.000	0.000	0.875	-0.634			
	4	-0.871	0.631	0.000	0.000	0.143	-0.055	0.000	0.000	-0.870	0.630	0.020	-0.014	0.005
Top	1	0.852	-0.618	0.026	-0.007	-0.135	0.527	-0.013	0.004	0.855	-0.624			
	2	-0.815	0.626	0.025	-0.007	0.140	-0.055	-0.013	0.005	-0.891	0.642			
	3	1.026	-0.722	0.026	-0.007	-0.140	0.050	-0.013	0.004	0.884	-0.643			
	4	**-0.243**	**0.181**	0.025	-0.007	0.102	-0.040	-0.013	0.005	-0.865	0.628	0.819	-0.059	0.760
Center	1	0.860	-0.621	**0.001**	**0.000**	-0.139	0.053	0.001	0.000	0.881	-0.638			
	2	-0.850	0.615	-0.001	0.000	0.138	-0.053	0.000	0.000	-0.873	0.633			
	3	0.859	-0.621	0.001	0.000	-0.139	0.053	0.001	0.000	0.881	-0.638			
	4	-0.856	0.618	-0.001	0.000	0.138	-0.053	0.000	0.000	-0.874	0.633	0.028	-0.018	0.009
Bridge	1	0.912	-0.680	0.031	-0.010	-0.129	0.048	-0.015	0.005	0.880	-0.608			
	2	**-0.328**	**0.266**	0.029	-0.010	0.115	-0.045	-0.014	0.005	-0.877	0.599			
	3	0.913	-0.680	0.057	-0.020	-0.129	0.048	-0.015	0.005	0.880	-0.608			
	4	**-0.327**	**0.266**	0.051	-0.018	0.115	-0.045	-0.015	0.005	-0.877	0.599	1.257	-0.880	0.377

The bare slab for the FM case has total magnetic moment of 2.383 μ_B. Also, the magnitudes of the spin moments and total moment of the surface and bottom layer atoms are larger than for the subsurface, center and sub-center. For the one-fold top site, we note a reduction of 0.36 μ_B in the spin moment and an increase of 0.24 μ_B in the orbital moment of the U atom bonded to the adatom, also, the moments for the remaining atoms are also altered compared to the clean metal. The entire slab sees a reduction in total moment of 0.13 μ_B for this adsorption site. A similar scenario can be observed for the one-fold center site but to a lesser degree, where the reduction of the spin moment of the U atom bonded to the adatom is about 0.03 μ_B and the increase of the orbital moment 0.01 μ_B. The center site actually increases in total magnetic moment of the slab by 0.01 μ_B. For the twofold bridge site, we see a reduction of about 0.15 μ_B in the total moment of the slab, where the two surface layer U atoms interacting with the adatom experience a decrease of spin moment of 0.263 μ_B and an increase of orbital moment of 0.17 μ_B, since the adatom sits exactly between the two U atoms. For the AFM case, the bare slab has a nearly zero total magnetic moment and each layer exhibits a nearly zero total magnetic moment. When the H atom approaches the surface a net magnetic moment is produced for the top and bridge sites but little effect is caused at the center site. For the top site, the spin magnetic moment of the bonded U atom is increased to -0.24 μ_B and the orbital moment is decreased to 0.181 μ_B. A ripple effect is seen through the remaining layers causing the net magnetic moment for the slab to increase to 0.76 μ_B. For the bridge site, both U atoms that bond with the H atom showed an increase in spin magnetic moment of 0.54 μ_B and an increase of the orbital moment of 0.37 μ_B. It is clear from this study that the adsorptions of the H atom on the (100) surface of γ-U changes the over-all magnetic moment on the slab and for the case of an AFM film induces a magnetic moment in most cases. An increase in the spin magnetic moment is not expected since in a few studies done by our group on AFM Pu a reduction of the spin magnetic moments as a result of chemisorption had been observed for C, N, and O adsorption on the (111) and (100) surfaces of δ-Pu.[119], [120]

Due to the nature of the L/APW+lo basis, the electronic charges inside the muffin tin spheres can be decomposed into contributions from the different angular momentum channels. We refer to these charges as partial charges. By comparing the partial charges QB of the U layers and adatoms before adsorption to the corresponding partial charges Q_A after adsorption, we get an idea of the nature of the interaction between the adsorbate and substrate. [122] These values, listed in Table 4.6, Table 4.7, and

Table 4.8, are stated for the NM, FM and AFM magnetic configuration at the SOC level of theory and, for the surface, are taken from atoms closest to the adatom. In addition, we calculated and listed the difference in partial charge, ΔQ, before and after adsorption to facilitate the discussion on charge transfer between the γ-U surface and the adatom. The results for the partial charges of the bare γ-U slab are as to be expected. The *d* orbitals have 10 e^- plus partial charges from the hybridizing 5*f* orbitals and approximately 2 5*f* electrons are in the f channel which is expected due to the iterant behavior of the 5f electrons I addition to hybridizing with the 6d orbitals. Also, for all levels of theory, the surface atoms of the slab have more 5*f* partial charges indicating slightly more localization of the 5f electrons at the surface, a phenomenon that is more prevalent with the application of spin-polarization. For the *d* channel, there are less electrons for the surface atom versus the subsurface atom for all levels of theory indicating less 5*f* hybridization at the surface. Because the increase of electrons for the *f* channel does not equal the loss for the *d* channel, there must be more itinerant behavior of electrons at the surface, as well. The single 1*s* electron of the lone H atom shows extremely itinerant behavior; only 0.1 e^- is present inside the muffin-tin sphere.

After adsorption, the H atom gains between 0.04 and 0.05 e^- inside the muffin-tin sphere for the top, center sites and bridge site at all levels of theory. For the NM case, the change in partial charges of the slab is negligible compared to the bare slab at all sites. In this case, we assume the H atom must be gaining charge from the itinerant electrons. For the FM case, the H atom causes the charge for the *f* electrons of the top layer atom to lose partial charge and the bottom layer gains partial charge for the top and bridge sites. For the center site, both the top and

bottom layer atoms gain about 0.01 e^-. For the AFM case, at the top site the atom of the surface layer loses about 0.06 e^- inside the muffin-tin sphere and for the bridge site the subsurface atom gains 0.06 e^-. The change in partial charge on the slab is negligible for the center site at the AFM level of theory.

The partial charges discussed above were analyzed solely inside the muffin tin, and this does not give us a complete picture of the nature of the bonds between the adatoms and the surface U atoms since it does not address the charge distribution in the interstitial region. To see any bonds that may have formed between the adatoms and the U atoms on the surface; we computed the difference charge-density distribution for the chemisorbed system, which gives us information about the nature of the chemical bonds formed as result of charge redistribution. We define the difference charge density $\Delta n(r)$ as follows:

$$\Delta n(r) = n(\mathrm{X} + \mathrm{U}) - n(\mathrm{U}) - n(\mathrm{X}), \tag{4.7}$$

where $n(\mathrm{X} + \mathrm{U})$ is the total electron charge density of the adatom adsorbed on the surface, $n(\mathrm{U})$ is the total charge density of the bare U metal slab, and $n(\mathrm{X})$ is the total charge density of the adatom. In computing $n(\mathrm{X})$ and $n(\mathrm{U})$, the U and adatoms are kept fixed at exactly the same positions as they were in the chemisorbed systems. The FORTRAN code used for these calculations is described in detail in Appendix II of this text. All densities reported here were computed in the plane passing through the adatom and the two surface U atoms using the XCrySDen utility [124]. For the onefold-coordinated sites, the plane passes through the adatom, the U atom interacting with the adatom, and a neighboring U atom. For the twofold-coordinated sites, the plane passes through the adatom and the two U atoms interacting with the adatom. Figure 4.7 through Figure 4.9 show the difference in charge density for H adsorption at the top, center and bridge sites, respectively, for the NM level of theory. From this we can see charge accumulation of the H atom, exchange of charge between the U atom orbitals, and slight loss of charge from the interstitial regions around the U atoms. We note here that the exchange of charge shown in the Δn plots are not indicated for our partial charge inside the muffin-tin spheres. Therefore, we must assume that the charges exchanged are from the interstitial region.

Table 4.6 Partial charges inside muffin-tin spheres for H at the top, center and bridge sites with SOC for the NM magnetic configuration

NM		Q_B			Q_A			$\Delta Q=Q_A-Q_B$		
Site	Atom/Layer	H *s*	U *d*	U *f*	H *s*	U *d*	U *f*	H *s*	U *d*	U *f*
Top	Hydrogen	0.102			0.146			0.043		
	U surface layer		10.422	1.985		10.422	1.984		0.001	0.000
	U subsurface layer		10.545	1.948		10.544	1.947		0.000	-0.001
	U middle layer		10.534	1.942		10.536	1.938		0.001	-0.004
	U submiddle layer		10.545	1.948		10.545	1.947		0.000	-0.001
	U bottom layer		10.422	1.984		10.422	1.984		0.000	0.000
Center	Hydrogen	0.102			0.142			0.039		
	U surface layer		10.422	1.985		10.419	1.983		-0.002	-0.002
	U subsurface layer		10.545	1.948		10.542	1.944		-0.003	-0.004
	U middle layer		10.534	1.942		10.534	1.942		-0.001	0.001
	U submiddle layer		10.545	1.948		10.545	1.948		0.001	0.000
	U bottom layer		10.422	1.984		10.422	1.988		0.000	0.003
Bridge	Hydrogen	0.102			0.154			0.052		
	U surface layer		10.422	1.985		10.423	1.983		0.001	-0.002
	U subsurface layer		10.545	1.948		10.544	1.947		-0.001	-0.001
	U middle layer		10.534	1.942		10.535	1.941		0.001	-0.001
	U submiddle layer		10.545	1.948		10.544	1.948		0.000	0.000
	U bottom layer		10.422	1.984		10.422	1.983		0.000	-0.002

Table 4.7 Partial charges inside muffin-tin spheres for H at the top, center and bridge sites with SOC for the FM magnetic configuration

FM		Q_B			Q_A			$\Delta Q=Q_A-Q_B$		
Site	Atom/Layer	H *s*	U *d*	U *f*	H *s*	U *d*	U *f*	H *s*	U *d*	U *f*
Top	Hydrogen	0.102			0.146			0.044		
	U surface layer		10.421	2.009		10.424	1.881		0.003	-0.128
	U subsurface layer		10.546	1.958		10.543	1.923		-0.003	-0.035
	U middle layer		10.536	1.952		10.542	1.949		0.006	-0.003
	U submiddle layer		10.546	1.959		10.545	1.996		-0.001	0.037
	U bottom layer		10.421	2.011		10.426	2.108		0.005	0.097
Center	Hydrogen	0.102			0.141			0.039		
	U surface layer		10.421	2.009		10.418	2.016		-0.003	0.007
	U subsurface layer		10.546	1.958		10.543	1.958		-0.003	0.000
	U middle layer		10.536	1.952		10.535	1.954		-0.001	0.002
	U submiddle layer		10.546	1.959		10.546	1.959		0.000	0.000
	U bottom layer		10.421	2.011		10.421	2.022		0.000	0.011
Bridge	Hydrogen	0.102			0.151			0.049		
	U surface layer		10.421	2.009		10.417	1.851		-0.004	-0.158
	U subsurface layer		10.546	1.958		10.542	1.904		-0.004	-0.054
	U middle layer		10.536	1.952		10.536	1.954		0.000	0.002
	U submiddle layer		10.546	1.959		10.549	2.016		0.003	0.057
	U bottom layer		10.421	2.011		10.428	2.154		0.007	0.143

Table 4.8 Partial charges inside muffin-tin spheres for H at the top, center and bridge sites with SOC for the AFM magnetic configuration

AFM		Q_B			Q_A			$\Delta Q=Q_A-Q_B$		
Site	Atom/Layer	H *s*	U *d*	U *f*	H *s*	U *d*	U *f*	H *s*	U *d*	U *f*
Top	Hydrogen	0.102			0.146			0.044		
	U surface layer		10.419	2.012		10.427	1.955		0.007	-0.057
	U subsurface layer		10.545	1.955		10.544	1.956		-0.001	0.001
	U middle layer		10.534	1.949		10.536	1.950		0.002	0.002
	U submiddle layer		10.545	1.955		10.544	1.956		-0.001	0.001
	U bottom layer		10.419	2.009		10.419	2.002		0.000	-0.006
Center	Hydrogen	0.102			0.142			0.040		
	U surface layer		10.419	2.012		10.417	2.011		-0.003	-0.001
	U subsurface layer		10.545	1.955		10.542	1.955		-0.003	0.001
	U middle layer		10.534	1.949		10.533	1.953		-0.001	0.004
	U submiddle layer		10.545	1.955		10.544	1.957		0.000	0.003
	U bottom layer		10.419	2.009		10.419	2.011		0.000	0.002
Bridge	Hydrogen	0.102			0.146			0.044		
	U surface layer		10.419	2.012		10.410	2.013		-0.009	0.001
	U subsurface layer		10.545	1.955		10.544	1.955		-0.135	0.058
	U middle layer		10.534	1.949		10.534	1.949		0.010	0.006
	U submiddle layer		10.545	1.955		10.545	1.954		-0.011	-0.005
	U bottom layer		10.419	2.009		10.420	2.008		0.125	-0.055

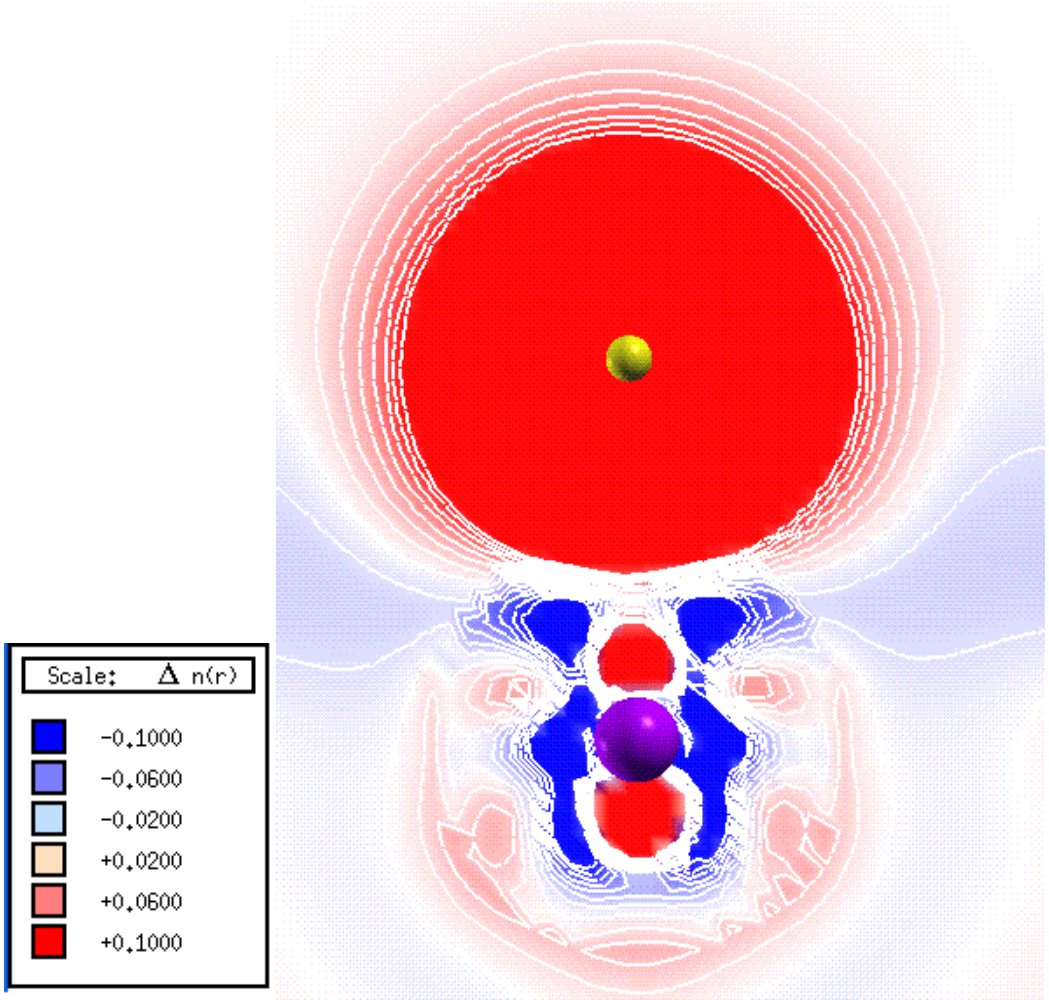

Figure 4.7 Change in partial charge for the H atom at the NM top site

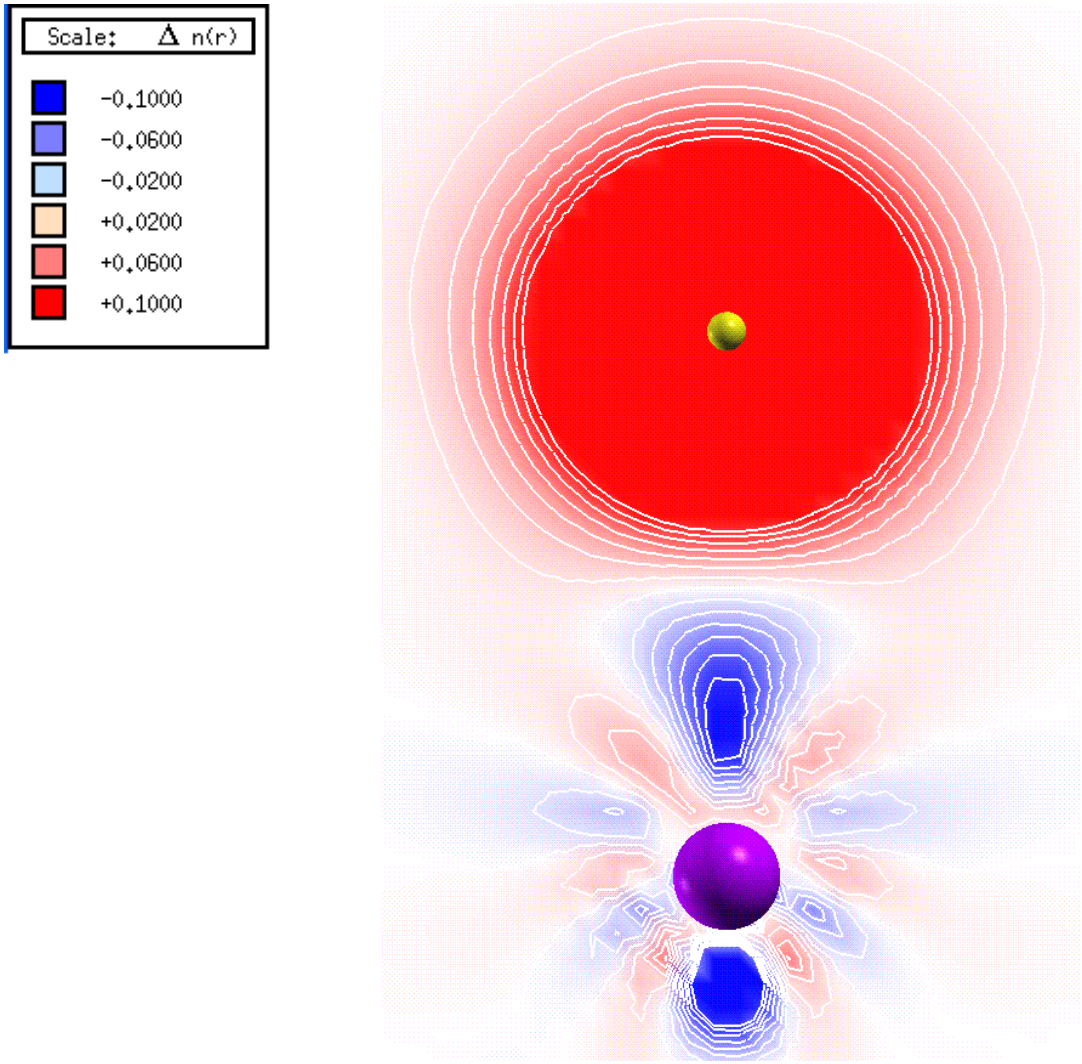

Figure 4.8 Change in partial charge for the H atom at the NM center site

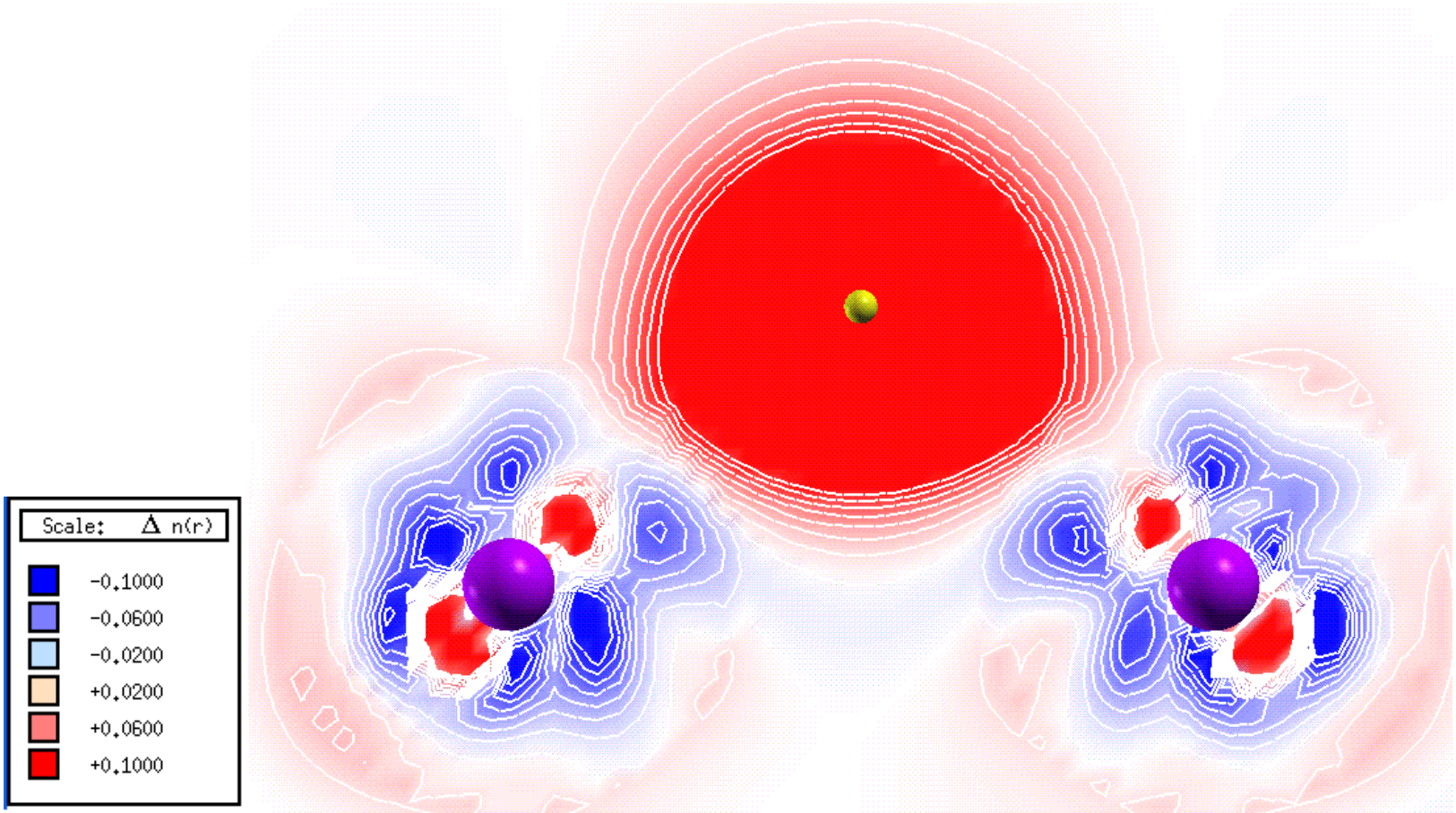

Figure 4.9 Change in partial charge for the H atom at the NM bridge site

Figure 4.10, Figure 4.11, and Figure 4.12 show the Δn plots for the adsorption of the H atom at the top, center and bridge sites, respectively, for the FM magnetic configuration. As with the NM case, we see an exchange of charge that is not indicated by the partial charge inside the muffin-tin sphere. For all sites, the H atom and the U atom of the surface look to be gaining electrons from the interstitial region, where our partial charges calculation indicates that for the top and bridge site the surface atoms lose electrons from the 5f channel. The least amount of charge is gained at the center site. For the top and center site, most charge is gained near the H atom indicating an ionic bond between the H and U atoms. For the AFM magnetic configuration depicted in Figure 4.13, Figure 4.14, and Figure 4.15 for the top, center and bridge sites, respectively, the exchange of charge is less than that for the FM case for all sites. The Δn plot for the top site at the AFM case is nearly identical to that of the FM case but with a lesser amount of electron exchange. For the center site, the surface U atom does not gain or lose electrons. The interstitial area of the surface loses electrons, while the H atom and the vacuum region around it gain electrons. For the bridge site, the U surface atoms and the H atom gain electrons from the interstitial region.

We have also examined the local density of electron states (LDOS). This is obtained by decomposing the total density of the single-particle Kohn-Sham eigenstates into contributions from each angular momentum channel *l* of the constituent atoms inside the muffin tin sphere. We have reported the LDOS for only the SOC computation. In Figure 4.16, the Gaussian-broadened (with a width of 0.003 eV) *f* and *d* LDOS curves for the surface and subsurface layers of the clean γ-U (100) metal slab are shown at the NM level of theory. The surface atom shows a slight localization of the 5f electrons at the Fermi level and hybridization of the 5*f* orbitals with the 6*d*. The subsurface atom demonstrates more delocalization of the 5*f* orbitals with more itinerant behavior of the electrons, in addition to the 5*f*-6*d* hybridization. As there are several nonequivalent atoms on the surface and subsurface, only the LDOS of the adatoms and the U atoms interacting with the adatoms are considered. In Figure 4.17, we show the LDOS plots for the H adatom and the surface U atom to which it is bonded in the top site. We note that the 5*f*

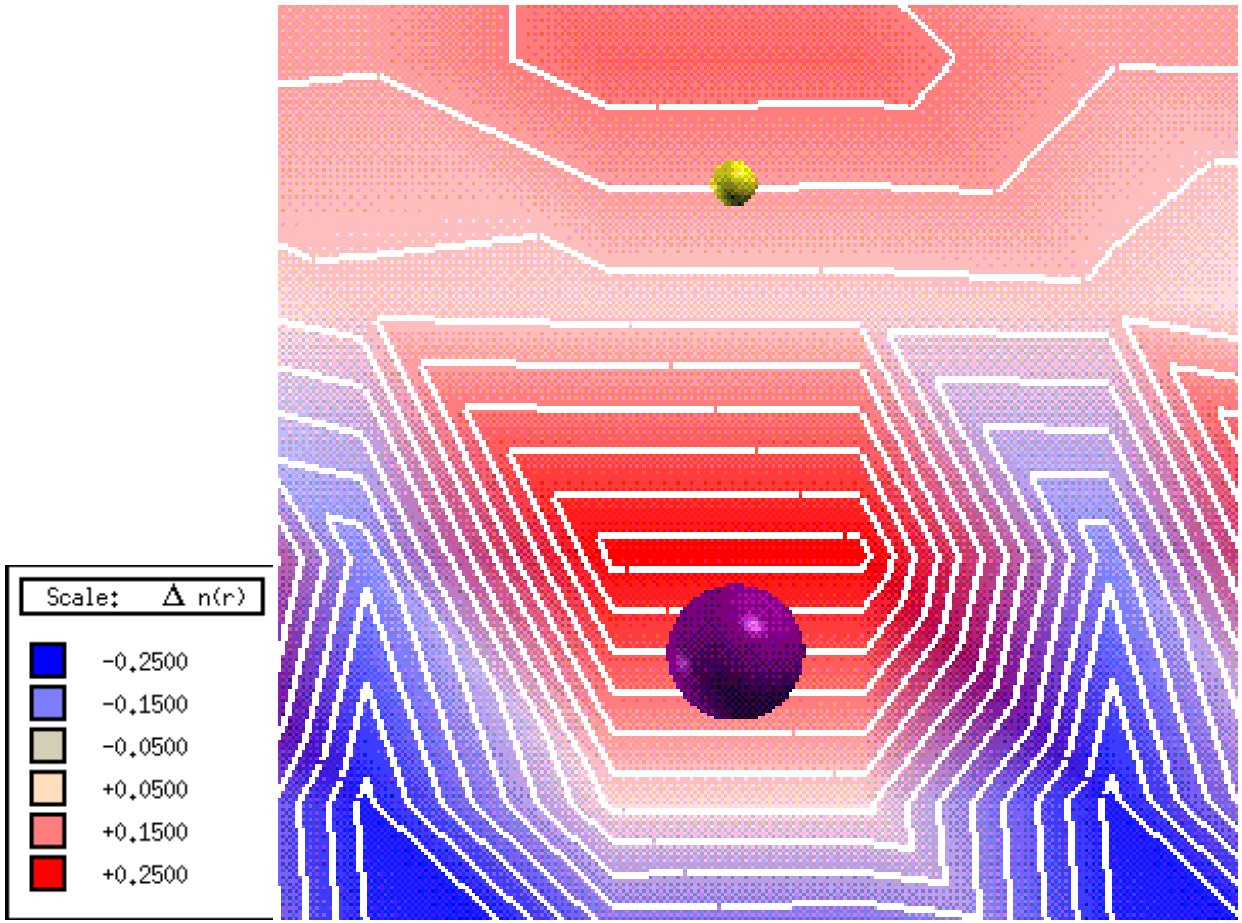

Figure 4.10 Change in partial charge for the H atom at the FM top site

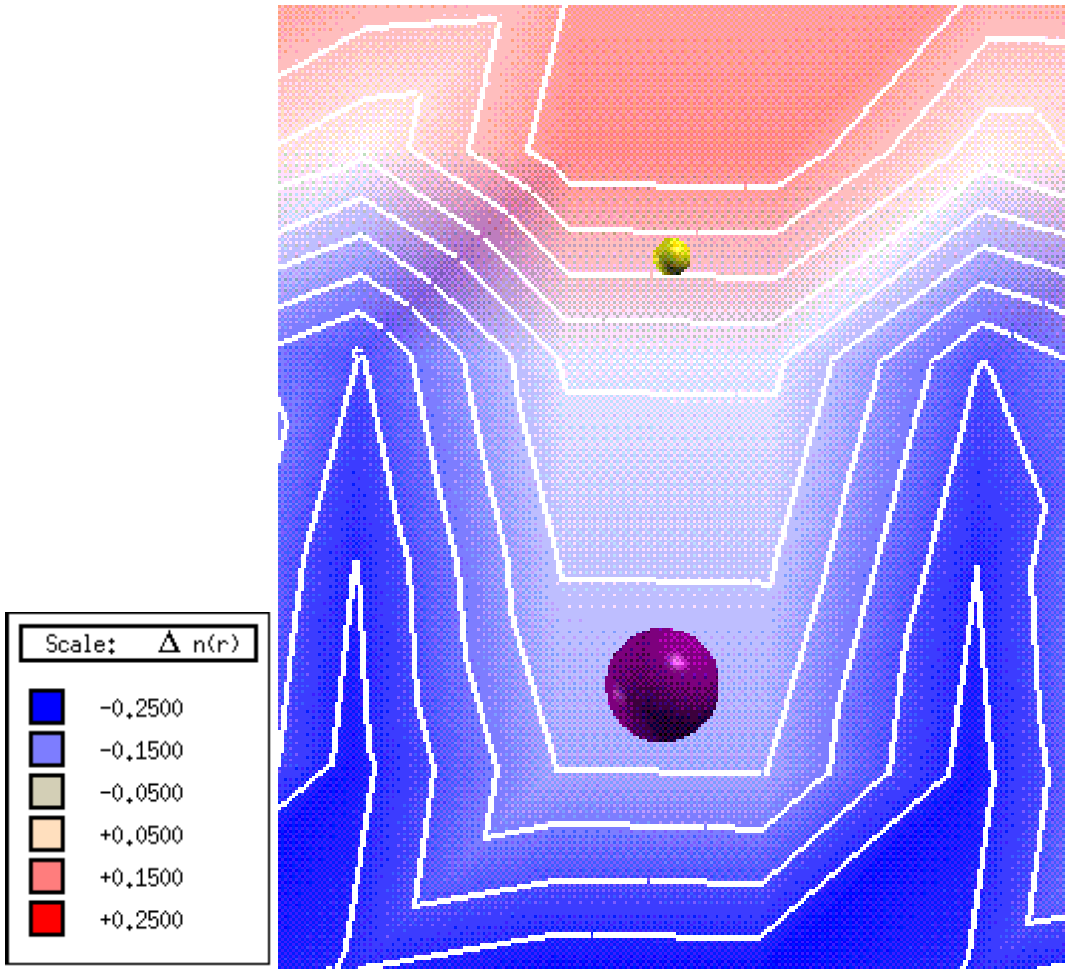

Figure 4.11 Change in partial charge for the H atom at the FM center site

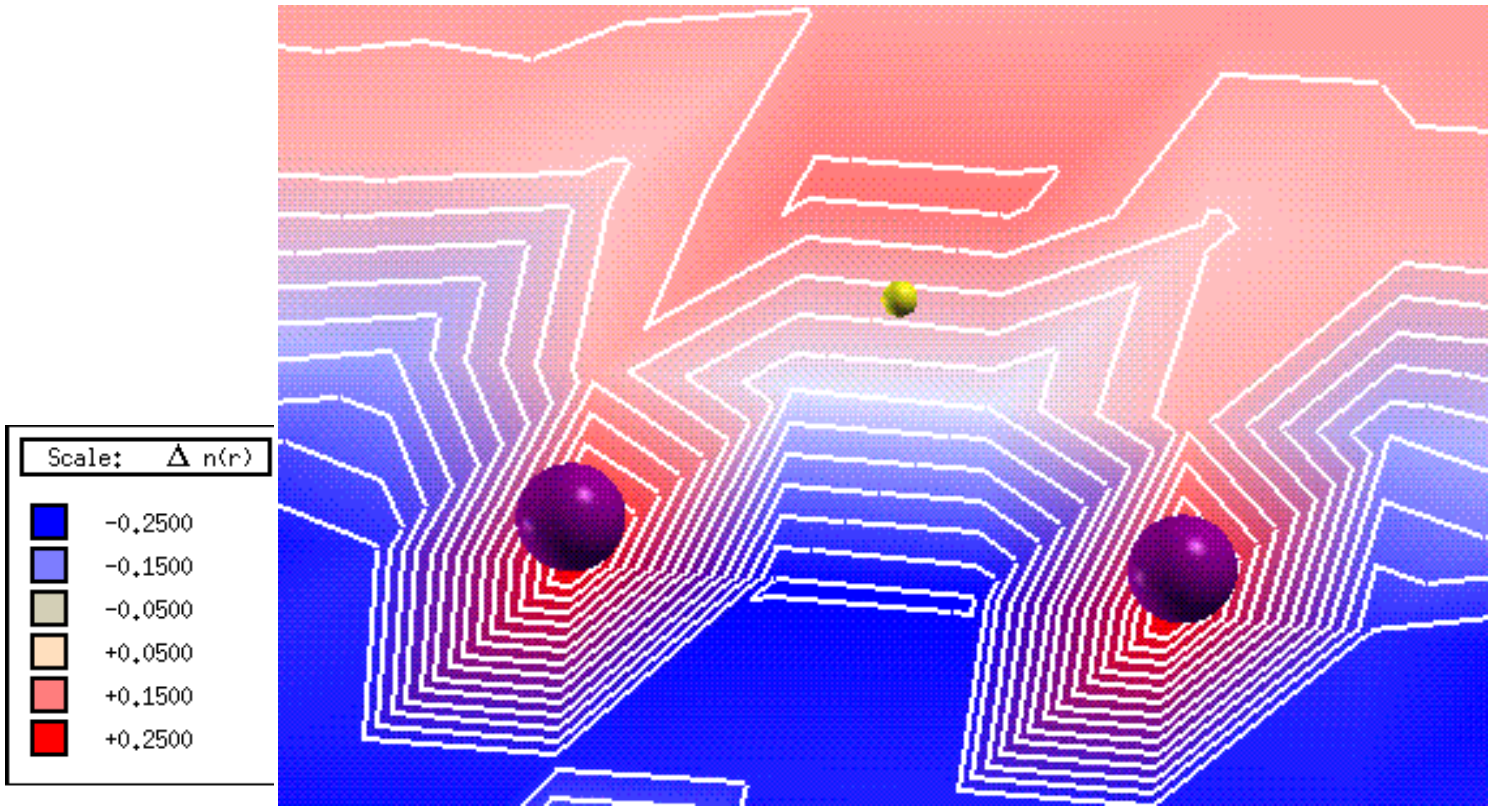

Figure 4.12 Change in partial charge for the H atom at the FM bridge site

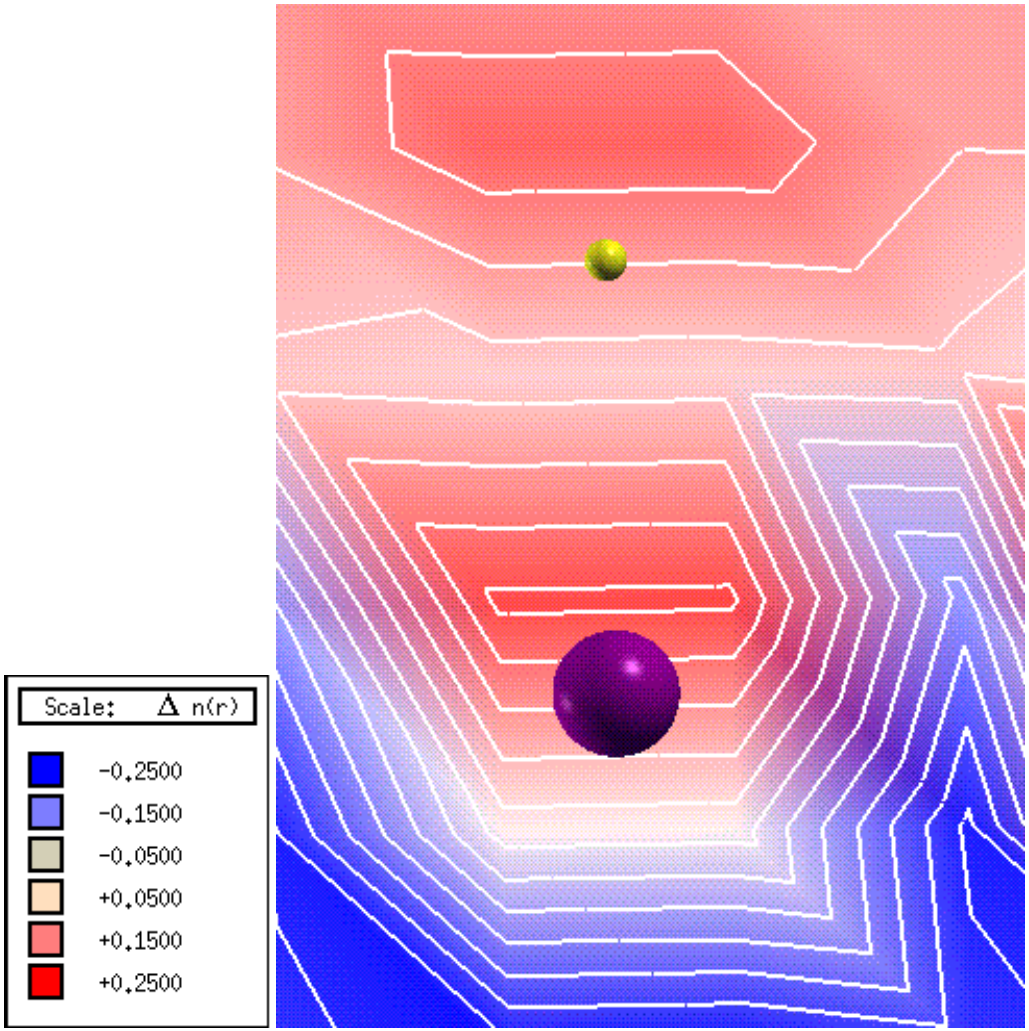

Figure 4.13 Change in partial charge for the H atom at the AFM top site

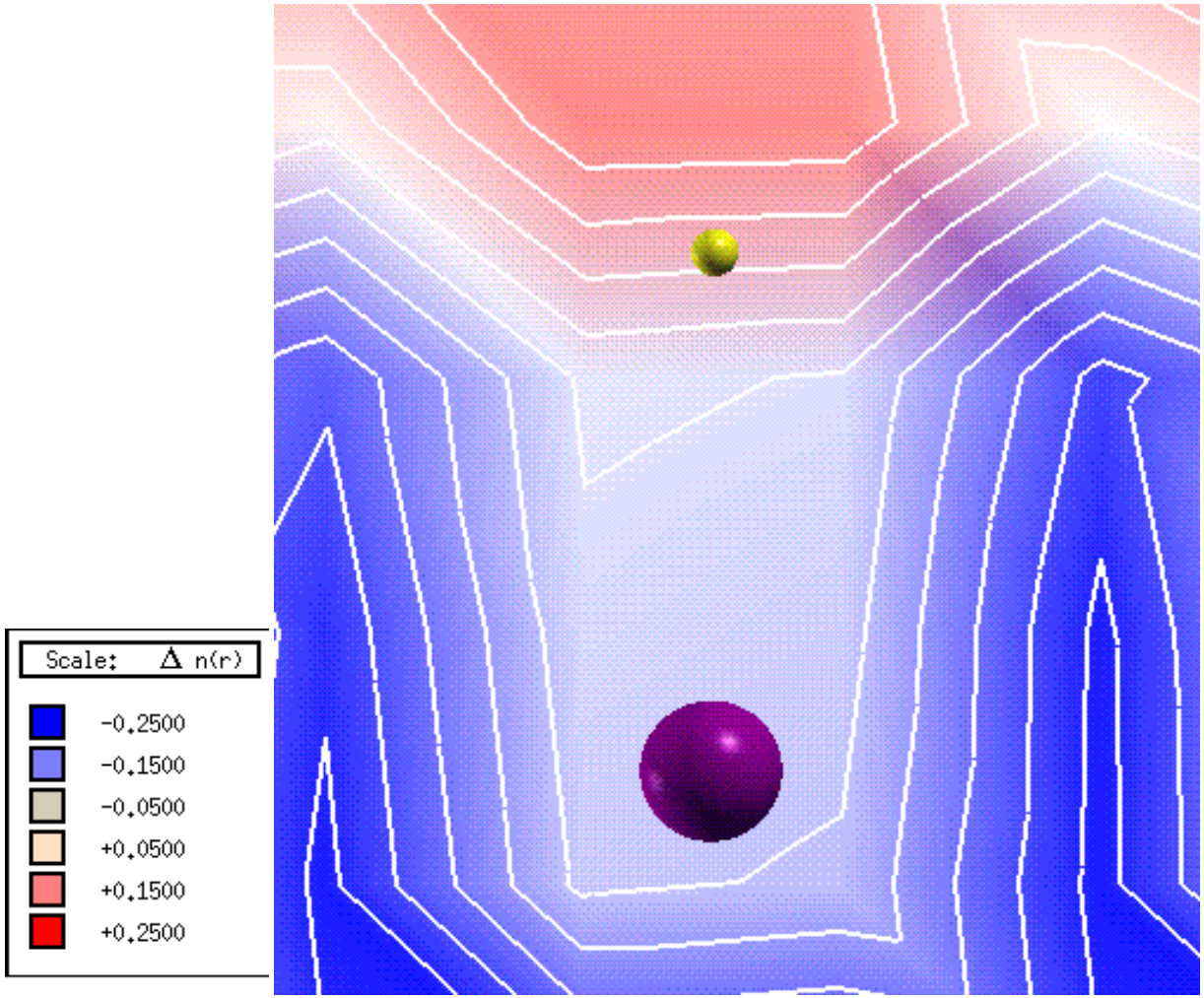

Figure 4.14 Change in partial charge for the H atom at the AFM center site

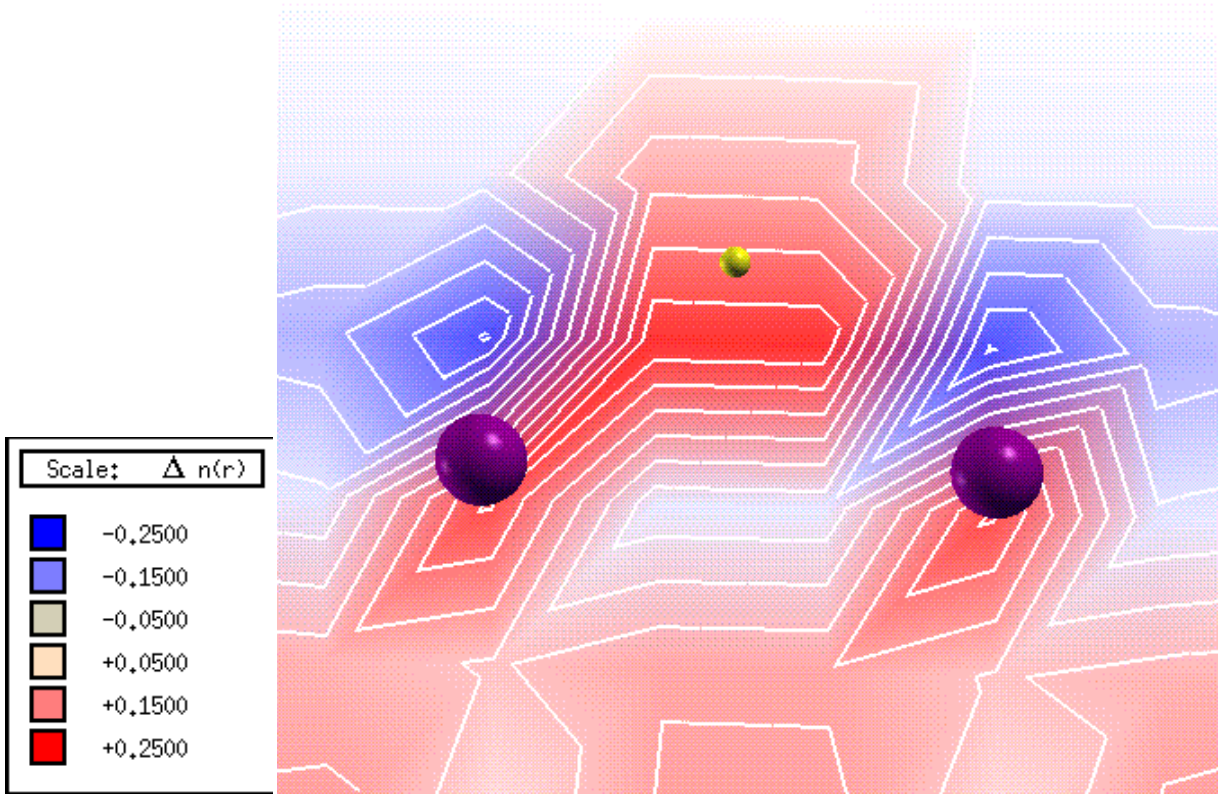

Figure 4.15 Change in partial charge for the H atom at the AFM bridge site

DOS of the U atom on which the adatom sits is modified, with an increase of the DOS at the Fermi level, in comparison to the surface layer LDOS for the clean U slab, which implies that the 5*f* electrons become further localized. We also observe complete 6*d*, 5*f* and H 1*s* overlaps below the Fermi level indicating 6*d* participation in bonding. At the center site, shown in Figure 4.18, the H atom interacts with the subsurface layer and has little effect on the distribution of the 5*f* electrons of the subsurface atom with which it reacts. As with the surface atom of the top site there is a U 6*d*-U 5*f* –H 1*s* overlap. The LDOS distribution for the bridge site, Figure 4.19, is similar to that of the top site except that the orbital overlaps occur further below the Fermi surface and the H 1s exhibits a higher peak. In addition, the 5f electron distribution is unchanged when compared with the bare slab. The FM level of theory LDOS plot is drawn in Figure 4.20 for the surface and subsurface U atoms of clean γ-U (100) metal slab, using the same parameters as for the NM case. This plot looks the same as that of the NM case except the intensity of the distributions are reduced by half because for spin polarized calculations only the spin up electrons are plotted. The top site adsorption of the H atom is shown in Figure 4.21 and looks very similar to the NM case except a higher peak for the 5f electrons is found at the Fermi level. Figure 4.22 and Figure 4.23 show the LDOS for the center and bridge site, which look nearly exact to the NM cases except for intensity and the bridge site illustrates a broader 5*f* band above the Fermi level. All sites demonstrate the same hybridization of the H 1*s*, U 6*d* and U 5*f* electrons. Depicted in Figure 4.24 is the AFM LDOS plot for the first and second layer atoms of the clean γ-U (100) metal slab, using the same parameters as for the NM and FM cases. As expected, the AFM plot has the same features as the FM case. As with the FM case, the LDOS plots for top and center site adsorption of the H atom for the AFM configuration, shown in Figure 4.25 and Figure 4.26, look very similar to the NM case except a high distribution of 5f electrons at the Fermi level for the top site. The LDOS distribution for the bridge site, Figure 4.27, has a broader 5*f* band above the Fermi level like in the FM calculations. Hybridization of the H 1*s*, U 6*d* and U 5*f* electrons for all sites is also indicated. This indicates that the AFM spin alignment has no effect on the charge distribution of the 6*d* and *5f* electrons of the U atoms.

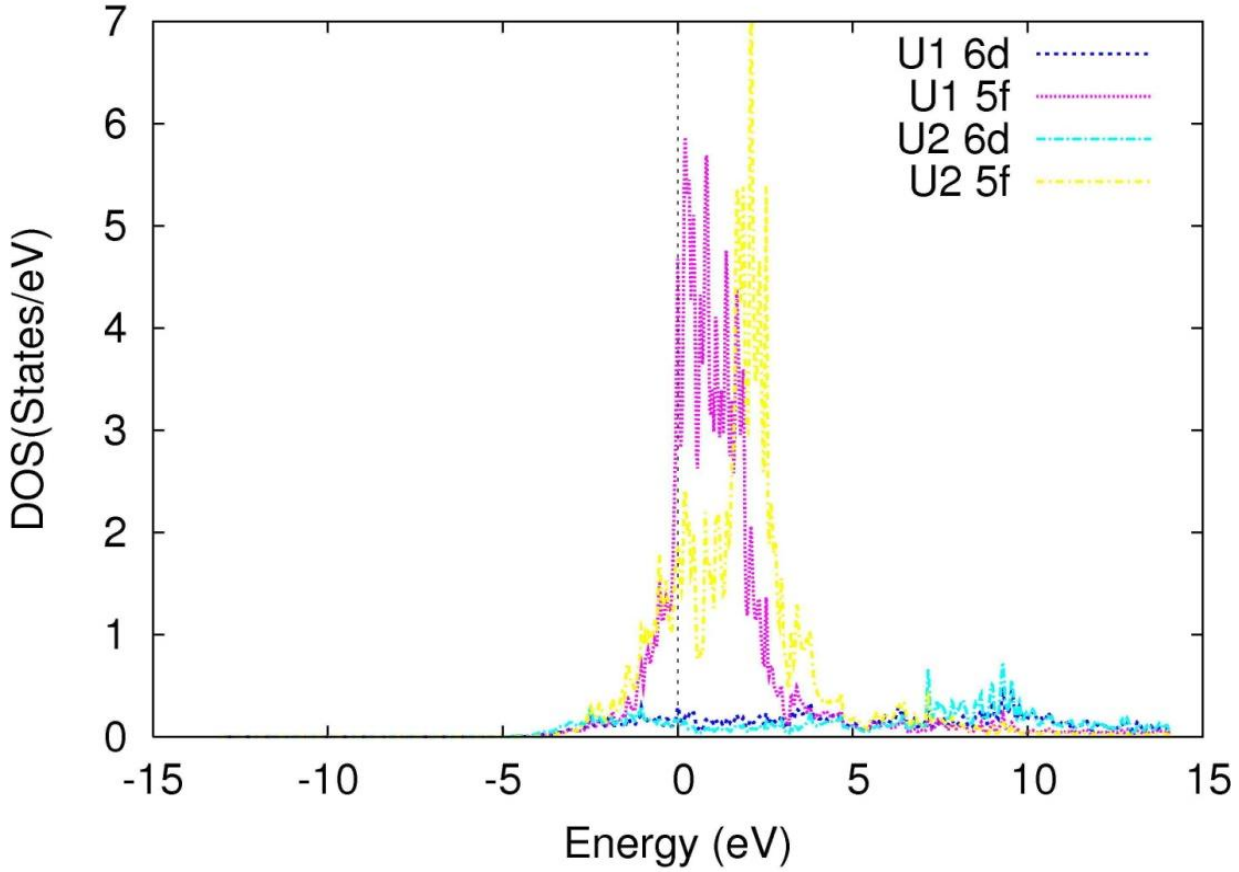

Figure 4.16 LDOS for the 6*d* and 5*f* electrons of the surface (U1) and subsurface (U2) atoms of the bare γ-U (100) slab at the NM level of theory

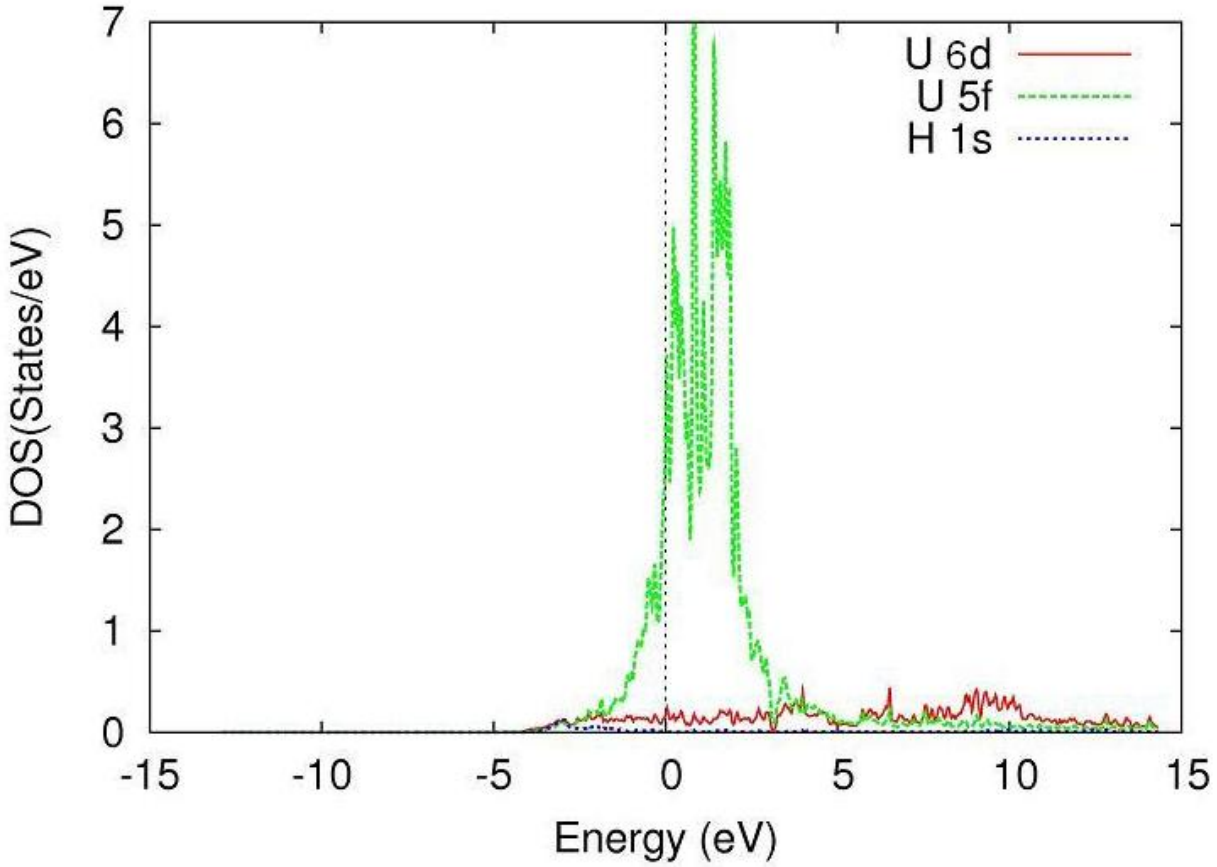

Figure 4.17 LDOS for H adsorption at the top site with the NM level of theory

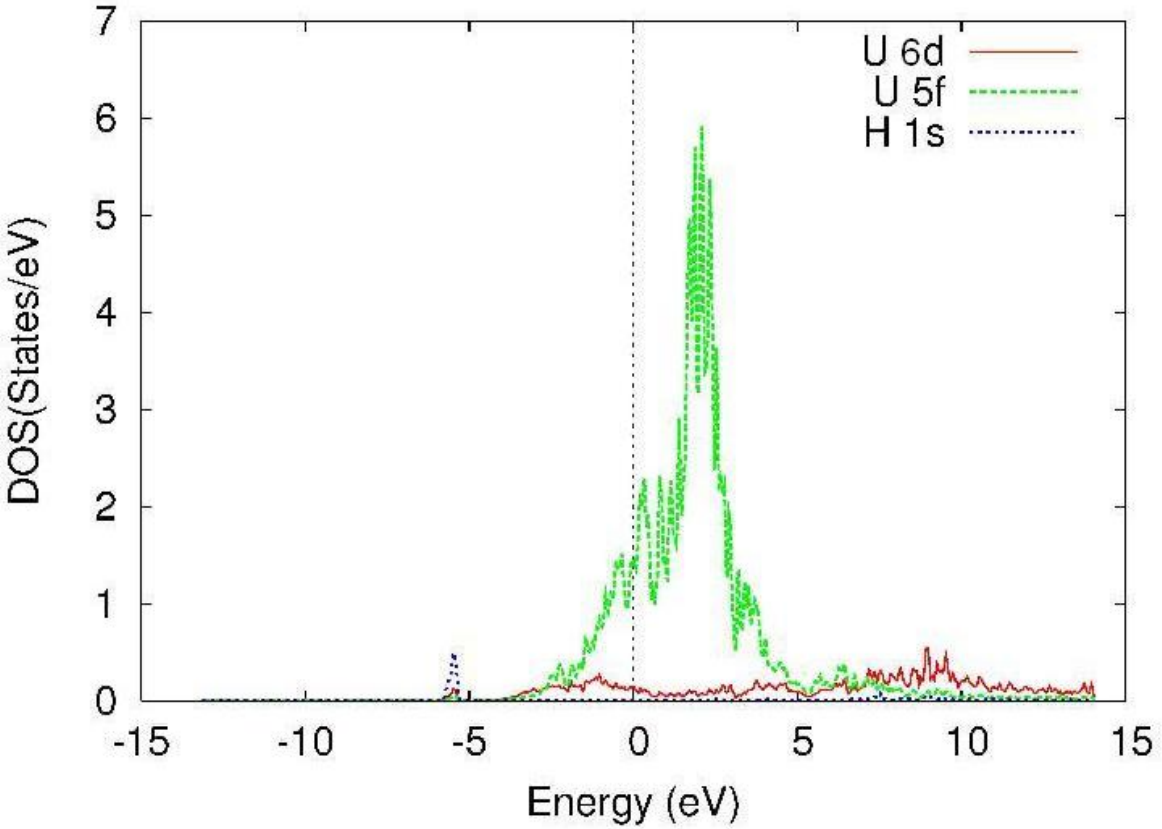

Figure 4.18 LDOS for H adsorption at the center site with the NM level of theory

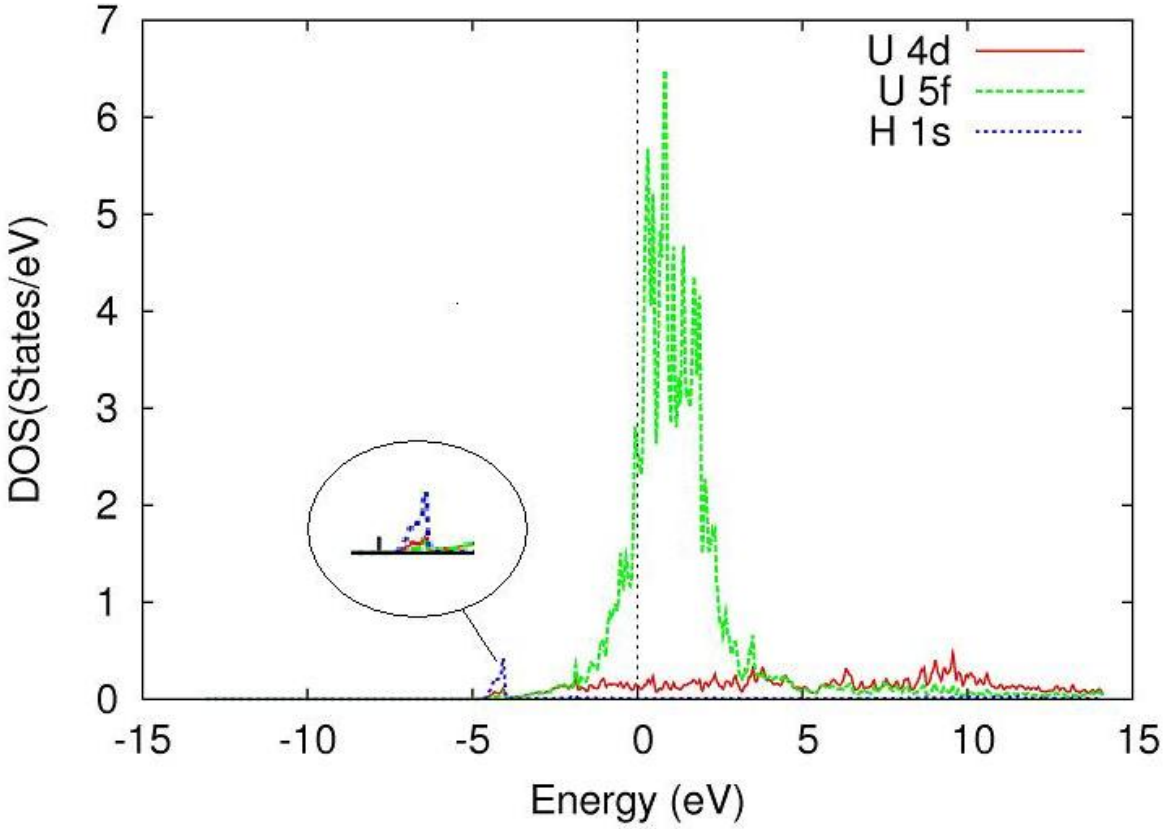

Figure 4.19 LDOS for H adsorption at the bridge site with the NM level of theory

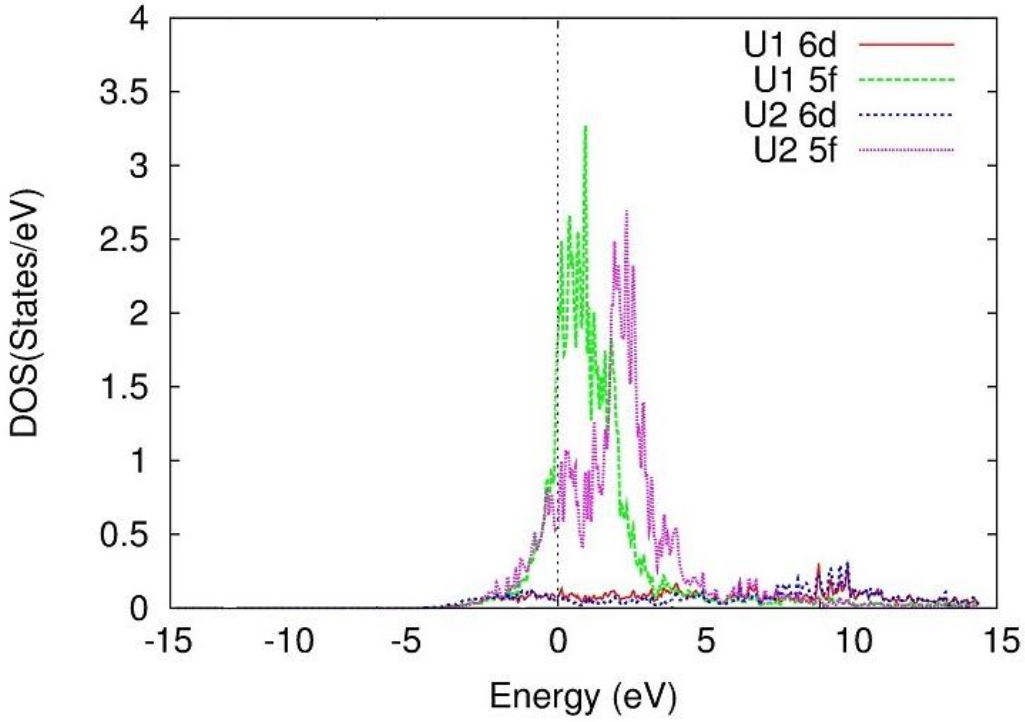

Figure 4.20 LDOS for the 6d and 5f electrons of the surface (U1) and subsurface (U2) atoms of the bare γ-U (100) slab at the FM level of theory

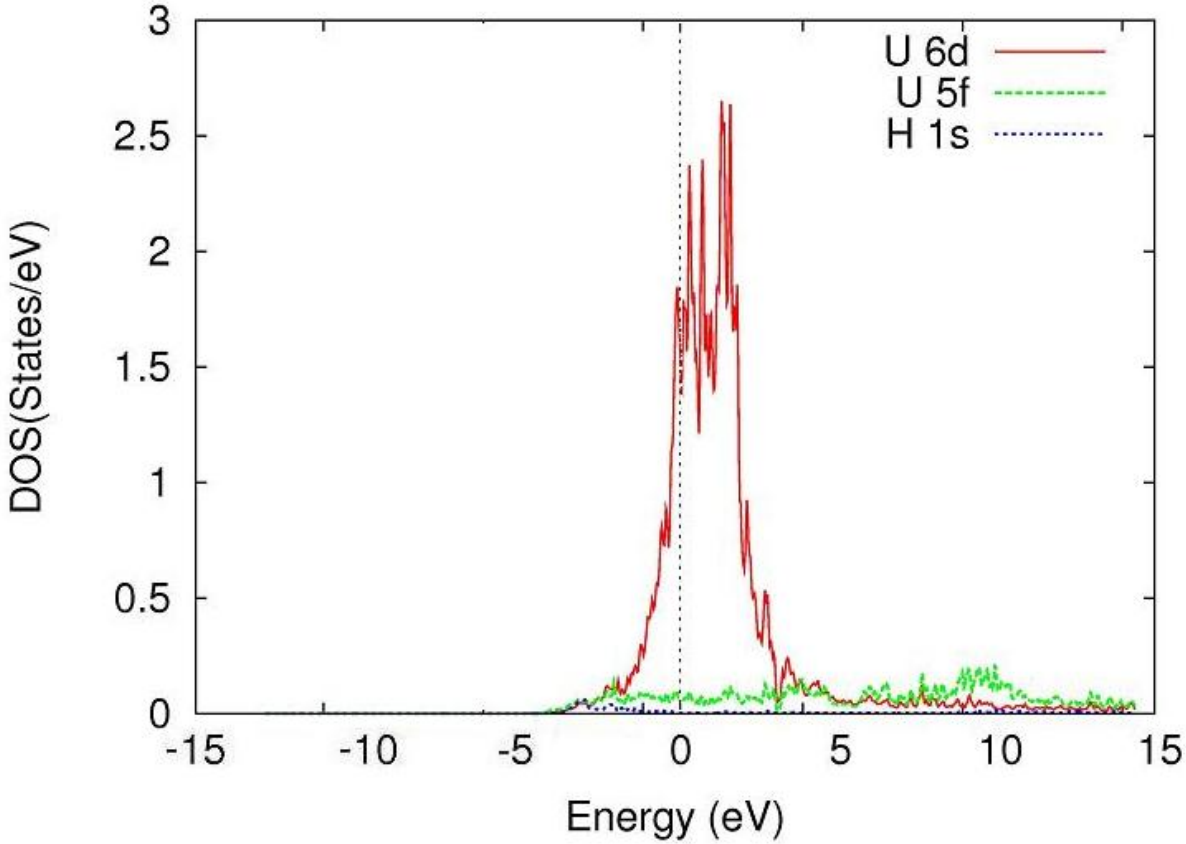

Figure 4.21 LDOS for H adsorption at the top site with the FM level of theory

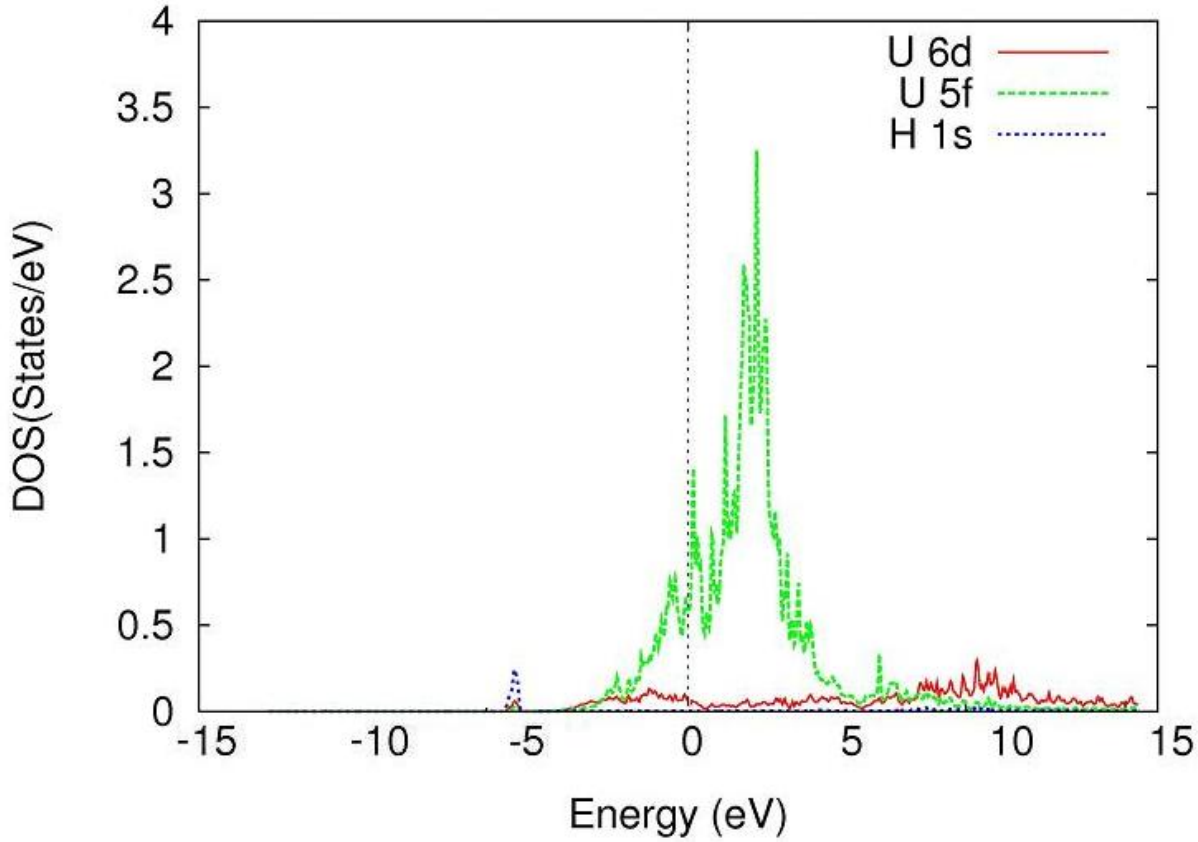

Figure 4.22 LDOS for H adsorption at the center site with the FM level of theory

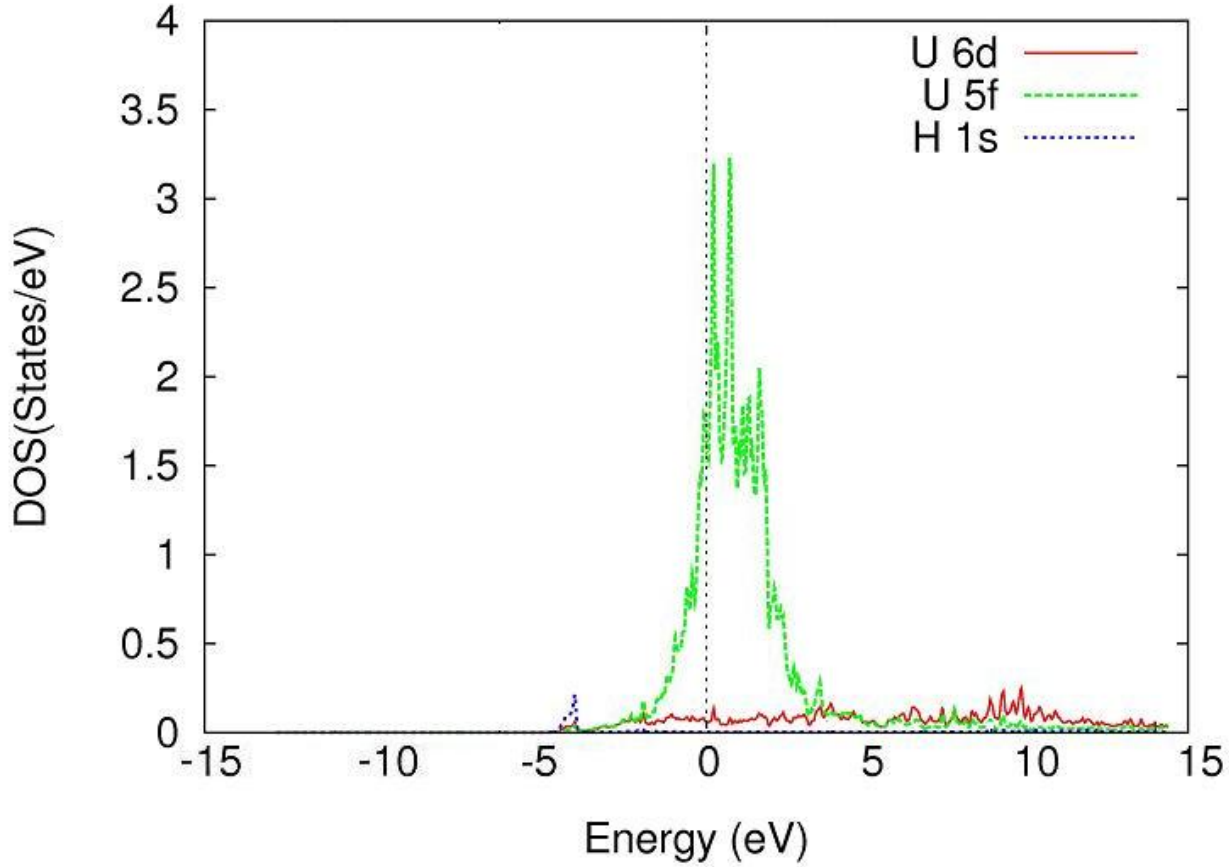

Figure 4.23 LDOS for H adsorption at the bridge site with the FM level of theory

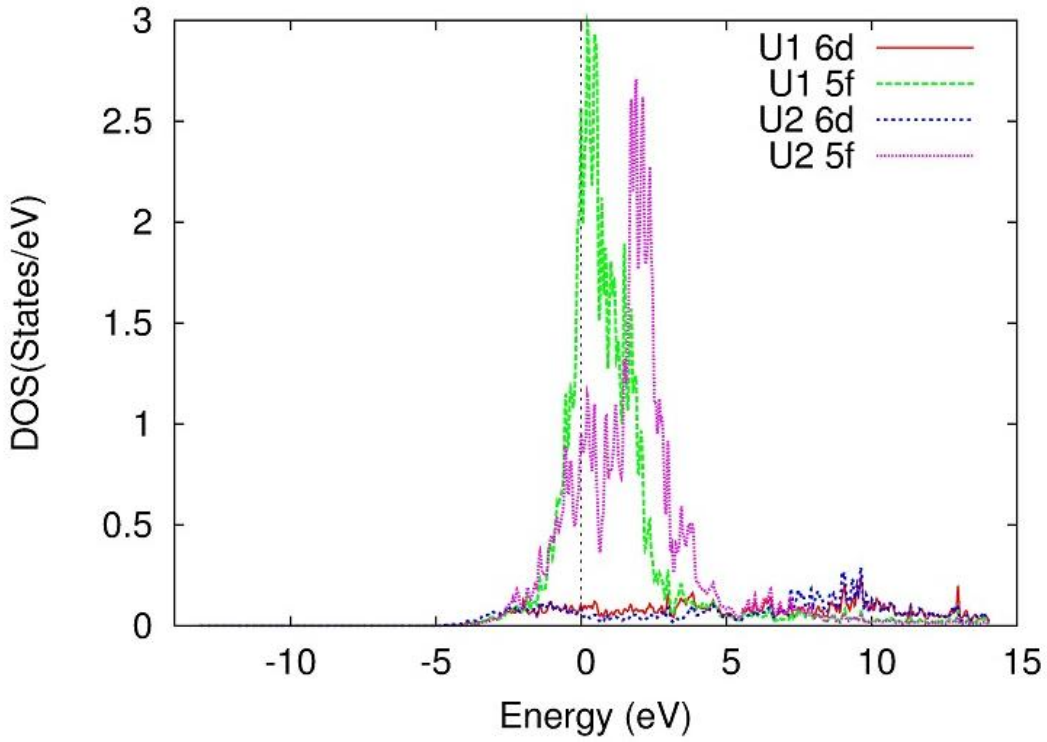

Figure 4.24 LDOS for the 6d and 5f electrons of the surface (U1) and subsurface (U2) atoms of the bare γ-U (100) slab at the FM level of theory

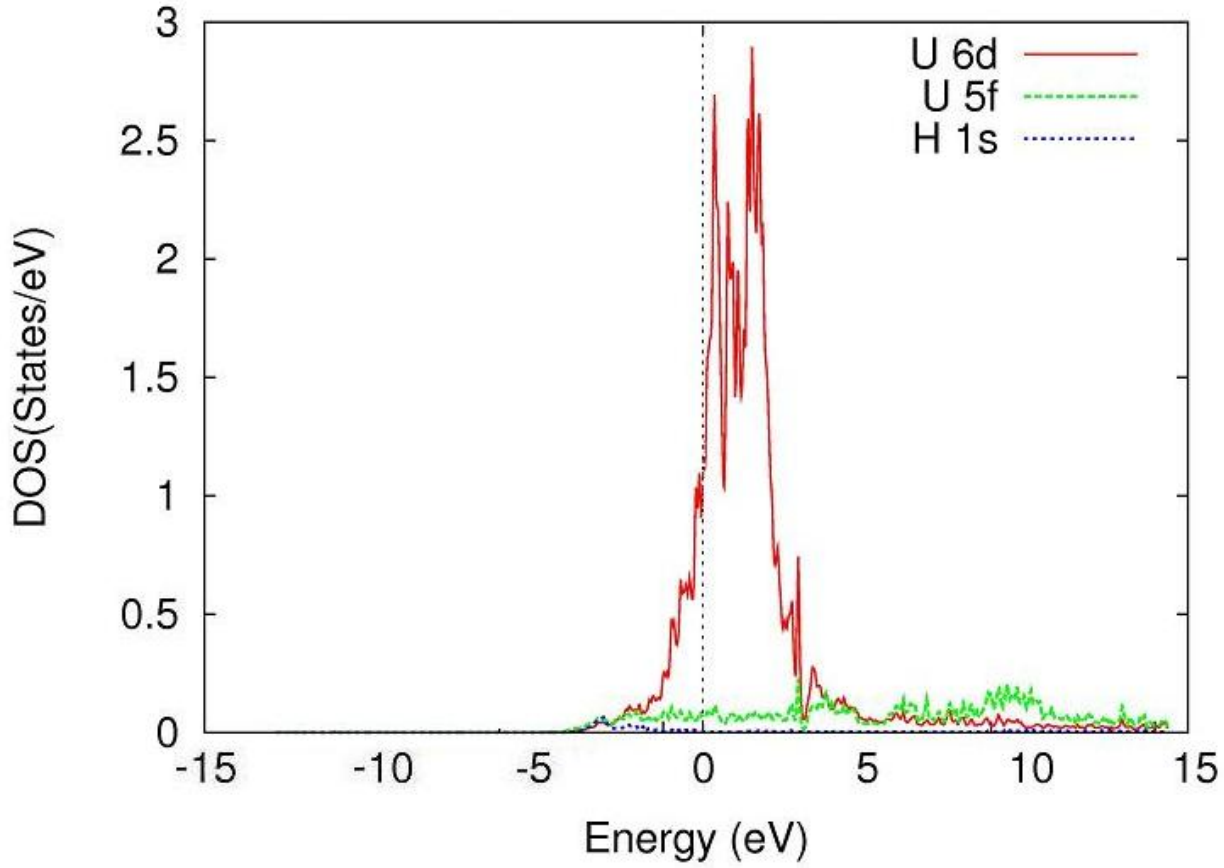

Figure 4.25 LDOS for H adsorption at the top site with the AFM level of theory

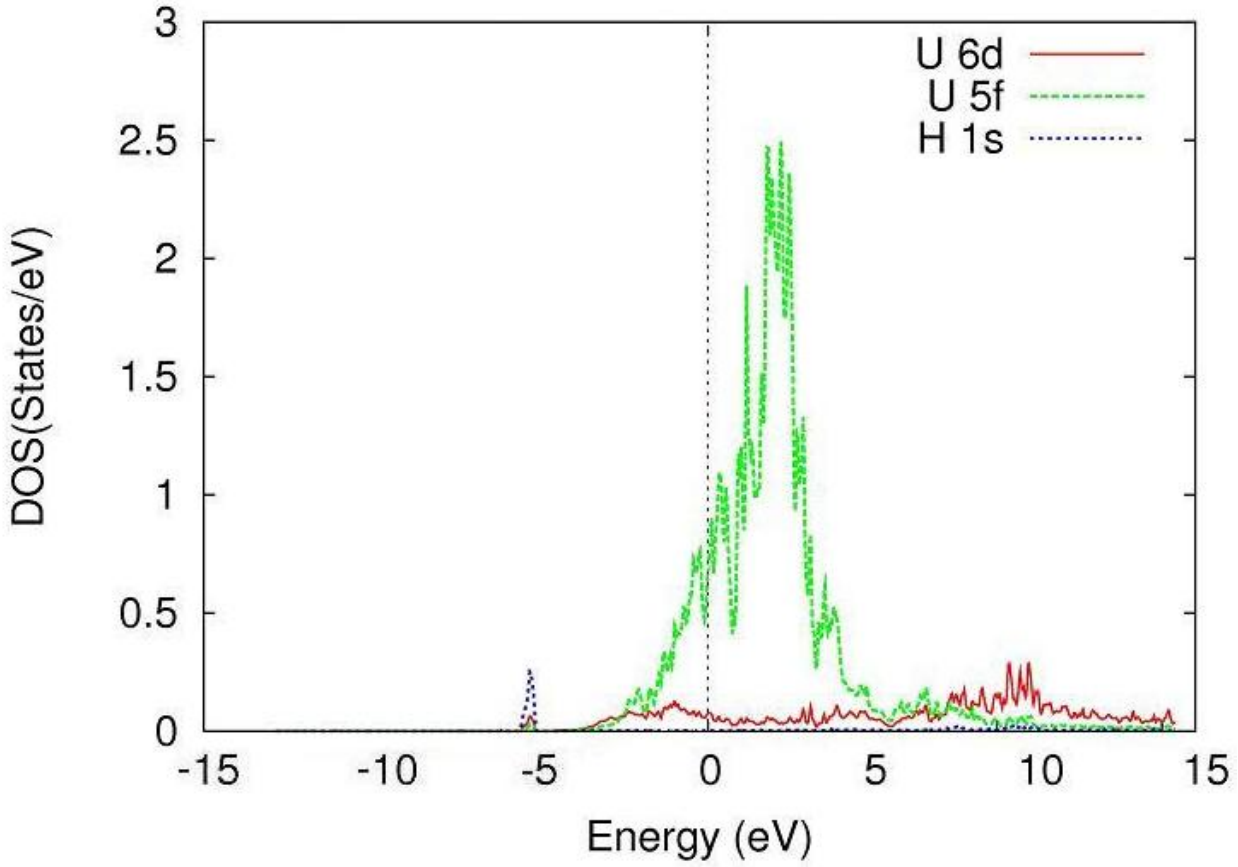

Figure 4.26 LDOS for H adsorption at the center site with the AFM level of theory

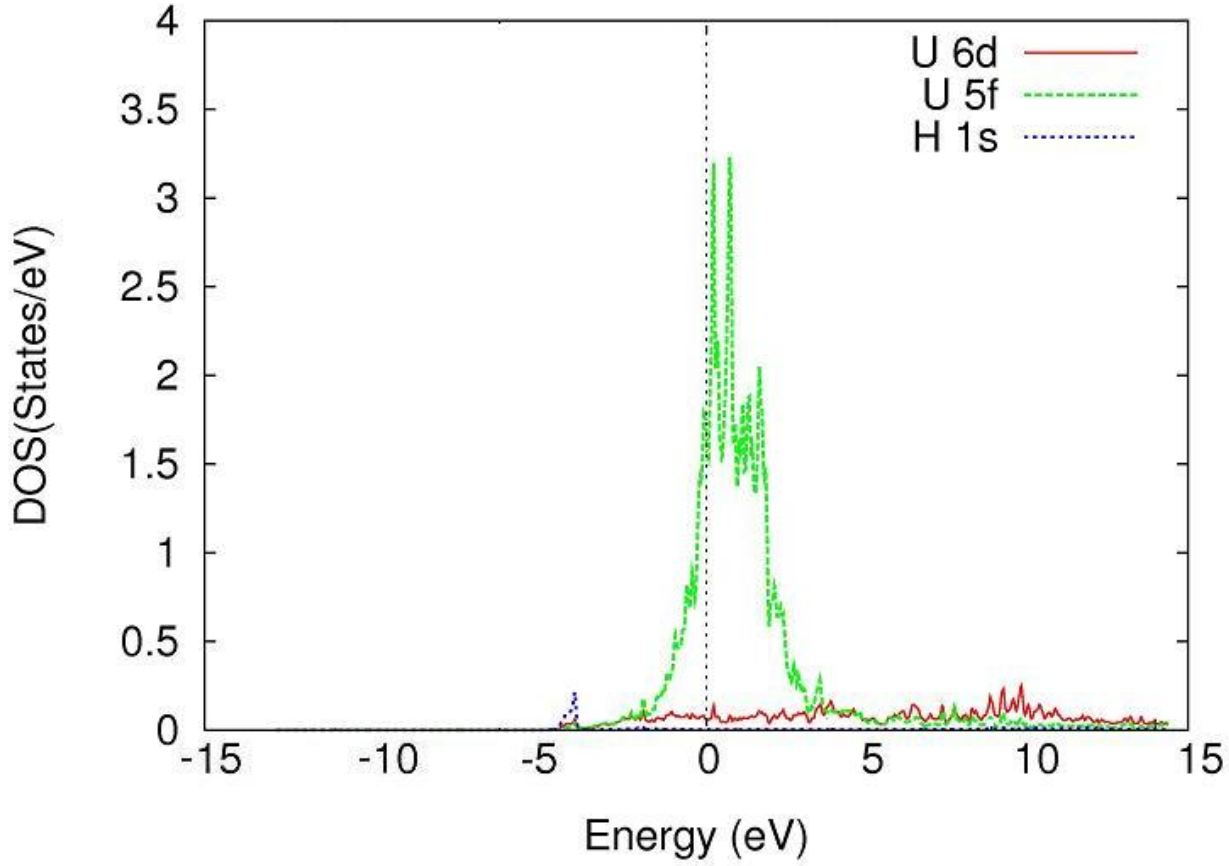

Figure 4.27 LDOS for H adsorption at the bridge site with the AFM level of theory

4.2.2 Interstitial lattice sites for H inside (100) oriented γ-U slab

Experimentally, H is known to have low solubility and diffusivity when exposed to α-U leading to UH_3 formation on the surface alone [61]. In this section we are going to look at H atoms placed in vacancy regions, or interstitial sites, of the slab that are a natural consequence of the bcc structure. This will determine H binding strength to the lattice and diffusion properties of the H atom with the γ-U surface. As described in the introduction of this section, we looked at three symmetrically different sites inside the lattice, the interstitial top, interstitial center and interstitial bridge sites. Of these, the interstitial bridge site was the only one in which the adatom could 1) move freely in the z direction and 2) enter the lattice. Therefore, we have optimized the adatom position with respect to the surface in the bridge interstitial site only. The chemisorption energy was calculated for positions with varying z and a polynomial fit was done to find the location inside the slab with the lowest total energy. For the NM case, the atom was allowed to move from the surface to the center of the slab. The chemisorption energy versus distance under the surface is plotted in Figure 4.28 for the NM, FM and AFM cases. As is shown, there are two minimum energy locations within the slab interstitial bridge site, at -0.74 Å and at -2.47 Å below the surface for the NM case. The potential barrier between these two positions is 0.71 eV, calculated as the difference in the highest and lowest chemisorption energy within the bridge site. The potential barrier between the surface and the first potential well under the surface is 0.41 eV, calculated as the chemisorption energy of the H atom at the optimized position minus the chemisorption energy at the surface. Given the disparity between the surface barrier and the first potential well barrier energies, 0.30 eV, it would seem that binding with the surface is preferred over binding with the lattice and the H atom is unlikely to diffuse further into the slab without adding energy to the atom. For the FM and AFM cases, the atom was allowed to move in the z direction near the minimum energy location to see how the magnetic configuration would affect the location of the potential well near the surface, where a polynomial fit of the energy versus distance curve was used to calculate the optimized position. From the FM and AFM chemisorption *versus* distance graphs we

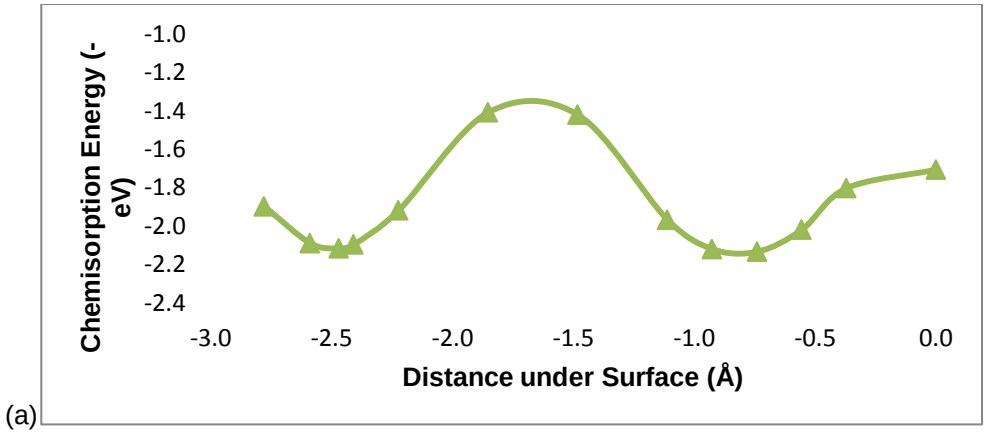

(a)

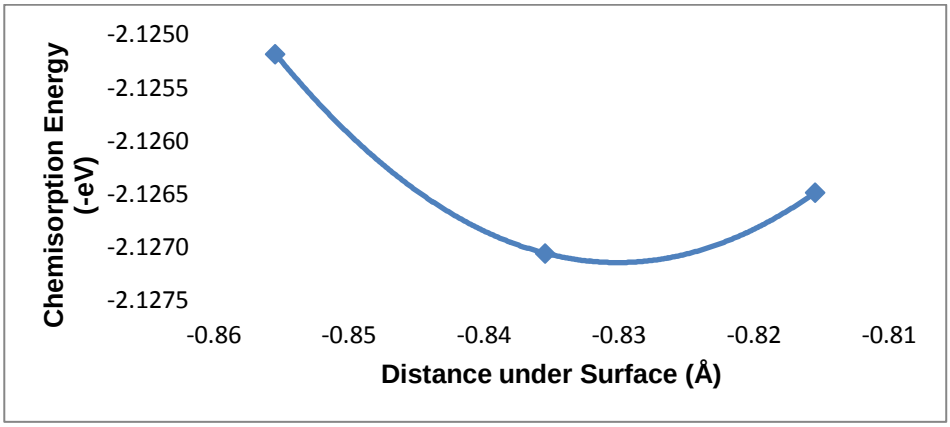

(b)

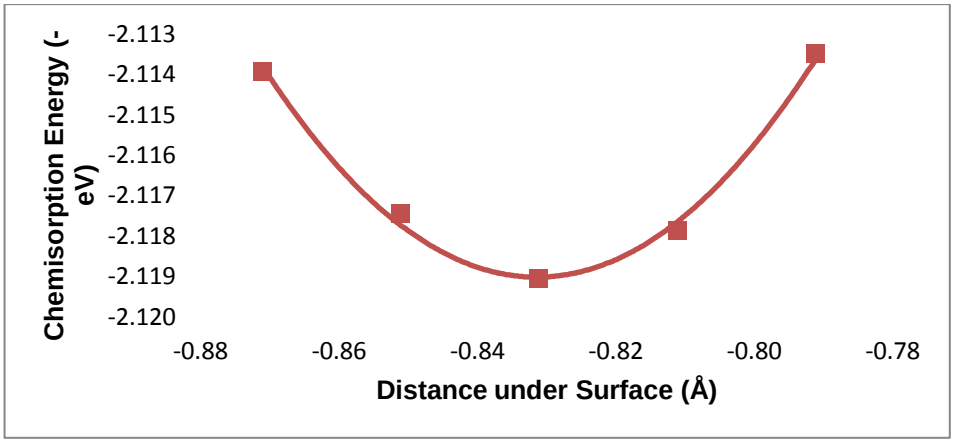

(c)

Figure 4.28 Optimized Ec of H atom at the interstitial bridge site for the NM (a), FM (b) and AFM (c) cases

can see that the minimum energy was found at 0.83 Å below the surface for both the FM and AFM magnetic configurations. Table 4.9 lists the adsorption energies calculated with equation 4.2 of the H atom in the interstitial regions of the (100) slab of γ-U at the NM, FM and AFM electronic spin configurations, respectively. As with the surface calculations the ΔE as described by equation 4.3, the NSOC and SOC energies are also listed, in addition to, the distance below the surface and the nearest neighbor U atom. At all levels of theory, the bridge interstitial site is the most stable at 2.12 eV with and without SOC. The interstitial top site is next at 1.33 eV and 1.27 eV for the NM case, 1.31 eV and 1.24 eV for the FM case, and 1.29 eV and 1.24 eV for the AFM case, at the NSOC and SOC levels of theory, respectively. All chemisorption energies are positive, indicating an exothermal reaction when H binds to the lattice. For the top and center sites a negative change in energy is induced by the addition of SOC. This may be due to the close proximity of the nearest U atom. For the bridge site, the optimal location inside the lattice resulted in a U-H bond length of 1.84 Å for the NM case and 1.87 Å for the FM and AFM cases. This is only slightly less than the optimal bond length of U and H computed by Taylor and Lillard of 2.1 Å using a pseudopotential method [61].

Table 4.10 lists $\Delta\Phi$, calculated using equation 4.5, and μ_{dipole}, using equation 4.6, for the H atom inside the γ-U (100) lattice at the NM, FM and AFM level of theory with SOC included. $\Delta\Phi$ for the top site is lowest in energy and negative at -0.06, -0.07 and -0.04 eV for the NM, FM and AFM magnetic configurations, respectively. Therefore, it would be more difficult to remove an electron from the surface if a H atom were bond to the lattice in this position. The H atom in the interstitial center position has no affect on the work function at any level of theory. For the bridge site, the change in work function is 0.00 for the NM case and 0.03 for the FM and AFM cases. The adsorbate-induced dipole moment came to -0.28, -0.29, and -0.20 D for the top site, -0.02, 0.02, and -0.02 D for the center site and -0.02, 0.12, and 0.12 D for the bridge site at the NM, FM and AFM levels of theory, respectively.

Table 4.9 Distances and chemisorption energies of the H atom in γ-U(100) lattice

NM				NSOC	SOC	
Adatom	Site	R (Å)	$d_{U\text{-}adatom}$ (Å)	E_c (eV)	E_c (eV)	ΔE_c (eV)
	Top	-1.67	1.67	1.33	1.27	-0.06
	Center	-3.34	1.67	1.20	1.19	-0.01
	Bridge	-0.74	1.84	2.13	2.12	-0.01
		-2.47	1.84	2.12	2.13	0.01

FM				NSOC	SOC	
Adatom	Site	R (Å)		E_c (eV)	E_c (eV)	ΔE_c (eV)
	Top	-1.67	1.67	1.31	1.24	-0.07
	Center	-3.34	1.67	1.20	1.17	-0.02
	Bridge	-0.83	1.87	2.13	2.11	-0.01

AFM				NSOC	SOC	
Adatom	Site	R (Å)		E_c (eV)	E_c (eV)	ΔE_c (eV)
	Top	-1.67	1.67	1.29	1.24	-0.05
	Center	-3.34	1.67	1.18	1.17	-0.01
	Bridge	-0.83	1.87	2.12	2.13	0.01

Table 4.10 Change in work function and surface dipole moment for the H atom inside the lattice at the NM, FM, and AFM level of theory

H	Interstitial		
Theory	Site	Δφ	μ_{dipole} (D)
NM	Top	-0.06	-0.28
	Center	0.00	-0.02
	Bridge	0.00	-0.02
FM	Top	-0.07	-0.29
	Center	0.00	0.02
	Bridge	0.03	0.12
AFM	Top	-0.04	-0.20
	Center	0.00	-0.02
	Bridge	0.03	0.12

In the same manner as the previous section, Table 4.11 for the FM magnetic configuration and Table 4.12 for the AFM lists for the clean metal surface and each of the chemisorbed systems the magnitude and alignment of the site projected spin magnetic moments, μ_S, and orbital magnetic moments, μ_L, inside the muffin tin sphere for each U atom on each atomic layer, as well as the net spin and orbital magnetic moment and the total magnetic moment, μ, per U atom at the SOC theoretical level. Again, the moments of U atoms bonded to the H atoms are printed in bold. We will first discuss the FM magnetic configuration. For the top site with two bound U atoms with the H atom, we see a reduction of 0.13 μ_B in the spin moment and an increase of 0.12 μ_B in the orbital moment of the surface U atom bonded to the adatom, also, the center atom shows an increase in the spin of 0.024 μ_B and a slight decrease for the orbital of -0.01 μ_B. The moments for all atoms of the first 3 layers of the slab also show a change compared to the clean metal when the atom is bound to the lattice at the top interstitial site. The entire slab sees an increase in total moment of 0.11 μ_B for this adsorption site. A similar scenario can be observed for the center interstitial lattice site but to a lesser extreme, where the decrease

of the spin moment of the U atom bonded to the adatom is about 0.01 μ_B and there is no change of the orbital moment. The center site lattice bonding of the H atom increases the total magnetic moment of the slab by 0.05 μ_B overall. The two U atoms bound to the H atom near the interstitial bridge site experience a decrease in spin magnetic moment of 0.08 μ_B and an increase in orbital magnetic moment of 0.05 μ_B. As with the top site, the moments of the first 3 layers also see a change. The total magnetic moment of the slab changes by an amount of -0.08 μ_B. For the AFM configuration at the top interstitial site, the surface U atom bound to the H atom sees an increase in spin magnetic moment of 0.27 μ_B and the orbital decreases 0.20 μ_B. The center atom decreases in spin magnetic moment slightly and a subsequent increase in orbital moment is seen. The total change in magnetic moment for the entire slab experienced by the bonding of the H atom to the lattice at the top interstitial position is -1.65 μ_B. Bonding at the center interstitial region by the H atom has no affect on the slab. At the interstitial bridge site the H atom induces an increase of 0.16 μ_B of the spin magnetic moment and decrease of 0.11 μ_B of the orbital moment, where the whole slab increases in total magnetic moment by 0.17 μ_B. Comparing the interstitial results with the surface adsorption, the interstitial bonding causes more of a change in the magnetic moment for the FM case. For the AFM, the top site total moment is negative for the interstitial region, where on the surface it is positive, and the bridge site under the surface shows less change regarding the total moment than for the surface bridge site.

Following the analysis of the surface calculations, we investigate the partial charges inside the muffin-tin sphere for the interstitial sites as well. The H atom gains electrons inside the muffin-tin sphere for the top, center and bridge site at all levels of theory. For the NM case at the top site, the charge on top and bottom layers of the slab sees a positive change in *f* electrons compared to the bare slab. For the center site, the second and fourth layers gain charge in both the 6*d* and 5*f* orbitals. The first two layers of the slab find an increase in charge in the 5*f* band for the bridge interstitial site. For the FM case, the top site has an increase of electrons for the 6*d* and 5*f* bands of the first and third layers, which is similar to the change in charge for the center

Table 4.11 Spin and orbital magnetic moment for the H atom inside the lattice at FM level of theory

FM		Layer												
H interstitial		1		2		3		4		5		total		total μ
Site	Atom	μ_S	μ_L	μ_S	μ_L	μ_S	μ_L	μ_S	μ_L	μ_S	μ_L	μ_S	μ_L	
bare	1	0.945	-0.642	0.079	-0.016	-0.075	0.013	0.080	-0.016	0.945	-0.642			
	2	0.946	-0.642	0.079	-0.016	-0.075	0.013	0.080	-0.016	0.944	-0.642			
	3	0.945	-0.641	0.079	-0.016	-0.075	0.013	0.080	-0.016	0.944	-0.642			
	4	0.946	-0.641	0.079	-0.016	-0.075	0.013	0.080	-0.016	0.944	-0.642	7.894	-5.211	2.683
Top	1	0.994	-0.681	0.089	-0.023	-0.080	0.017	0.086	-0.018	0.955	-0.647			
	2	0.966	-0.647	0.089	-0.023	-0.076	0.014	0.086	-0.018	0.953	-0.642			
	3	0.966	-0.647	0.089	-0.023	-0.076	0.014	0.086	-0.018	0.953	-0.643			
	4	**0.821**	**-0.519**	0.089	-0.023	**-0.052**	**0.004**	0.086	-0.018	0.952	-0.642	7.975	-5.183	2.792
Center	1	0.951	-0.639	**0.067**	**-0.013**	-0.075	0.016	**0.066**	**-0.016**	0.950	-0.639			
	2	0.951	-0.639	0.082	-0.017	-0.075	0.016	0.081	-0.017	0.950	-0.638			
	3	0.951	-0.639	0.082	-0.017	-0.075	0.016	0.081	-0.017	0.950	-0.638			
	4	0.951	-0.639	0.086	-0.018	-0.075	0.016	0.067	-0.018	0.950	-0.638	7.912	-5.180	2.732
Bridge	1	0.960	-0.648	0.058	-0.015	-0.082	0.017	0.080	-0.015	0.942	-0.641			
	2	**0.871**	**-0.587**	0.058	-0.015	-0.067	0.012	0.080	-0.015	0.939	-0.635			
	3	0.960	-0.648	0.060	-0.010	-0.082	0.017	0.086	-0.020	0.942	-0.641			
	4	**0.871**	**-0.587**	0.060	-0.010	-0.067	0.012	0.086	-0.020	0.939	-0.635	7.694	-5.086	2.608

Table 4.12 Spin and orbital magnetic moment for the H atom inside the lattice at AFM level of theory

AFM		Layer												
H interstitial		1		2		3		4		5		total		total μ
Site	Atom	μ_S	μ_L	μ_S	μ_L	μ_S	μ_L	μ_S	μ_L	μ_S	μ_L	μ_S	μ_L	
bare	1	0.876	-0.634	0.000	0.000	-0.144	0.056	0.000	0.000	0.875	-0.634			
	2	-0.871	0.631	0.000	0.000	0.143	-0.055	0.000	0.000	-0.870	0.630			
	3	0.876	-0.634	0.000	0.000	-0.144	0.056	0.000	0.000	0.875	-0.634			
	4	-0.871	0.631	0.000	0.000	0.143	-0.055	0.000	0.000	-0.870	0.630	0.020	-0.014	0.005
Top	1	0.895	-0.655	0.009	-0.003	-0.142	0.056	-0.005	0.001	0.875	-0.636			
	2	-0.849	0.623	0.009	-0.003	0.140	-0.057	-0.005	0.001	-0.875	0.630			
	3	0.954	-0.671	0.009	-0.003	-0.141	0.053	-0.005	0.001	-0.875	-0.634			
	4	**-0.604**	**0.426**	0.009	-0.003	**0.113**	**-0.042**	-0.005	0.001	-0.858	0.620	-1.352	-0.293	-1.644
Center	1	0.875	-0.629	**0.000**	**0.000**	-0.143	0.059	**-0.001**	**0.000**	0.872	-0.628			
	2	-0.871	0.626	0.000	0.000	0.142	-0.059	0.000	0.000	-0.868	0.625			
	3	0.875	-0.629	0.000	0.000	-0.143	0.059	0.000	0.000	0.872	-0.628			
	4	-0.871	0.626	0.000	0.000	0.142	-0.059	0.000	0.000	-0.868	0.625	0.014	-0.011	0.003
Bridge	1	0.901	-0.644	0.018	-0.004	-0.139	0.056	-0.001	0.000	0.883	-0.641			
	2	**-0.708**	**0.521**	0.015	-0.003	0.133	-0.053	0.001	-0.001	-0.855	0.617			
	3	0.901	-0.644	0.010	-0.003	-0.139	0.055	-0.006	0.002	0.883	-0.640			
	4	**-0.708**	**0.521**	0.009	-0.003	0.133	-0.053	-0.004	0.001	-0.855	0.617	0.470	-0.300	0.170

site second and fourth layers. Adsorption at the bridge site causes little change in partial charge inside the muffin-tin sphere of the first and second layers. The partial charges inside the muffin-tin sphere for atoms of the slab at the AFM level of theory show a similar trend to those in the FM case.

To investigate the nature of the bonds that have formed between the H atom and the U atom, we have plotted the Δn as described in equation (4.7) in Figure 4.29, Figure 4.30, and Figure 4.31 for the NM spin configuration of the slab. From these we can see that both the H and U atoms gain charge at the top and center interstitial sites, which corresponds with the results we obtained for our partial charges inside the muffin-tin sphere. For the bridge site, a clear exchange of ions is seen. For the FM case, the top and center sites, shown in Figure 4.32 and Figure 4.33, Δn for the U atoms is neutral and the H atom is losing charge. For the bridge site, there is a clear ionic exchange between the H and U atoms. At the AFM level of theory, the bonding relationship between the H and U atoms,seen in Figure 4.35, Figure 4.36, and Figure 4.37 is the same as for the FM case but for the bridge site the bond is less ionic and the U atoms gain a small bit of charge.

For reference purposes the Gaussian-broadened (with a width of 0.003 eV) *f* and *d* LDOS curves for atoms of the surface, subsurface, and center layers of the clean γ-U (100) metal slab are shown at the NM level of theory in Figure 4.38. As with the surface analysis, only the LDOS of the adatoms and the U atoms interacting with the adatoms are considered. In Figure 4.39, we show the LDOS plots for the H adatom and the surface (U1) and center (U3) atom to which it is bound at the top interstitial site. 5f -1s bonding is evident due to the overlap of those orbitals below the Fermi surface. No change in electron distribution, compared to the LDOS of the bare slab surface and center atoms, can be seen. For the interstitial center site, the H atom binds with the subsurface (U2) and subcenter (U4) and the LDOS for these atoms is shown in Figure 4.40. It is evident that the U2 and U4 atoms are symmetrically equivalent. The bonding is similar to that of the interstitial top site with 1s-5f overlap and no clear change in distribution at or above the Fermi level. When bound at the interstitial bridge site, the H 1s orbital shows a less distinct

Table 4.13 Partial charges inside muffin-tin spheres for H at the top, center and bridge interstitial sites for the NM magnetic configuration

NM		Q_B			Q_A			$\Delta Q=Q_A-Q_B$		
Site	Atom/Layer	H *s*	U *d*	U *f*	H *s*	U *d*	U *f*	H *s*	U *d*	U *f*
Top	Hydrogen	0.102			0.195			0.093		
	U surface layer		10.422	1.985		10.421	1.992		-0.001	0.008
	U subsurface layer		10.545	1.948		10.540	1.946		-0.004	-0.002
	U middle layer		10.534	1.942		10.533	1.940		-0.002	-0.001
	U submiddle layer		10.545	1.948		10.545	1.947		0.000	-0.001
	U bottom layer		10.422	1.984		10.422	1.992		0.001	0.008
Center	Hydrogen	0.102			0.196			0.093		
	U surface layer		10.422	1.985		10.421	1.986		-0.001	0.002
	U subsurface layer		10.545	1.948		10.571	1.972		0.026	0.025
	U middle layer		10.534	1.942		10.531	1.944		-0.004	0.003
	U submiddle layer		10.545	1.948		10.571	1.972		0.026	0.025
	U bottom layer		10.422	1.984		10.421	1.986		-0.001	0.002
Bridge	Hydrogen	0.102			0.192			0.090		
	U surface layer		10.422	1.985		10.417	1.989		-0.005	0.005
	U subsurface layer		10.545	1.948		10.547	1.955		0.002	0.008
	U middle layer		10.534	1.942		10.535	1.942		0.000	0.000
	U submiddle layer		10.545	1.948		10.544	1.949		-0.001	0.001
	U bottom layer		10.422	1.984		10.422	1.983		0.001	-0.001

Table 4.14 Partial charges inside muffin-tin spheres for H at the top, center and bridge interstitial sites for the FM magnetic configuration

FM		Q_B			Q_A			$\Delta Q=Q_A-Q_B$		
Site	Atom/Layer	H *s*	U *d*	U *f*	H *s*	U *d*	U *f*	H *s*	U *d*	U *f*
Top	Hydrogen	0.102			0.196			0.093		
12	U surface layer		10.421	2.009		10.446	2.033		0.026	0.024
20	U subsurface layer		10.546	1.958		10.542	1.961		-0.004	0.003
8	U middle layer		10.536	1.952		10.558	1.971		0.022	0.019
16	U submiddle layer		10.546	1.959		10.546	1.959		0.000	0.000
4	U bottom layer		10.421	2.011		10.421	2.014		0.000	0.003
Center	Hydrogen	0.102			0.196			0.094		
9	U surface layer		10.421	2.009		10.420	2.013		-0.001	0.004
17	U subsurface layer		10.546	1.958		10.571	1.965		0.025	0.007
5	U middle layer		10.536	1.952		10.533	1.956		-0.003	0.004
13	U submiddle layer		10.546	1.959		10.572	1.985		0.026	0.026
1	U bottom layer		10.421	2.011		10.420	2.013		-0.001	0.002
Bridge	Hydrogen	0.102			0.193			0.091		
10	U surface layer		10.421	2.009		10.427	2.011		0.006	0.002
18	U subsurface layer		10.546	1.958		10.551	1.963		0.005	0.004
6	U middle layer		10.536	1.952		10.535	1.953		-0.001	0.001
14	U submiddle layer		10.546	1.959		10.546	1.958		0.000	-0.001
2	U bottom layer		10.421	2.011		10.421	2.010		0.000	-0.001

Table 4.15 Partial charges inside muffin-tin spheres for H at the top, center and bridge interstitial sites for the AFM magnetic configuration

AFM		Q_B			Q_A			$\Delta Q=Q_A-Q_B$		
Site	Atom/Layer	H *s*	U *d*	U *f*	H *s*	U *d*	U *f*	H *s*	U *d*	U *f*
Top	Hydrogen	0.102			0.196			0.094		
12	U surface layer		10.419	2.012		10.445	2.026		0.026	0.014
20	U subsurface layer		10.545	1.955		10.540	1.958		-0.004	0.003
8	U middle layer		10.534	1.949		10.556	1.969		0.022	0.020
16	U submiddle layer		10.545	1.955		10.545	1.955		0.000	0.001
4	U bottom layer		10.419	2.009		10.419	2.009		0.000	0.000
Center	Hydrogen	0.102			0.196			0.094		
9	U surface layer		10.419	2.012		10.418	2.012		-0.001	0.000
17	U subsurface layer		10.545	1.955		10.569	1.982		0.025	0.027
5	U middle layer		10.534	1.949		10.530	1.955		-0.004	0.006
13	U submiddle layer		10.545	1.955		10.570	1.983		0.025	0.028
1	U bottom layer		10.419	2.009		10.418	2.013		-0.001	0.004
Bridge	Hydrogen	0.102			0.193			0.090		
10	U surface layer		10.419	2.012		10.427	2.006		0.008	-0.006
18	U subsurface layer		10.545	1.955		10.550	1.959		0.005	0.005
6	U middle layer		10.534	1.949		10.533	1.951		-0.001	0.002
14	U submiddle layer		10.545	1.955		10.545	1.955		0.000	0.000
2	U bottom layer		10.419	2.009		10.419	2.009		0.000	0.000

peak at approximately -6 eV below the Fermi level, where there is also hybridization of the 1s and 5f electrons. Figure 4.41 shows a slightly wider peak at the Fermi level for the surface atom indicating slightly more delocalization at the surface. The FM level of theory LDOS plot is drawn in Figure 4.42 for the surface (U1), subsurface (U2) and center (U3) atoms of clean γ-U (100) metal slab, using the same parameters as for the NM case. Again, the FM and NM LDOS plots are nearly identical except for the intensity of the electron distributions. The interstitial top site binding of the H atom is shown in Figure 4.43 and looks very similar to the NM case. 5*f* -1*s* binding is evident below the Fermi surface. Figure 4.44 shows the LDOS for the interstitial center site. Compared to the NM case there is an extra tall peak at the Fermi surface for the subsurface 5*f* orbitals which indicates that the 5*f* electrons are participating in bonding. Also, a hybridization of the 6*d* and H 1*s* electrons is exposed through this LDOS distribution below the Fermi level. For the bridge interstitial site, the LDOS is graphed in Figure 4.45. From this we see hybridization of the 5*f* U electrons of the surface atom with the H 1*s* electron, like for the center and top interstitial sites, in addition, the 5*f* electrons of the surface atom localize to the Fermi surface. For the subsurface atom, a spike in the electron distribution of the 5*f* electrons can be seen at the Fermi level, as with the center site, indicating those electrons participation in the U-H bonding. For the AFM level of theory, the LDOS for the 6d and 5f electrons of the surface (U1), subsurface (U2) and center (U3) atoms of the bare γ-U (100) metal slab is shown in Figure 4.46. Figure 4.47 illustrates the LDOS for the interstitial top site binding of the H atom. The intensity of the 5f peak for the surface atom at the Fermi level is less than that for the FM interstitial top site case. Otherwise the LDOS plot is similar to the FM case, where the H 1s and U 5f distribution overlap. For the center interstitial site adsorption, it is obvious that there is 1s, 6d and 5f hybridization of the electrons of the surface and center U atoms of the slab which also compliments the FM case which is clearly seen in Figure 4.48. The LDOS at the interstitial bridge site, depicted in Figure 4.49, just as in the FM case the subsurface U atom 5f electrons, show a sharp peak at the Fermi

surface indicating participation in bind but the 6d electrons of the subsurface U atom hybridize with the H 1*s*.

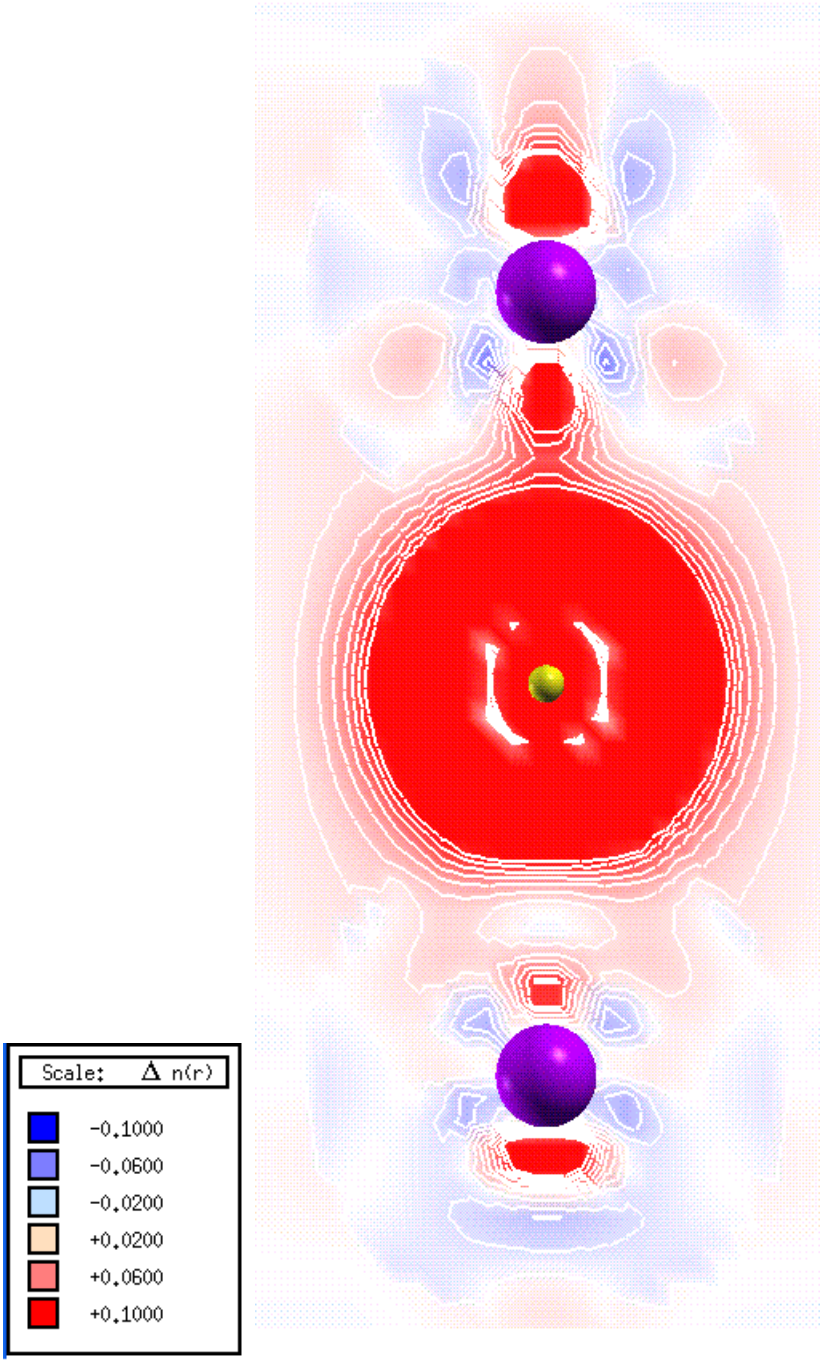

Figure 4.29 Change in charge density for the H atom at the interstitial NM top site

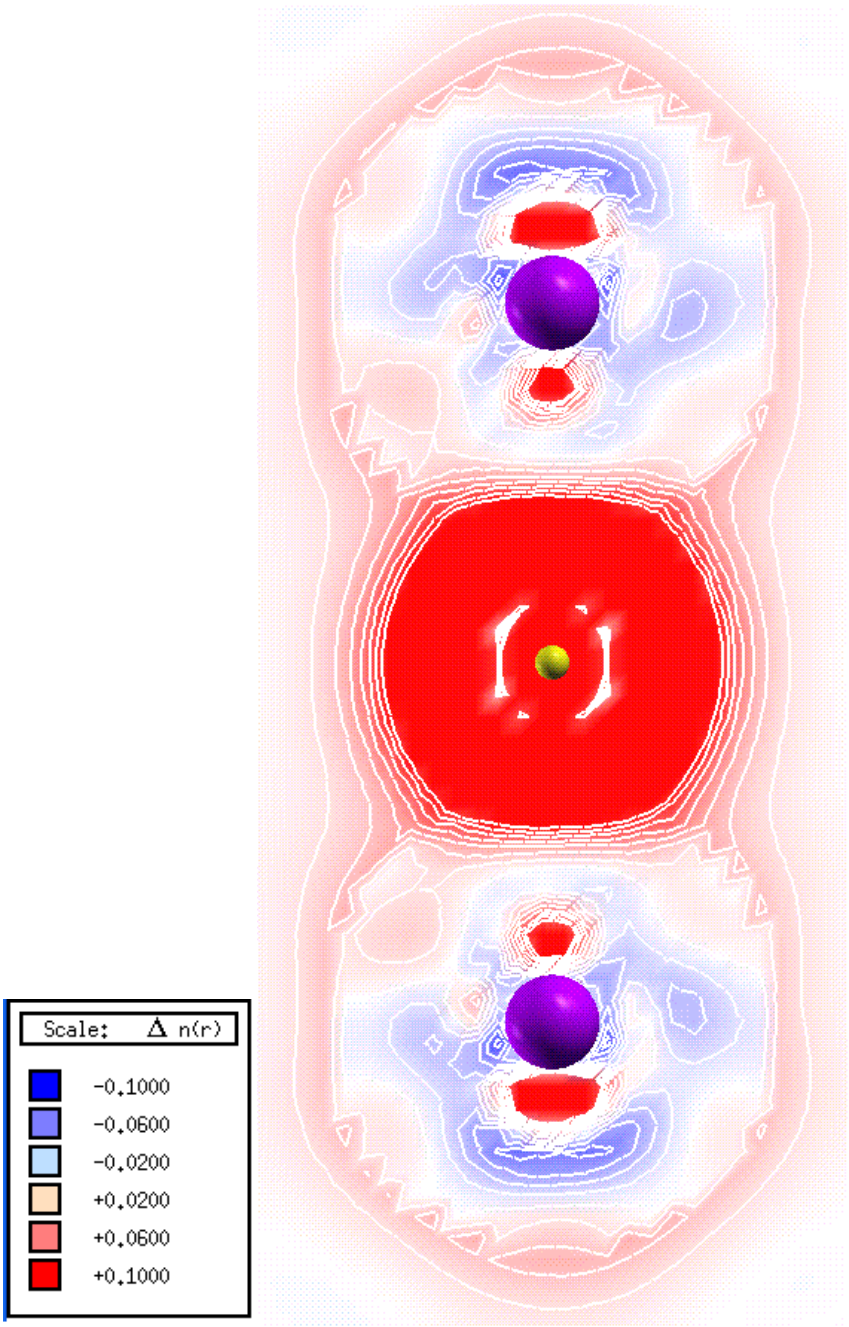

Figure 4.30 Change in charge density for the H atom at the interstitial NM center site

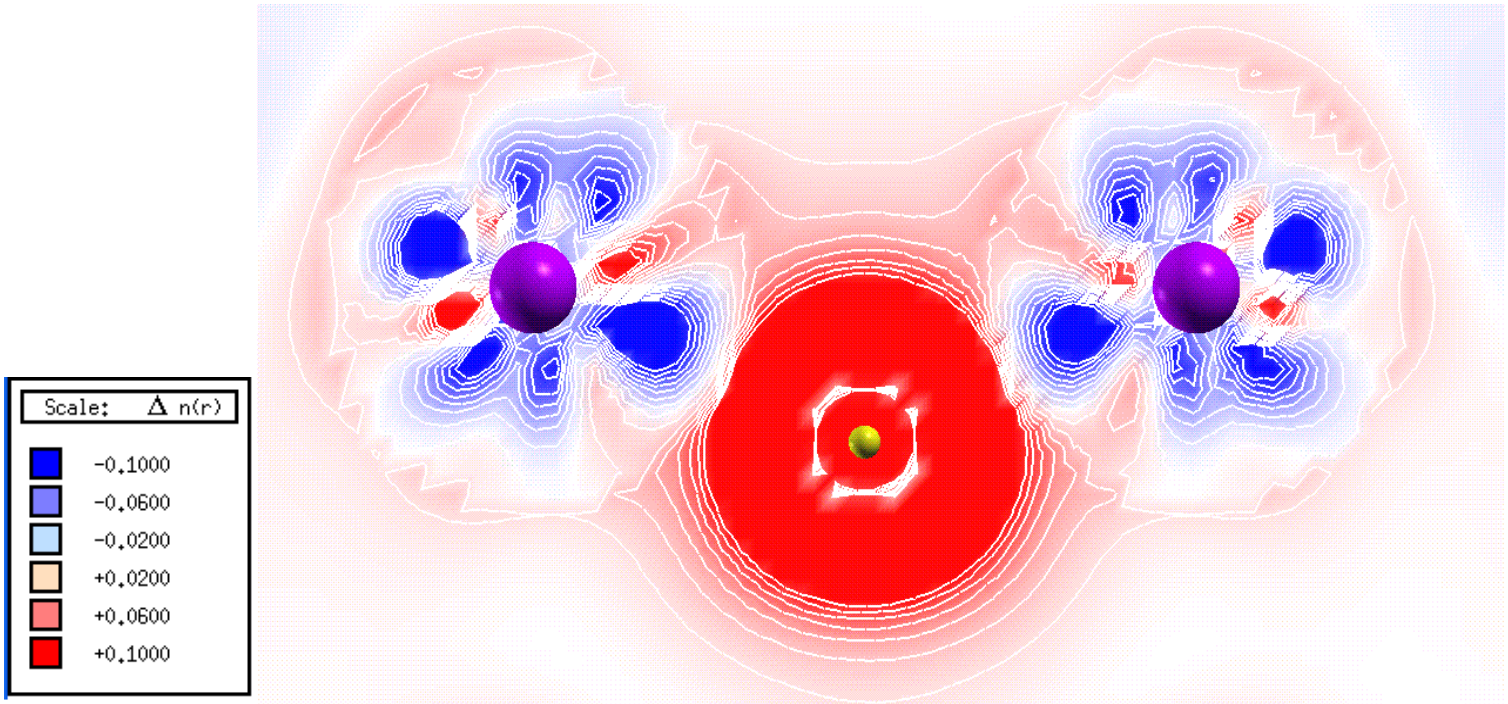

Figure 4.31 Change in charge density of the H atom at the interstitial NM bridge site

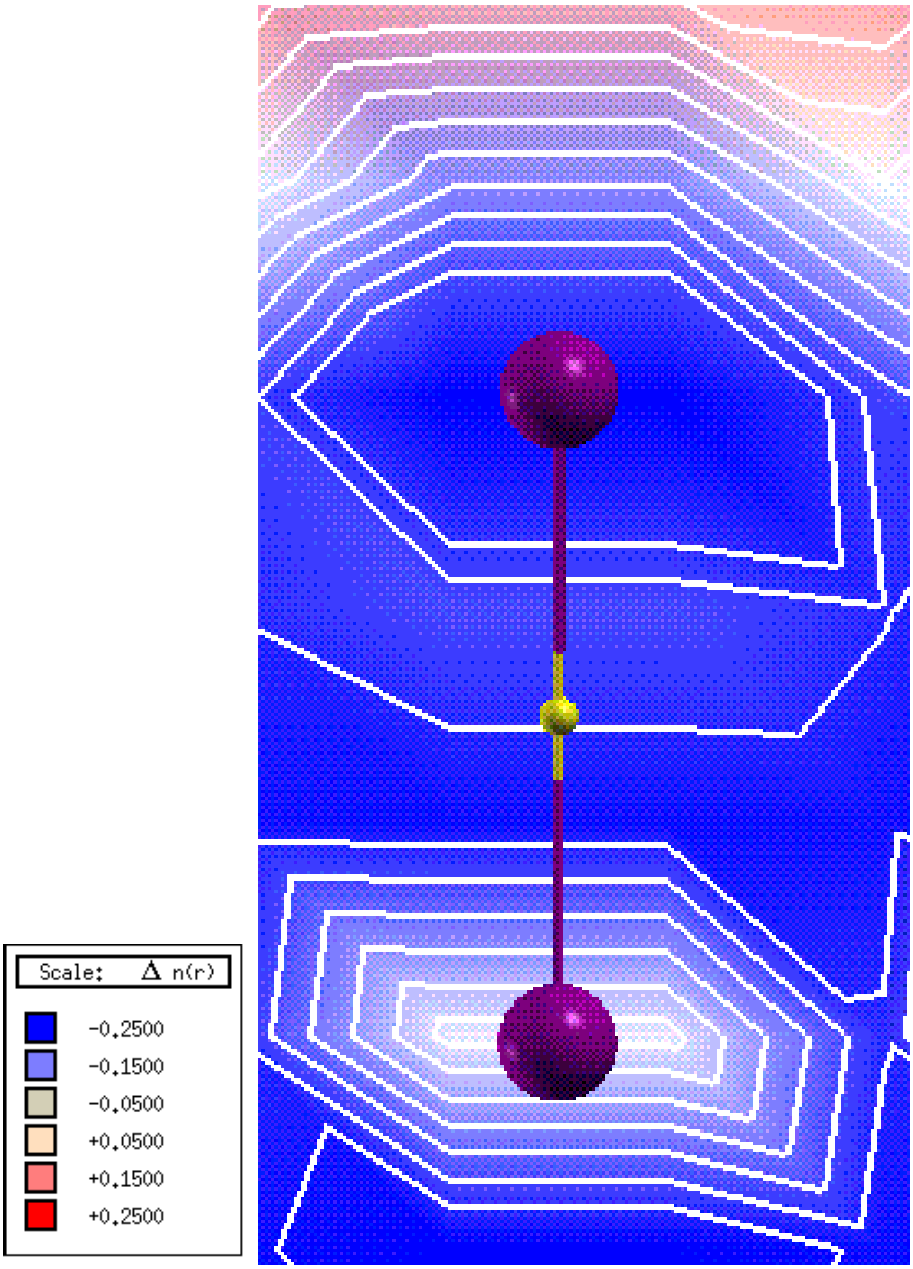

Figure 4.32 change in charge density of the H atom at the interstitial FM top site

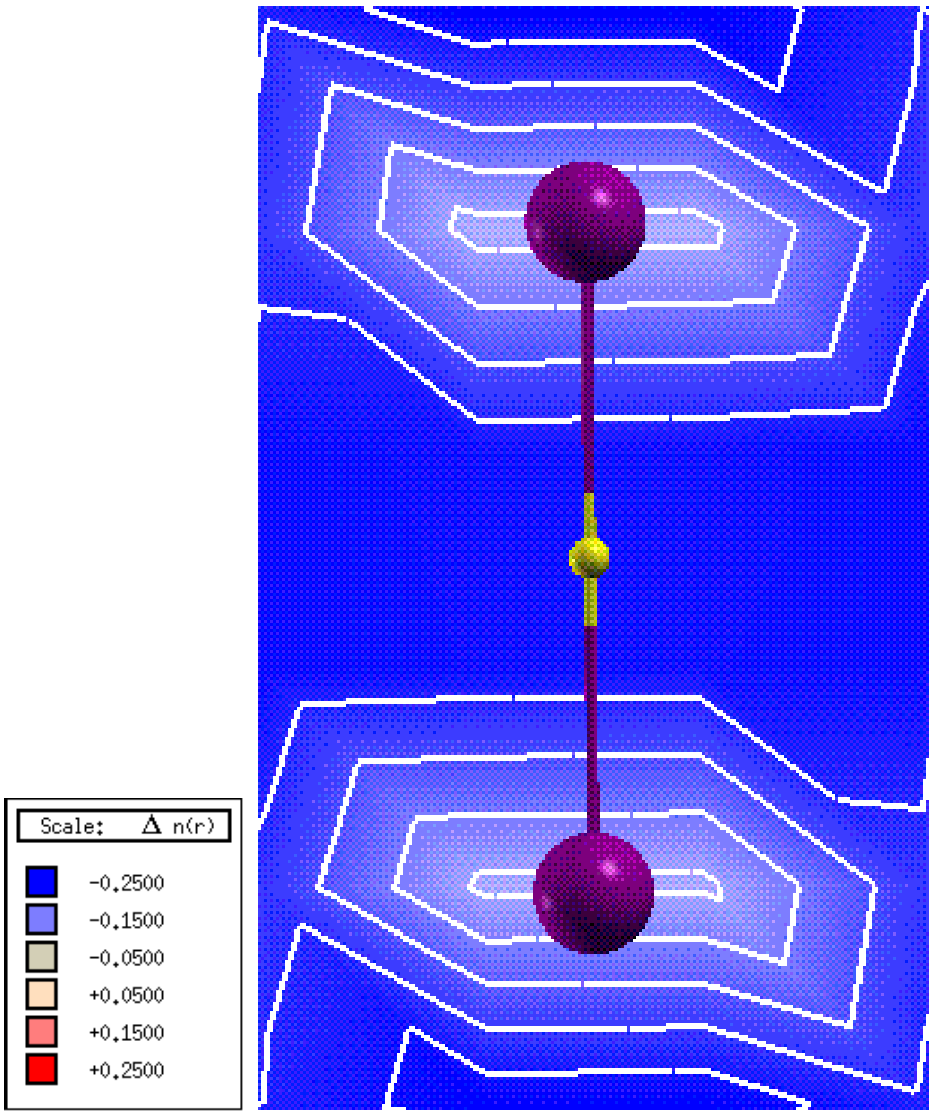

Figure 4.33 Change in charge density for the H atom at the interstitial FM center site

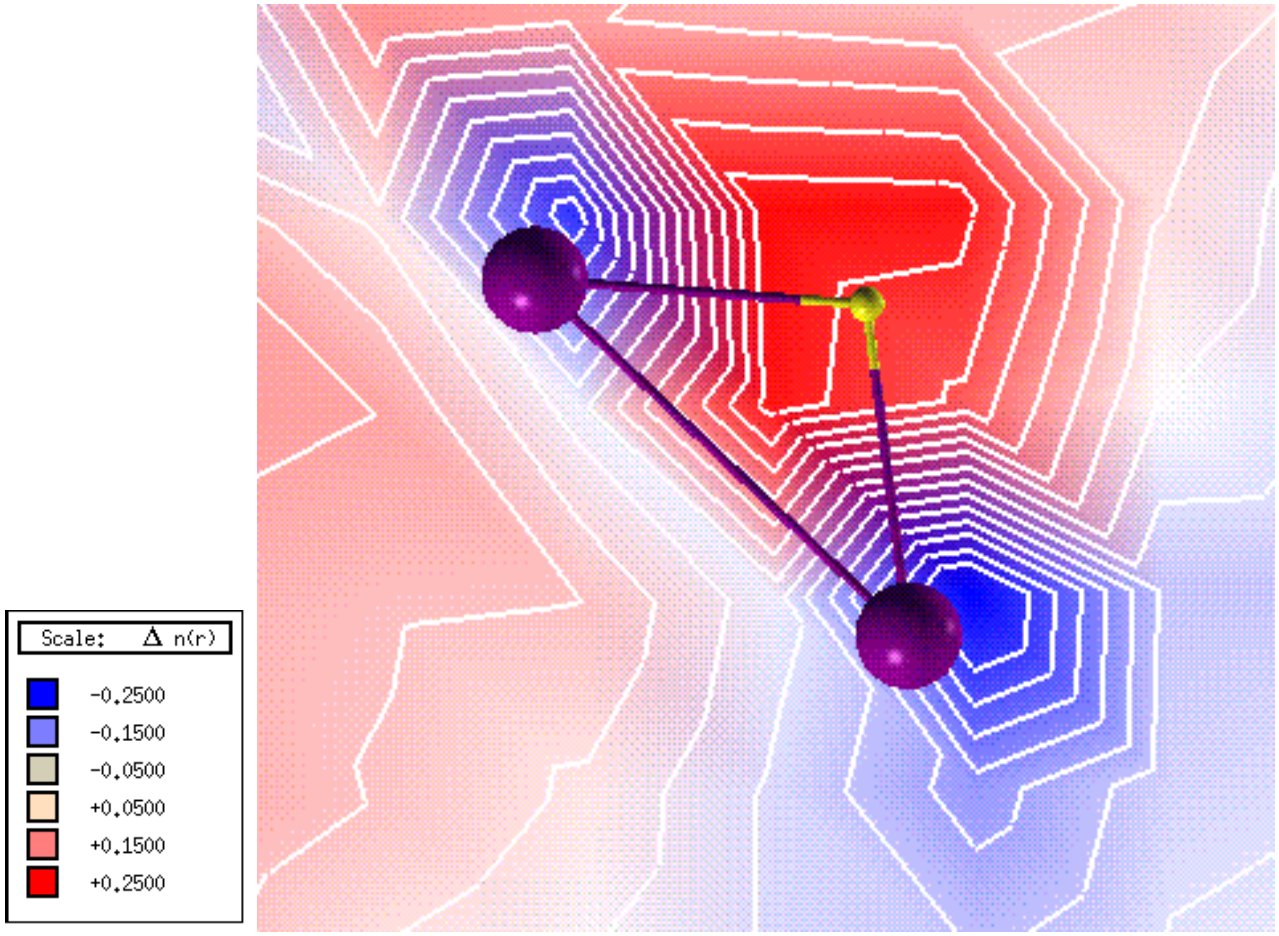

Figure 4.34 Change in charge density for the H atom at the FM interstitial bridge site

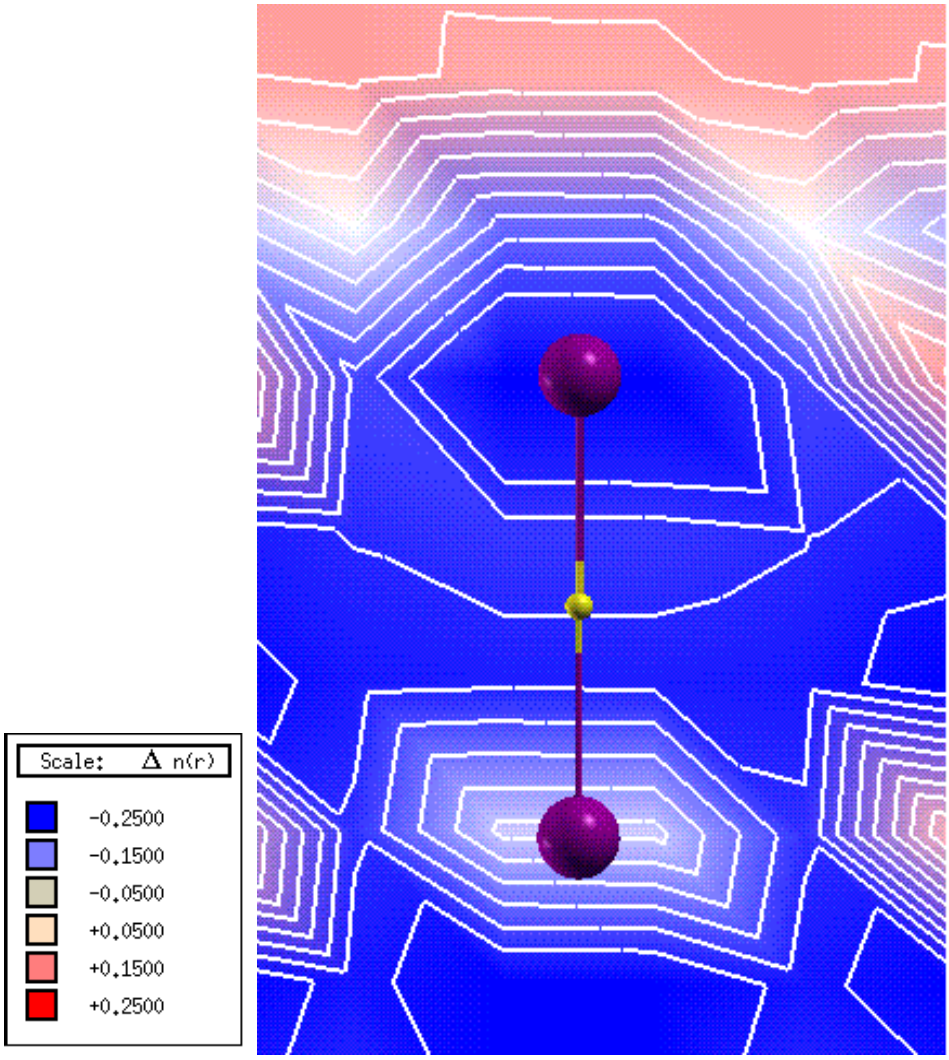

Figure 4.35 change in charge density of the H atom at the interstitial AFM top site

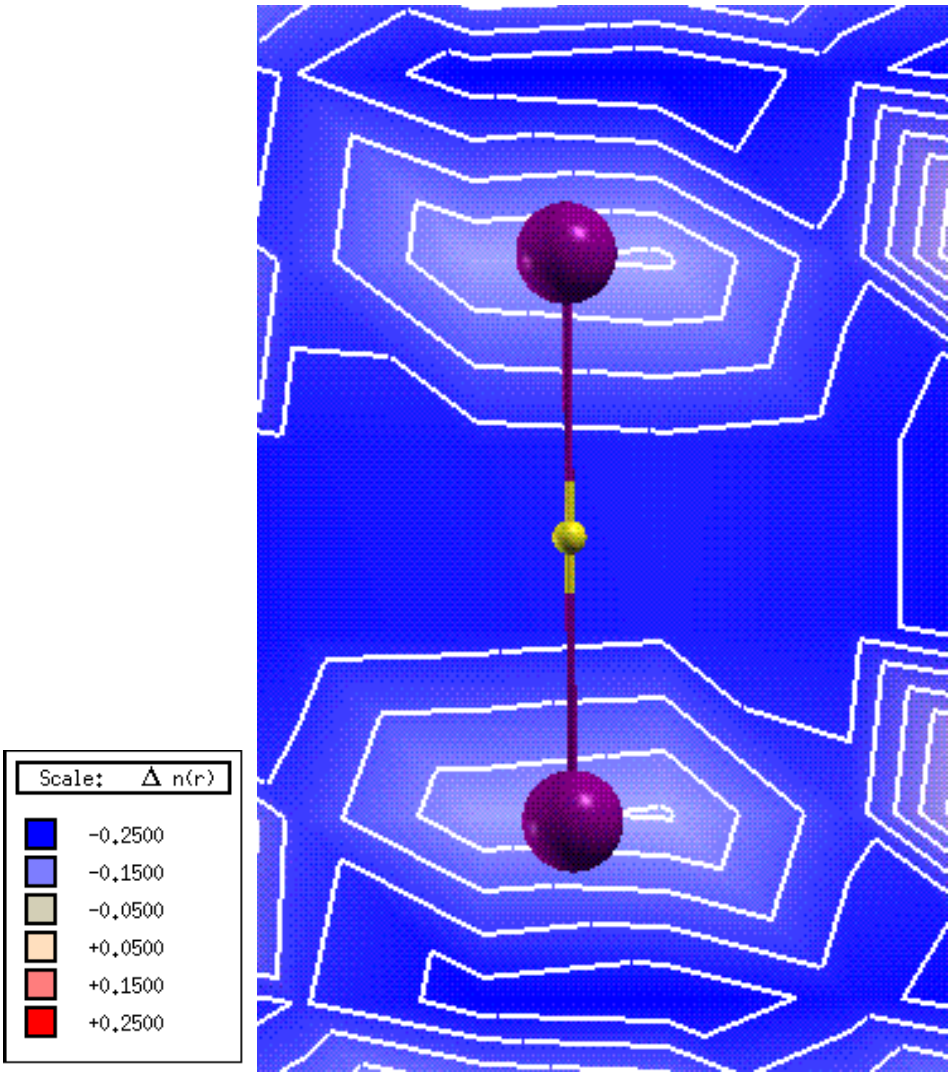

Figure 4.36 Change in charge density for the H atom at the interstitial AFM center site

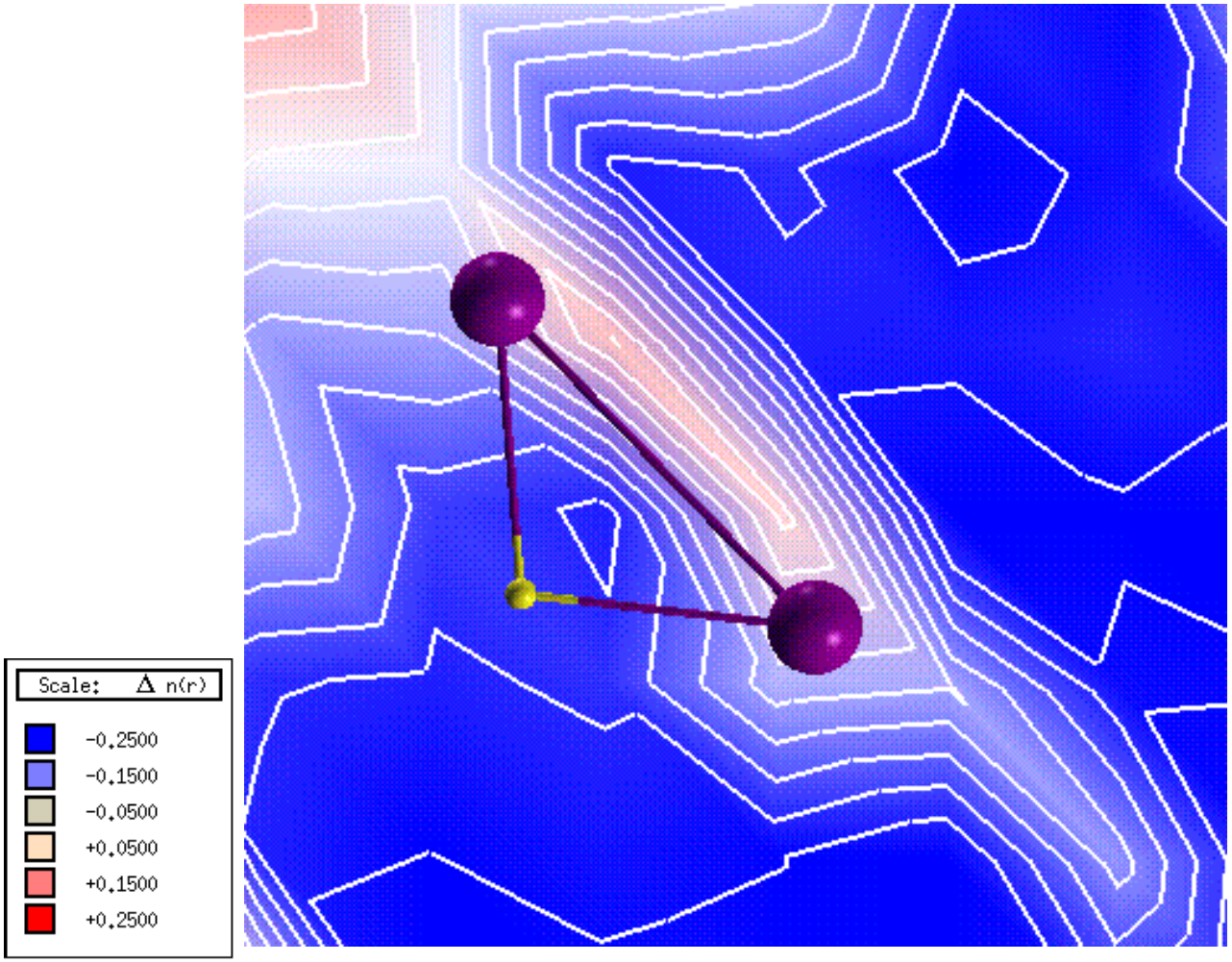

Figure 4.37 Change in charge density for the H atom at the AFM interstitial bridge site

4.2.3 Surface adsorption of O on the (100) γ-U surface

Similar surface adsorption work on the O-U system has been done by our group but with several inadequacies [69], [72]. First, the previous study used a psuedopotential to represent the core electrons; in our study an all electron code will be used. Second, the study was only conducted at the NM and FM level of theory; we will be also looking at the AFM magnetic configuration. Third, spin-orbit interaction was not taken into account for the previous study; we have included SOC in a second variational method using the scalar-relativistic wave functions as basis. In addition, we will be taking a more intensive look at the exchange of charge between the substrate and the adatom and the interaction of the orbitals. In the same fashion as the H investigation, the adatom approached the (100) surface of the 5 layer film of γ-U from one side and the energy was optimized with respect to distance from the surface at the symmetrically different sites, top, center and bridge, at the NSO level of theory. SOC was taken into consideration at the NSOC optimized geometry. Seen in Figure 4.50, Figure 4.51, and Figure 4.52 is a polynomial fit to the curve of chemisorption energy versus distance of the adatom to the surface. This was used to find the minimum energy of the system at each site for the NM, FM, and AFM case. The distance of the O atom from the surface was about 1.86 Å for the top site, 0.75 Å for the center site, and 1.32 Å for the bridge site at the FM and AFM level of theory and came to 1.98, 0.75 and 1.32 Å for the top, center and bridge sites respectively for the NM level of theory.

Table 4.16 lists the distance of the adatom from the surface (R), distance of the adatom from the nearest U atom ($d_{U\text{-}adatom}$), chemisorption energy (E_c), and the ΔE_c, which is the difference between the E_c, at the NSOC and SOC levels of theory at the NM, FM and AFM electronic spin configurations. All values for E_c are positive indicating an exothermic reaction between the O atom and the γ-U surface. For all levels of theory the bridge site is the most stable adsorption location. The NM configuration came out to be the ground magnetic state for this system with chemisorption energies of 7.86, 7.84 and 8.43 eV at the top, center and bridge

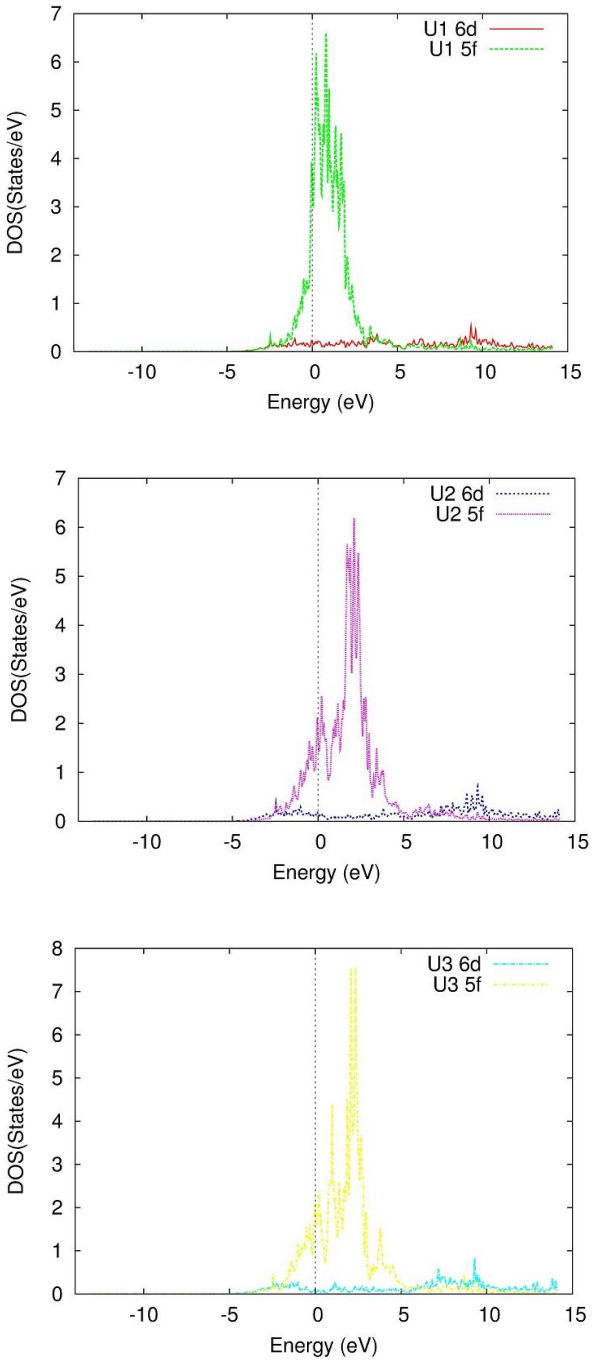

Figure 4.38 LDOS for the surface (U1), subsurface (U2), and center (U3) atoms of the 5 layer slab at the NM level of theory

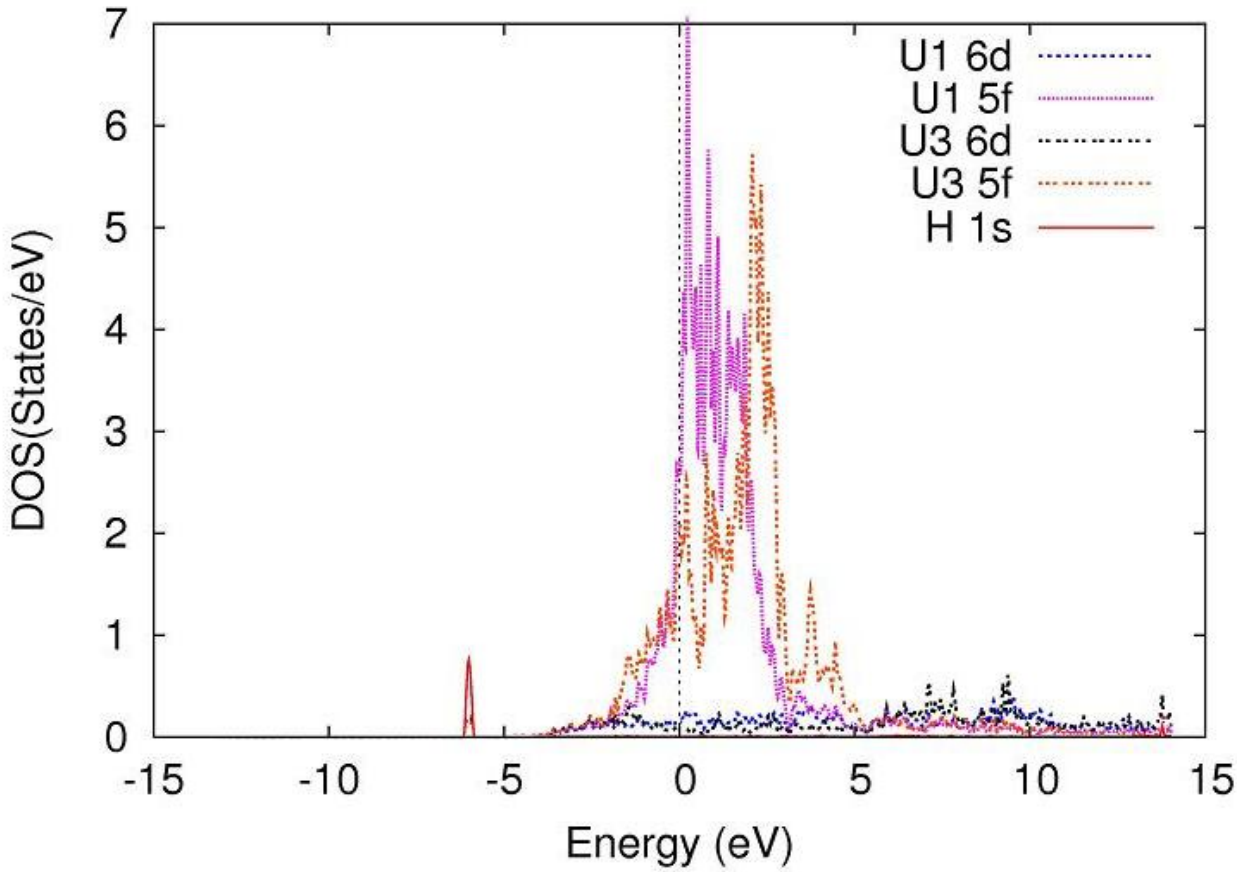

Figure 4.39 LDOS for H at the top interstitial site at the NM level of theory. U1 is the surface atom and U3 is the center atom.

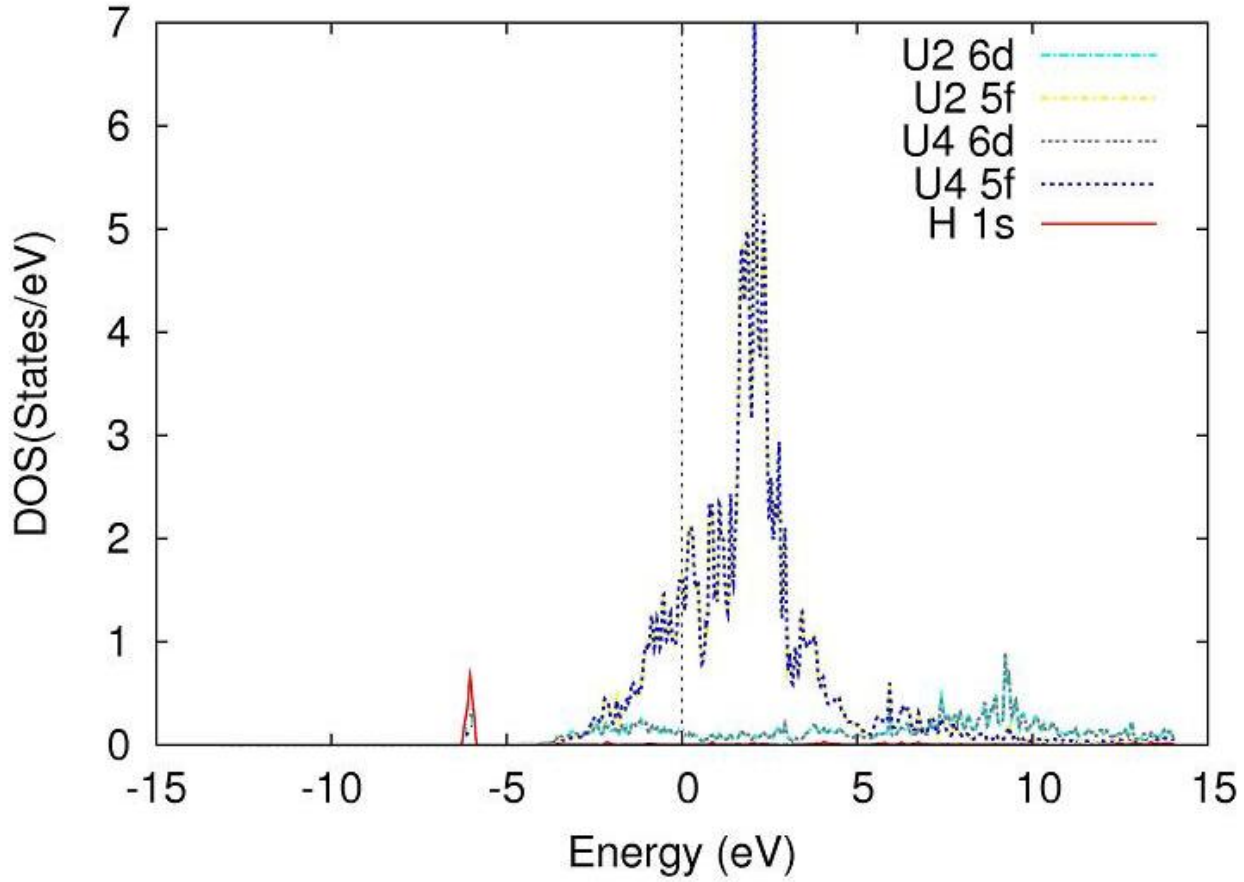

Figure 4.40 LDOS for H at the center interstitial site at the NM level of theory. U2 is the subsurface and U4 is the subcenter atom.

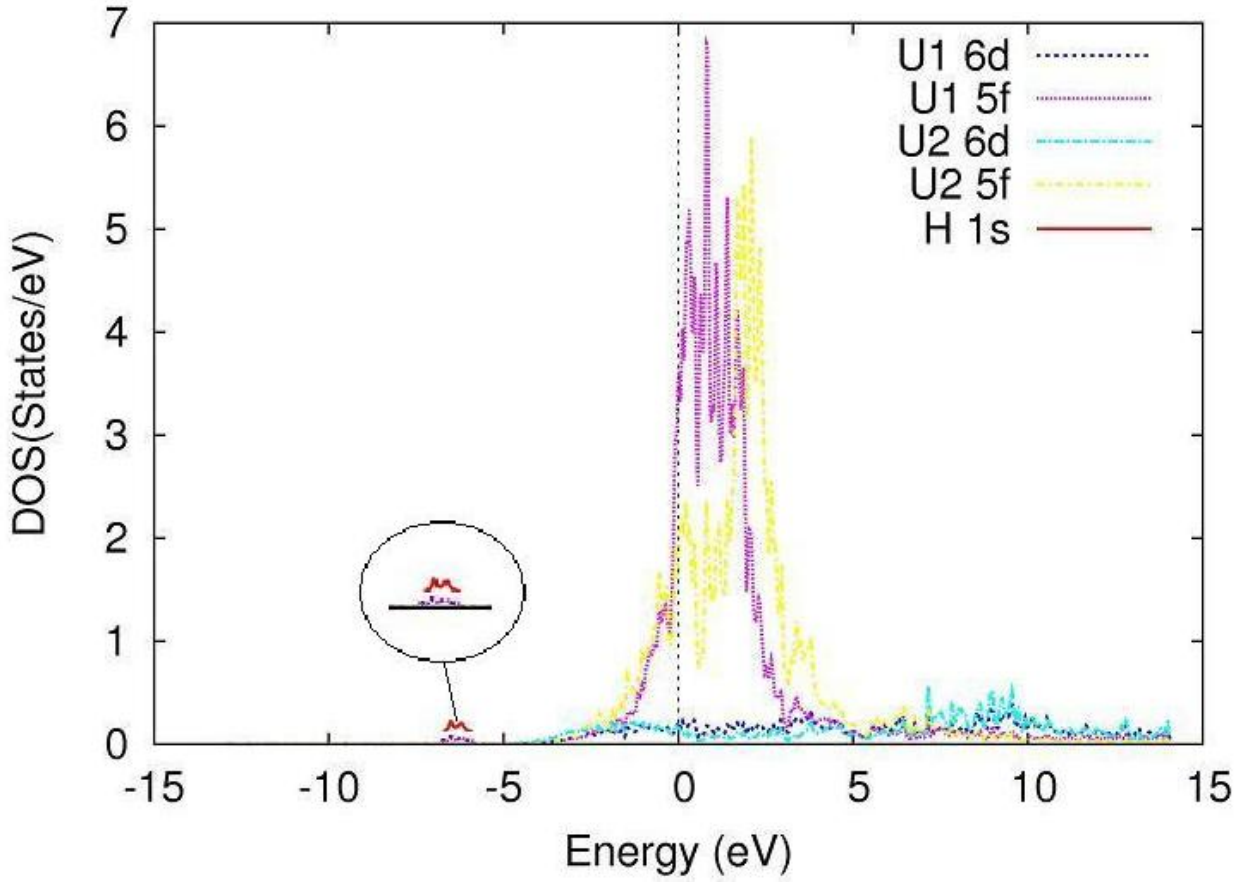

Figure 4.41 LDOS for H at the bridge interstitial site at the NM level of theory. U1 is the surface atom and U2 is the subsurface atom

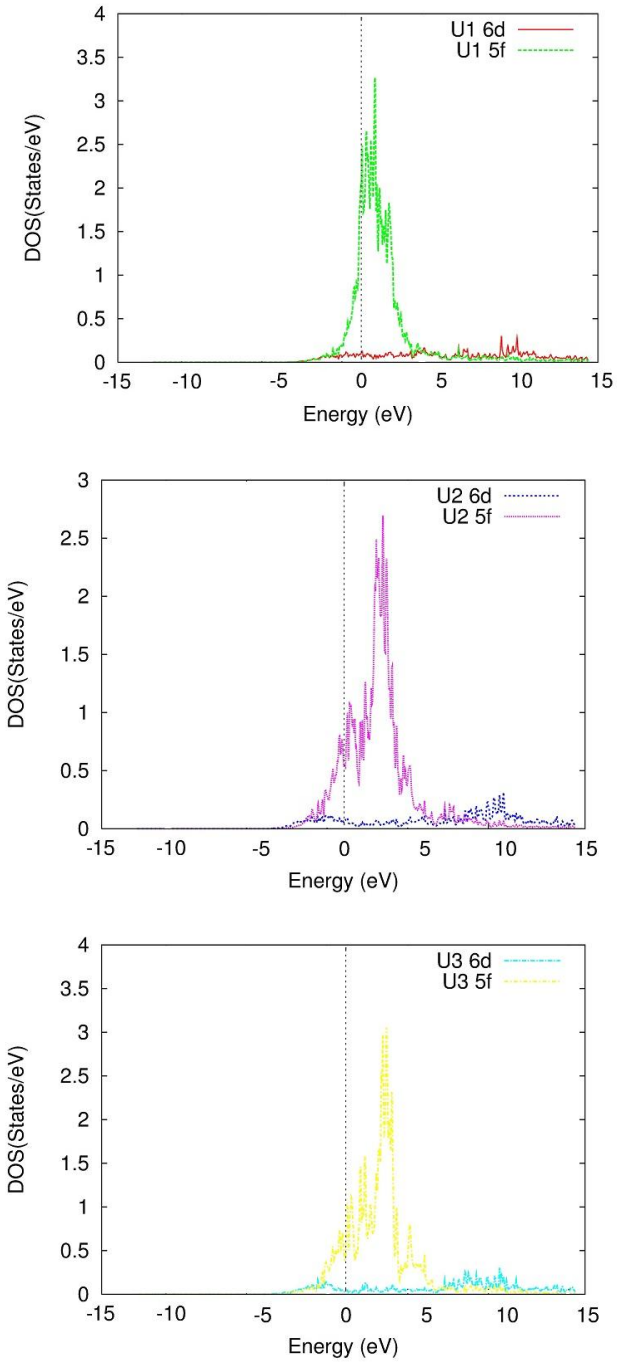

Figure 4.42 LDOS for the 6d and 5f electrons of the surface (U1) subsurface (U2) and center (U3) atoms of the bare γ-U (100) slab at the FM level of theory

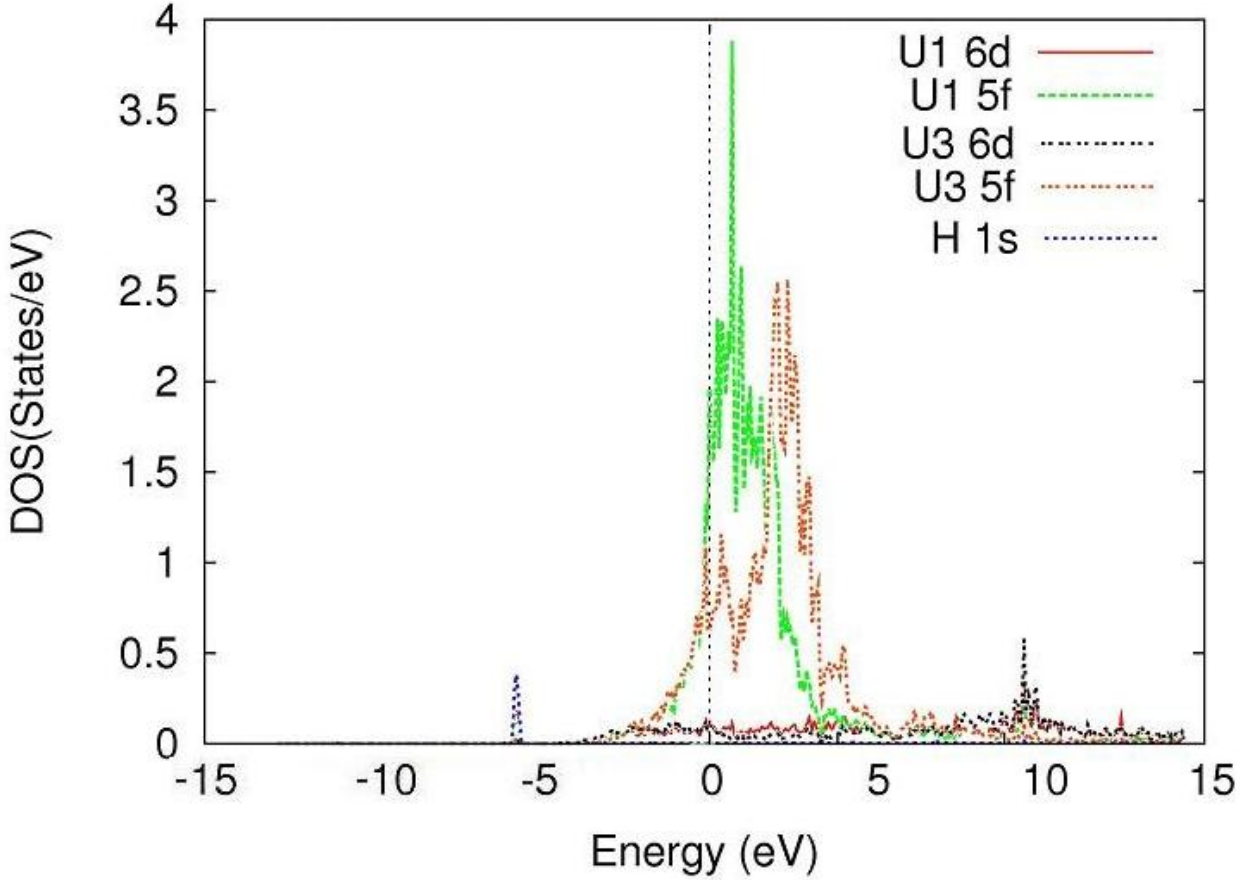

Figure 4.43 LDOS for H adsorption at the top interstitial site with the FM level of theory. U1 is the surface U atom and U3 is the center U atom of the slab.

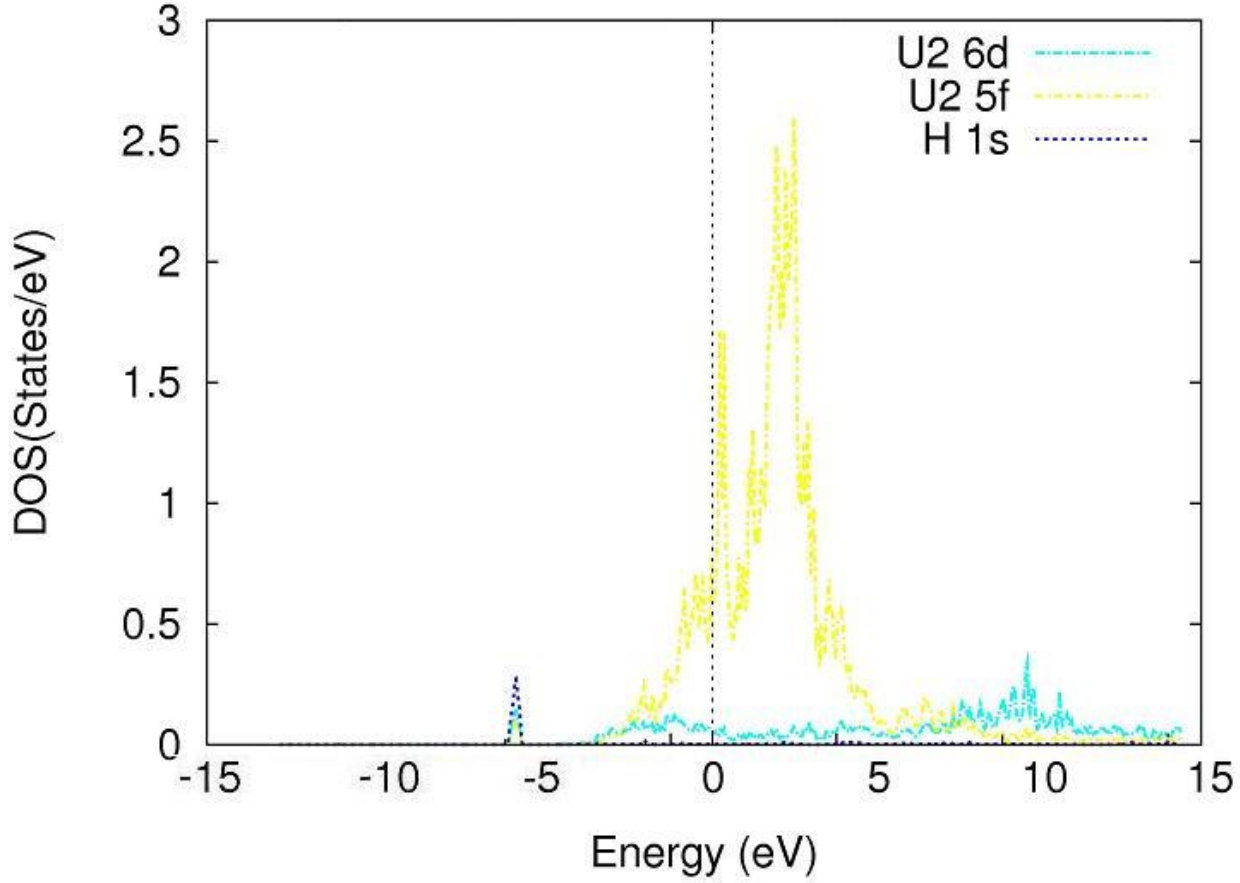

Figure 4.44 LDOS for H adsorption at the center interstitial site with the FM level of theory. U2 is the subsurface U of the slab.

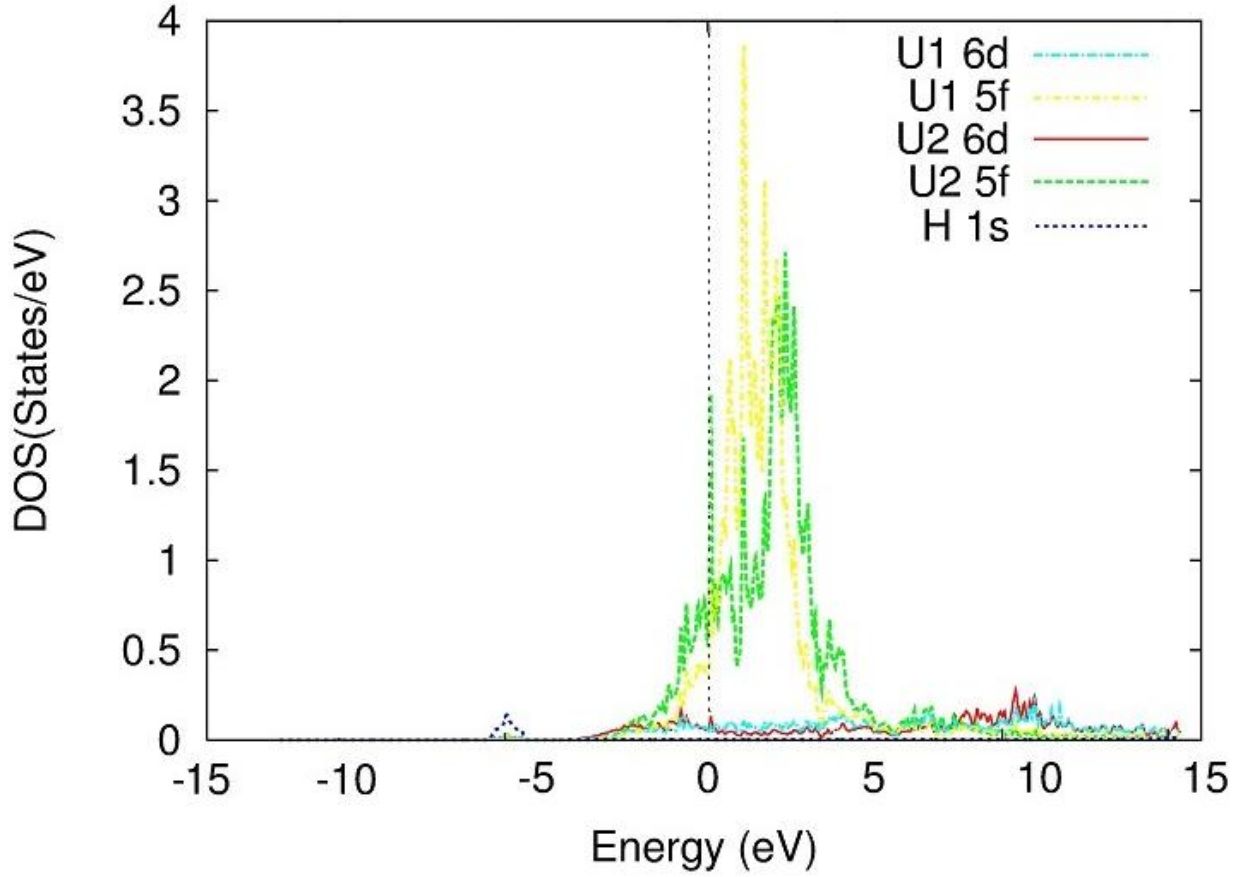

Figure 4.45 LDOS for H adsorption at the bridge interstitial site with the FM level of theory. U1 is the surface U atom and U2 is the subsurface U atom of the slab.

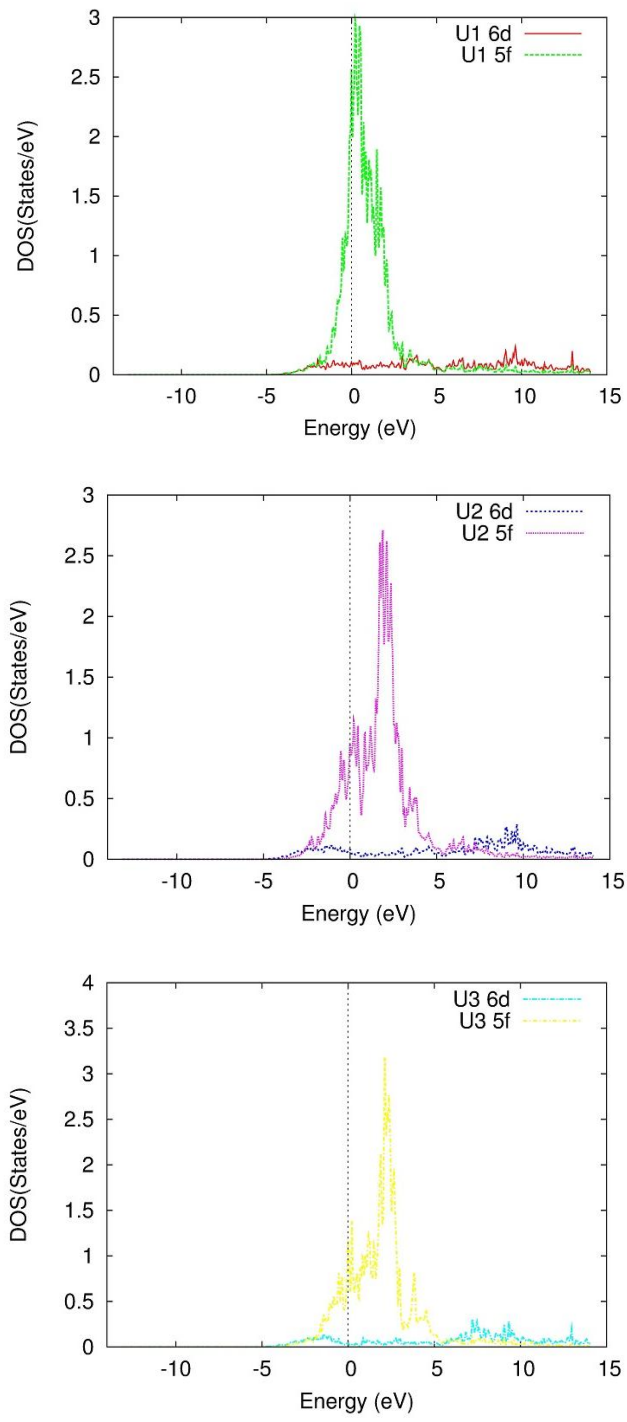

Figure 4.46 LDOS for the 6d and 5f electrons of the, surface (U1), subsurface (U2) and center (U3) atom of the bare γ-U (100) slab at the AFM level of theory

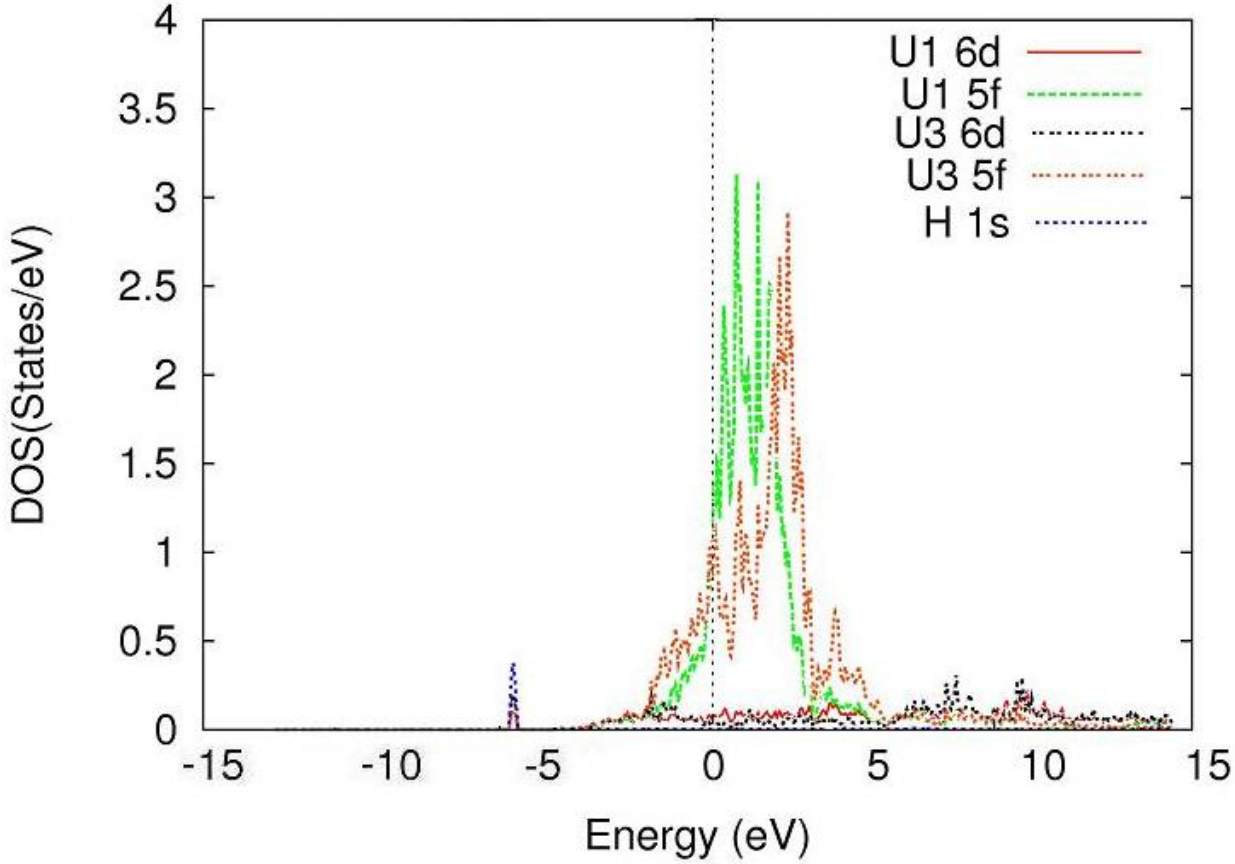

Figure 4.47 LDOS for H adsorption at the top interstitial site with the AFM level of theory. U1 is the surface U atom and U3 is the center U atom of the slab.

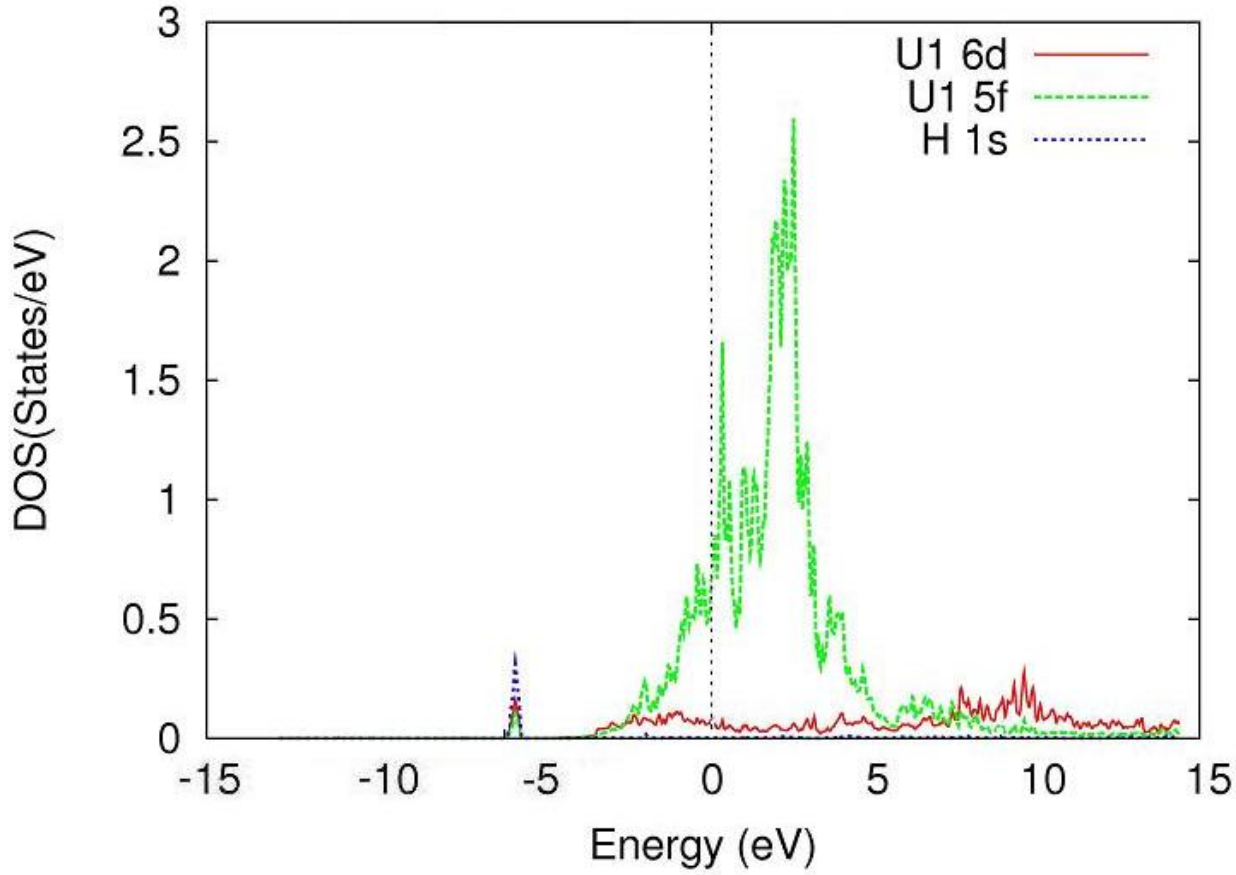

Figure 4.48 LDOS for H adsorption at the center interstitial site with the AFM level of theory. U2 is the subsurface U of the slab.

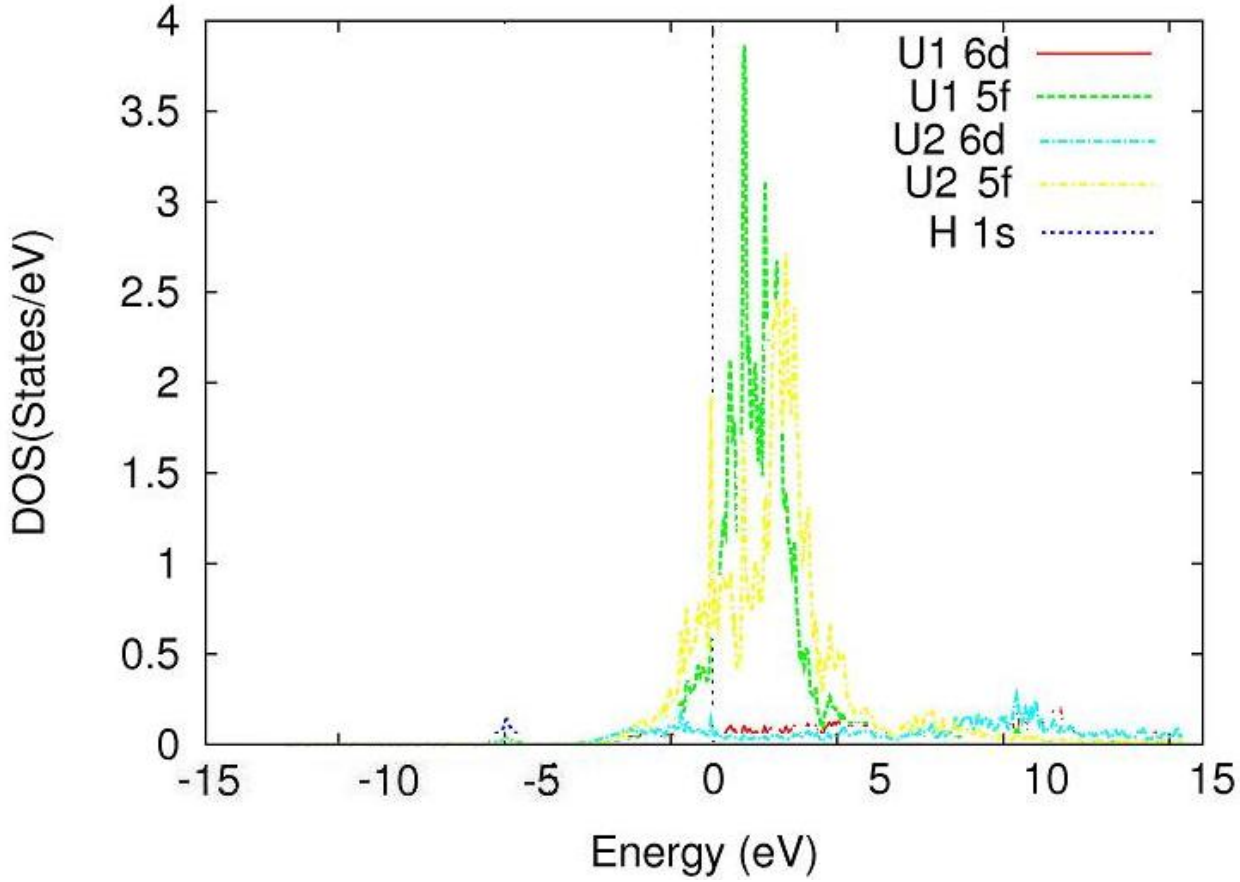

Figure 4.49 LDOS for H adsorption at the bridge interstitial site with the AFM level of theory. U1 is the surface U atom and U2 is the subsurface U atom of the slab.

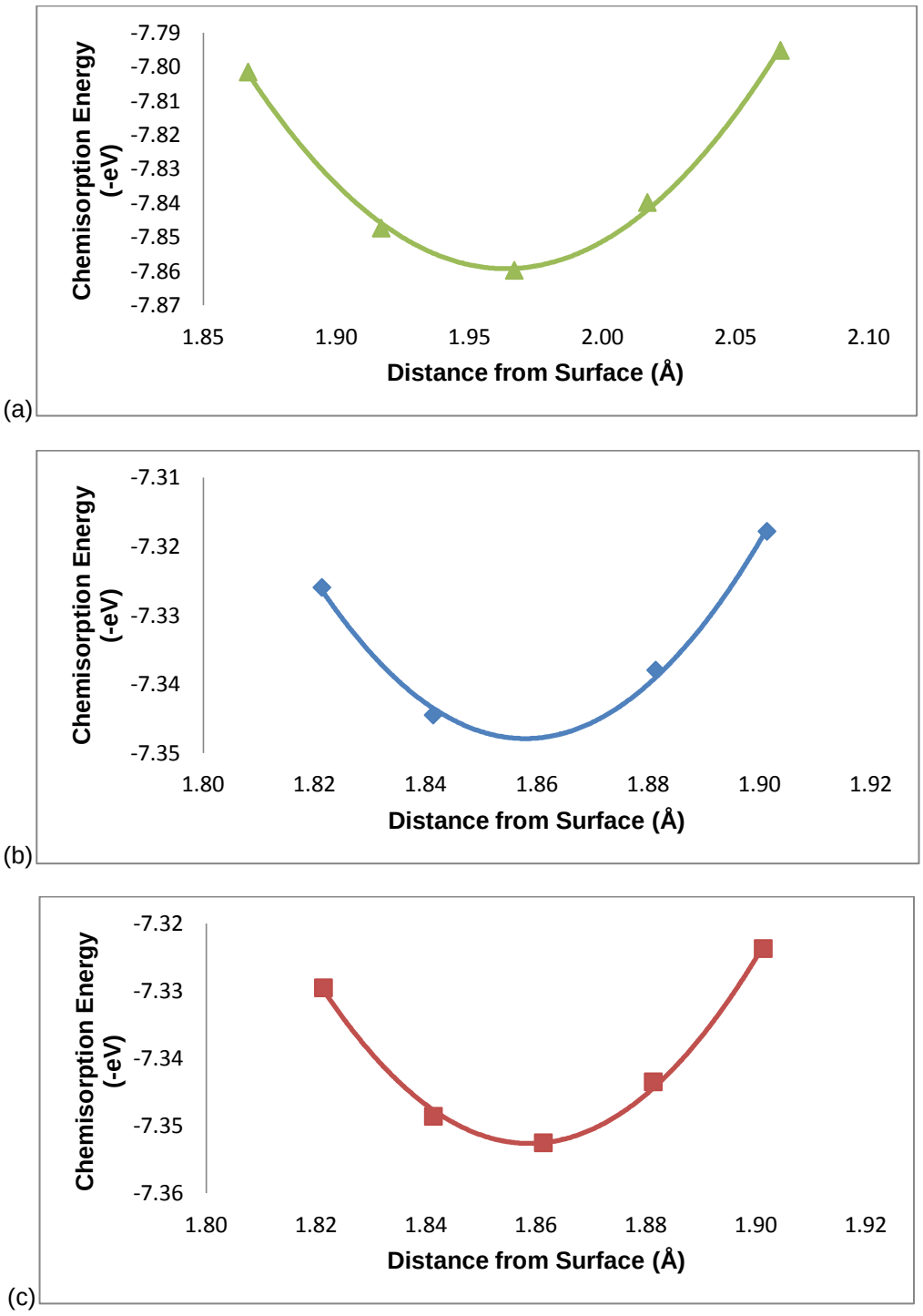

Figure 4.50 Optimized E_c of O atom at the top site at the NM (a), FM (b), and AFM (c) level

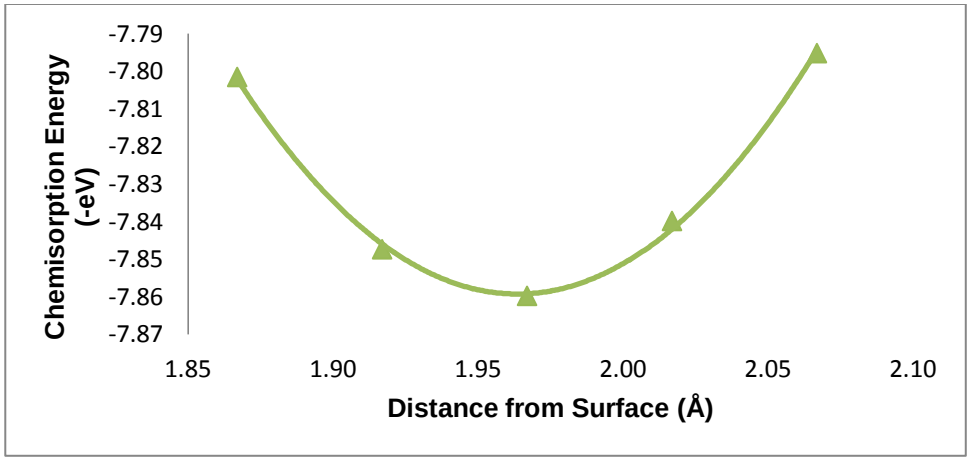

(a)

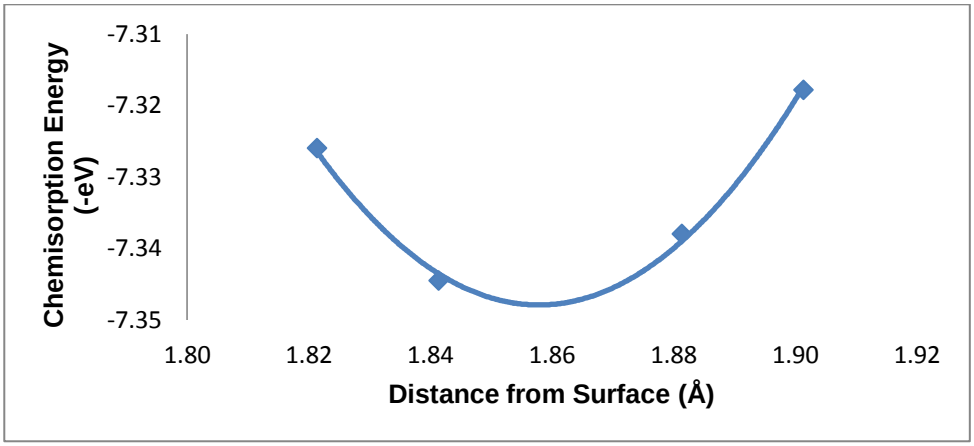

(b)

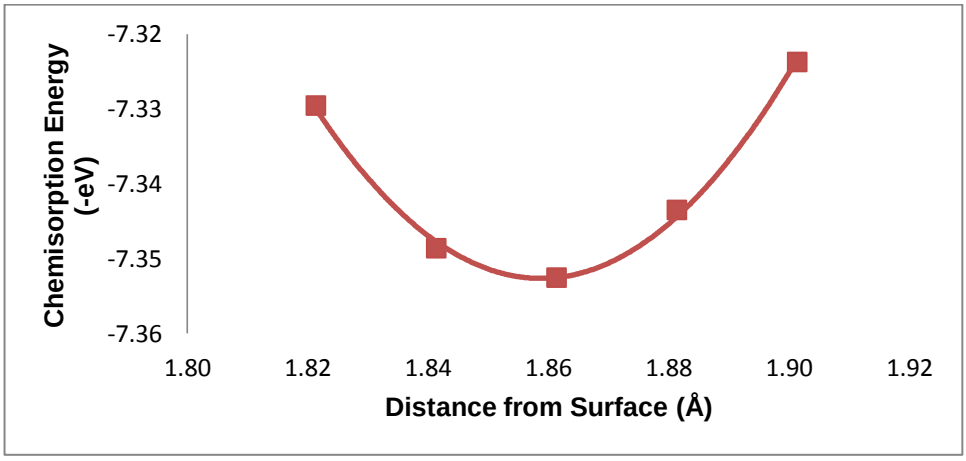

(c)

Figure 4.51 Optimized E_c of O atom at the center site at the NM (a), FM (b), and AFM (c) level

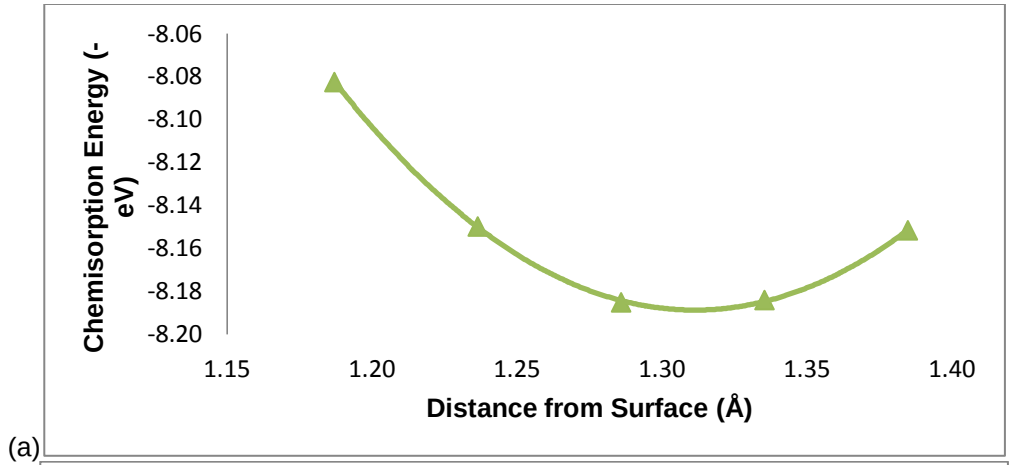

(a)

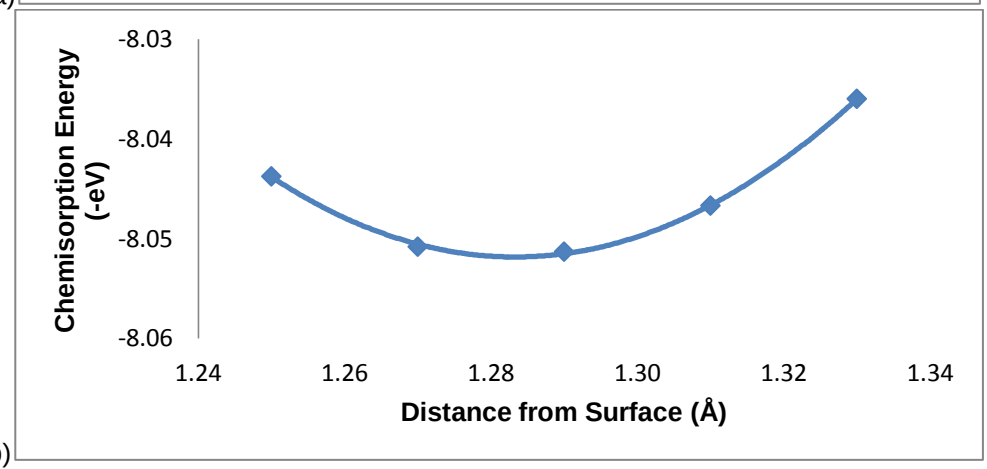

(b)

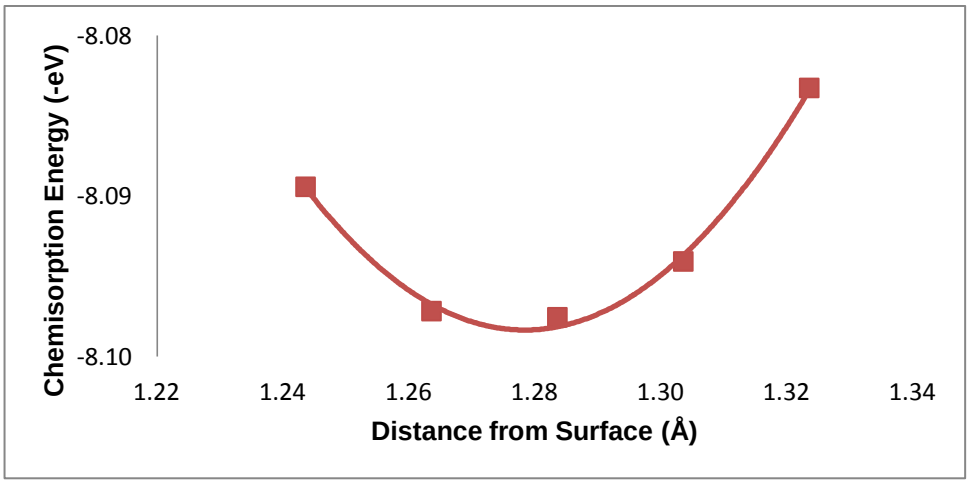

(c)

Figure 4.52 Optimized E_c of H atom at the bridge site at the NM (a), FM (b), and AFM (c) level

Table 4.16 Distances and chemisorption energies of the O atom on γ-U(100) at the NM, FM and AFM levels of theory

NM			NSOC	SOC	
Site	R (Å)	$d_{U\text{-}adatom}$ (Å)	E_c (eV)	E_c (eV)	ΔE_c (eV)
Top	1.98	1.98	7.23	7.86	0.63
Center	0.75	2.41	7.82	7.84	0.03
Bridge	1.32	2.14	8.19	8.43	0.24

FM			NSOC	SOC	
Site	R (Å)	$d_{U\text{-}adatom}$ (Å)	E_c (eV)	E_c (eV)	ΔE_c (eV)
Top	1.86	1.86	7.34	7.76	0.42
Center	0.75	2.42	7.81	7.80	-0.01
Bridge	1.28	2.11	8.05	8.26	0.21

AFM			NSOC	SOC	
Site	R (Å)	$d_{U\text{-}adatom}$ (Å)	E_c (eV)	E_c (eV)	ΔE_c (eV)
Top	1.86	1.86	7.35	7.80	0.44
Center	0.75	2.42	7.76	~7.77	~0.01
Bridge	1.28	2.11	8.10	~8.33	~0.23

sites, respectively, with SOC included. For the FM magnetic state, the chemisorption energy at the top site is 7.76 eV, at the center it is 7.80 eV and at the bridge it is 8.26 eV at the SOC level of theory. All calculations relevant to our previous study, at the NSOC level, are in good comparison. Spin-orbit interaction has the most affect when the O atom is in a position closest to the U atom, in this case at the top site. This was also true for the H-γ-U system, reinforcing the relation of the distance of the adatom from its nearest neighbor surface atom and the stability of the system with the addition of SOC. The distance between the adatom and the nearest neighbor U surface atom was 2.41 Å for the center site, 2.11 Å for the bridge site, and 1.86 Å for the top site and remained

consistent at each level of theory. Table 4.17 lists $\Delta\Phi$ as described by equation 4.4 and the μ_{dipole} described by equation 4.6 for the adsorption of the O atom on the surface with SOC added at the NM and FM level of theory. $\Delta\Phi$ for the top site, which has the closest nearest neighbor distance, is, as expected, higher than the other sites at 0.92 to 0.66 eV, for the NM and FM cases, respectively, followed by the bridge site, at 0.33 to 0.28 eV, and then the center site, 0.02 and 0.03 eV. Using the Helmholtz relation the adsorbate-induced dipole moment would be 4.18 and 2.99 D for the top site, 0.07 and 0.13 D for the center site and 1.48, and 1.27 D for the bridge site at the NM and FM levels of theory, respectively. These values are also listed in Table 4.17.

Table 4.17 $\Delta\Phi$ and surface dipole moment μ_{dipole} for the adsorption of the O atom at the NM and FM level of theory

Theory	Site	Δφ	μ_{dipole} (D)
NM	Top	0.92	4.18
	Center	0.02	0.07
	Bridge	0.33	1.48
FM	Top	0.66	2.99
	Center	0.03	0.13
	Bridge	0.28	1.27

Listed Table 4.18 for the FM magnetic configuration are the magnitude and alignment of the site projected spin magnetic moments, μ_S, and orbital magnetic moments, μ_L, inside the muffin tin sphere for each U atom on each atomic layer, as well as the net spin and orbital magnetic moment and the total magnetic moment, μ, per U atom at the SOC theoretical level. In these tables, layer 1 is the surface layer; layer 2 is the subsurface layer; layer 3 is the center layer; layer 4 is the subcenter layer; and layer 5 is the bottom layer. The moments of U atoms bonded to the O atom are printed in bold. Also, the spin, orbital and total magnetic moment for the bare is listed

at the top of each table for each level of theory. At the FM level of theory, for the one-fold top site, we note a reduction of 0.83 μ_B in the spin moment and an increase of 0.59 μ_B in the orbital moment of the U atom bonded to the adatom, The moments for the other atoms do not exhibit a change it spin or orbital magnetic moments compared to the clean metal. The entire slab sees a reduction in total moment of 0.18 μ_B for this adsorption site. While the O atom is bound to the center site, the second layer of the γ-U slab sees a change in orbital and spin magnetic moment but the U atom bound to the O atom shows no change. The overall change in total magnetic moment is -0.05 μ_B . For the twofold bridge site, we see a decrease of about 0.75 μ_B in the spin moment and an increase of 0.5 μ_B of the U atoms interacting with the O atom. The change in total moment for the slab is -0.55n μ_B compared to the bare slab. For the AFM case, the O atom bound at the top site induces a total magnetic moment of 0.36 μ_B on the AFM slab where the spin magnetic moment of the surface atom bound to the O atom increases by 0.82 μ_B and the orbital magnetic moment reduces by 0.60 μ_B .

Listed in Table 4.19 and Table 4.20 is partial charges inside the muffin-tin spheres before adsorption, Q_B, and after adsorption, Q_A, stated for the NM, FM and AFM magnetic configuration at the SOC level of theory and, for the surface, are taken from atoms closest to the adatom. In addition, we calculated and listed the difference in partial charge, ΔQ, before and after adsorption to facilitate the discussion on charge transfer between the γ-U surface and the adatom. After adsorption, the O atom gains charge inside the muffin-tin sphere for the all sites at all levels of theory. For the NM case, the partial charges inside the atomic spheres of the top and bottom layer atoms decreases the 5*f* orbitals, but the subsurface, center and subcenter atoms gain charge in these channels for the top and bridge adsorption sites. The same is also true for the center site except the subsurface layer atom do not show any change in charge for either the 6*d* or 5*f* orbitals. For the FM case, the center and bridge sites see a decrease in the partial charge of the 5*f* orbitals of the surface and subsurface atoms. For the bridge site, it seems the charge is given to the 2*p* orbital of the O atom but in the center site the bottom slab gains charge in the 5*f*

Table 4.18 Spin and orbital magnetic moment for surface adsorption of the O atom at FM level of theory

FM		Layer												
O		1		2		3		4		5		total		total μ
Site	Atom	μ_S	μ_L	μ_S	μ_L	μ_S	μ_L	μ_S	μ_L	μ_S	μ_L	μ_S	μ_L	
bare	1	0.95	-0.64	0.08	-0.02	-0.08	0.01	0.08	-0.02	0.94	-0.64			
	2	0.95	-0.64	0.08	-0.02	-0.08	0.01	0.08	-0.02	0.94	-0.64			
	3	0.95	-0.64	0.08	-0.02	-0.08	0.01	0.08	-0.02	0.94	-0.64			
	4	0.95	-0.64	0.08	-0.02	-0.08	0.01	0.08	-0.02	0.94	-0.64	7.89	-5.21	2.68
Top	1	0.96	-0.63	0.05	-0.01	-0.08	0.02	0.11	-0.02	0.97	-0.65			
	2	0.96	-0.64	0.05	-0.01	-0.05	0.01	0.11	-0.02	0.96	-0.64			
	3	0.85	-0.64	0.05	-0.01	-0.05	0.01	0.11	-0.02	0.96	-0.64			
	4	**0.11**	**-0.05**	0.05	-0.01	-0.01	-0.01	0.11	-0.02	0.95	-0.64	7.16	-4.66	2.50
Center	1	0.93	-0.68	**0.08**	**-0.02**	-0.08	0.02	0.11	-0.03	0.95	-0.64			
	2	0.93	-0.68	0.06	0.00	-0.08	0.02	0.07	-0.02	0.95	-0.64			
	3	0.93	-0.68	0.06	0.00	-0.08	0.02	0.07	-0.02	0.95	-0.64			
	4	0.93	-0.68	0.22	-0.08	-0.08	0.02	0.08	-0.02	0.95	-0.64	7.99	-5.37	2.63
Bridge	1	0.90	-0.64	0.02	0.00	-0.08	0.02	0.10	-0.02	0.95	-0.64			
	2	**0.19**	**-0.14**	0.02	0.00	-0.02	0.00	0.10	-0.02	0.94	-0.63			
	3	0.90	-0.64	0.04	-0.01	-0.08	0.02	0.10	-0.03	0.95	-0.64			
	4	**0.19**	**-0.14**	0.04	-0.01	-0.02	0.00	0.10	-0.03	0.94	-0.63	6.30	-4.17	2.13

Table 4.19 Partial charges inside muffin-tin spheres for O at the top, center and bridge sites with SOC for the NM magnetic configuration

		Q_B			Q_A			$\Delta Q=Q_A-Q_B$		
Site	Atom/Layer	O *p*	U *d*	U *f*	O *p*	U *d*	U *f*	O *p*	U *d*	U *f*
Top	Oxygen	2.054			2.244			0.190		
	U surface layer		10.422	1.985		10.455	1.902		0.034	-0.083
	U subsurface layer		10.545	1.948		10.550	1.974		0.006	0.027
	U middle layer		10.534	1.942		10.540	1.968		0.005	0.027
	U submiddle layer		10.545	1.948		10.553	1.972		0.008	0.024
	U bottom layer		10.422	1.984		10.432	1.813		0.011	-0.171
Center	Oxygen	2.054			2.277			0.223		
	U surface layer		10.422	1.985		10.420	1.829		-0.002	-0.155
	U subsurface layer		10.545	1.948		10.546	1.947		0.001	-0.001
	U middle layer		10.534	1.942		10.537	1.963		0.002	0.021
	U submiddle layer		10.545	1.948		10.554	1.977		0.009	0.029
	U bottom layer		10.422	1.984		10.434	1.817		0.012	-0.168
Bridge	Oxygen	2.054			2.287			0.233		
	U surface layer		10.422	1.985		10.426	1.855		0.004	-0.130
	U subsurface layer		10.545	1.948		10.556	1.967		0.011	0.019
	U middle layer		10.534	1.942		10.538	1.959		0.004	0.017
	U submiddle layer		10.545	1.948		10.553	1.970		0.008	0.022
	U bottom layer		10.422	1.984		10.433	1.813		0.011	-0.171

Table 4.20 Partial charges inside muffin-tin spheres for O at the top, center and bridge sites with SOC for the FM magnetic configuration

		Q_B			Q_A			$\Delta Q=Q_A-Q_B$		
Site	Atom/Layer	O *p*	U *d*	U *f*	O *p*	U *d*	U *f*	O *p*	U *d*	U *f*
Top	Oxygen	2.054			2.276			0.222		
	U surface layer		10.421	2.009		10.481	1.966		0.060	-0.043
	U subsurface layer		10.546	1.958		10.543	1.969		-0.003	0.010
	U middle layer		10.536	1.952		10.538	1.955		0.002	0.003
	U submiddle layer		10.546	1.959		10.546	1.955		0.000	-0.004
	U bottom layer		10.421	2.011		10.420	1.997		-0.001	-0.014
Center	Oxygen	2.054			2.263			0.209		
	U surface layer		10.421	2.009		10.401	1.903		-0.020	-0.106
	U subsurface layer		10.546	1.958		10.535	1.903		-0.011	-0.056
	U middle layer		10.536	1.952		10.535	1.953		-0.001	0.001
	U submiddle layer		10.546	1.959		10.548	2.013		0.002	0.054
	U bottom layer		10.421	2.011		10.427	2.137		0.006	0.126
Bridge	Oxygen	2.054			2.290			0.236		
	U surface layer		10.421	2.009		10.419	1.972		-0.002	-0.037
	U subsurface layer		10.546	1.958		10.549	1.954		0.003	-0.004
	U middle layer		10.536	1.952		10.537	1.953		0.001	0.001
	U submiddle layer		10.546	1.959		10.547	1.961		0.001	0.002
	U bottom layer		10.421	2.011		10.422	2.016		0.001	0.005

channel. For the top site, the partial charge for the 5*f* band decreases but the 6*d* band gains electrons.

The Δn plots for the surface adsorption of the O atom with the 5 layer slab at the NM magnetic configuration is displayed in Figure 4.53, Figure 4.54, and Figure 4.55 for the top, center and bridge sites, respectively. These plots correspond with the partial charge inside the muffin-tin sphere perfectly. It can be seen that the outer shell of the U surface atom is losing electrons while the O atom and the inner shells of the U atom are gaining electrons at each adsorption site. Figure 4.56, Figure 4.57, and Figure 4.58 are the Δn plots at the FM level of theory. For the top and bridge site the inner shell of the surface U atom look to be gaining electrons, while the outer shell is losing charge. For the center site the surface U atom is losing charge from both the d and f bands. The O atom is gaining charge at each site. From this we can see that the bond between the U surface and O atom are more ionic with distance from the surface.

In Figure 4.59, the Gaussian-broadened (with a width of 0.003 eV) *f* and *d* LDOS curves for the surface and subsurface layers of the clean γ-U (100) metal slab are shown at the NM level of theory. As with the other analysis of this paper, only the LDOS of the adatoms and the U atoms interacting with the adatoms are considered. In Figure 4.60 we show the LDOS plots for the H adatom and the surface U atom to which it is bonded in the top site. We note that the 5*f* DOS of the U atom on which the adatom sits is modified with a delocalization at the Fermi level in comparison to the surface layer LDOS for the clean U slab. We also observe complete 6*d*, 5*f* and O 2*p* overlaps at approximately -4 eV below the Fermi level indicating 6*d* and 5*f* participation in bonding. At the center site, shown in Figure 4.61, the O atom interacts with the subsurface layer and modifies the distribution of the 5*f* electrons of the subsurface atom with a decrease in the peak at the Fermi level. As with the top site adsorption of the O atom an overlap of 6d, 5f and 2p orbitals can be seen but at -5.5 eV below the Fermi level and the 2p peak has become broad. The LDOS distribution for the bridge site, Figure 4.62, is similar to that of the center site except

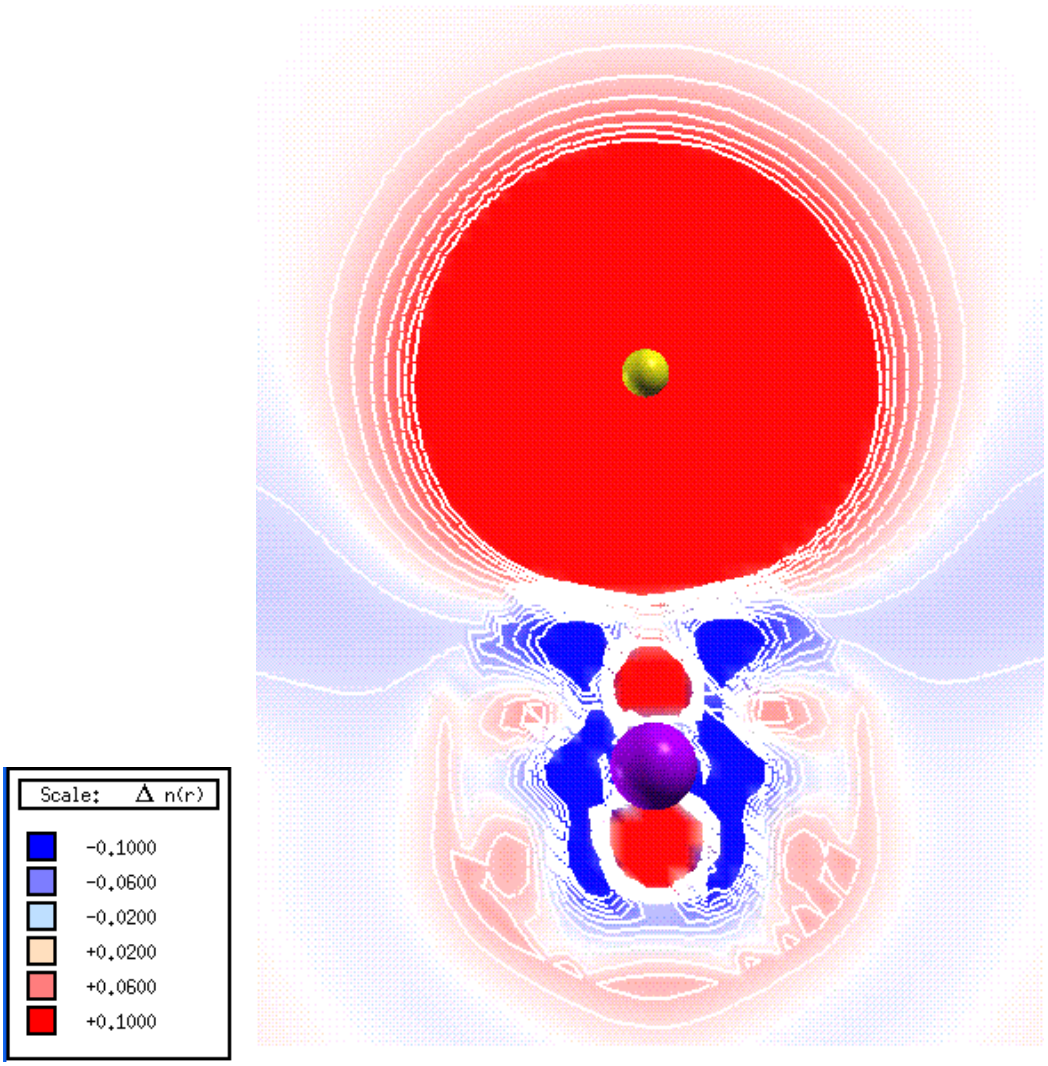

Figure 4.53 Change in charge density for the O atom at the NM top site

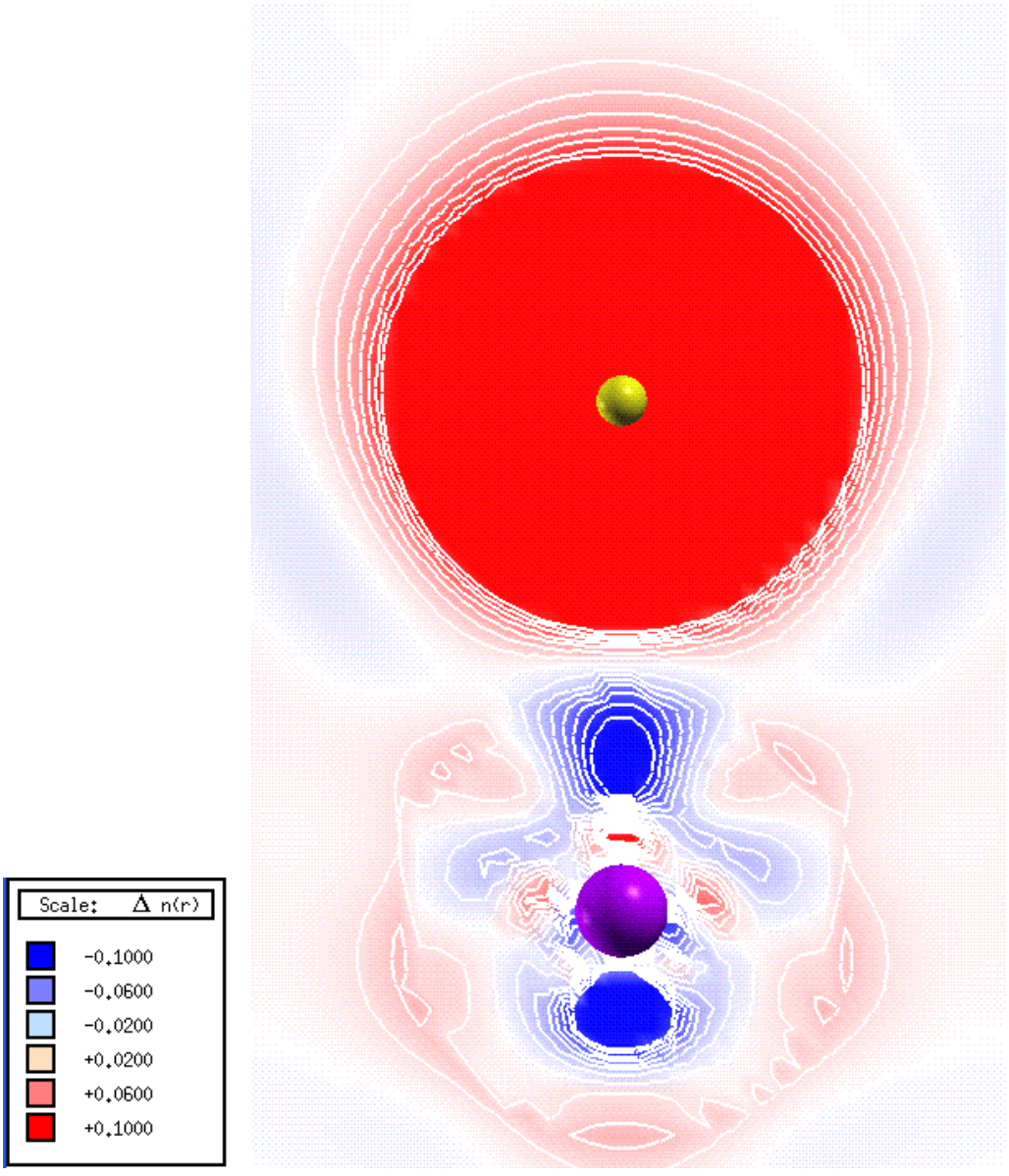

Figure 4.54 Change in charge density for the O atom at the NM center site

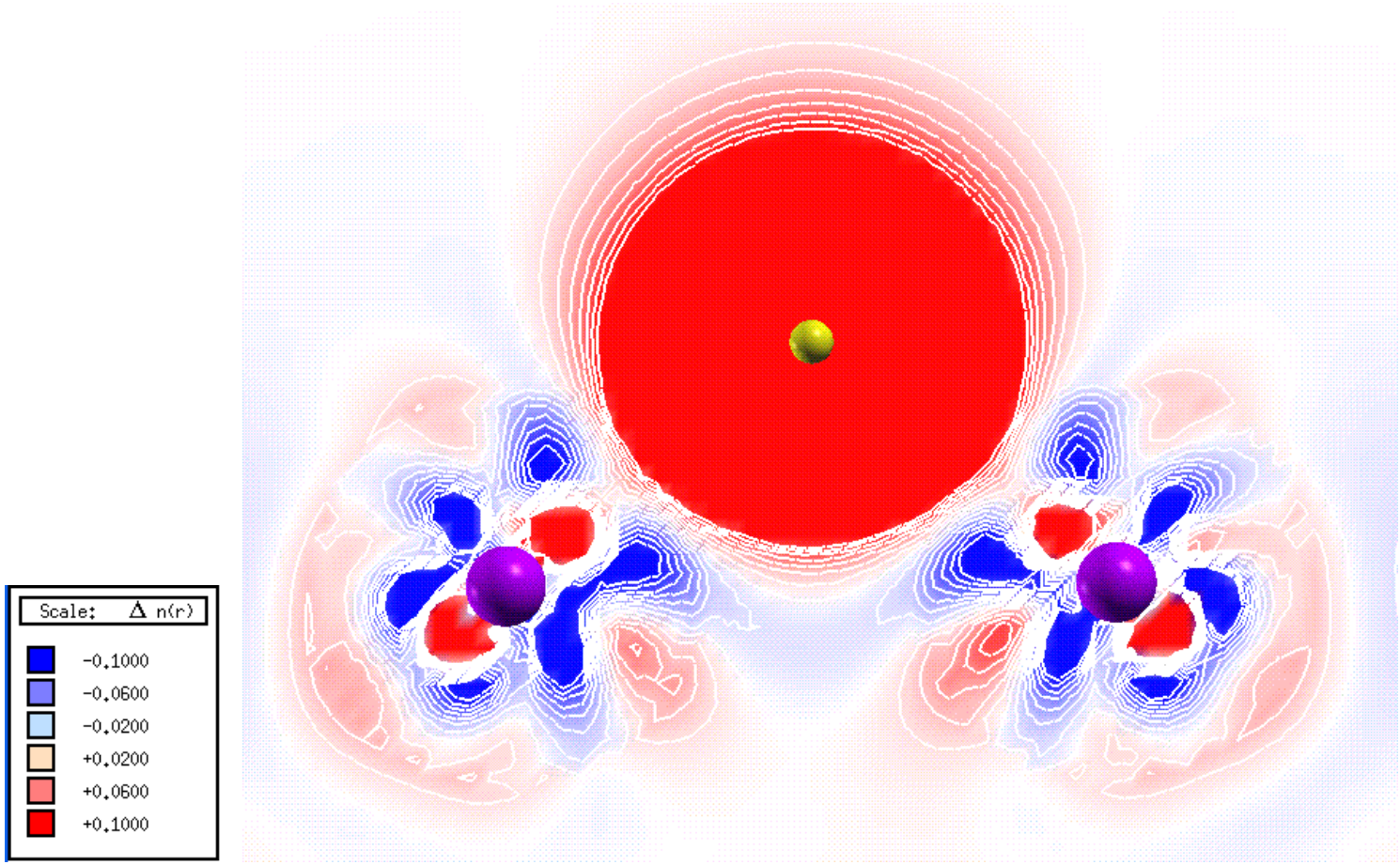

Figure 4.55 Change in charge density for the O atom at the NM bridge site

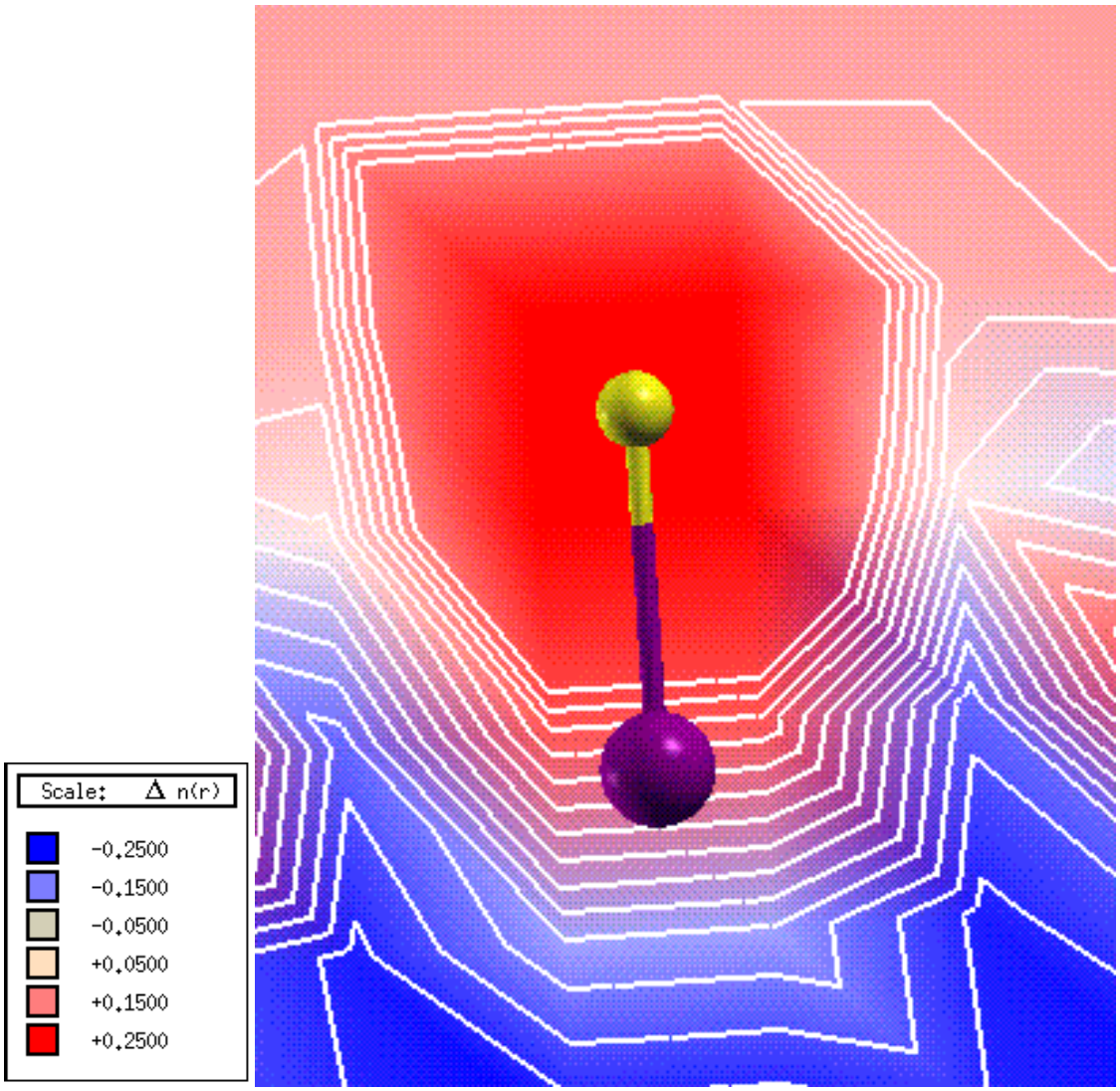

Figure 4.56 Change in charge density for th O atom at the FM top site

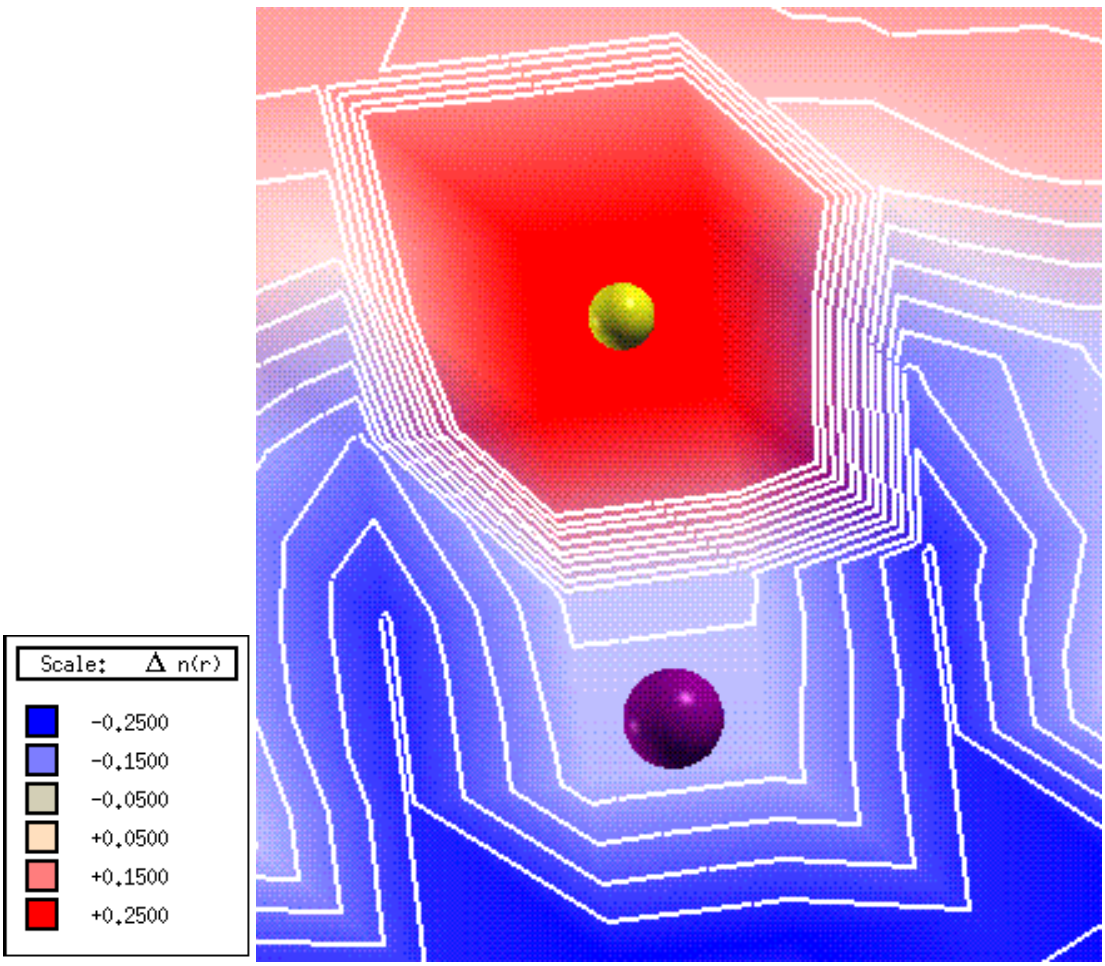

Figure 4.57 Change in charge density for the O atom at the FM center site

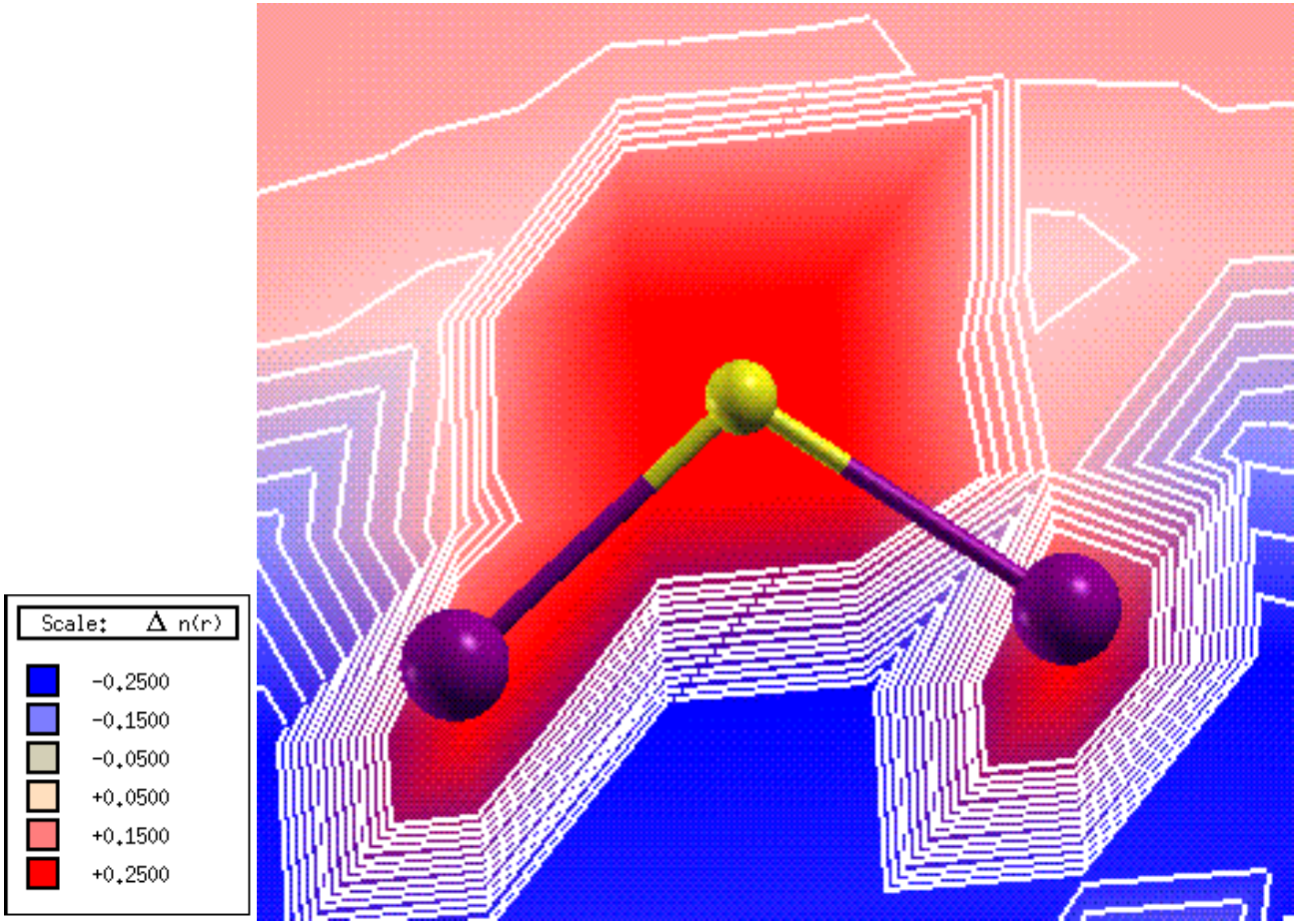

Figure 4.58 Change in charge density for the O atom at the FM bridge site

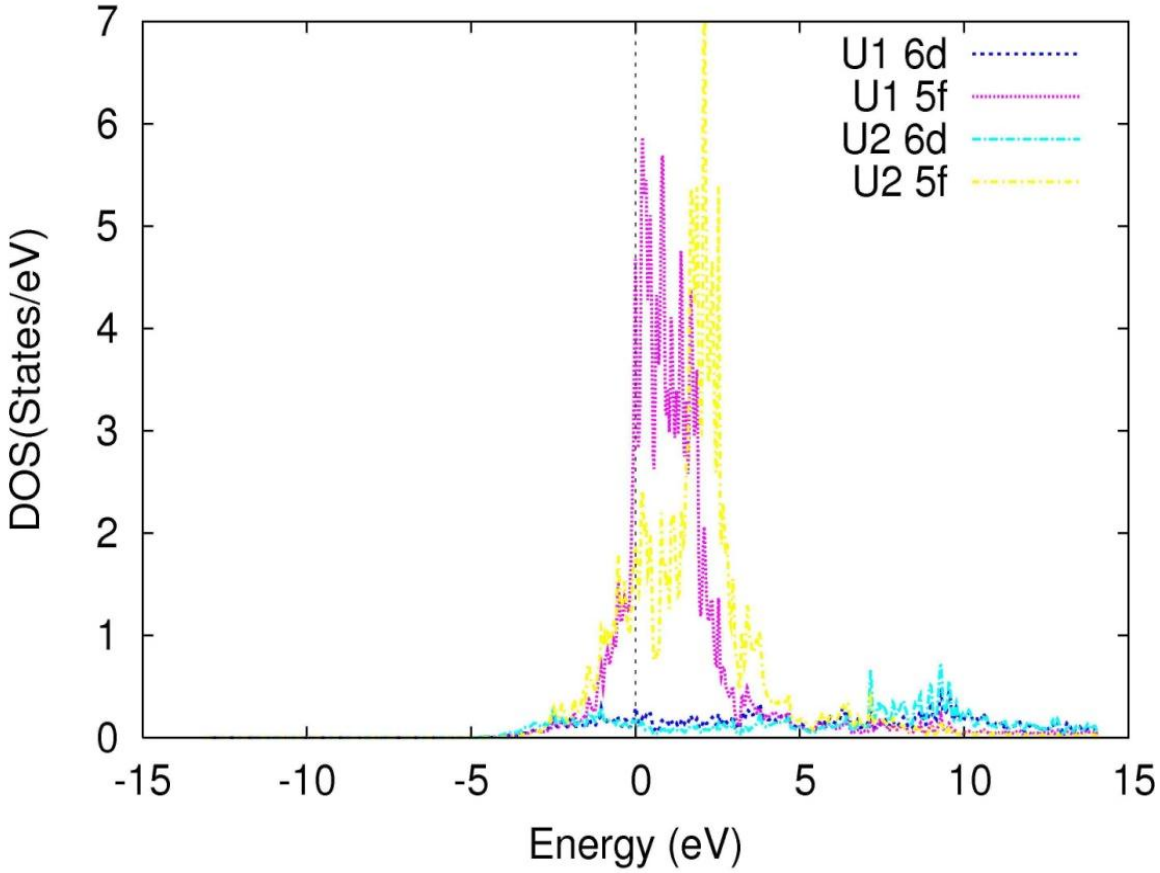

Figure 4.59 LDOS for the 6*d* and 5*f* electrons of the surface (U1) and subsurface (U2) atoms of the bare γ-U (100) slab at the NM level of theory

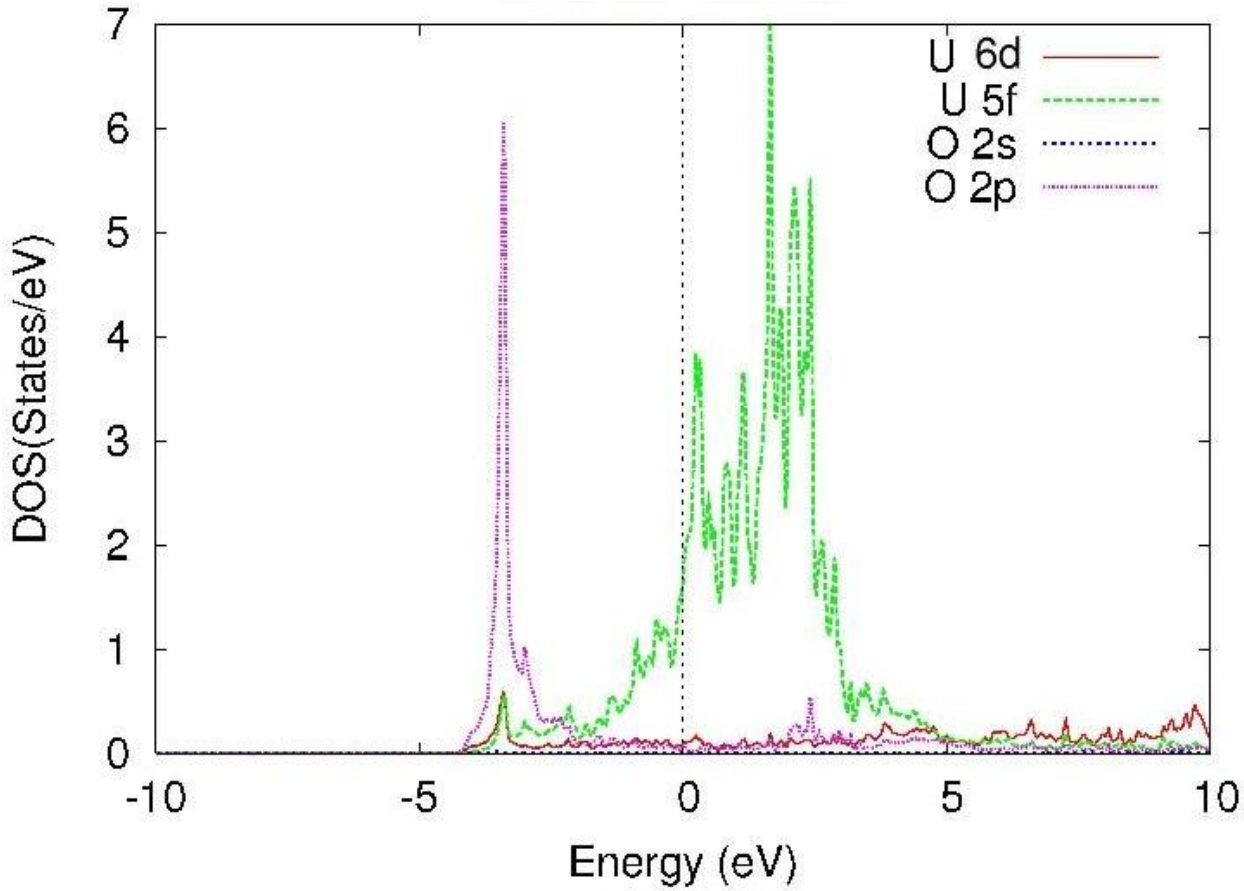

Figure 4.60 LDOS for O adsorption at the top site with the NM level of theory

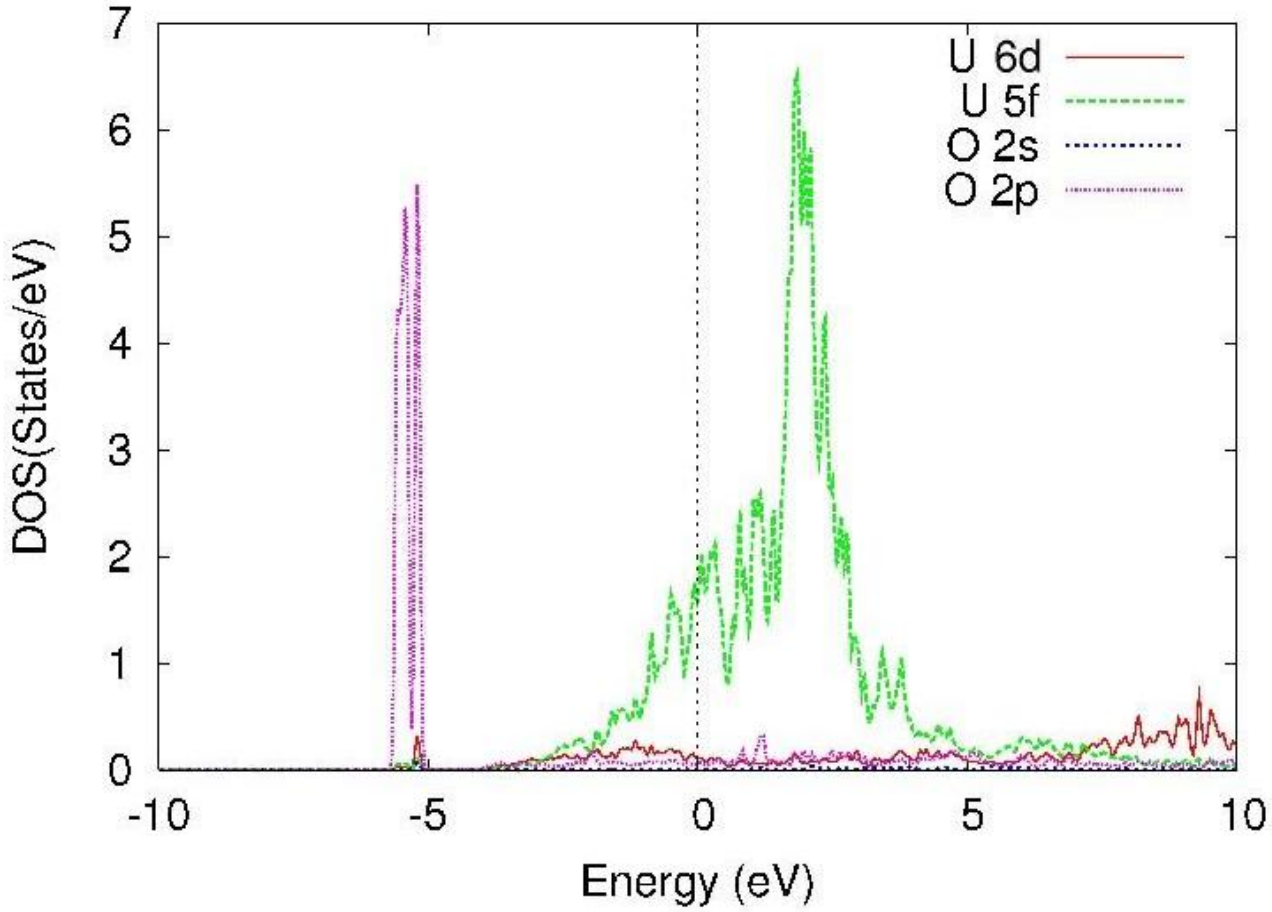

Figure 4.61 LDOS for O adsorption at the center site with the NM level of theory

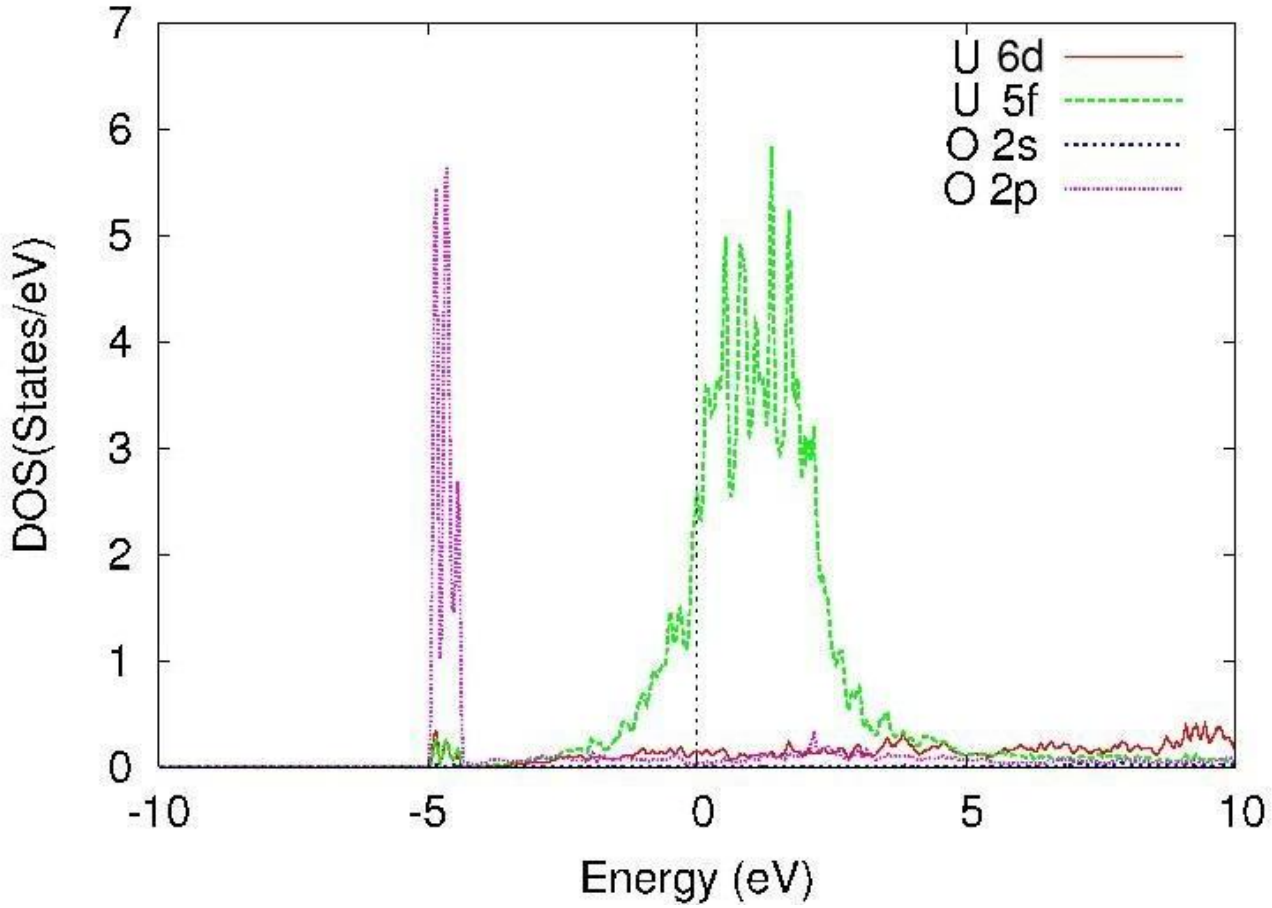

Figure 4.62 LDOS for O adsorption at the bridge site with the NM level of theory

that the 5f electrons have a higher distribution at the point where the orbitals overlap and the 5f distribution at the Fermi level is decreased. The FM level of theory LDOS plot is drawn in Figure 4.63 for the surface (U1) and subsurface (U2) of clean γ-U (100) metal slab, using the same parameters as for the NM case. Again, the intensities of the electron distributions for the FM case are half that of the NM LDOS plots, as explained previously in this work. The top site adsorption of the H atom is shown in Figure 4.64 and looks very similar to the NM case except for an increase of the 5f and 6d electron distribution hybridizing with the O 2p orbitals. Also, a decrease in the 5f population compared with the bare slab is found at the Fermi level. Figure 4.65 and Figure 4.66 show the LDOS for the adsorption of the O atom at the center and bridge sites. Compared to the NM calculation there is no real change for the spin-polarized case. Distinct 6d-5f-2p hybridization can be seen around -5 eV below the Fermi level with a slight decrease in the 5f population at the Fermi level indicating 5f participation in bonding.

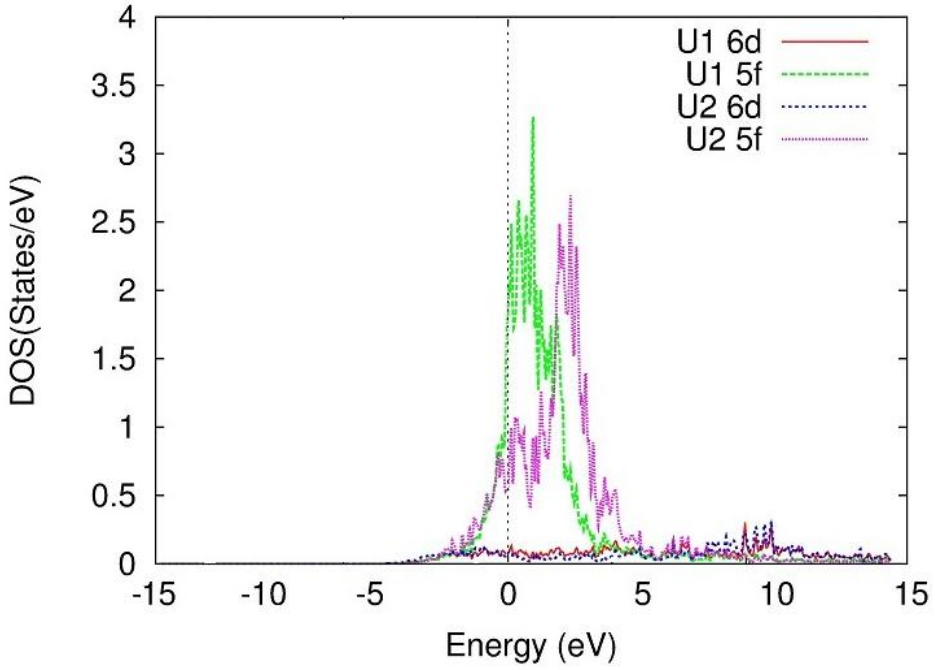

Figure 4.63 LDOS for the 6d and 5f electrons of the surface (U1) and subsurface (U2) atoms of the bare γ-U (100) slab at the FM level of theory

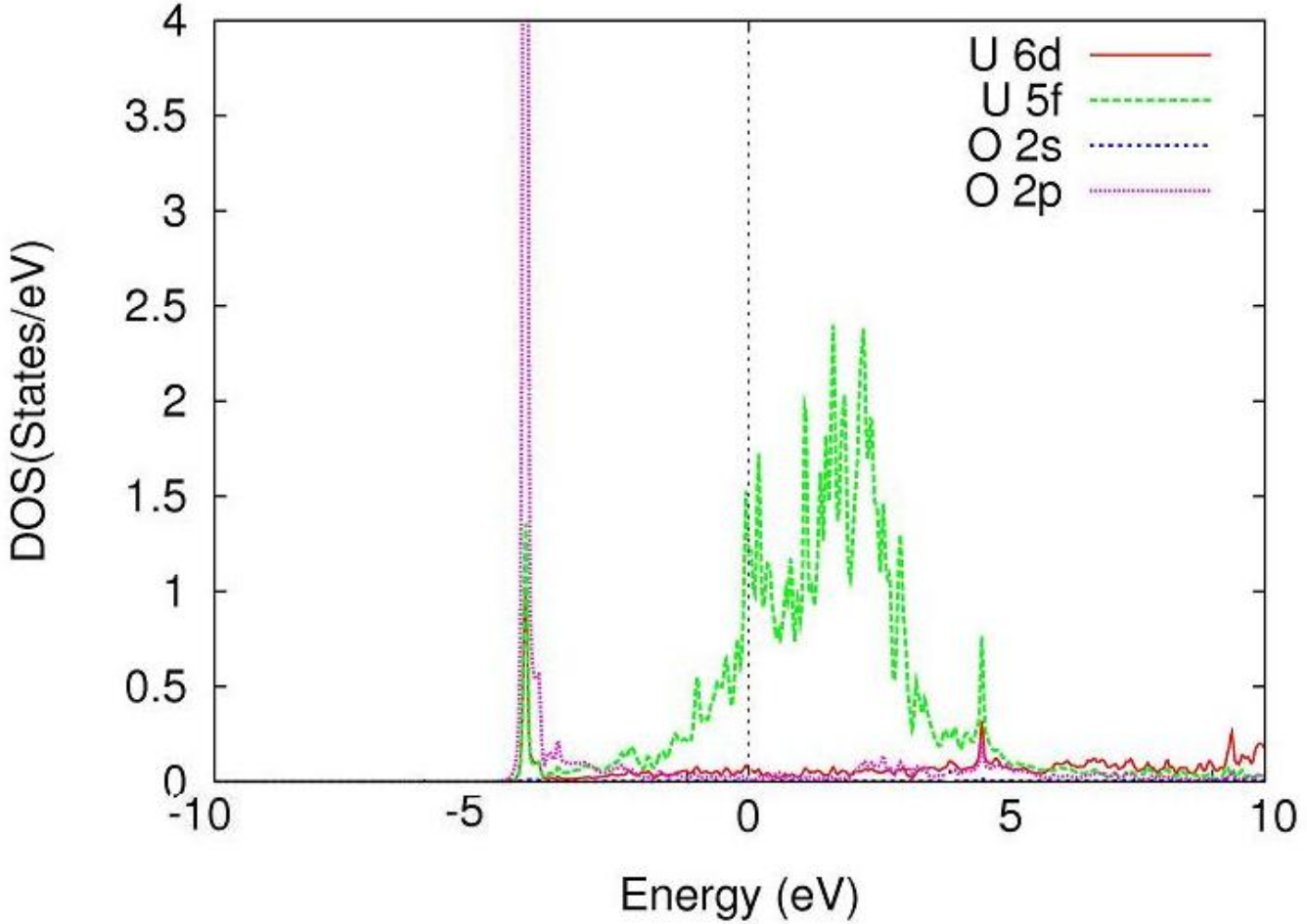

Figure 4.64 LDOS for O adsorption at the top site with the FM level of theory

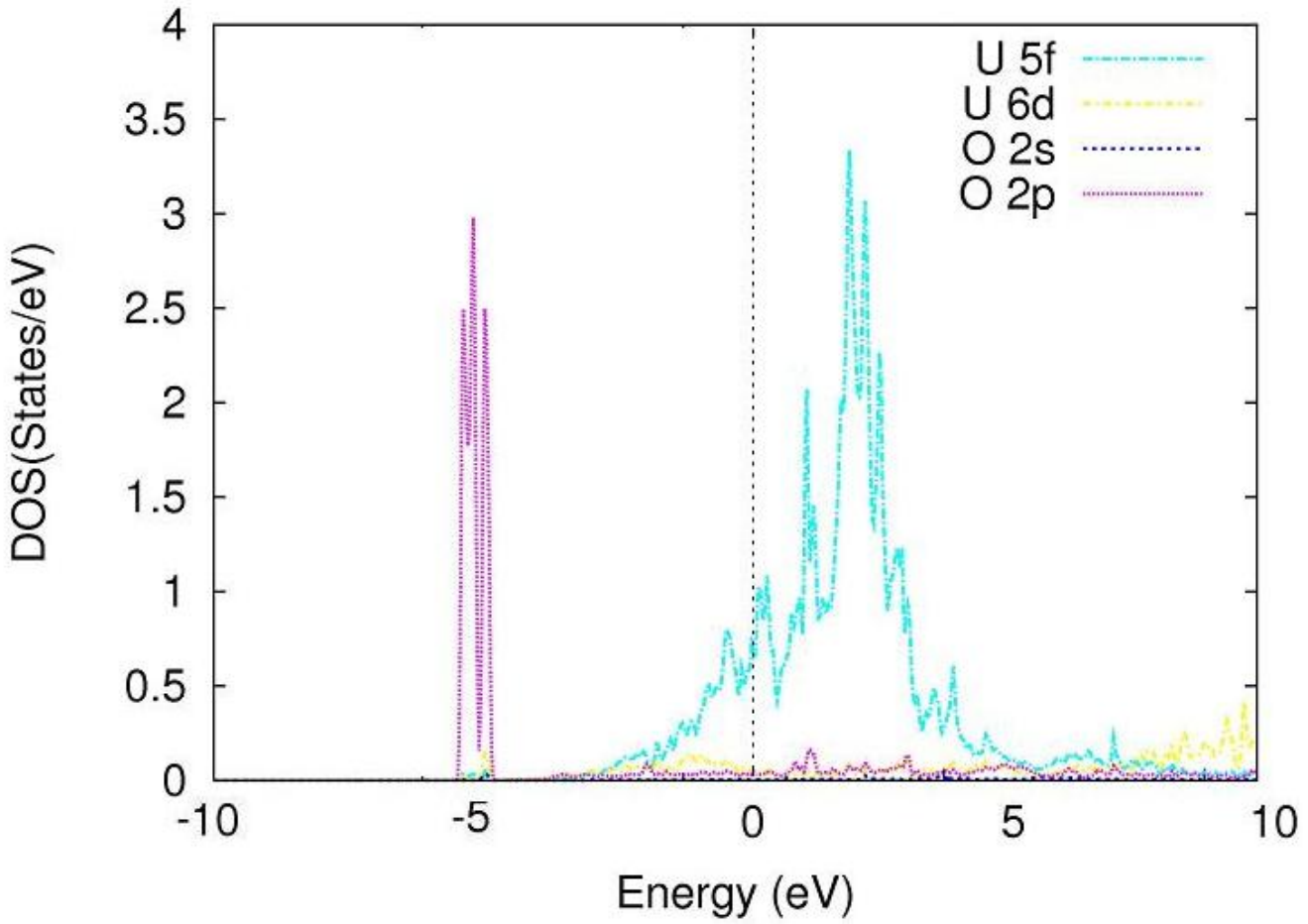

Figure 4.65 LDOS for O adsorption at the center site with the FM level of theory

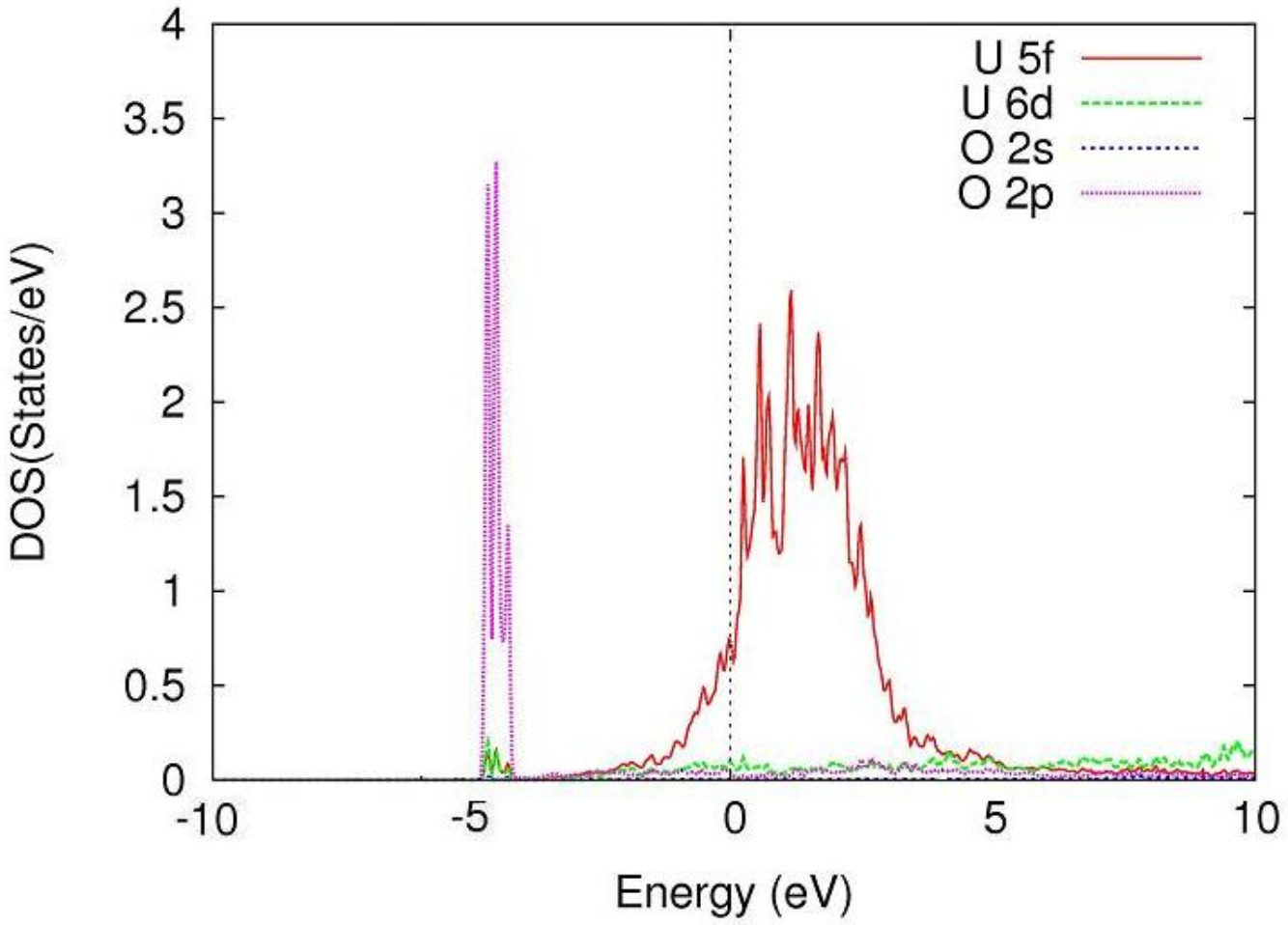

Figure 4.66 LDOS for O adsorption at the bridge site with the FM level of theory

4.2.4 Interstitial lattice sites for O inside (100) oriented γ-U slab

It has been noted that while O has high reactivity with U surfaces, it prefers the staying on the surface with little reaction with the bulk and even forming a UO2 surface boundary to prevent further oxidation. Previous studies that our group has done on γ-U have looked at the reaction of O with the surface but have not extensively looked at the bound states within the lattice. In this section we are going to investigate the O atoms placed in interstitial sites of the bcc lattice to determine the binding strength of U-O within the lattice and the diffusion properties of O into the γ-U (100) surface. As with the case of H, three symmetrically different sites inside the lattice, the interstitial top, interstitial center and interstitial bridge sites, were studied. Following the analysis of the H atom, we have varied the adatom position with respect to the surface in the z direction in the bridge interstitial site only because the bridge site is the only interstitial site that allowed free movement and lattice entry of the atom. The chemisorption energy versus the distance was plotted in Figure 4.67 for the NM, FM and AFM cases where a polynomial fit was done to find the optimal location inside the slab. For the NM case, the atom was allowed to move from the surface to the center of the slab.

The most noted feature of Figure 4.67 is the disparity between the chemisorption energy at the surface and the first peak. From this we can see that upon entering the γ-U lattice the O atom sees a potential barrier of nearly 3 eV, calculated as the difference between the chemisorption energy at the surface and the first energy peak. This size of an inequality would cause the O atom to not diffuse into the bulk without the addition of extra energy. Comparing with the H atom results from F, we see the second potential well below the surface is in the same location for both the H and O atoms indicating that this well is a consequence of the γ-U bcc lattice. If trapped in the second potential well the O atom would see a barrier of 1.85 eV. From the AFM and FM graphs we can see that the minimum energy was found at 2.51 Å below the surface for both the FM and AFM magnetic configurations.

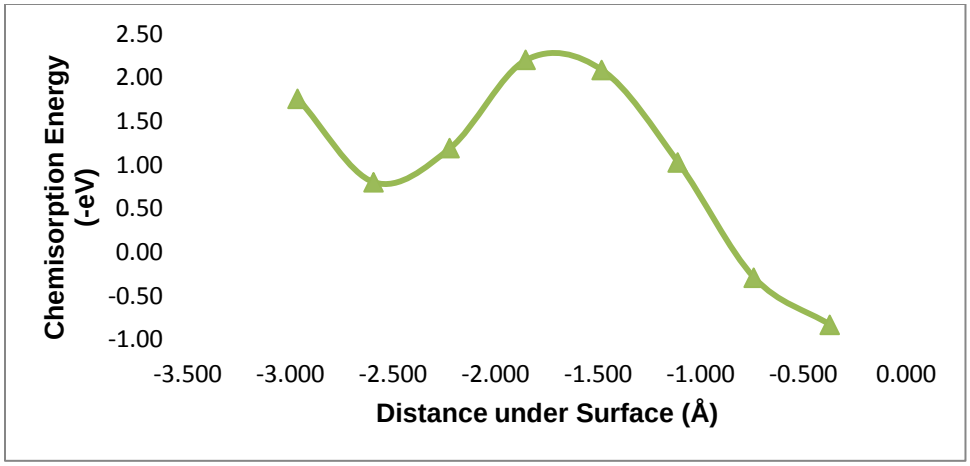

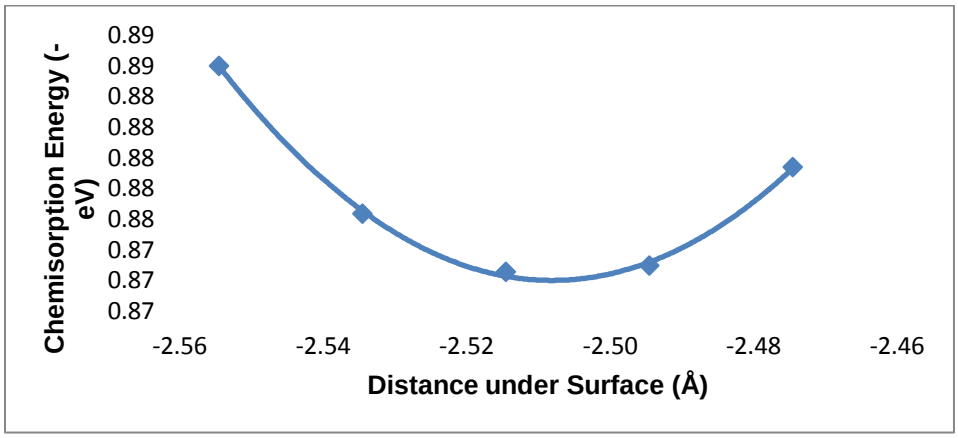

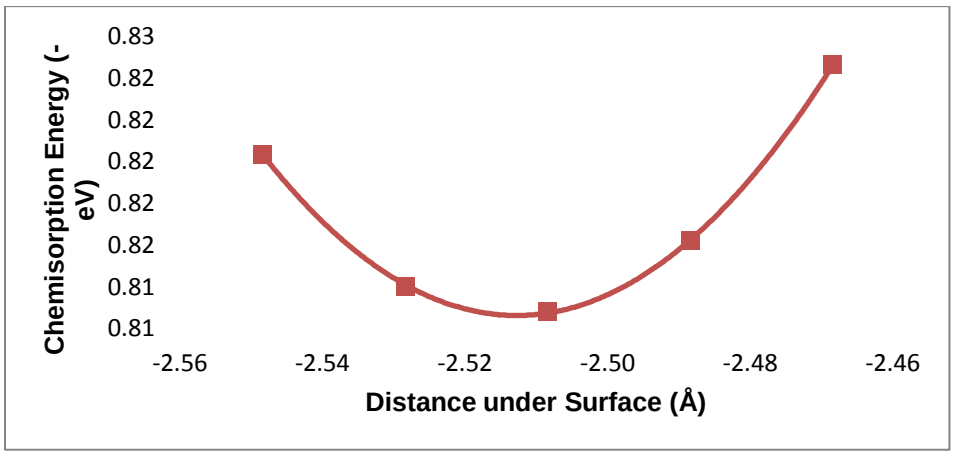

Figure 4.67 Optimized E_c of O atom at the interstitial bridge site for the NM (a), FM (b) and AFM (c) cases

Table 4.21 lists the adsorption energies calculated with equation 4.2 of the H atom in the interstitial regions of the (100) slab of γ-U at the NM, FM and AFM electronic spin configurations, respectively. As with the surface calculations the ΔE as described by equation 4.3, the NSOC and SOC energies are also listed, in addition to, the distance below the surface, R, and the nearest neighbor U atom, $d_{U\text{-}adatom}$. It is noted that for the FM and AFM calculations a reduction to 1.1 Å for the R_{mt} of the O atom was needed in order for the atom to fit into the relaxed FM and AFM slab. The R_{mt} K_{max} was also decreased in these cases to insure comparability to the other calculations. All chemisorption energies are negative, indicating an endothermic reaction when O binds to the lattice. For the top and center sites the addition of SOC led to instability of the system with regard to the NSOC level of theory. At all levels of theory, the bridge interstitial site is the most stable at -0.63 and -0.53 eV for NM, -0.87 and -0.77 eV for FM, and -0.81 and -0.68 eV for AFM, with NSOC and without SOC, respectively, where the optimal location inside the lattice resulted in a U-H bond length of 3 Å for the NM, FM and AFM cases. It is clear that the NM magnetic configuration is favored in these calculations, followed by AFM. This magnetic state does not correspond to experimental findings of UO_2 but a recent *ab initio* study of UO_2 found that hybrid density functional theory with at least 25% exact Hartree-Fock exchange energy was needed to properly describe the UO_2 bulk. In contrast, our previous study found FM to be the ground state at the DFT-SOC level of theory for the bulk UO_2. [125]

Table 4.22 lists $\Delta\Phi$, calculated using equation 4.5, and μ_{dipole} , using equation 4.6, for the O atom inside the γ-U (100) lattice at the NM, FM and AFM level of theory with SOC included. Interestingly these values are the same as those calculated for the H atom in the interstitial region., where $\Delta\Phi$ for the top site is lowest in energy and negative at -0.06, -0.07 and -0.04 eV for the NM, FM and AFM magnetic configurations, respectively, and there is no really change in work function for the bridge and center interstitial sites. The adsorbate induced dipole moment between the adsorbate and substrate is also the same as in the H atom case. The top site has a

Table 4.21 Distances and chemisorption energies of the O atom in γ-U(100) lattice at the NM, FM and AFM levels of theory

NM			NSOC	SOC		
Site	R (Å)	$d_{U\text{-}adatom}$ (Å)	E_c (eV)	E_c (eV)	ΔE_c (eV)	
Top	-1.67	1.67	-2.88	-2.92	-0.04	
Center	-3.34	1.67	-3.08	-3.12	-0.04	
Bridge	-2.47	2.99	-0.63	-0.53	0.10	

FM			NSOC	SOC		
Site	R (Å)	$d_{U\text{-}adatom}$ (Å)	E_c (eV)	E_c (eV)	ΔE_c (eV)	
Top	-1.67	1.67	-3.85	-3.86	-0.01	*
Center	-3.34	1.67	-4.08	-4.07	0.01	*
Bridge	-2.51	3.02	-0.87	-0.77	0.10	

AFM			NSOC	SOC		
Site	R (Å)	$d_{U\text{-}adatom}$ (Å)	E_c (eV)	E_c (eV)	ΔE_c (eV)	
Top	-1.67	1.67	-3.81	-3.78	0.03	*
Center	-3.34	1.67	-3.88	-4.02	-0.14	*
Bridge	-2.51	3.02	-0.81	-0.68	0.13	

dipole moment of -0.28 D, -0.29 D, and -0.20 D for the NM, FM and AFM levels of theory, respectively. The dipole moment for the center site is -0.02 D for NM and AFM and 0.02 D for FM. For the bridge site the surface dipole is -0.02 D for NM and 0.12 D for the FM and AFM cases.

Table 4.22 Change in work function and surface dipole moment for the O atom inside the lattice at the NM, FM, and AFM level of theory

O	Interstitial		
Theory	Site	$\Delta\varphi$	μ_{dipole} (D)
NM	Top	-0.06	-0.28
	Center	0.00	-0.02
	Bridge	0.00	-0.02
FM	Top	-0.07	-0.29
	Center	0.00	0.02
	Bridge	0.03	0.12
AFM	Top	-0.04	-0.20
	Center	0.00	-0.02
	Bridge	0.03	0.12

Table 4.23 for the FM magnetic configuration and Table 4.24 for the AFM lists the magnitude and alignment of the site projected spin magnetic moments, μ_S, and orbital magnetic moments, μ_L, inside the muffin tin sphere for each U atom on each layer, as well as, the net spin and orbital magnetic moment and the total magnetic moment, μ, per U atom at the SOC theoretical level for the clean metal surface and each chemisorbed system. Again, the moments of U atoms bonded to the O atoms are printed in bold. For the FM case at the top site, the O atom is bound to two U atoms of the surface and center layers. Here we see a reduction of 0.37 μ_B in the spin moment and an increase of 0.36 μ_B in the orbital moment of the surface U atom bonded to the adatom. Very little change in moment is seen with the center U atom bounded with the O atom or with the remaining atoms of the slab. The entire slab sees an increase in total moment of 0.07 μ_B for this adsorption site. For the center interstitial lattice site, the O atom increases the total magnetic moment of the slab by 0.10 μ_B, overall, which is caused by the summation of little changes in spin and orbital moment throughout the slab. The two U atoms bound to the O atom inside the interstitial bridge site experience an increase in spin magnetic moment of 0.06 μ_B and a

decrease in orbital magnetic moment of 0.03 μ_B. The moments of the first 3 layers see the most change and the total moment of the slab changes by 0.20 μ_B. For the AFM configuration, the top interstitial site sees a positive change in total magnetic moment of 1.62 μ_B, the bridge a negative one of -0.07 μ_B and at the center no induced magnetic moment is noticed. For the top site, the surface U atom bound to the O atom sees an increase in spin magnetic moment of 1.44 μ_B and the orbital decreases 0.91 μ_B. The center atom decreases in total magnetic moment only slightly and the atoms of the first and second layers see the most change. In this case the magnetic ordering of the moments resembles those of the FM O induced moments. At the interstitial bridge and center site the O atom induces negligible spin and orbital magnetic moment on the system. Comparing the interstitial results with those of the surface adsorption, the interstitial bonding causes a positive change in the magnetic moment for the FM case.

Following the analysis of the surface calculations, we investigate the partial charges inside the muffin-tin sphere for the interstitial sites as well. For the NM case, listed in Table 4.25, the O atom gains electrons inside the muffin-tin sphere for the top, center and bridge site at all levels of theory. At the top interstitial site, the charge on the second layer atom sees a positive change of *f* electrons and loses some charge in the *d* orbitals compared to the bare slab. No other exchange of electrons is seen for this site. For the center site, the second and fourth layer atoms gain electrons in the 6*d* orbitals, in addition, the middle layer U atom gains electrons in the 5*f* orbitals. The second layer of the slab finds an increase in charge in the 5*f* band for the bridge interstitial site. Table 4.26 lists the partial charges for the FM case, where the O atom gains electrons inside the muffin-tin sphere for the *p* orbital at all interstitial sites. The top site has an increase for the 6*d* and 5*f* bands of the first and third layers, which is similar to the change in charge for the O atoms at the center site but for the atoms of the second and fourth layers. At the bridge site the 5f electrons of the U atoms of the second and third layers increase and the 6d

Table 4.23 Spin and orbital magnetic moment for the O atom inside the lattice at FM level of theory

FM		Layer												
O interstitial		1		2		3		4		5		total		total μ
Site	Atom	μ_S	μ_L	μ_S	μ_L	μ_S	μ_L	μ_S	μ_L	μ_S	μ_L	μ_S	μ_L	
bare	1	0.95	-0.64	0.08	-0.02	-0.08	0.01	0.08	-0.02	0.94	-0.64			
	2	0.95	-0.64	0.08	-0.02	-0.08	0.01	0.08	-0.02	0.94	-0.64			
	3	0.95	-0.64	0.08	-0.02	-0.08	0.01	0.08	-0.02	0.94	-0.64			
	4	0.95	-0.64	0.08	-0.02	-0.08	0.01	0.08	-0.02	0.94	-0.64	7.89	-5.21	2.68
Top	1	1.10	-0.77	0.09	-0.02	-0.14	0.04	0.09	-0.02	1.01	-0.67			
	2	0.99	-0.65	0.09	-0.02	-0.07	0.01	0.09	-0.02	0.95	-0.63			
	3	0.99	-0.65	0.09	-0.02	-0.14	0.01	0.09	-0.02	0.95	-0.63			
	4	**0.57**	**-0.28**	0.09	-0.02	**-0.07**	**-0.03**	0.09	-0.02	0.91	-0.62	7.80	-5.05	2.75
Center	1	0.93	-0.62	**0.06**	**-0.02**	-0.09	0.03	**0.06**	**-0.02**	0.93	-0.62			
	2	0.93	-0.62	0.08	-0.01	-0.09	0.03	0.08	-0.01	0.93	-0.62			
	3	0.93	-0.62	0.08	-0.01	-0.09	0.03	0.08	-0.01	0.93	-0.62			
	4	0.93	-0.62	0.09	-0.02	-0.09	0.03	0.09	-0.02	0.93	-0.62	7.74	-4.96	2.78
Bridge	1	0.96	-0.63	0.03	0.01	-0.08	0.02	0.09	-0.02	0.95	-0.63			
	2	**1.00**	**-0.68**	0.03	0.01	-0.07	0.02	0.09	-0.02	0.95	-0.63			
	3	0.96	-0.63	0.12	-0.03	-0.08	0.02	0.08	-0.01	0.95	-0.63			
	4	**1.00**	**-0.68**	0.12	-0.03	-0.07	0.02	0.08	-0.01	0.95	-0.63	8.05	-5.17	2.88

Table 4.24 Spin and orbital magnetic moment for the O atom inside the lattice at AFM level of theory

AFM		Layer												
O interstitial		1		2		3		4		5		total		total μ
Site	Atom	μ_S	μ_L	μ_S	μ_L	μ_S	μ_L	μ_S	μ_L	μ_S	μ_L	μ_S	μ_L	
bare	1	0.88	-0.63	0.00	0.00	-0.14	0.06	0.00	0.00	0.88	-0.63			
	2	-0.87	0.63	0.00	0.00	0.14	-0.06	0.00	0.00	-0.87	0.63			
	3	0.88	-0.63	0.00	0.00	-0.14	0.06	0.00	0.00	0.88	-0.63			
	4	-0.87	0.63	0.00	0.00	0.14	-0.06	0.00	0.00	-0.87	0.63	0.02	-0.01	0.01
Top	1	1.11	-0.77	0.13	-0.04	-0.16	0.06	-0.02	0.01	0.96	-0.69			
	2	0.97	-0.65	0.13	-0.04	0.04	-0.03	-0.02	0.01	-0.76	0.56			
	3	1.00	-0.66	0.13	-0.04	-0.10	0.03	-0.02	0.01	0.89	-0.64			
	4	**0.57**	**-0.28**	0.13	-0.04	**0.11**	**-0.05**	-0.02	0.01	-0.78	0.58	4.29	-2.66	1.63
Center	1	0.87	-0.62	0.00	0.00	-0.13	0.05	0.00	0.00	0.87	-0.62			
	2	-0.86	0.61	**0.00**	**0.00**	0.13	-0.05	**0.00**	**0.00**	-0.87	0.61			
	3	0.87	-0.62	0.00	0.00	-0.13	0.06	0.00	0.00	0.87	-0.62			
	4	-0.86	0.61	0.00	0.00	0.13	-0.05	0.00	0.00	-0.87	0.61	0.02	-0.02	0.01
Bridge	1	**0.86**	**-0.61**	0.02	-0.02	-0.15	0.06	0.01	0.00	0.88	-0.62			
	2	-0.89	0.65	0.02	-0.02	0.08	-0.03	0.01	0.00	-0.88	-0.62			
	3	**0.86**	**-0.61**	-0.02	0.00	-0.15	0.06	0.00	0.00	0.88	-0.62			
	4	-0.89	0.65	-0.02	-0.01	0.08	-0.03	0.00	0.00	-0.88	-0.62	-0.16	-2.41	-2.56

orbitals increase as well. For the AFM case, the adatom adds electrons when at all locations. The partial charges inside the muffin-tin sphere for atoms of the slab at the AFM level of theory, in Table 4.27, show a similar trend to those in the FM case for the center and bridge interstitial sites. For the top site, the adatom induces a loss of electrons inside the muffin-tin sphere of the first and second layer atoms lose electrons in the 5*f* band. The *d* orbitals of the atoms of the first and second layer gain charge.

As with the other sections, we look at the change in charge density for the O atom and the U atoms of the slab interacting with it. Figure 4.68 shows the top site, Figure 4.69 shows the center site and Figure 4.70 shows the bridge site for the NM slab configuration. For each site the O atom gains charge. At the top and bridge site, the O atom and U atoms near it are all gaining charge. The center site bonding is the most ionic where there doesn't appear to be ion sharing between the O and U atoms. With spin polarization, depicted in Figure 4.71, Figure 4.72, and Figure 4.73 for the top, center and bridge sites, respectively, the top and center site bonding looks to have covalent characteristics, while the bridge site bonding seems more ionic with a clear exchange of ions from the U atoms to the O atom. The same is true for the AFM magnetic ordering, depicated in Figure 4.74, through Figure 4.76, for NM, FM and AFM, respectiviel, except the bridge site bonding appears to have more electron sharing characteristics.

Figure 4.77 shows the Gaussian-broadened (with a width of 0.003 eV) *f* and *d* LDOS curves for atoms of the surface, subsurface, and center layers of the clean γ-U (100) metal slab at the NM level of theory. Again, only the LDOS of the adatoms and the U atoms interacting with the adatoms are considered. In Figure 4.78, we show the LDOS plots for the O adatom 2*s* and 2*p* electrons and the surface (U1) and center (U3) atom 6d and 5f electrons at the top interstitial site. 5*f* -6*d*-2*p* hybridization is evident due to the overlap of those orbitals at -11 and -7 eV below the Fermi surface. Also, the intensity of the 5*f* band for both the top and center atoms bound with the O atom show a decrease which indicates their participation in bonding. LDOS for the interstitial center site is shown in Figure 4.79, from it we can see the same 5*f*-6*d*-2*p* hybridization and the

Table 4.25 Partial charges inside muffin-tin spheres for O at the top, center and bridge interstitial sites for the NM magnetic configuration

		Q_B			Q_A			$\Delta Q=Q_A-Q_B$		
Site	Atom/Layer	O *p*	U *d*	U *f*	O *p*	U *d*	U *f*	O *p*	U *d*	U *f*
Top	Oxygen	2.054			2.563			0.509		
	U surface layer		10.422	1.985		10.422	1.987		0.000	0.003
	U subsurface layer		10.545	1.948		10.530	1.977		-0.014	0.029
	U middle layer		10.534	1.942		10.534	1.950		-0.001	0.009
	U submiddle layer		10.545	1.948		10.542	1.952		-0.002	0.004
	U bottom layer		10.422	1.984		10.422	1.986		0.000	0.001
Center	Oxygen	2.054			2.561			0.507		
	U surface layer		10.422	1.985		10.418	1.991		-0.003	0.006
	U subsurface layer		10.545	1.948		10.624	2.109		0.079	0.161
	U middle layer		10.534	1.942		10.520	1.974		-0.014	0.032
	U submiddle layer		10.545	1.948		10.624	2.109		0.079	0.162
	U bottom layer		10.422	1.984		10.418	1.991		-0.003	0.007
Bridge	Oxygen	2.054			2.551			0.497		
	U surface layer		10.422	1.985		10.416	1.996		-0.005	0.011
	U subsurface layer		10.545	1.948		10.609	2.093		0.064	0.146
	U middle layer		10.534	1.942		10.531	1.948		-0.004	0.006
	U submiddle layer		10.545	1.948		10.543	1.949		-0.001	0.001
	U bottom layer		10.422	1.984		10.423	1.983		0.001	-0.002

Table 4.26 Partial charges inside muffin-tin spheres for O at the top, center and bridge interstitial sites for the FM magnetic configuration

		Q_B			Q_A			$\Delta Q=Q_A-Q_B$		
Site	Atom/Layer	O *p*	U *d*	U *f*	O *p*	U *d*	U *f*	O *p*	U *d*	U *f*
Top	Oxygen	2.054			2.563			0.509		
	U surface layer		10.421	2.009		10.521	2.116		0.100	0.107
	U subsurface layer		10.546	1.958		10.532	1.989		-0.014	0.031
	U middle layer		10.536	1.952		10.620	2.103		0.084	0.151
	U submiddle layer		10.546	1.959		10.544	1.964		-0.002	0.004
	U bottom layer		10.421	2.011		10.419	2.020		-0.002	0.009
Center	Oxygen	2.054			2.369			0.315		
	U surface layer		10.421	2.009		10.418	2.016		-0.003	0.007
	U subsurface layer		10.546	1.958		10.625	2.118		0.079	0.159
	U middle layer		10.536	1.952		10.523	1.986		-0.013	0.034
	U submiddle layer		10.546	1.959		10.628	2.124		0.082	0.165
	U bottom layer		10.421	2.011		10.419	2.020		-0.002	0.009
Bridge	Oxygen	2.054			2.540			0.486		
	U surface layer		10.421	2.009		10.423	2.011		0.002	0.002
	U subsurface layer		10.546	1.958		10.562	2.016		0.017	0.058
	U middle layer		10.536	1.952		10.552	2.010		0.016	0.058
	U submiddle layer		10.546	1.959		10.549	1.960		0.003	0.001
	U bottom layer		10.421	2.011		10.421	2.022		0.000	0.011

Table 4.27 Partial charges inside muffin-tin spheres for O at the top, center and bridge interstitial sites for the AFM magnetic configuration

		Q_B			Q_A			$\Delta Q=Q_A-Q_B$		
Site	Atom/Layer	O *p*	U *d*	U *f*	O *p*	U *d*	U *f*	O *p*	U *d*	U *f*
Top	Oxygen	2.054			2.371			0.317		
	U surface layer		10.419	2.012		10.514	1.996		0.094	-0.016
	U subsurface layer		10.545	1.955		10.527	1.928		-0.018	-0.027
	U middle layer		10.534	1.949		10.617	2.089		0.082	0.140
	U submiddle layer		10.545	1.955		10.545	2.008		0.001	0.054
	U bottom layer		10.419	2.009		10.424	2.173		0.005	0.164
Center	Oxygen	2.054			2.368			0.314		
	U surface layer		10.419	2.012		10.416	2.017		-0.004	0.005
	U subsurface layer		10.545	1.955		10.623	2.118		0.079	0.163
	U middle layer		10.534	1.949		10.520	1.986		-0.014	0.037
	U submiddle layer		10.545	1.955		10.625	2.120		0.080	0.166
	U bottom layer		10.419	2.009		10.416	2.016		-0.004	0.007
Bridge	Oxygen	2.054			2.539			0.485		
	U surface layer		10.419	2.012		10.426	2.010		0.006	-0.003
	U subsurface layer		10.545	1.955		10.560	2.015		0.015	0.060
	U middle layer		10.534	1.949		10.550	2.008		0.016	0.059
	U submiddle layer		10.545	1.955		10.545	1.955		0.000	0.000
	U bottom layer		10.419	2.009		10.419	2.011		-0.001	0.002

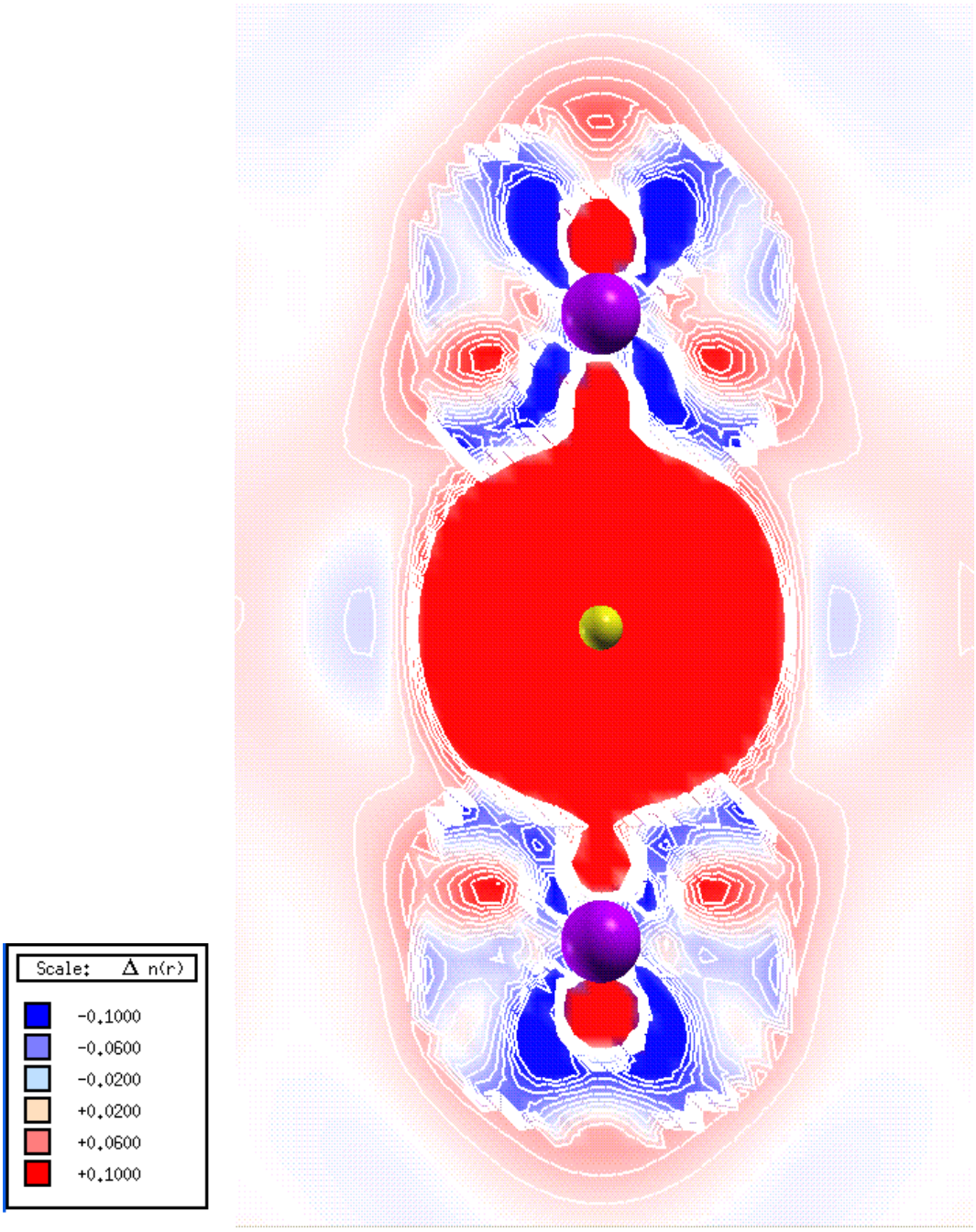

Figure 4.68 Change in charge density for the O atom at the NM interstitial top site

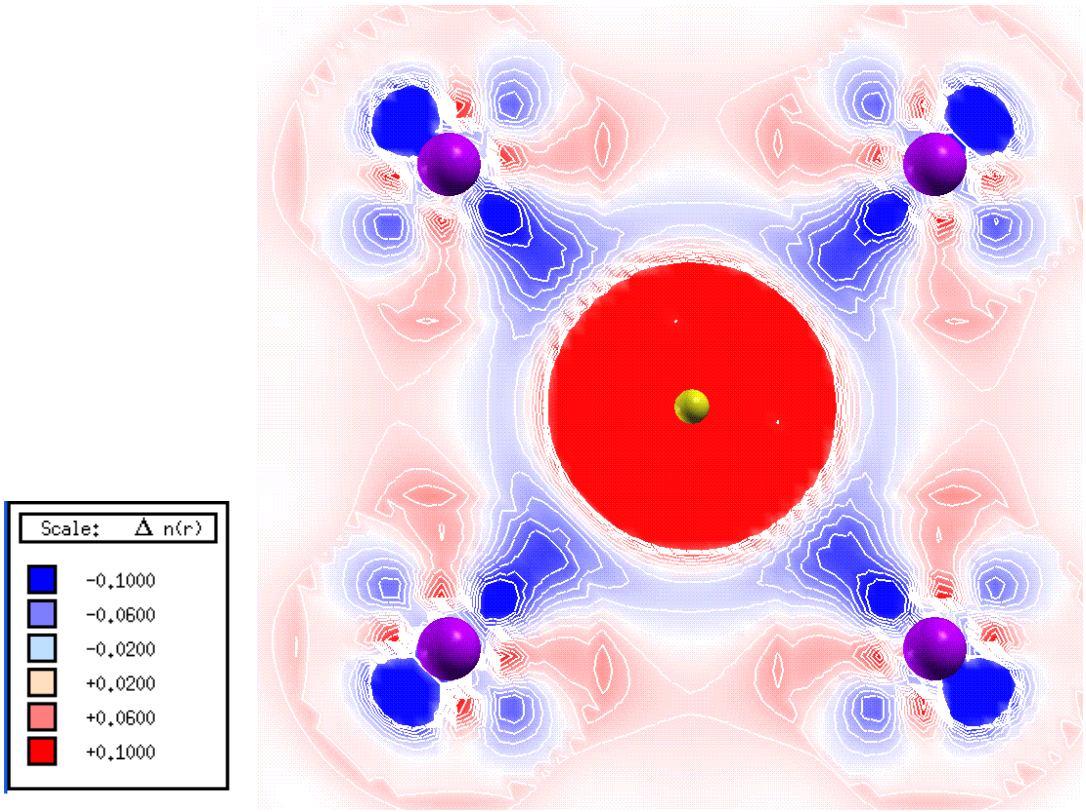

Figure 4.69 Change in charge density for the O atom at the NM interstitial center site

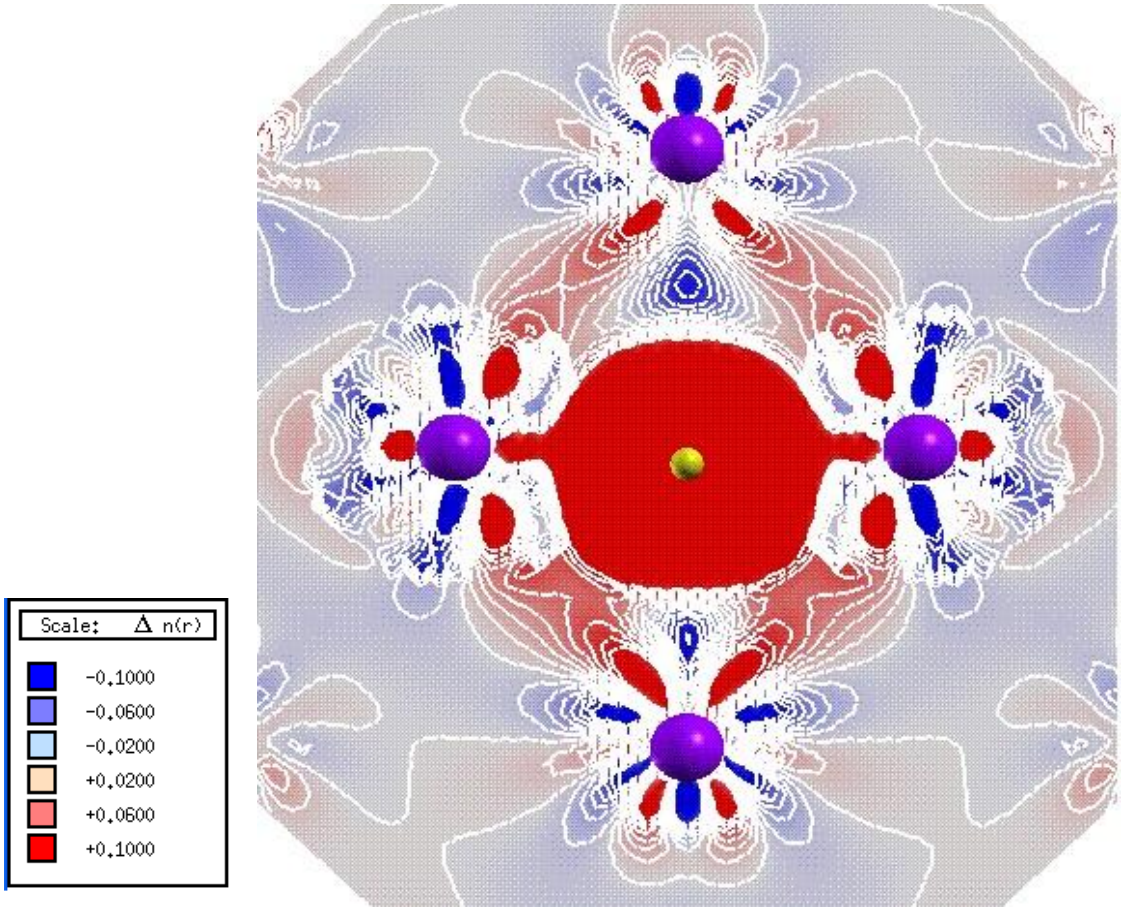

Figure 4.70 Change in charge density for the O atom at the NM interstitial bridge site

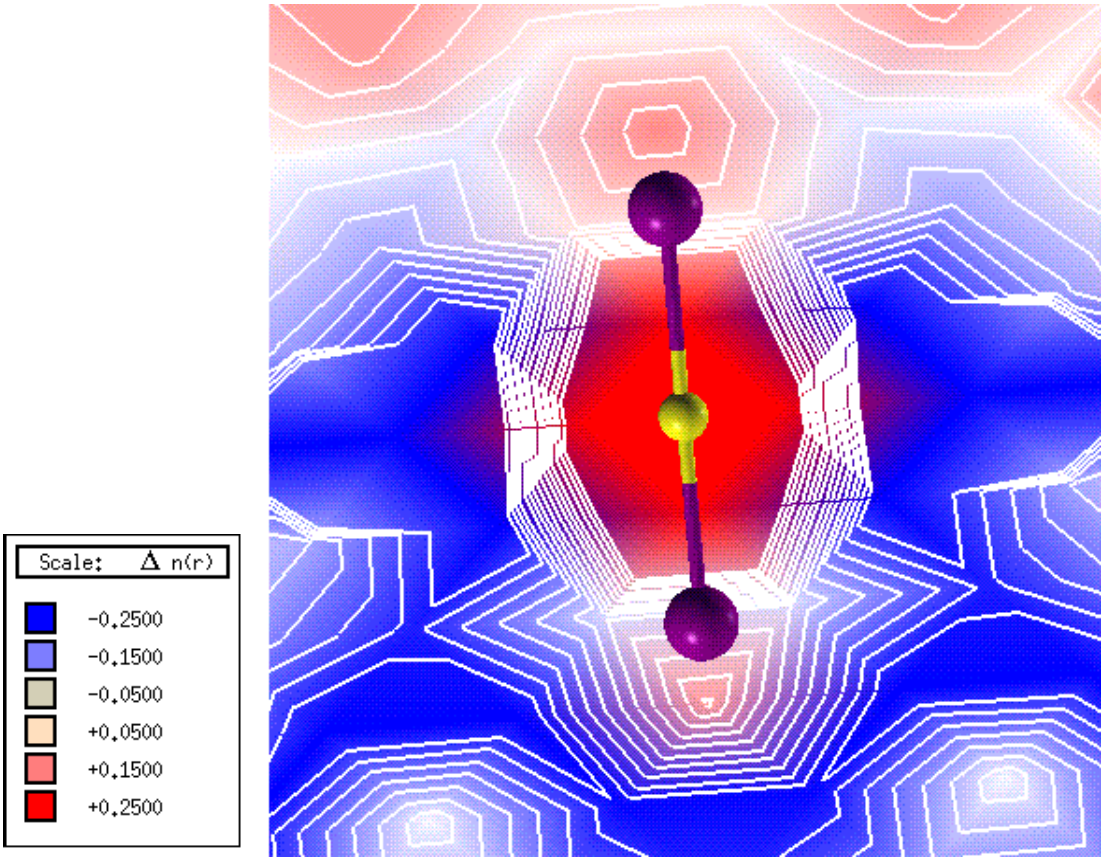

Figure 4.71 Change in charge density for the O atom at the FM interstitial top site

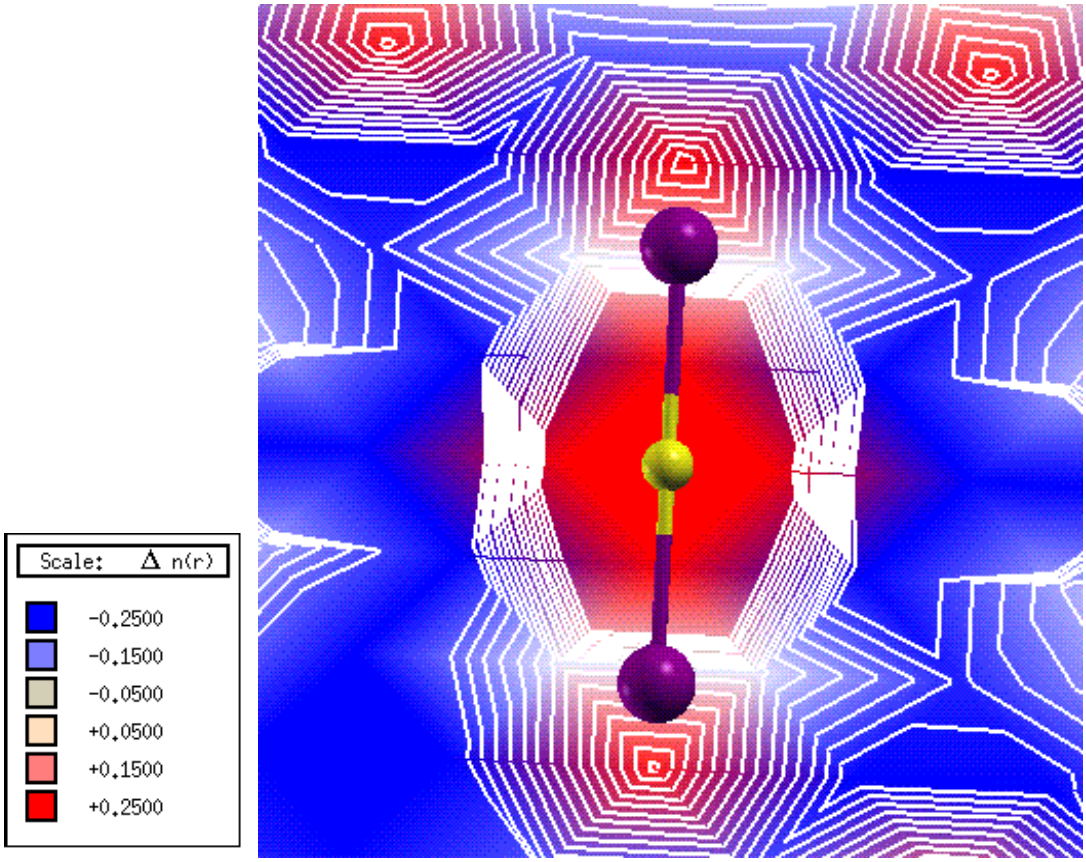

Figure 4.72 Change in charge density for the O atom at the FM interstitial center site

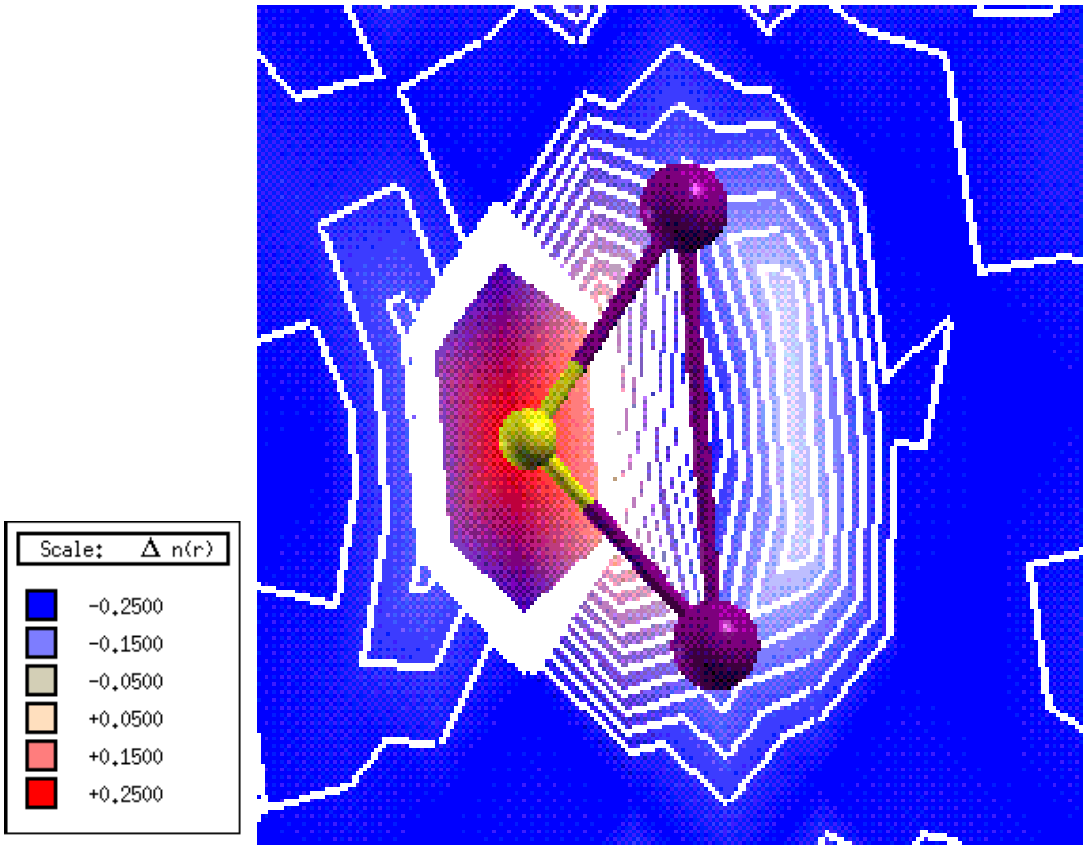

Figure 4.73 Change in charge density for the O atom at the FM interstitial bridge site

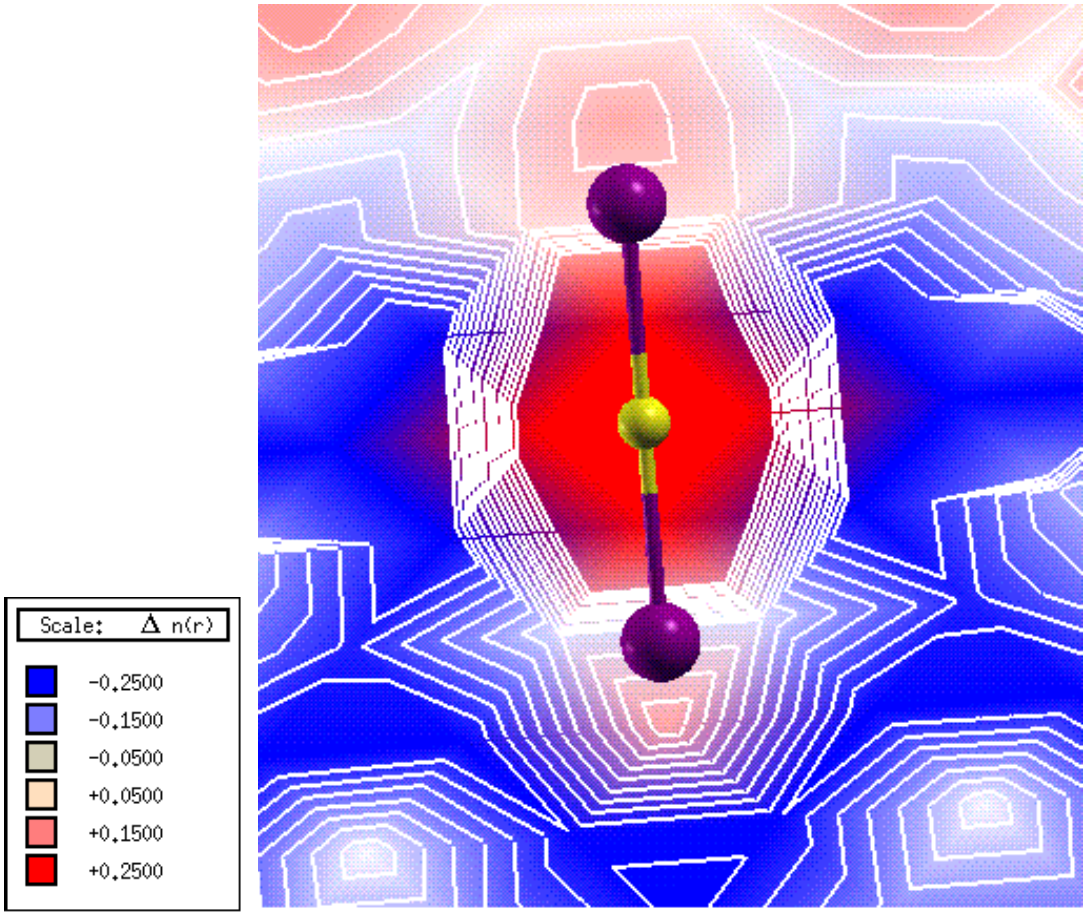

Figure 4.74 Change in charge density for the O atom at the AFM interstitial top site

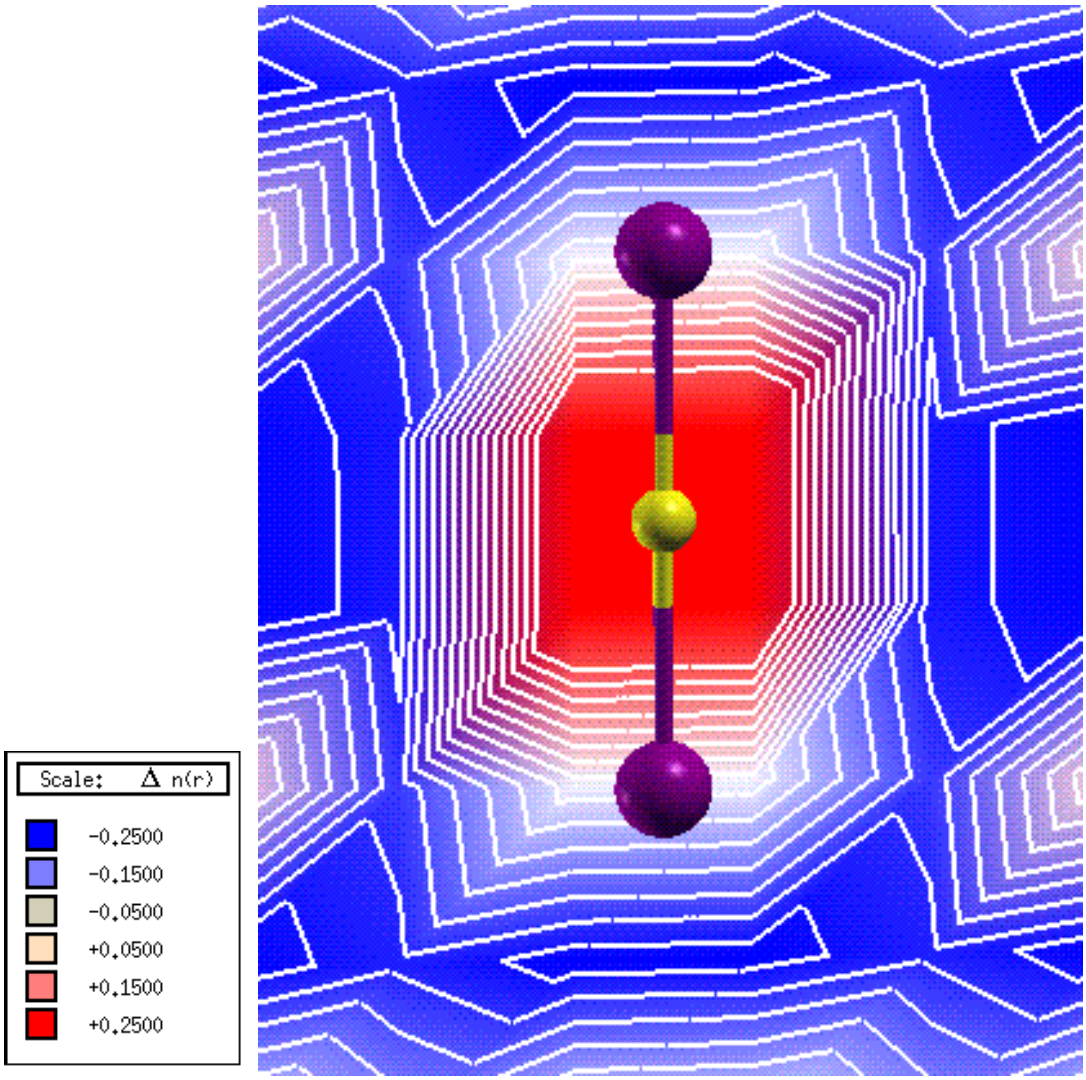

Figure 4.75 Change in charge density for the O atom at the AFM interstitial center site

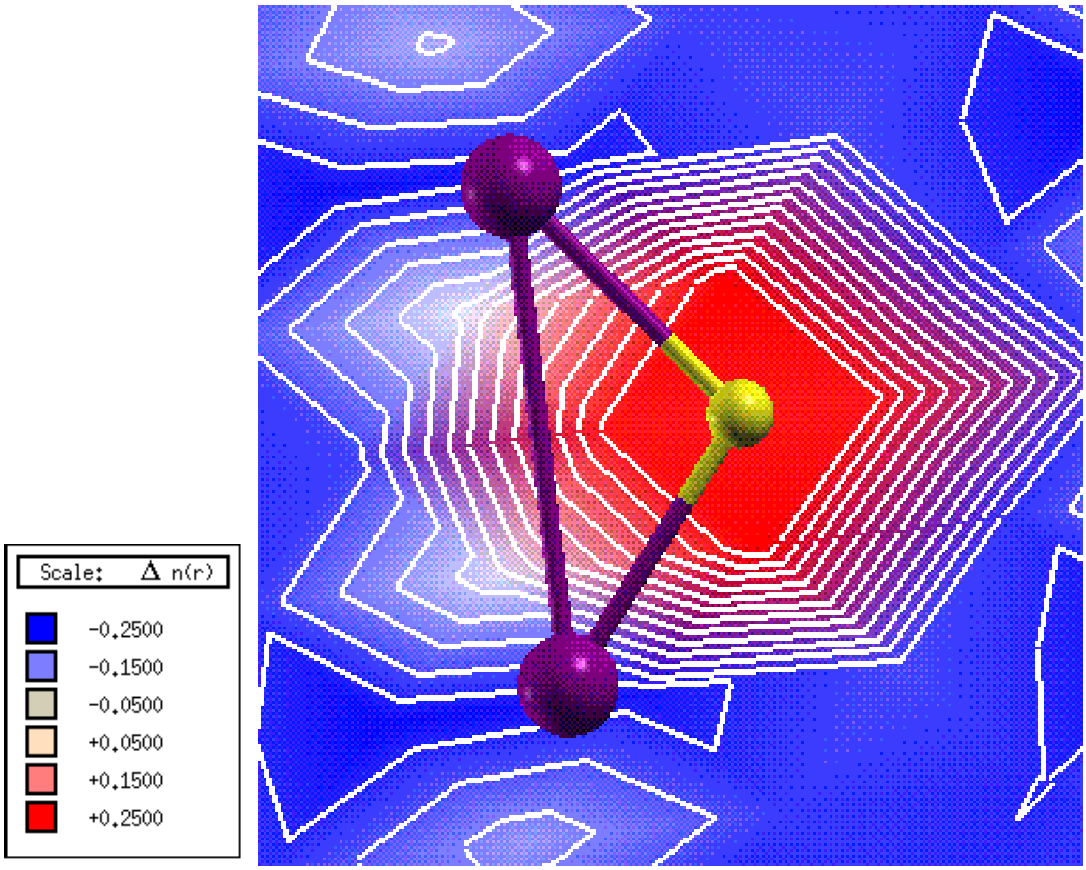

Figure 4.76 Change in charge density for the O atom at the AFM interstitial bridge site

loss of intensity of the 5*f* band above the Fermi level but in addition there seems to be a slight increase in delocalization of the 5*f* band above the Fermi level and the 2*s* peak of the O atom is evident at -13.5 eV. Figure 4.80 shows the LDOS for the bridge site system which looks to have a different bonding behavior than for the interstitial top and center interstitial sites. The subsurface atom seems to be the only atom participating in bonding due to the decrease of intensity of the 5*f* band of that atom and only the 6*d* orbital is hybridizing with the 2*p* orbital of the O atom. In addition, the first peak of the 2*p* band has decreased in intensity and broadened. Following the method of the NM case, the FM level of theory LDOS plot is drawn in Figure 4.81 for the surface (U1) and in Figure 4.81 for the subsurface (U2) and center (U3) atoms of clean γ-U (100) metal slab. The interstitial top site binding of the O atom is shown in Figure 4.82. 6*d*-2*p* binding is evident at the two peaks found below the Fermi surface. The 5*f* electrons of both the surface and center atoms show delocalization above the Fermi surface and a decreased intensity. Figure 4.83 shows the LDOS for the interstitial center site. As with the NM case, there is a 2*s* peak at -13.5 eV and 6*d*-5*f*-2*p* hybridization is evident with the overlapping of peaks. In addition, the 5*f* band shows a decrease in intensity and a broader peak at the Fermi surface. For the bridge interstitial site, the LDOS is graphed in Figure 4.84. The 5*f* electrons of the surface and subsurface atoms seem to be unaffected by the presence of the O atom. Only the 6*d* and 5*f* orbitals of the subsurface are hybridizing with the 2*p* bands of the O atom. Also, the gap between the two 2*p* bands decreased by 3.5 eV compared to the other sites. For the AFM level of theory, the LDOS for the 6*d* and 5*f* electrons of the surface (U1), subsurface (U2) and center (U3) atoms of the bare γ-U (100) metal slab is shown in Figure 4.85. Figure 4.86 illustrates the LDOS for the O atom binding at the interstitial top site. In it we see the 6*d* and 5*f* of the center U atom hybridizing with the 2*p* orbital of the O atom. The 5*f* peak of the U surface and center atoms are slightly narrower than that for the bare AFM slab and the intensity of the peak has decreased indicating participation of the 5*f* electrons of the surface and center atoms in bonding. For the interstitial center site adsorption,as with the NM and FM cases the 2*s* orbital of the O atom shows a peak

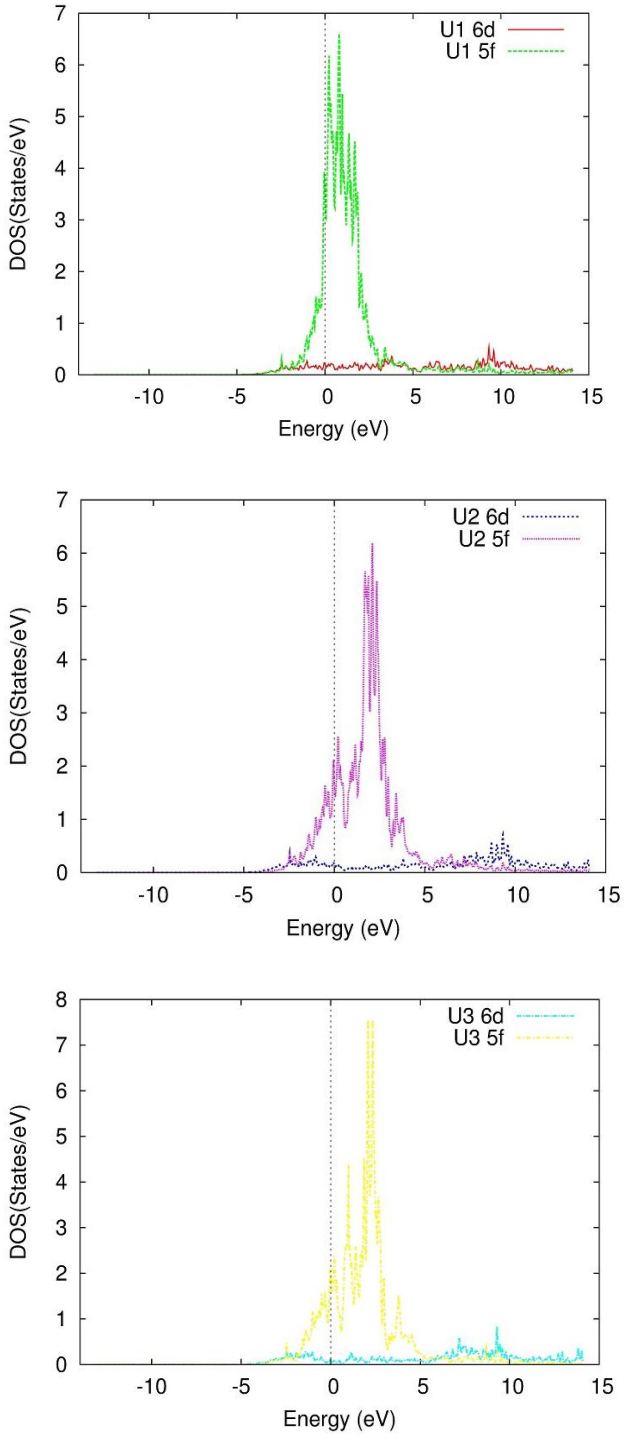

Figure 4.77 LDOS for the surface (U1), subsurface (U2), and center (U3) atoms of the 5 layer slab at the NM level of theory

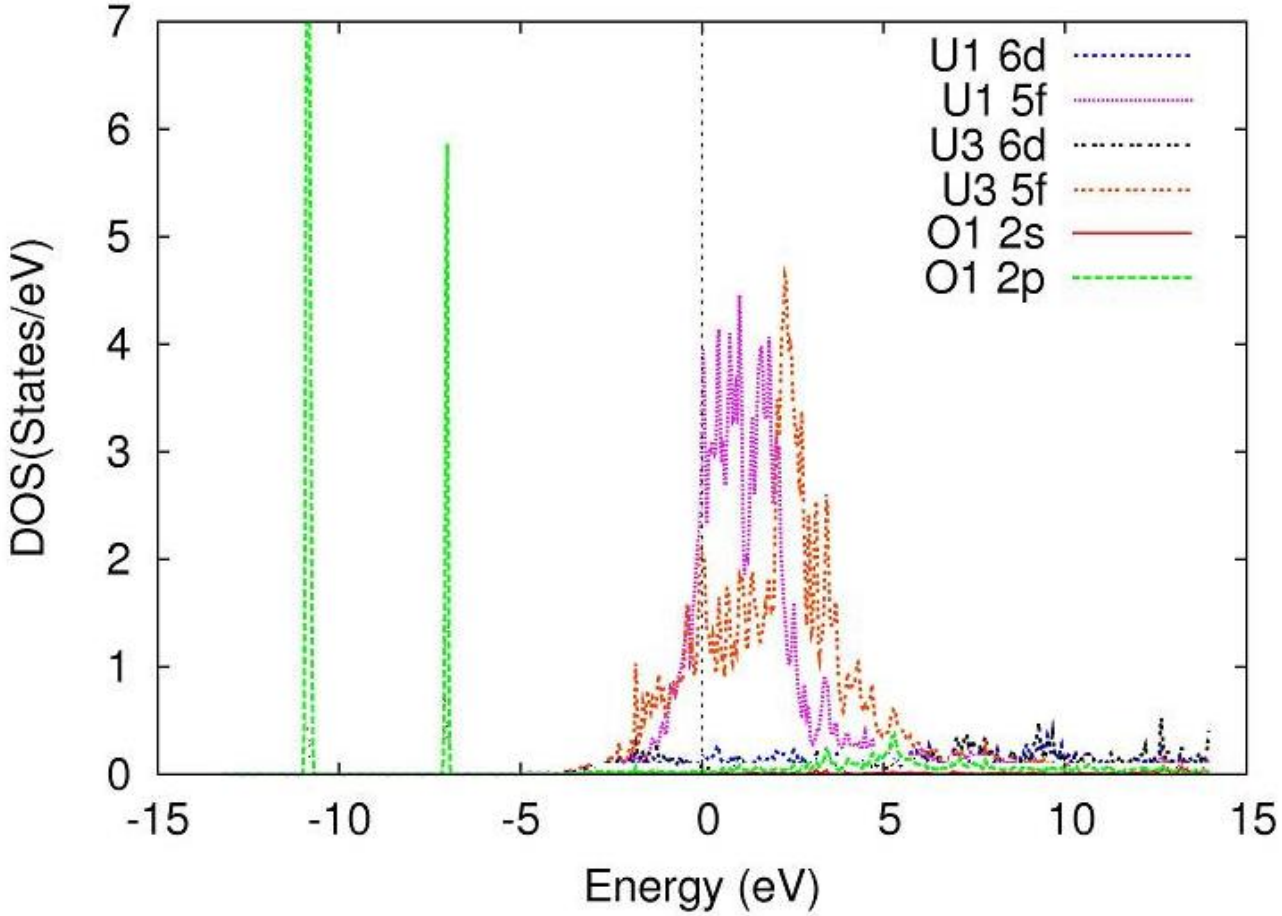

Figure 4.78 LDOS for O at the top interstitial site at the NM level of theory. U1 is the surface atom and U3 is the center atom.

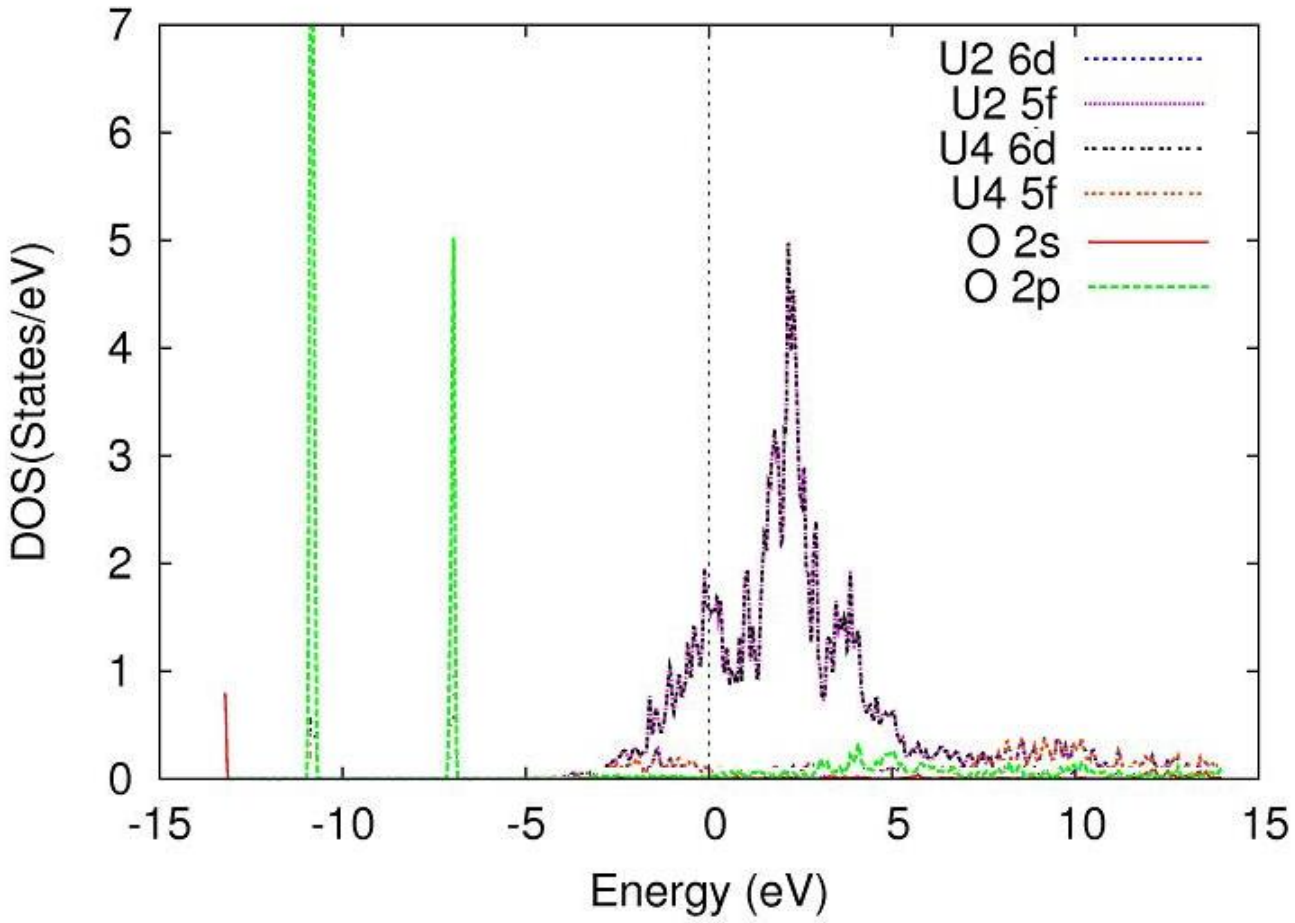

Figure 4.79 LDOS for O at the center interstitial site at the NM level of theory. U2 is the subsurface and U4 is the subcenter atom.

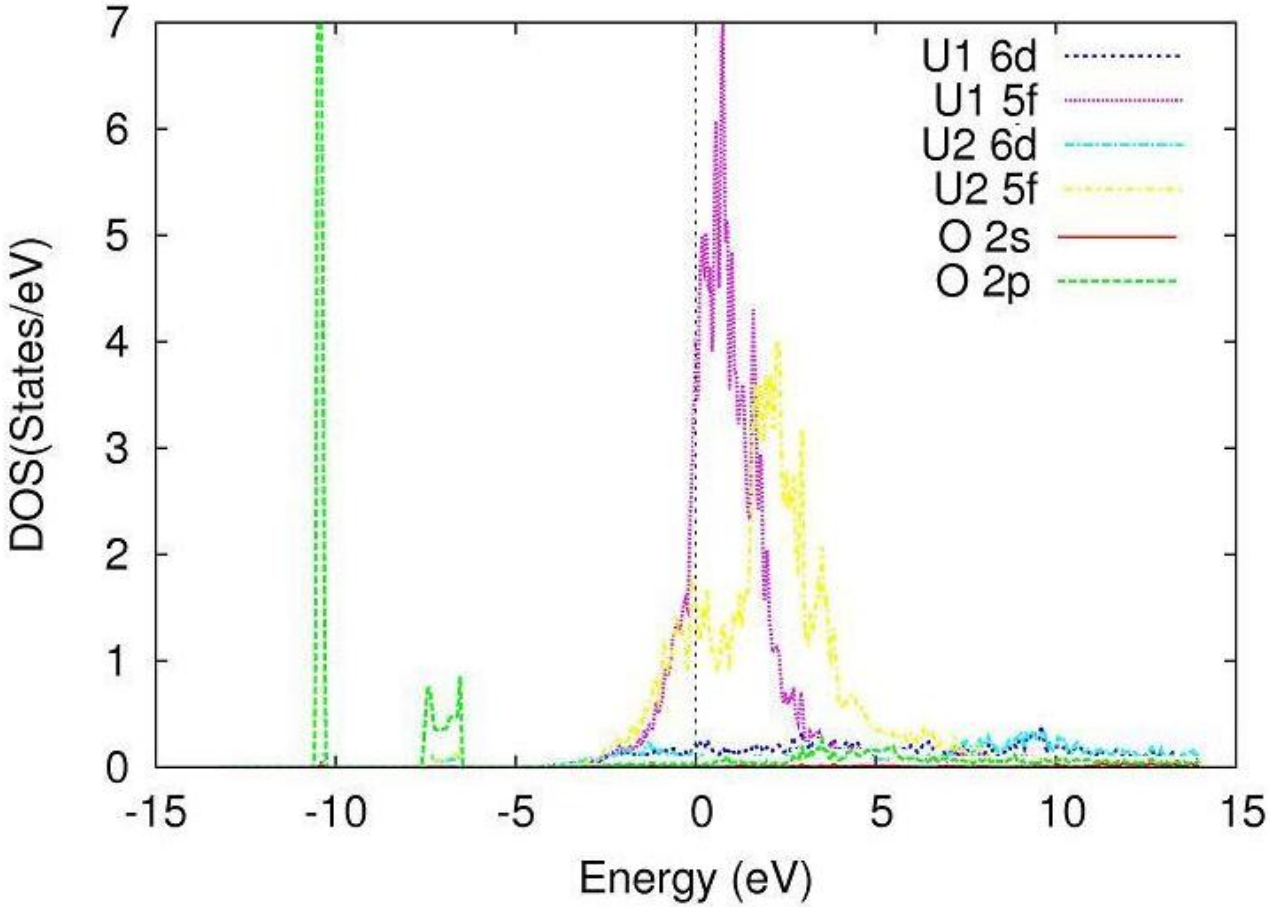

Figure 4.80 LDOS for O at the bridge interstitial site at the NM level of theory. U1 is the surface atom and U2 is the subsurface atom

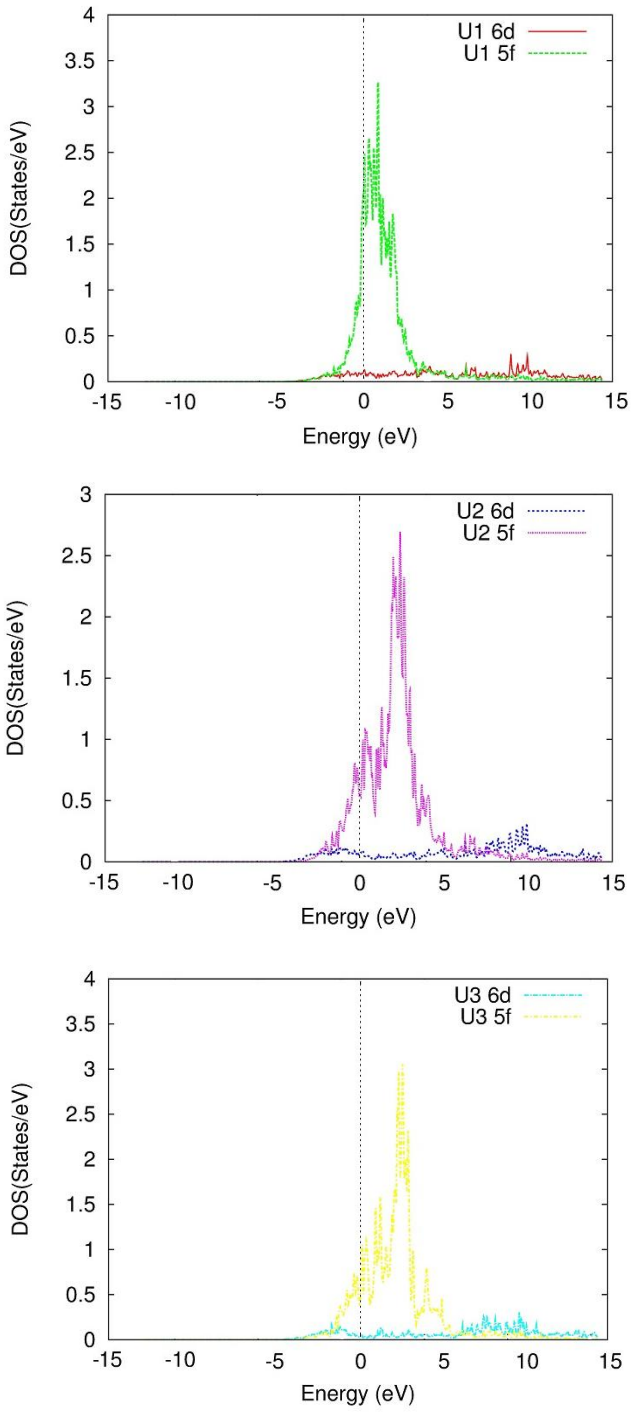

Figure 4.81 LDOS for the 6d and 5f electrons of the surface (U1), subsurface (U2) and center (U3) atoms atom of the bare γ-U (100) slab at the FM level of theory

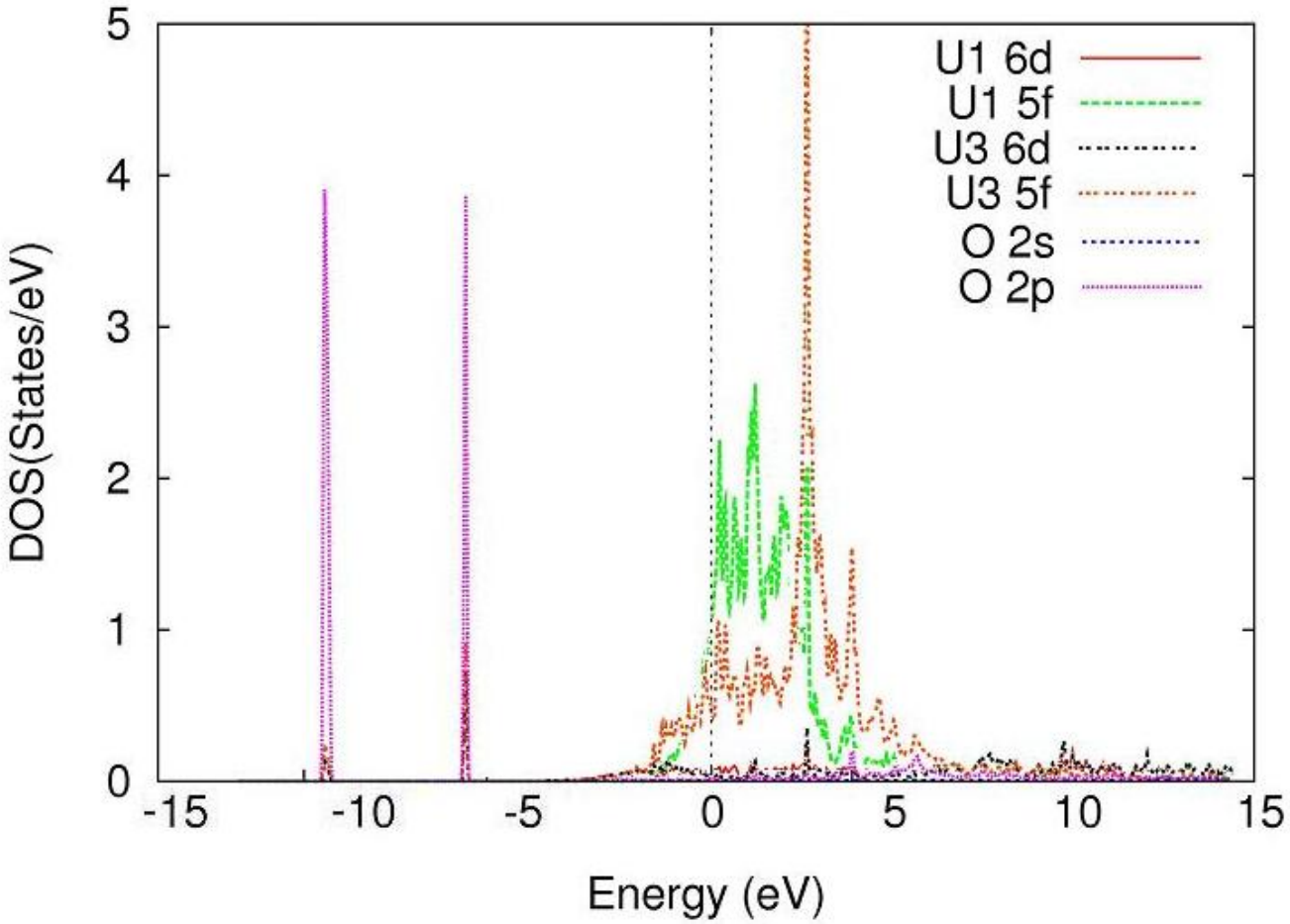

Figure 4.82 LDOS for O adsorption at the top interstitial site with the FM level of theory. U1 is the surface U atom and U3 is the center U atom of the slab.

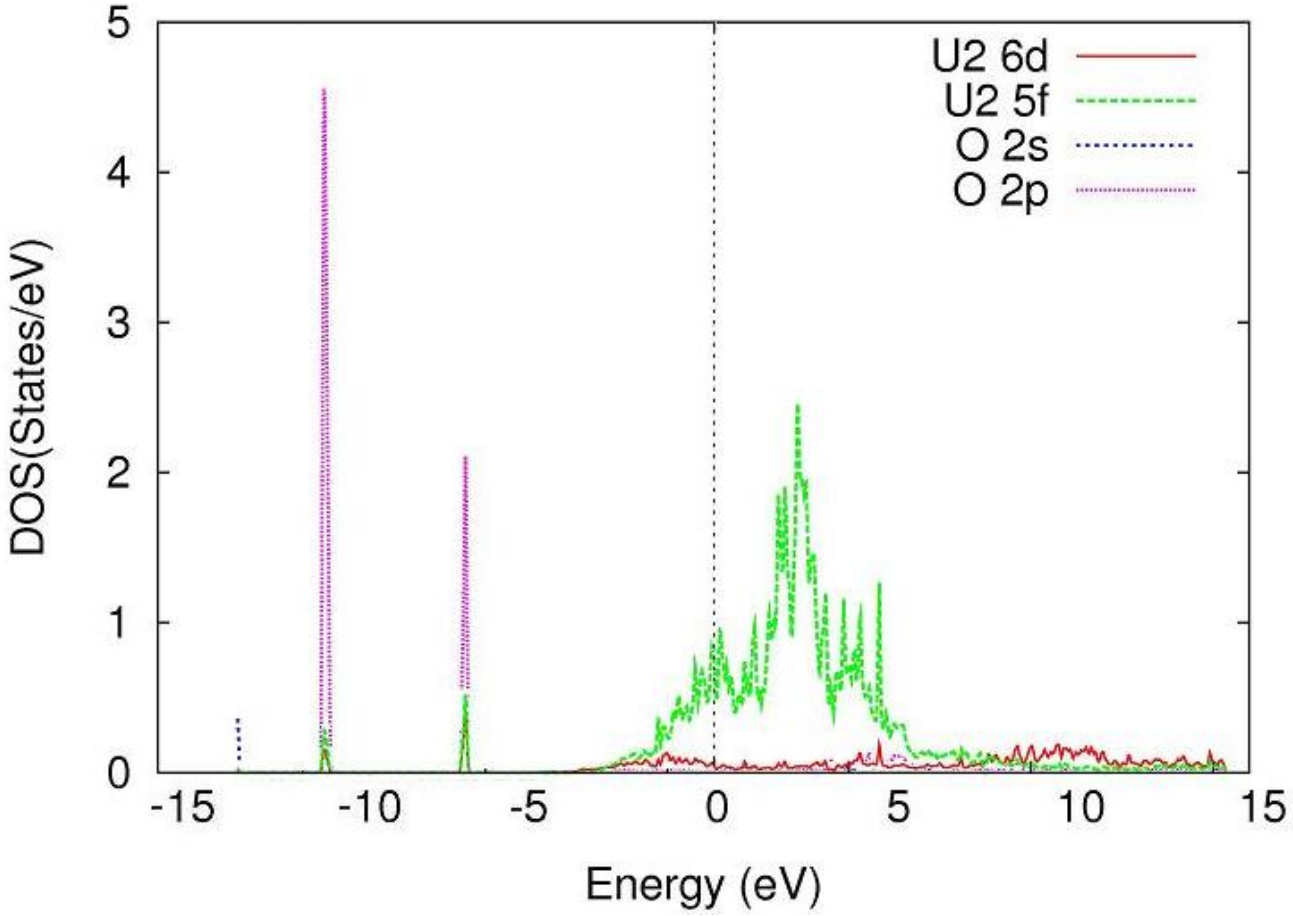

Figure 4.83 LDOS for O adsorption at the center interstitial site with the FM level of theory. U2 is the subsurface U of the slab.

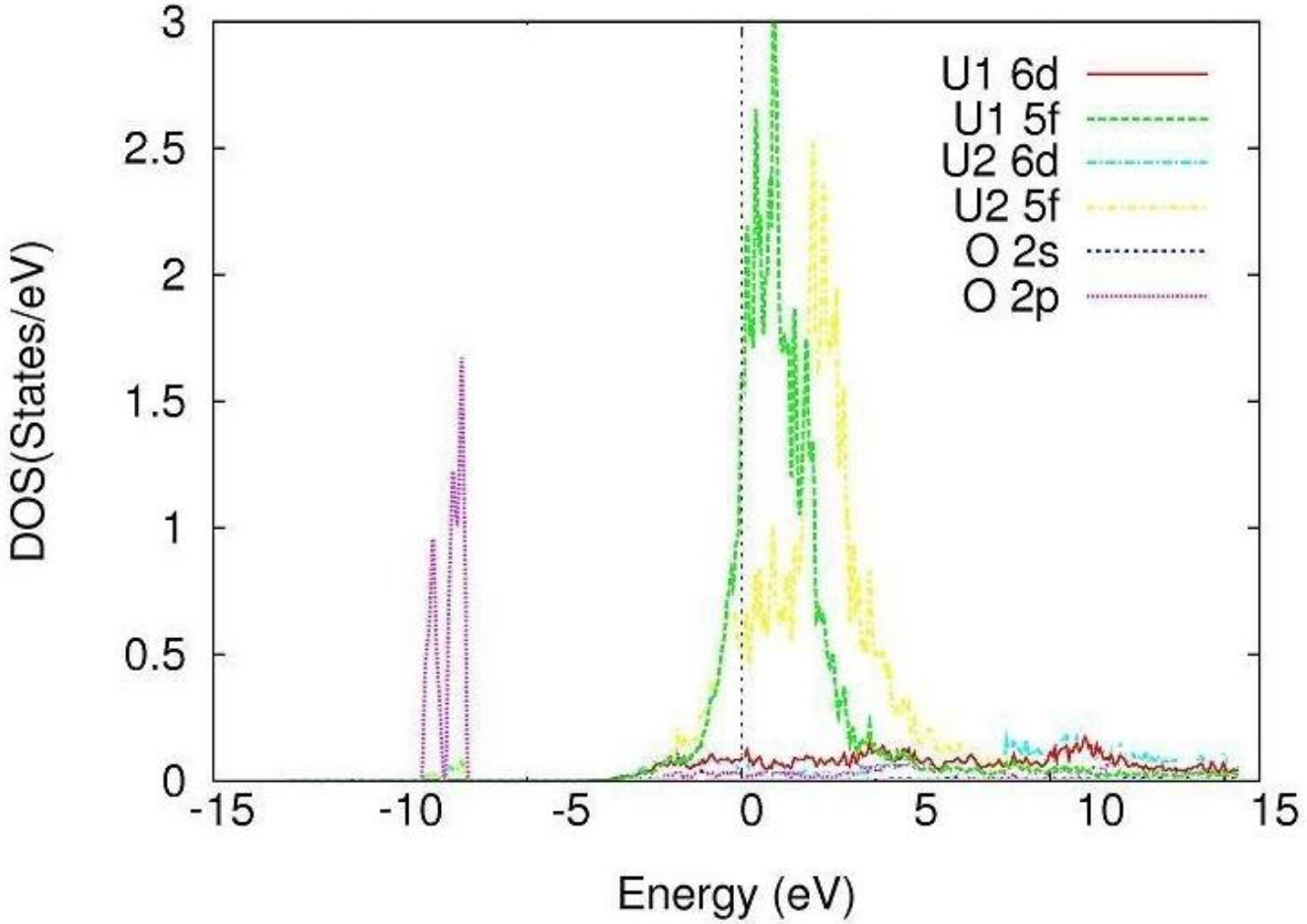

Figure 4.84 LDOS for O adsorption at the bridge interstitial site with the FM level of theory. U1 is the surface U atom and U2 is the subsurface U atom of the slab.

below Fermi surface. Also, seen in Figure 4.87, the 6*d* and 5*f* electrons of the subsurface U atom can be witnessed hybridizing with the 2*p* bands of the O atom. The 5*f* peak of the subsurface U atom is slightly broader above the Fermi level when compared to a subsurface atom of the bare slab. The LDOS for the interstitial bridge is plotted in Figure 4.88. This plot looks nearly identical to the LDOS plot of the FM case at this site, in that only the subsurface orbitals are hybridizing with the O 2*p* orbitals.

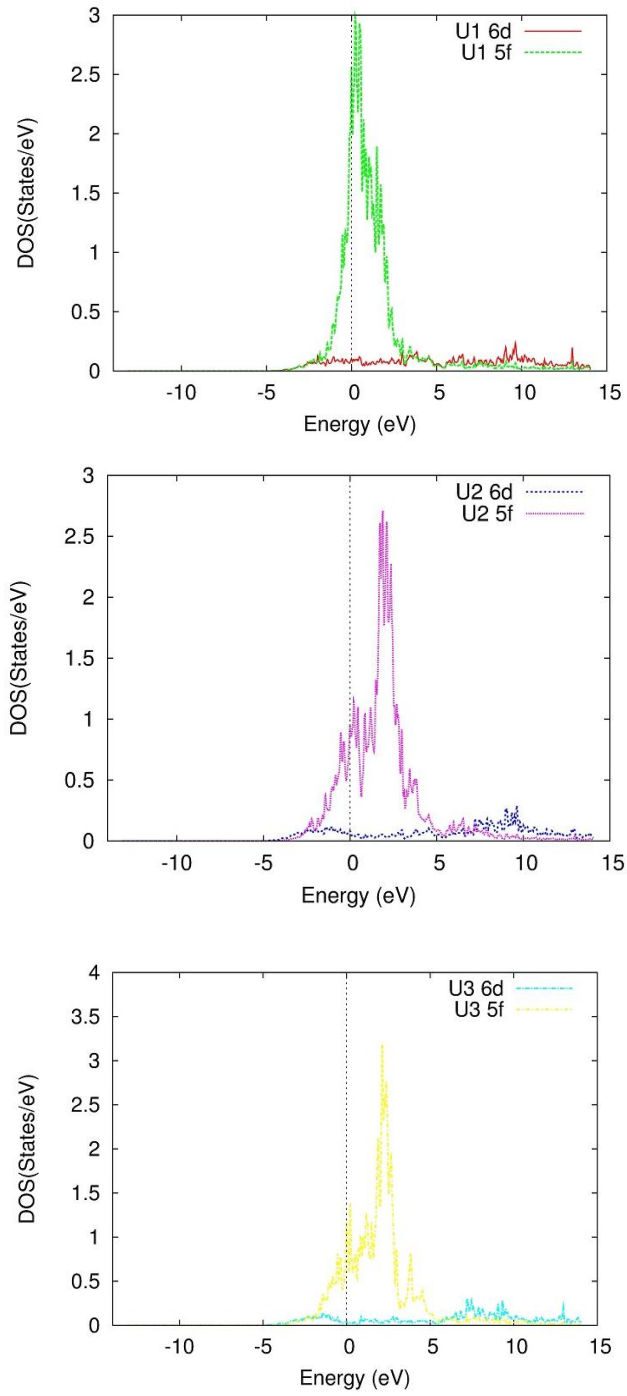

Figure 4.85 LDOS for the 6d and 5f electrons of the surface (U1), subsurface (U2) and center (U3) atom of the bare γ-U (100) slab at the AFM level of theory

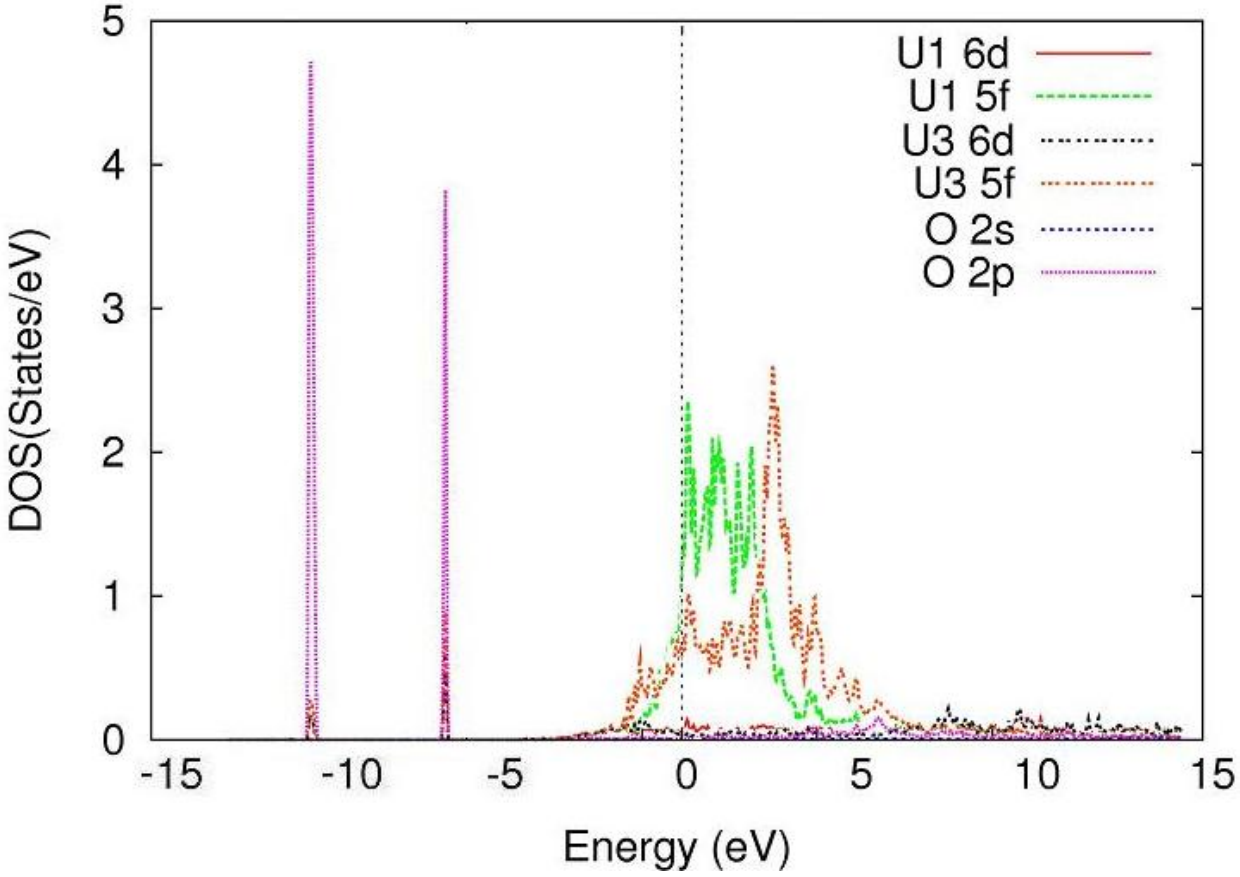

Figure 4.86 LDOS for O adsorption at the top interstitial site with the AFM level of theory. U1 is the surface U atom and U3 is the center U atom of the slab.

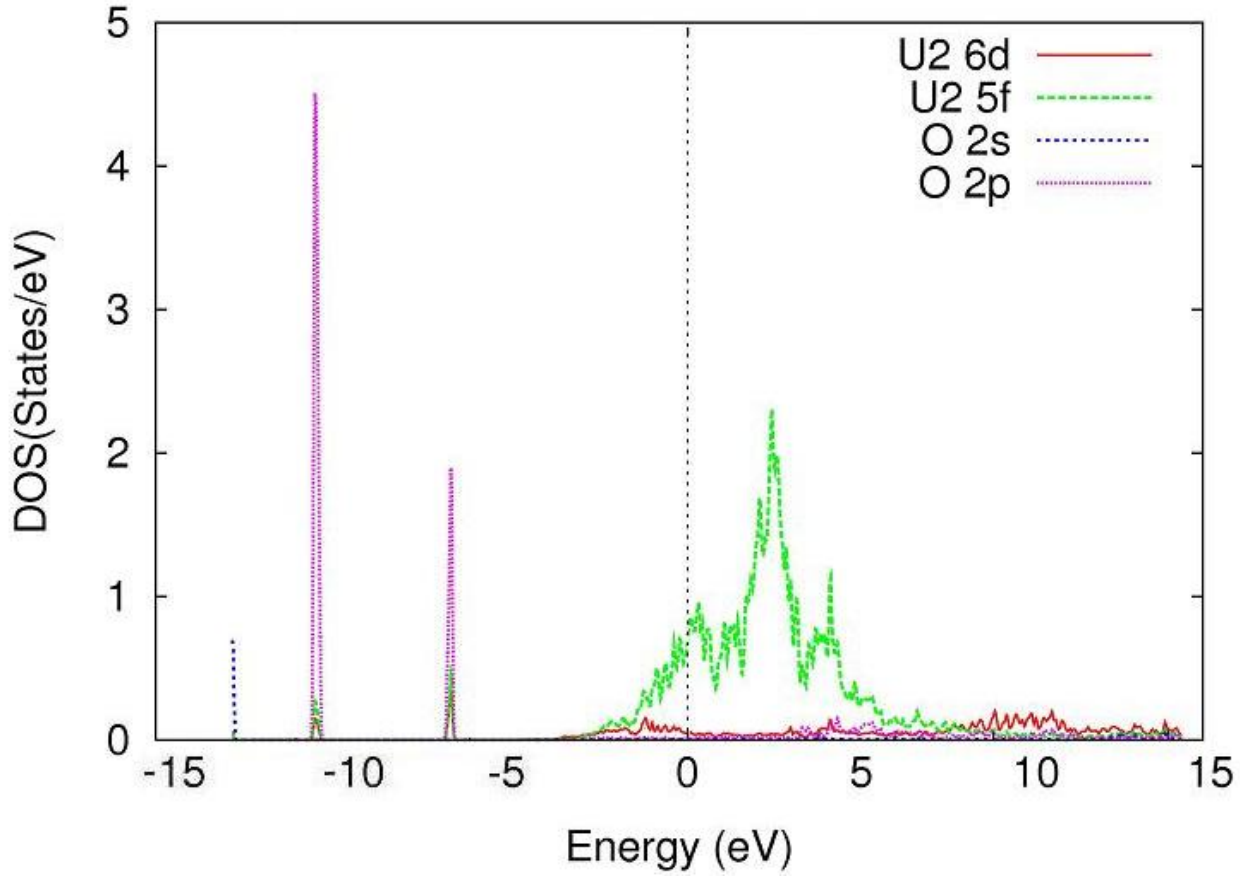

Figure 4.87 LDOS for O adsorption at the center interstitial site with the AFM level of theory. U2 is the subsurface U of the slab.

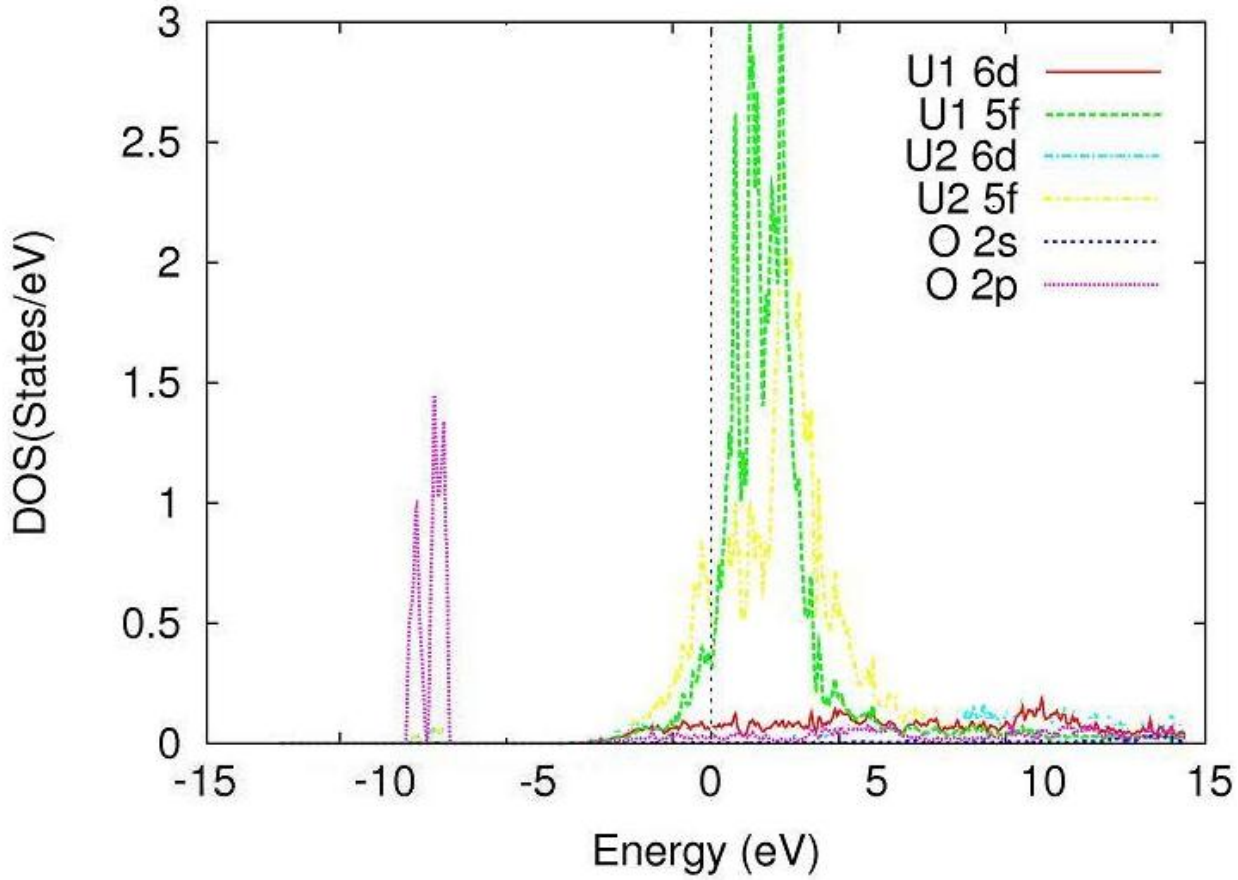

Figure 4.88 LDOS for O adsorption at the bridge interstitial site with the AFM level of theory. U1 is the surface U atom and U2 is the subsurface U atom of the slab.

CHAPTER 5

CONCLUSIONS

The all-electron full-potential linearized augmented plane wave plus local orbitals basis (FP-L/APW+lo) method as implemented in the *WIEN2k* suite of software has been used to study the properties bulk and surface properties of γ-uranium. The ground state bulk lattice constant and bulk modulus are found to be 3.46 A and 113.75 GPa, respectively at the non-magnetic with spin-orbit coupling level (NM+SOC) of theory. The monolayer displays a significant shrinking of the "effective" lattice constant of about 23.55% from bulk theoretical values. Further analysis of the change in energy per added "bulk" indicates that after 5 layers the energy stabilizes and does not change by more than 10 mRy. The surface energy and the work function of the γ-U (100) surface are predicted to be 1.56 J/m^2 and 3.24 eV respectively. We infer that at least a 5- layer film is necessary to study related surface phenomena, such as interactions with environmental atomic and molecular systems. Electronic density of states plots of atoms located at the surface, subsurface and center of a hexa-layer slab indicate *some* localization of the *5f* electrons at or near the Fermi level with a gradual trend towards delocalization with increased depth within the slab.

The FP-L/APW+lo method to DFT was also used to look at corrosive properties when exposed to atomic O and H of the 5 layer γ-U (100) slab at the NM, FM and AFM magnetic configurations. The approach of the adatoms at three symmetrically different sites to the surface, the top, center and bridge, was optimized with respect to energy at the scalar relativistic level of theory and then a single point calculation at the lowest energy distance was conducted at the fully relativistic level. All chemisorption energies for the adsorption of H on the γ-U are positive

pointing toward an exothermic reaction. Comparing the chemisorption energy of the surface adsorption of the H atom, the bridge site is the most favored for adsorption, followed by the center and then top sites. The most favored magnetic state for the H-γ-U system is nonmagnetic, where the chemisorption energy for the bridge site is 3.80 eV at the fully-relativistic level of theory. The change in the work function of the slab with the addition of the H atom ranged from 0.0 to 0.6 eV for all levels of theory. The highest change in the work function occurred at the top site where the H atom has the closest nearest neighbor U atom and the lowest was at the center site with the furthest H-U atom distance. After analyzing the site projected spin and orbital magnetic moment for the FM γ-U (100) slab, a negative change in total magnetic moment on the slab was noticed of 0.13 μ_B at the top site and 0.15 μ_B at the bridge site but a positive change was seen at the center site of 0.1 μ_B. For the AFM slab, the total moment increased by 0.76 μ_B at the top and 0.38 μ_B at the bridge site. No change was seen for the center site adsorption of the H atom possibly due to the distance between the U and H atoms at that location. Looking at the partial charges inside the muffin-tin sphere, the H atom gains an average of 0.045 e^- at all levels of theory although little charge has left the muffin-tin spheres of the atoms of the slab indicating those partial charges are from the interstitial region. Examination of the LDOS of the H 1*s* and U 6*d* and 5*f* electrons indicates both 6*d* and 5*f* participation in bonding with the H atom.

To further the analysis into the diffusion characteristics of the monatomic gases with the γ-U (100) nanolayer, the adatoms were placed inside the lattice at interstitial regions corresponding to the surface sites, top, center and bridge, to determine diffusion properties of the gas. The bridge site was the only site that allowed entry into the slab; therefore the energy was minimized with respect to distance of the adatom below the surface in the z direction. For the H atom, two distinct potential wells were found from the surface to the center of the slab. The barrier between the surface and the first well was found to be 0.41 eV and from the first well to the second 0.71 eV, indicating the H atom prefers binding with the surface over further diffusion into the bulk. H atom binding with the lattice is exothermic as indicated by the positive chemisorption energies of the system. The nonmagnetic state is only slightly more preferred for all sites. The

highest chemisorption energy is at the bridge site at 2.13, 2.11, and 2.13 eV for the NM, FM and AFM levels of theory, respectively, with SOC, followed by the top interstitial site at 1.27 eV at the NM-SOC level and then the center interstitial site at 1.19 eV at the NM-SOC level. The work function decreases by a maximum of 0.07 eV for any interstitial binding of the H atom. The total magnetic moment of the slab increases by approximately 0.1 μ_B. for the top and center interstitial sites and decreases by 0.08 μ_B. for the bridge site in the FM case. For the AFM case, the H atom induces a total magnetic moment of -1.64, 0.00, and 0.17 μ_B. for the top, center and bridge interstitial sites, respectively. The H atom gains about 0.09 e^- in partial charge inside the muffin-tin sphere while bound to the lattice for all sites and all levels of theory. The atoms participating in bonding gain approximately 0.03 e- in their 6d and 5f shells for the top and center sites at the FM and AFM level. For the NM case, only the center site shows the increased distribution in 6d and 5f shells. LDOS plots for these systems show mostly U 6*d* – H 1*s* hybridization and sharp peak of the 5*f* electrons at the U Fermi surface indicating their participation in bonding.

Adsorption of the O atom on the (100) surface of γ-U is more stable than the H-γ-U system and is exothermic with chemisorption energy of 8.43 eV at the most stable bridge site including SOC. The preferred magnetic ordering of the atomic spins is nonmagnetic, which does not coincide with experimental findings of O adsorption on α-U. Since previous theoretical work on UO_2 suggests that at least 25% hybrid DFT is needed to properly describe the UO_2 system, we suggest that the O-γU should also be studied at this level. The optimized distance to the surface for the O atom is 1.98 Å for the top site, 0.75 Å for the center site and 1.32 Å for the bridge site. The change in work function of the bare slab after adsorption of the O atom was 0.92 eV, 0.02 eV and 0.33 eV for the top, center and bridge sites, respectively, at the NM level of theory and was directly related to the distance of the adatom to the surface of the slab. The adsorption of the O atom causes a reduction in the total magnetic moment of the slab for all sites at the FM level of theory. At the NM level of theory, the addition of the adatom reduces the amount of partial charges inside the muffin-tin sphere for atoms on the surface and bottom layers of the slab but increases the charges inside the sphere for atoms of the central layer. Δn plots

indicate ionic exchange between the O atom and the atoms of the surface. Upon entry into the slab at the bridge site the O atom sees a potential barrier of nearly 3 eV approximately 2 Å below the surface causing the atom to remain on the surface and not diffuse into the bulk. Chemisorption energies at interstitial regions within the lattice are endothermic at -0.53 eV for the bridge site with SOC for the most preferred nonmagnetic state. Addition of the O atom in the lattice increased the total magnetic moment of the slab at the FM level of theory. For the AFM level of theory, the O atom in the interstitial top site induced a positive total magnetic moment; in the bridge site it induced a negative magnetic moment and the in the center site no moment was induced. For the interstitial sites, the bond between the O and U atoms is ionic by nature. LDOS plots indicate both 6d and 5f participation in bonding with the O atom on the surface or under it.

APPENDIX A

OPTIMIZED ATOMIC POSITIONS FOR THE (100) γ-U SLAB AND ITS ADSORBATES

Table A. 1 Coordinates for the bare slab relaxed at the NM, FM and AFM level of theory

U1	0.00000	0.00000	0.00000
U2	0.50000	0.00000	0.00000
U3	0.00000	0.50000	0.00000
U4	0.50000	0.50000	0.00000
U5	0.00000	0.00000	0.13739
U6	0.50000	0.00000	0.13739
U7	0.00000	0.50000	0.13739
U8	0.50000	0.50000	0.13739
U9	0.00000	0.00000	0.27478
U10	0.50000	0.00000	0.27478
U11	0.00000	0.50000	0.27478
U12	0.50000	0.50000	0.27478
U13	0.25000	0.25000	0.06869
U14	0.75000	0.25000	0.06869
U15	0.25000	0.75000	0.06869
U16	0.75000	0.75000	0.06869
U17	0.25000	0.25000	0.20608
U18	0.75000	0.25000	0.20608
U19	0.25000	0.75000	0.20608
U20	0.75000	0.75000	0.20608

Table A. 2 Coordinates for the H atom adsorbed on the U surface at the NM top site

0.50000	0.50000	0.36007

Table A. 3 Coordinates for the H atom adsorbed on the U surface at the NM center site

0.25000 0.25000 0.29813

Table A. 4 Coordinates for the H atom adsorbed on the U surface at the NM bridge site

0.50000 0.25000 0.32626

Table A. 5 Coordinates for the H atom adsorbed on the U surface at the NM interstitial top site

0.50000 0.50000 0.20608

Table A. 6 Coordinates for the H atom adsorbed on the U surface at the NM interstitial center site

0.25000 0.25000 0.13739

Table A. 7 Coordinates for the H atom adsorbed on the U surface at the NM interstitial bridge site

0.50000 0.25000 0.17304

Table A. 8 Coordinates for the O atom adsorbed on the U surface at the NM top site

0.50000 0.50000 0.35637

Table A. 9 Coordinates for the O atom adsorbed on the U surface at the NM center site

0.25000 0.25000 0.30566

Table A. 10 Coordinates for the O atom adsorbed on the U surface at the NM bridge site

0.50000 0.25000 0.32934

Table A. 11 Coordinates for the O atom adsorbed on the U surface at the NM interstitial top site

0.50000 0.50000 0.20608

Table A. 12 Coordinates for the O atom adsorbed on the U surface at the NM interstitial center site

0.25000 0.25000 0.13738

Table A. 13 Coordinates for the O atom adsorbed on the U surface at the NM interstitial bridge site

0.50000 0.25000 0.17287

Table A. 14 Coordinates for the H atom adsorbed on the U surface at the FM top site

0.50000 0.50000 0.35982

Table A. 15 Coordinates for the H atom adsorbed on the U surface at the FM center site

0.25000 0.25000 0.29939

Table A. 16 Coordinates for the H atom adsorbed on the U surface at the FM bridge site

0.50000 0.25000 0.33107

Table A. 17 Coordinates for the H atom adsorbed on the U surface at the FM interstitial top site

0.50000 0.50000 0.20601

Table A. 18 Coordinates for the H atom adsorbed on the U surface at the FM interstitial center site

0.25000 0.25000 0.13723

Table A. 19 Coordinates for the H atom adsorbed on the U surface at the FM interstitial bridge site

0.50000 0.25000 0.24051

Table A. 20 Coordinates for the O atom adsorbed on the U surface at the FM top site

0.50000 0.50000 0.35137

Table A. 21 Coordinates for the O atom adsorbed on the U surface at the FM center site

0.25000 0.25000 0.30579

Table A. 22 Coordinates for the O atom adsorbed on the U surface at the FM bridge site

0.50000 0.25000 0.32770

Table A. 23 Coordinates for the O atom adsorbed on the U surface at the FM interstitial top site

0.50000 0.50000 0.20601

Table A. 24 Coordinates for the O atom adsorbed on the U surface at the FM interstitial center site

0.25000 0.25000 0.13723

Table A. 25 Coordinates for the O atom adsorbed on the U surface at the FM interstitial bridge site

0.50000 0.25000 0.17136

Table A. 26 Coordinates for the H atom adsorbed on the U surface at the AFM top site

0.50000 0.50000 0.35993

Table A. 27 Coordinates for the H atom adsorbed on the U surface at the AFM center site

0.25000 0.25000 0.29803

Table A. 28 Coordinates for the H atom adsorbed on the U surface at the AFM bridge site

0.50000 0.25000 0.33056

Table A. 29 Coordinates for the H atom adsorbed on the U surface at the AFM interstitial top site

0.50000 0.50000 0.20604

Table A. 30 Coordinates for the H atom adsorbed on the U surface at the AFM interstitial center site

0.25000 0.25000 0.13729

Table A. 31 Coordinates for the H atom adsorbed on the U surface at the AFM interstitial bridge site

0.50000 0.25000 0.24049

Table A. 32 Coordinates for the O atom adsorbed on the U surface at the AFM top site

0.50000 0.50000 0.35139

Table A. 33 Coordinates for the O atom adsorbed on the U surface at the AFM center site

0.25000 0.25000 0.30577

Table A. 34 Coordinates for the O atom adsorbed on the U surface at the AFM bridge site

0.50000 0.25000 0.32746

Table A. 35 Coordinates for the O atom adsorbed on the U surface at the AFM interstitial top site

0.50000 0.50000 0.20604

Table A. 36 Coordinates for the O atom adsorbed on the U surface at the AFM interstitial center site

0.25000 0.25000 0.13729

Table A. 37 Coordinates for the O atom adsorbed on the U surface at the AFM interstitial bridge site

0.50000 0.25000 0.17123

APPENDIX B

FORTRAN CODE FOR CHANGE IN CHARGE DENSITY PLOTS

```
      implicit none

      integer ii,jj,kk,npxup,npyup,npxdn,npydn,npx,npy
      real  chargeup(5000,5000), chargedn(5000,5000),xlup
      real  ylup,xldn,yldn, xl,yl
      real  charge(5000,5000),charge1(5000,5000)

      open(14,file='rho.1',status='old')
      open(15,file='rho.2',status='old')
      open(17,file='rho.3',status='old')
      open(16,file='SOC.rho',status='unknown')
      open(18,file='gnu_dat',status='unknown')


      read(14,*)npxup, npyup, xlup, ylup
      read(15,*)npxdn, npydn, xldn, yldn
      read(17,*)npx, npy, xl, yl

      read(14,11) ((chargeup(ii,jj),jj=1,npyup),ii=1,npxup)
      read(15,11) ((chargedn(ii,jj),jj=1,npydn),ii=1,npxdn)
      read(17,11) ((charge1(ii,jj),jj=1,npy),ii=1,npx)


      close(14)
      close(15)
      close(17)

      do ii=1,npxup
        do jj=1,npyup
          charge(ii,jj)=chargeup(ii,jj)-chargedn(ii,jj)-charge1(ii,jj)
          write(18,*)charge(ii,jj)
        end do
          write(18,*)
      end do

      write(16,11) ((charge(ii,jj),jj=1,npydn),ii=1,npxdn)

      close(16)
      close(18)

11     format(5e16.8)

      stop
      end
```

REFERENCES

[1] J. Katz, *The chemistry of uranium*, 1st ed. New York: McGraw-Hill, 1951.

[2] L. R. Morss, *Transuranium Elements: A Half Century (American Chemical Society Publication)*, 1st ed. Washington, D.C.: American Chemical Society, 1992, pp. 1-562.

[3] J. J. Katz, *The Chemistry of the Actinide and Transactinide Elements (5 Volume Set) (v. 1-5)*, 3rd ed. New York: Springer, 2007, pp. 1-3682.

[4] E. Fermi, "Possible production of elements of atomic number higher than 92," *nature*, vol. 133, pp. 898-899, 1934.

[5] O. R. Hahn and F. Strassmann, "Concerning the existence of alkaline earth metals resulting from neutron irradiation of uranium," *Die Naturwissenschaften* , vol. 27, pp. 11-15, 1939.

[6] I. Joliot-Curie and P. Savitch, "Sur le radioelement de periode 3,5 h. forme dans l'uranium par les neutrons," *Comptes Rendus*, vol. 206, pp. 1643-1644, 1938.

[7] L. Meitner and O. R. Hahn, "Disintegration of uranium by neutrons: a new type of reaction," *nature*, vol. 143, no. 3615, pp. 239-240, 1939.

[8] G. T. Seaborg, "Origin of the actinide concept," in *Handbook on the Physics and Chemistry of Rare Earths*, 18th ed., vol. 18, K. A. Gschneidner Jr., L. Eyring, G. R. Choppin, and G. H. Landet, Eds. Elsevier, 1994, pp. 4-6, 10-14.

[9] M. Englert, L. Krall, and R. C. Ewing, "Is nuclear fission a sustainable source of energy?," *MRS Bullletin*, vol. 37, no. 4, pp. 417-424, 2012.

[10] C. Pistner, W. Liebert, and F. Fujara, "Neutronics calculations on the impact of burnable poisons to safety and non-proliferation aspects of inert matrix fuel," *Journal of Nuclear Materials*, vol. 352, no. 1–3, pp. 268-275, Jun. 2006.

[11] "Fast Reactor Technology - Reactors designed/built by Argonne National Laboratory." [Online]. Available: http://www.ne.anl.gov/About/reactors/frt.shtml. [Accessed: 30-May-2012].

[12] "Prototype Prism proposed for Savannah River," *World Nuclear News*, 2010. [Online]. Available: http://www.world-nuclear-news.org/NN-Prototype_Prism_proposed_for_Savannah_River-2810104.html. [Accessed: 30-May-2012].

[13] L. C. Walters, “Metallic nuclear fuels,” in *Encyclopedia of Materials Science and Engineering*, 4th ed., Pergamon Press, 1986, pp. 2980-2981.

[14] “Uranium | uranium for nuclear power,” *World Nuclear Association*, 2011. [Online]. Available: http://www.world-nuclear.org/education/uran.htm. [Accessed: 04-Mar-2012].

[15] M. I. Mirandou, S. N. Balart, M. Ortiz, and M. S. Granovsky, “Characterization of the reaction layer in U–7wt%Mo/Al diffusion couples,” *Journal of Nuclear Materials*, vol. 323, no. 1, pp. 29-35, Nov. 2003.

[16] K. H. Kim, D. B. Lee, C. K. Kim, G. E. Hofman, and K. W. Paik, “Characterization of U-2 wt% Mo and U-10 wt% Mo alloy powders prepared by centrifugal atomization,” *Journal of Nuclear Materials*, vol. 245, no. 2–3, pp. 179-184, Jun. 1997.

[17] J. M. Park et al., “Effect of Si and Zr on the interdiffusion of U–Mo alloy and Al,” *Journal of Nuclear Materials*, vol. 374, no. 3, pp. 422-430, Mar. 2008.

[18] H. J. Ryu, Y. S. Han, J. M. Park, S. D. Park, and C. K. Kim, “Reaction layer growth and reaction heat of U–Mo/Al dispersion fuels using centrifugally atomized powders,” *Journal of Nuclear Materials*, vol. 321, no. 2–3, pp. 210-220, Sep. 2003.

[19] S. Van den Berghe, W. Van Renterghem, and A. Leenaers, “Transmission electron microscopy investigation of irradiated U–7wt%Mo dispersion fuel,” *Journal of Nuclear Materials*, vol. 375, no. 3, pp. 340-346, Apr. 2008.

[20] J.-S. Lee, C.-H. Lee, K. H. Kim, and V. Em, “Study of decomposition and reactions with aluminum matrix of dispersed atomized U-10 wt% Mo alloy,” *Journal of Nuclear Materials*, vol. 306, no. 2–3, pp. 147-152, Dec. 2002.

[21] A. Leenaers et al., “Post-irradiation examination of uranium?7wt% molybdenum atomized dispersion fuel,” *Journal of Nuclear Materials*, vol. 335, no. 1, pp. 39-47, Oct. 2004.

[22] J. L. Snelgrove, G. L. Hofman, M. K. Meyer, C. L. Trybus, and T. C. Wiencek, “Development of very-high-density low-enriched-uranium fuels,” *Nuclear Engineering and Design*, vol. 178, no. 1, pp. 119-126, 1997.

[23] N. Wieschalla et al., “Heavy ion irradiation of U–Mo/Al dispersion fuel,” *Journal of Nuclear Materials*, vol. 357, no. 1–3, pp. 191-197, Oct. 2006.

[24] M. K. Meyer et al., “Low-temperature irradiation behavior of uranium–molybdenum alloy dispersion fuel,” *Journal of Nuclear Materials*, vol. 304, no. 2–3, pp. 221-236, Aug. 2002.

[25] B.-S. Seong et al., “Neutron diffraction study of U-10 wt% Mo alloy,” *Journal of Nuclear Materials*, vol. 277, no. 2, p. 6, 2000.

[26] V. P. Sinha et al., “Development, preparation and characterization of uranium molybdenum alloys for dispersion fuel application,” *Journal of Alloys and Compounds*, vol. 473, no. 1–2, pp. 238-244, Apr. 2009.

[27] J.-S. Lee, C.-H. Lee, K. H. Kim, and V. Em, “Neutron diffraction study of U-5.4 wt% Mo alloy,” *Journal of Nuclear Materials*, vol. 280, no. 1, p. 4, 2000.

[28] F. Mazaudier, C. Proye, and F. Hodaj, “Further insight into mechanisms of solid-state interactions in UMo/Al system,” *Journal of Nuclear Materials*, vol. 377, no. 3, pp. 476-485, Jul. 2008.

[29] I. C. Martins, G. Z. Soriano, M. Durazzo, E. F. U. de Carvalho, L. S. Montagna, and A. M. Saliba-Silva, “Thermal Interdiffusion Products of U-10Mo in Al Matrix,” *Materials Science Forum*, vol. 660–661, pp. 69-75, Nov. 2010.

[30] F. B. Vaz de Oliveira, M. Durazzo, E. Fontenele Urano de Carvalho, A. M. Saliba-Silva, and H. Gracher Riella, “Powder formation of {gamma} uranium-molybdenum alloys via hydration-dehydration,” in *The Rertr-2007 International Meeting on Reduced Enrichment for Research and Test Reactors*, 2008.

[31] W. M. Haynes, Ed., *CRC Handbook of Chemistry and Physics*, 91st . Boca Raton, FL: CRC Press/Taylor and Francis Group, 2011, p. 2610.

[32] P. Söderlind, O. Eriksson, B. Johansson, J. M. Wills, and A. M. Boring, “A unified picture of the crystal structures of metals,” *Nature*, vol. 374, no. 6522, pp. 524-525, Apr. 1995.

[33] Y. Hao, O. Eriksson, G. Fernando, and B. Cooper, “Surface electronic structure of γ-uranium,” *Physical Review B*, vol. 47, no. 11, pp. 6680-6684, Mar. 1993.

[34] L. Fast et al., “Theoretical aspects of the charge density wave in uranium,” *Physical Review Letters*, vol. 81, no. 14, pp. 2978-2981, Oct. 1998.

[35] A. C. Lawson, C. E. Olsen, J. W. Richardson Jr., M. H. Mueller, and G. H. Lander, “Structure of beta-uranium,” *Acta Crystallographica Section B: Structural Science*, vol. 44, pp. 89-96, 1988.

[36] J. Donohue, “Structures of the elements,” Jan. 1974.

[37] E. M. Collins, N. Kioussis, S. P. Lim, and B. R. Cooper, “Ab initio study of anisotropic magnetism in uranium compounds,” *Journal of Applied Physics*, vol. 85, no. 8, p. 6226, Apr. 1999.

[38] O. Eriksson, B. Johansson, and M. S. S. Brooks, “Meta-magnetism in UCoAl,” *Journal of Physics: Condensed Matter*, vol. 1, no. 25, pp. 4005-4011, Jun. 1989.

[39] O. Yoshichika et al., “Recent advances in the magnetism and superconductivity of heavy fermion systems,” *Journal of the Physical Society of Japan*, vol. 73, no. 4, pp. 769-787, 1946.

[40] M. S. S. Brooks, O. Eriksson, B. Johansson, J. J. M. Franse, and P. H. Frings, “Chemical bonding and magnetism in 3d-5f intermetallics,” *Journal of Physics F: Metal Physics*, vol. 18, no. 3, p. L33-L39, Mar. 1988.

[41] B. T. Matthias, C. W. Chu, E. Corenzwit, and D. Wohlleben, “Ferromagnetism and superconductivity in uranium compounds.,” *Proceedings of the National Academy of Sciences of the United States of America*, vol. 64, no. 2, pp. 459-461, 1969.

[42] L. F. Bates and J. R. Mallard, “The Magnetic Properties of Uranium and Uranium-Iron Alloys,” *Proceedings of the Physical Society. Section B*, vol. 63, no. 7, pp. 520-526, Jul. 1950.

[43] A. Hjelm, O. Eriksson, and B. Johansson, “Break-down of Hund’s third rule for induced magnetism in U metal,” *Physical Review Letters*, vol. 71, no. 9, pp. 1459-1461, Aug. 1993.

[44] N. Stojić, J. Davenport, M. Komelj, and J. Glimm, “Surface magnetic moment in α-uranium by density-functional theory,” *Physical Review B*, vol. 68, no. 9, Sep. 2003.

[45] M. Kurihara, M. Hirata, R. Sekine, J. Onoe, and H. Nakamatsu, “Theoretical study on the alloying behavior of γ-uranium metal: γ-uranium alloy with 3d transition metals,” *Journal of Nuclear Materials*, vol. 326, no. 2–3, pp. 75-79, Mar. 2004.

[46] C.-S. Yoo, H. Cynn, and P. Söderlind, “Phase diagram of uranium at high pressures and temperatures,” *Physical Review B*, vol. 57, no. 17, pp. 10359-10362, May 1998.

[47] T. Gouder, “Thin layers in actinide research,” *Journal of Alloys and Compounds*, vol. 271–273, pp. 841-845, Jun. 1998.

[48] S. Erkoc, T. Bastug, M. Hirata, and S. Tachimori, “Molecular-dynamics simulations of uranium microclusters,” *Journal of the Physical Society of Japan*, vol. 68, no. 2, pp. 440-445, 1999.

[49] T. . Totemeier, “Characterization of uranium corrosion products involved in a uranium hydride pyrophoric event,” *Journal of Nuclear Materials*, vol. 278, no. 2–3, pp. 301-311, Apr. 2000.

[50] E. Swissa, J. Bloch, U. Atzmony, and M. H. Mintz, “Interactions of oxygen and uranium studied by combined AES, XPS and DRS techniques,” *Surface Science*, vol. 214, no. 1–2, pp. 323-333, Apr. 1989.

[51] J. Bloch, U. Atzmony, M. P. Dariel, M. H. Mintz, and N. Shamir, “Surface spectroscopy studies of the oxidation behavior of uranium,” *Journal of Nuclear Materials*, vol. 105, no. 2–3, pp. 196-200, Feb. 1982.

[52] J. Haschke, “Corrosion of uranium in air and water vapor: consequences for environmental dispersal,” *Journal of Alloys and Compounds*, vol. 278, no. 1–2, pp. 149-160, Aug. 1998.

[53] W. McLean, C. Colmenares, R. Smith, and G. Somorjai, “Electron-spectroscopy studies of clean thorium and uranium surfaces. Chemisorption and initial stages of reaction with O_{2}, CO, and CO_{2},” *Physical Review B*, vol. 25, no. 1, pp. 8-24, Jan. 1982.

[54] K. A. Winer, “Initial stages of uranium oxidation: a surface study,” California Univ., Davis (USA), 1985.

[55] J. B. Condon, “Kinetics of the uranium-hydrogen system,” *The Journal of Chemical Physics*, vol. 59, no. 2, p. 855, Jul. 1973.

[56] E. Wiberg, A. F. Holleman, and N. Wiberg, *Inorganic Chemistry*. Academic Press, 2001, p. 1884.

[57] G. T. Seaborg, “Uranium,” in *The Encyclopedia of the Chemical Elements*, C. A. Hampel, Ed. Skokie, Illinois: Reinhold Book Corporation, 1968, p. 782.

[58] C. W. Solbrig, J. R. Krsul, and D. N. Olsen, “Pyrophoricity of uranium in long-term storage environments,” Dec. 1994.

[59] C. J. Beevers and G. T. Newman, “Hydrogen embrittlement in uranium,” *Journal of Nuclear Materials*, vol. 23, no. 1, pp. 10-18, Jul. 1967.

[60] J. B. Condon, “Alternative model for nonstoichiometry in uranium hydride,” *The Journal of Physical Chemistry*, vol. 79, no. 1, pp. 42-48, Jan. 1975.

[61] C. D. Taylor and R. Scott Lillard, “Ab-initio calculations of the hydrogen–uranium system: Surface phenomena, absorption, transport and trapping,” *Acta Materialia*, vol. 57, no. 16, pp. 4707-4715, Sep. 2009.

[62] O. G. Peterson, “patent us - self-regulating nuclear power module,” U.S. Patent US 2008/0069289 A12008.

[63] T. Gouder, C. Colmenares, J. R. Naegele, and J. Verbist, “Study of the surface oxidation of uranium by UV photoemission spectroscopy,” *Surface Science*, vol. 235, no. 2–3, pp. 280-286, Sep. 1990.

[64] A. Arrott and J. Goldman, “Magnetic analysis of the uranium-oxygen system,” *Physical Review*, vol. 108, no. 4, pp. 948-953, Nov. 1957.

[65] M. Shuai, H. Hairong, W. Xin, Z. Pengji, and T. Anmin, “Theoretical study on the reaction between uranium and O2,” *Journal of Molecular Structure: THEOCHEM*, vol. 536, no. 2–3, pp. 269-276, Feb. 2001.

[66] J. C. Boettger and A. K. Ray, “All-electron LCGTO calculations for uranium dioxide,” *International Journal of Quantum Chemistry*, vol. 80, no. 4–5, pp. 824-830, 2000.

[67] J. C. Boettger and A. K. Ray, “Fully relativistic density functional calculations on hydroxylated actinide oxide surfaces,” *International Journal of Quantum Chemistry*, vol. 90, no. 4–5, pp. 1470-1477, Oct. 2002.

[68] K. Kudin, G. Scuseria, and R. Martin, “Hybrid density-functional theory and the insulating gap of UO2,” *Physical Review Letters*, vol. 89, no. 26, Dec. 2002.

[69] M. N. Huda and a. K. Ray, “Density functional study of O2 adsorption on (100) surface of γ-uranium,” *International Journal of Quantum Chemistry*, vol. 102, no. 1, pp. 98-105, 2005.

[70] J. Paulovič, L. Gagliardi, J. M. Dyke, and K. Hirao, “A theoretical study of the gas-phase chemi-ionization reaction between uranium and oxygen atoms,” *The Journal of Chemical Physics*, vol. 122, no. 14, p. 144317, Apr. 2005.

[71] C. Guéneau, M. Baichi, D. Labroche, C. Chatillon, and B. Sundman, “Thermodynamic assessment of the uranium–oxygen system,” *Journal of Nuclear Materials*, vol. 304, no. 2–3, pp. 161-175, Aug. 2002.

[72] P. P. Dholabhai and A. K. Ray, “A density functional study of atomic oxygen and carbon adsorptions on (100) surface of γ-Uranium,” *Physica Scripta*, vol. 75, no. 4, pp. 506-514, Apr. 2007.

[73] P. P. Dholabhai, “On The Behavior Of The 5f Electrons,” Physics, 2007.

[74] P. Hohenberg and W. Kohn, “Inhomogeneous electron gas,” *Physical Review B*, vol. 136, no. 3, pp. 864-871, Nov. 1964.

[75] W. Kohn and L. J. Sham, “Self-consistent equations including exchange and correlation effects,” *Physical Review A*, vol. 140, no. 4, pp. 1133-1138, Nov. 1965.

[76] E. Lieb, “Variational Principle for Many-Fermion Systems,” *Physical Review Letters*, vol. 46, no. 7, pp. 457-459, Feb. 1981.

[77] R. G. Parr and W. Yang, “Density functional approach to the frontier-electron theory of chemical reactivity,” *Journal of the American Chemical Society*, vol. 106, no. 14, pp. 4049-4050, Jul. 1984.

[78] R. G. Parr and W. Yang, *Density-Functional Theory of Atoms and Molecules*. New York, New York: Oxford University Press, 1994, p. 333.

[79] K. Capelle, “A bird’s-eye view of density-functional theory,” *cond-mat/0211443v5*, p. 69, Nov. 2002.

[80] A. Nagy, “Excitation energies calculated with parameter-free exchange potential in the density functional theory,” *Journal of Physics B: Atomic, Molecular and Optical Physics*, vol. 24, no. 22, pp. 4691-4694, Nov. 1991.

[81] A. Nagy, “Exchange energy in the exact exchange-only density functional theory,” *Journal of Physics B: Atomic, Molecular and Optical Physics*, vol. 26, no. 1, pp. 43-48, Jan. 1993.

[82] A. Nagy and I. Andrejkovics, “Excitation energies in the local density functional theory,” *Journal of Physics B: Atomic, Molecular and Optical Physics*, vol. 27, no. 2, pp. 233-240, Jan. 1994.

[83] T. Kato, “On the eigenfunctions of many-particle systems in quantum mechanics,” *Communications on Pure and Applied Mathematics*, vol. 10, no. 2, pp. 151-177, 1957.

[84] M. Levy, “Electron densities in search of Hamiltonians,” *Physical Review A*, vol. 26, no. 3, pp. 1200-1208, Sep. 1982.

[85] J. P. Perdew and Y. Wang, “Accurate and simple analytic representation of the electron-gas correlation energy,” *Physical Review B*, vol. 45, no. 23, pp. 13244-13249, Jun. 1992.

[86] J. Perdew et al., “Erratum: Atoms, molecules, solids, and surfaces: Applications of the generalized gradient approximation for exchange and correlation,” *Physical Review B*, vol. 48, no. 7, pp. 4978-4978, Aug. 1993.

[87] J. P. Perdew, K. Burke, and M. Ernzerhof, “Generalized gradient approximation made simple,” *Physical Review Letters*, vol. 77, no. 18, pp. 3865-3868, Oct. 1996.

[88] C. Lee, W. Yang, and R. G. Parr, “Development of the Colle-Salvetti correlation-energy formula into a functional of the electron density,” *Physical Review B*, vol. 37, no. 2, pp. 785-789, Jan. 1988.

[89] A. D. Becke, “Density-functional thermochemistry. II. The effect of the Perdew–Wang generalized-gradient correlation correction,” *The Journal of Chemical Physics*, vol. 97, no. 12, p. 9173, Dec. 1992.

[90] A. D. Becke, “Density-functional thermochemistry. I. The effect of the exchange-only gradient correction,” *The Journal of Chemical Physics*, vol. 96, no. 3, p. 2155, Feb. 1992.

[91] A. D. Becke, “Density-functional thermochemistry. III. The role of exact exchange,” *The Journal of Chemical Physics*, vol. 98, no. 7, p. 5648, Apr. 1993.

[92] P. Novák, J. Kuneš, L. Chaput, and W. E. Pickett, “Exact exchange for correlated electrons,” *physica status solidi (b)*, vol. 243, no. 3, pp. 563-572, Mar. 2006.

[93] R. Atta-Fynn and A. K. Ray, “Probing the 5f electrons in Am-I by hybrid density functional theory,” *Chemical Physics Letters*, vol. 482, no. 4–6, pp. 223-227, Nov. 2009.

[94] A. D. Becke, “A new mixing of Hartree–Fock and local density-functional theories,” *The Journal of Chemical Physics*, vol. 98, no. 2, p. 1372, Jan. 1993.

[95] M. Ernzerhof and G. E. Scuseria, “Assessment of the Perdew–Burke–Ernzerhof exchange-correlation functional,” *The Journal of Chemical Physics*, vol. 110, no. 11, p. 5029, Mar. 1999.

[96] C. Adamo and V. Barone, “Toward reliable density functional methods without adjustable parameters: The PBE0 model,” *The Journal of Chemical Physics*, vol. 110, no. 13, p. 6158, Apr. 1999.

[97] R. Atta-Fynn and A. K. Ray, “Does hybrid density functional theory predict a non-magnetic ground state for δ-Pu?,” *EPL (Europhysics Letters)*, vol. 85, no. 2, p. 27008, Jan. 2009.

[98] J. Heyd, G. E. Scuseria, and M. Ernzerhof, “Hybrid functionals based on a screened Coulomb potential,” *The Journal of Chemical Physics*, vol. 118, no. 18, p. 8207, May 2003.

[99] J. J. Sakurai, *Advanced Quantum Mechanics*. Addison Wesley, 1967, p. 336.

[100] P. Strange, *Relativistic Quantum Mechanics: with applications in condensed matter and atomic physics*. Cambridge, UK: Cambridge University Press, 1998, p. 594.

[101] *Relativistic Effects in Heavy-Element Chemistry and Physics (Wiley Series in Theoretical Chemistry)*. Wiley, 2003, p. 328.

[102] J. Slater, "Wave functions in a periodic potential," *Physical Review*, vol. 51, no. 10, pp. 846-851, May 1937.

[103] P. Blaha, K. Schwarz, G. K. H. Madsen, D. Kvasnicka, and J. Luitz, "WIEN2k an augmented plane wave plus local orbitals program for calculating crystal properties." Univ.Tech. Austria, Vienna, 2011.

[104] O. K. Andersen, "Linear methods in band theory," *Physical Review B*, vol. 12, no. 8, pp. 3060-3083, Oct. 1975.

[105] D. Singh, "Ground-state properties of lanthanum: Treatment of extended-core states," *Physical Review B*, vol. 43, no. 8, pp. 6388-6392, Mar. 1991.

[106] E. Sjöstedt, L. Nordström, and D. . Singh, "An alternative way of linearizing the augmented plane-wave method," *Solid State Communications*, vol. 114, no. 1, pp. 15-20, Mar. 2000.

[107] G. Madsen, P. Blaha, K. Schwarz, E. Sjöstedt, and L. Nordström, "Efficient linearization of the augmented plane-wave method," *Physical Review B*, vol. 64, no. 19, Oct. 2001.

[108] A. H. MacDonald, W. E. Picket, and D. D. Koelling, "A linearised relativistic augmented-plane-wave method utilising approximate pure spin basis functions," *Journal of Physics C: Solid State Physics*, vol. 13, no. 14, pp. 2675-2683, May 1980.

[109] J. Wang, L. Ma, and A. K. Ray, "On the magnetic and thermodynamic properties of Americium-II: A hybrid density functional theoretic study," *Physics Letters A*, vol. 374, no. 46, pp. 4704-4712, Oct. 2010.

[110] J. C. Fuggle, A. F. Burr, L. M. Watson, D. J. Fabian, and W. Lang, "X-ray photoelectron studies of thorium and uranium," *Journal of Physics F: Metal Physics*, vol. 4, no. 2, pp. 335-342, Feb. 1974.

[111] D. Gao and A. K. Ray, "On the convergence of the electronic structure properties of the fcc americium (001) surface," *Surface Science*, vol. 600, no. 22, pp. 4941-4952, Nov. 2006.

[112] D. Gao and A. K. Ray, "The 5f localization/delocalization in square and hexagonal americium monolayers: a FP-LAPW electronic structure study," *The European Physical Journal B*, vol. 50, no. 3, pp. 497-503, May 2006.

[113] E. N. Hodkin, D. A. Mortimer, M. G. Nicholas, and D. M. Poole, "The surface and interfacial energies of the uranium-uranium carbide system," *Journal of Nuclear Materials*, vol. 39, no. 1, pp. 59-68, Apr. 1971.

[114] J. C. Rivière, “The work function of uranium,” *Proceedings of the Physical Society*, vol. 80, no. 1, pp. 116-123, Jul. 1962.

[115] D. E. Barry, B. J. Hopkins, and A. J. Sargood, “Some work functions of vapour deposited uranium on polycrystalline tungsten foil,” *Surface Science*, vol. 7, no. 3, pp. 365-379, Jul. 1967.

[116] C. Lea and C. H. B. Mee, “The photoelectric work function of monolayer films of uranium on polycrystalline tungsten,” *Surface Science*, vol. 8, no. 4, pp. 417-425, Nov. 1967.

[117] D. R. Morrison and A. K. Ray, “Quantum size effects in the electronic structure properties of γ-U (100) nanolayers,” *Journal of Computational and Theoretical Nanoscience*, vol. 9, pp. 637-644, 2012.

[118] F. Wagner, T. Laloyaux, and M. Scheffler, “Errors in Hellmann-Feynman forces due to occupation-number broadening and how they can be corrected,” *Physical Review B*, vol. 57, no. 4, pp. 2102-2107, Jan. 1998.

[119] R. Atta-Fynn and A. K. Ray, “A full-potential linearized augmented plane wave (FP-LAPW) study of atomic carbon, nitrogen, and oxygen chemisorption on the (100) surface of δ-Pu,” *Physica B: Condensed Matter*, vol. 392, no. 1–2, pp. 112-126, Apr. 2007.

[120] R. Atta-Fynn and A. Ray, “Ab initio full-potential fully relativistic study of atomic carbon, nitrogen, and oxygen chemisorption on the (111) surface of δ-Pu,” *Physical Review B*, vol. 75, no. 19, May 2007.

[121] R. Atta-Fynn and A. K. Ray, “Relaxation of the (111) surface of δ-Pu and effects on atomic adsorption: An ab initio study,” *Physica B: Condensed Matter*, vol. 400, no. 1–2, pp. 307-316, Nov. 2007.

[122] R. Atta-Fynn and A. Ray, “Atomic adsorption on the (020) surface of α-Pu: A density functional study,” *Physical Review B*, vol. 77, no. 8, Feb. 2008.

[123] A. Soon, M. Todorova, B. Delley, and C. Stampfl, “Oxygen adsorption and stability of surface oxides on Cu(111): A first-principles investigation,” *Physical Review B*, vol. 73, no. 16, Apr. 2006.

[124] A. Kokalj, “XCrySDen—a new program for displaying crystalline structures and electron densities,” *Journal of Molecular Graphics and Modelling*, vol. 17, no. 3–4, pp. 176-179, Jun. 1999.

[125] L. Ma, R. Atta-Fynn, and A. Ray, “Elemental and mixed actinide dioxides: an ab initio study,” *Journal of Theoretical and Computational Chemistry*, vol. 11, no. 3, pp. 611-629, 2011.

BIOGRAPHICAL INFORMATION

The author received a Bachelor of Science degree in Liberal Arts with a focus in physics and Arabic from Excelsior College and an Associates of Arts degree in Arabic language while serving in the U. S. Navy. Afterwards, she attended Texas A&M University at College Station, Texas and participated in many research projects focusing on physical properties of the ocean at their Galveston campus before beginning graduate study at the University of Texas at Arlington in 2010.